AUTONOMOUS LOCALIZATION BY INTEGRATING Wi-Fi AND MEMS SENSORS IN LARGE-SCALE INDOOR SPACES

YU YUE

PhD

The Hong Kong Polytechnic University

This programme is jointly offered by The Hong Kong Polytechnic University and Wuhan University

2023

This page is intentionally left blank

The Hong Kong Polytechnic University

Department of Land Surveying and Geo-Informatics

Wuhan University

State Key Laboratory of Information Engineering in Surveying,

Mapping and Remote Sensing

Autonomous Localization by Integrating Wi-Fi and MEMS Sensors in Large-scale Indoor Spaces

YU Yue

A Thesis Submitted in Partial Fulfilment of the Requirements

for the Degree of Doctor of Philosophy

Mar 2022

This page is intentionally left blank

CERTIFICATE OF ORIGINALITY

I hereby declare that this thesis is my own work and that, to the best of my knowledge and belief, it reproduces no material previously published or written, nor material that has been accepted for the award of any other degree or diploma, except where due acknowledgement has been made in the text.

____________(Signed)

YU Yue (Name of student)

This page is intentionally left blank

Abstract

Location-based services (LBS) have become more and more important with the development of Internet of Things (IoT) technology and increasing popularity of IoT terminals in recent years. Global Navigation Satellite System (GNSS) is widely used for positioning outdoors while it is still challenging to realize autonomous, precise and universal indoor localization based on the existing devices. Among most indoor positioning technologies, the Wireless Fidelity (Wi-Fi) based positioning is regarded as an effective way for realizing ubiquitous and high-precision indoor navigation, especially the presentation of next generation Wi-Fi access point which supports the state-of-art Wi-Fi Fine Time Measurement (FTM) protocol. Micro-Electro-Mechanical System (MEMS) sensors can provide an accurate short-term navigation solution, which also provides a potential way for autonomously generating the crowdsourced Wi-Fi received signal strength indication (RSSI) based fingerprinting database, by collecting and mining the users' daily-life trajectories and corresponding signals of opportunity.

This thesis proposes an automatic and precision-controllable algorithm for multi-source fusion based wireless positioning using the combination of Wi-Fi FTM, crowdsourced Wi-Fi RSSI fingerprinting, and IoT terminals integrated MEMS sensors, by which the realized ubiquitous positioning accuracy can reach 1.5~4.5m (within 75th percentile), and meter-level accuracy can be achieved under Wi-Fi FTM covered indoor scenes. Compared with previous hybrid navigation algorithms or structures, the main innovation points of this research are:

1) This research presents an autonomous three-dimensional (3D) positioning algorithm for low-cost MEMS sensors. This algorithm is based on the inertial navigation system (INS) mechanization and comprehensively utilizes multi-level constraints and observables (including: pseudo observations, gravity vector, altitude increment, pedestrian dead reckoning (PDR), zero velocity update (ZUPT), zero angular rate update (ZARU), quasi-static magnetic field (QSMF), non-holonomic constraint (NHC)). The proposed algorithm can be used without any external equipment and user intervention, and the autonomous 3D indoor positioning performance can be realized under changeable motion and handheld modes and environmental interference.
2) This research proposes and compares three different Wi-Fi FTM bias estimation algorithms to solve the problem of Wi-Fi FTM based ranging biases between

changing terminals and Wi-Fi access points (APs). In which the polynomial-based (PB) approach can provide the best performance of ranging bias estimation, but requires the priori information; The Gradient Descent (GD) based calibration algorithm does not need the priori information, but needs to extract the initial quasi-static status information; The tightly-coupled bias estimation algorithm integrates multiple location sources and pedestrian's motion information, and calculates and feedbacks the ranging bias estimation result in real-time to obtain the optimal convergence value. In this point, corresponding error and iterative models are designed, which can realize adaptive ranging bias estimation towards different scenarios and improve the accuracy and universality at the signal source level.

3) This research develops an autonomous 3D indoor localization and trajectory reconstruction framework based on MEMS sensors and sparsely deployed Wi-Fi FTM stations, Bluetooth Low Energy (BLE) nodes, and Quick Response (QR) codes based landmarks, and proposes and testes two corresponding trajectory error optimization algorithms, including the two-sided filtering and smoothing algorithm based on the adaptive unscented Kalman filter (AUKF) and Rauch-Tung-Striebel (RTS), and the GD based global optimization algorithm. The proposed trajectory optimization algorithms can effectively eliminate the cumulative error caused by the MEMS/landmarks integration framework and maintain the calculation efficiency, and more accurate smoothed navigation results can be acquired compared with one-sided filtering.
4) This research proposes a deep-learning based crowdsourced Wi-Fi fingerprinting database generation and updating framework based on the daily-life trajectories of public users. The influencing factors and time correlation of the optimized crowdsourced trajectory error are modeled and predicted by the multi-layer perception (MLP) network. In addition, the results of trajectories error prediction are further applied for crowdsourced trajectories classification, segmentation, merging, and the final Wi-Fi RSSI fingerprinting database construction and updating, which can effectively reduce the redundancy of the generated database and improve the accuracy and the stability of database matching.
5) This research proposes a 3D navigation architecture based on the integration of MEMS sensors, Wi-Fi FTM, and crowdsourced RSSI fingerprinting, and makes the comprehensively experimental analysis. In which the MEMS sensors/Wi-Fi FTM tightly-coupled integration model can realize meter-level positioning accuracy in

Wi-Fi FTM covered indoor environments, and has strong anti-interference ability; the MEMS sensors/RSSI fingerprint loosely-coupled integration model can provide a more universal and wide-coverage positioning solution and compensate for the limited deployment of Wi-Fi FTM stations; and the final hybrid MEMS sensors/Wi-Fi FTM/RSSI fingerprint integration model can effectively achieve automatic, and precision-controllable positioning in large-scale 3D indoor spaces. In addition, this research designs corresponding signal quality evaluation strategies for all three integration models to achieve adaptive weight adjustment of each observation.

Therefore, by taking better advantage of the merits of low-cost sensors, Wi-Fi FTM, and crowdsourced RSSI fingerprinting, the proposed algorithm has the following advantages:

1) The algorithm can significantly improve the performance of attitude estimation and 3D dead reckoning by self-calibrating the navigation parameters without the need for any external equipment or user intervention, which can be applied in case of complex indoor environments and changeable handheld modes of smartphones.
2) The algorithm can provide accurate and reliable 3D indoor navigation results in large-scale indoor spaces using smartphone integrated MEMS sensors and sparsely deployed landmarks such as Wi-Fi stations, BLE nodes, and QR codes; In addition, different error optimization methods are further applied for decreasing the cumulative error of forward navigation.
3) The algorithm can realize the automatic construction of Wi-Fi fingerprinting database using the collected crowdsourced trajectories, and develops a comprehensive deep-learning based trajectories evaluation, selection, partition, and merging framework to improve the robustness and efficiency of final generated database.
4) The algorithm can provide universal and precision-controllable positioning performance by integrating both Wi-Fi FTM and RSSI fingerprinting based absolute location sources and MEMS sensors based DR approach. Autonomous 3D localization can be realized in large-scale indoor spaces and meter-level positioning accuracy can be realized in Wi-Fi FTM covered indoor scenes.

There are various potential applications for the outcomes of this research, for example:

- Precise location based services that use IoT terminals;
- Mobile mapping and crowd-sensing;

- Crowdsourced navigation by using daily-life data provided by public users;
- Crowdsourced data mining and geo-spatial big data analysis;
- Multi-source fusion based seamless localization towards pedestrians and vehicles;

Publications Arising from the Thesis

Articles:

1. **Yu Y**, Chen R. Z., Shi W. Z., et al. Precise 3D Indoor Localization and Trajectory Optimization Based on Sparse Wi-Fi FTM Anchors and Built-in Sensors[J]. IEEE TRANSACTIONS ON VEHICULAR TECHNOLOGY, 2022, 71(4): 4042-4056.
2. **Yu Y.**, Shi W. Z., et al. Map-Assisted Seamless Localization Using Crowdsourced Trajectories Data and Bi-LSTM Based Quality Control Criteria[J]. IEEE Sensors Journal, 2022, 22(16): 16481-16491.
3. **Yu Y.,** Shi W. Z., Chen R. Z., et al. AP Detector: Crowdsourcing-based Approach for Self-localization of Wi-Fi FTM Stations[C]. The International Archives of Photogrammetry, Remote Sensing and Spatial Information Sciences, 2022, 46: 249-254.
4. Shi W. Z., **Yu Y.**, et al. A Deep-learning Approach for Modelling Pedestrian Movement Uncertainty in Large- Scale Indoor Areas, International Journal of Applied Earth Observation and Geo-information, 2022. (Under Review)

Patents:

1. Shi W. Z., **Yu Y.**, A novel seamless positioning and navigation database self-construction method, Chinese patent number: 202110805104X. (Under Review)
2. Shi W. Z., **Yu Y.**, A novel algorithm of multi-source fusion based indoor positioning using the combination of Wi-Fi ranging, fingerprinting and MEMS sensors, Chinese patent number: 2021114820557. (Under Review)
3. Shi W. Z., **Yu Y.**, A method of 3D indoor localization and optimization using sparsely deployed landmarks and MEMS sensors, Chinese patent number: 2021114702940. (Under Review)
4. Shi W. Z., **Yu Y.**, A method and device for anti-jamming position estimation under the constraint of multi-source information. (Under Review)
5. Shi W. Z., **Yu Y.**, A multi-source fusion positioning method and device in a large-scale indoor scene. (Under Review)

Acknowledgements

I would like to thank Dr. Wenzhong Shi and Dr. Ruizhi Chen for being the most considerate and trusted supervisors. Dr. Wenzhong Shi, thank you for giving me too many supports and encourages on my study and life. Your tireless attitude and enthusiasm for academics has always influenced me and made me more firmer on the way forward. Your insistence on excellence also enlightens me that there is no shortcut to success, except hard work and persistence. Dr. Ruizhi Chen, thank you for leading me into the treasure house of research and enjoy the happiness it brings to me. You encourage me to publish my first article, win my first international competition, and extend research communication to obtain eye-opening experiences. You are the best supervisor who always considers for the students more than yourself.

I would also like to thank all my supervisors and colleagues at the Smart Cities Research Institute, Department of Land surveying and Geo-informatics, The Kong Hong Polytechnic University (Dr. Wenzhong Shi, Dr. Min Zhang, Dr. Anshu Zhang, Dr. Pengfei Chen, Dr. Wenzheng Fan, Dr. Zhewei Liu, Dr. Zhipeng Luo, Haodong Xiang, Yepeng Yao, Muyang Wang, Pengxin Chen, Sheng Bao, Shanxiong Chen, Zhao Zhan, Xiaosheng Zhu, Chao Zhang, Chengzhuo Tong) for giving me so many supports both in academic and life.

I would like to thank all my supervisors and colleagues at the Ubiquitous Navigation Lab (UNL), State Key Laboratory of Information Engineering in Surveying, Mapping and Remote Sensing, Wuhan university (Dr. Ruizhi Chen, Dr. Liang Chen, Dr. Yuan Zhuang, Dr. You Li, Dr. Lei Wang, Dr. Ming Li, Dr. Wenju Fu, Dr. Mengyun Liu, Dr. Guangyi Guo, Dr. Feng Ye, Dr. Xuesheng Peng, Yu Pei, Xingyu Zheng, Zuoya Liu, Dewen Wu, Yan Xu, Wei Li, Yuan Wu, Haitao Zhou, Long Qian, Zheng Li, Yi Han, Ke Yan, Kaiyue Qiu, Shihao Xu, Lixiong Huang) for their selfless supports and help. In addition, special thanks to Qiao Wan, Xiaoqi Duan, Fangli Guan, Dr. Rong Gui, for their friendship and supports during my PhD study period in both Wuhan University and The Hong Kong Polytechnic University.

There are so many people that have supported me in my life. I could not list all your names in this acknowledgements, but thank you all for every moment we shared and every help you gave me. I really appreciate them. This thesis should be a gift for all of you: I could not make it without everything you have gave to me.

Dad and Mom, thank you for giving the best things to me but never asking for any return. You are always the idols in my life, who lead me to be a man with integrity and enthusiasm. Father-in-law and Mother-in-law, thank you for being my parents and giving me every support you can. Thank you for encouraging us to choose our own life. Your kindness and love inspire me to become a better man.

Table of Contents

List of Figures

List of Tables

List of Abbreviations

Acronyms/Abbreviations	Definition
AP	Access point
AI	Artificial Intelligence
BLE	Bluetooth Low Energy
CF	Complementary Filter
CV	Computer Vision
CDF	Cumulative Distribution Function
DR	Dead Reckoning
DNN	Deep Neural Network
DTW	Dynamic Time Warping
EKF	Extended Kalman filter
GMM	Gaussian Mixture Model
GNSS	Global Navigation Satellite System
GPS	Global Positioning System
GD	Gradient Descent
IMU	Inertial Measurement Unit
INS	Inertial Navigation System
IoT	Internet of Things
IQR	Interquartile Range
KF	Kalman Filter
KNN	K-Nearest Neighbor
LS	Least Squares
LOS	Line-of–Sight
LMF	Local Magnetic Field
LBS	Location-based Services
LC	Loosely-coupled
ML	Machine Learning
MM	Magnetic Matching
MSE	Mean Square Error
MEMS	Micro-Electro-Mechanical System
MLP	Multi-layer Perceptron

NED	North-East-Down
NHC	Non-Holonomic Constraint
NLS	Nonlinear Least Squares
NLOS	Non-Line-of–Sight
PF	Particle Filter
PDR	Pedestrian Dead Reckoning
QE	Quality Evaluation
QS	Quasi-Static
QSMF	Quasi-Static Magnetic Field
QR	Quick Response
RF	Radio Frequency
RSSI	Received Signal Strength Indication
RP	Reference Point
RTT	Round-Trip Time
SOP	Signals of Opportunity
SLAM	Simultaneous Localization and Mapping
SGD	Stochastic Gradient Descent
SINS	Strap-down Inertial Navigation System
3D	Three-dimensional
TC	Tightly-coupled
TDOA	Time Difference of Arrival
TOA	Time of Arrival
TOF	Time of Flight
2D	Two-dimensional
UWB	Ultra-wideband
UKF	Unscented Kalman filter
UPF	Unscented Particle Filter
VPS	Visual Positioning System
WGS	World Geodetic System
WPS	Wi-Fi positioning system
Wi-Fi	Wireless Fidelity
ZARU	Zero Angular Rate Update
ZUPT	Zero-velocity Update Technology

Chapter 1: Introduction

1.1 Background and Problem Statement

With the coming era of universal navigation facing the public and the rapid development of various Internet of Things (IoT) terminals and wearable devices, there is an increasing demand for obtaining personal location information anytime and anywhere and providing associated services based on acquired indoor and outdoor location information [1]. As an important means of obtaining geo-spatial location information, positioning and navigation technologies are regarded as the most essential part in various research field, for example artificial intelligence (AI), autonomous driving, and smart city platform [2]. Although the mainstream Global Navigation Satellite System (GNSS) technology is maturely developed and applied in large-scale commercial applications, and the positioning accuracy in outdoor open environments has already meet the most daily requirements of localization and navigation, and the meter-level positioning accuracy can be achieved in some outdoor open scenarios. The disadvantage is that the GNSS signal cannot cover or received well in most indoor spaces, thus it is difficult to exert efficient positioning capabilities in complex and changeable indoor spaces [3].

Indoor positioning is a very important application in mobile computing and a key technology based on location services. Indoor positioning has wide application prospects in all walks of life, for example tracking items in the logistics and warehousing industry; navigation in shopping malls, airports, and other indoor venues. According to the state-of-art reports, about 87% of human activity time is indoors, which has brought huge commercial impetus to the application of indoor location-based services, and also promoted the development of indoor positioning technology [4].

It is reported that the market of indoor navigation will reach 58 billion U.S. dollars in 2023, and domestic and foreign technology giants have begun to deploy in this market. For example, Google has launched the visual positioning system (VPS), an indoor positioning system using mobile terminals integrated cameras; Apple has acquired the Wi-Fi Simultaneous Localization and Mapping (SLAM) system, an indoor positioning startup, and Microsoft has also opened an IPIN conference in this area to explore commercial positioning technology. Technology companies such as Alibaba, Baidu, and Huawei have also increased their investment in indoor localization application and promoted the advancement of indoor localization technology.

The Ministry of Science and Technology of China issued the "Twelve Five "Special Planning", and in 2013 released the "White Paper on Indoor and Outdoor High-Precision Positioning and Navigation", which proposed the systematic construction of industrial support for navigation and location services, and indoor navigation has higher technical requirements based on indoor positioning [5].

In recent years, the indoor location information has become increasingly important for many emerging fields, such as emergency rescue solutions, smart city based applications, and analytics of geo-spatial big data. Although the Global Positioning System (GPS) has been widely used for positioning outdoors, the most indoor environments are GPS-denied. To realize location-based services (LBS) in indoor environments, different systems and techniques are developed, for example ultra-wideband (UWB) [6], Bluetooth Low Energy (BLE) [7], Wireless Fidelity (Wi-Fi) [8], acoustic source [9], and Micro-Electro-Mechanical System (MEMS) sensors [10].

The IoT technology integrates sensing, communication, and computing technology. This will make the communication of human to human more convenient, and the communication of human to thing or thing to thing possible. As an important IoT based application, indoor positioning integrates sensing, communication, and AI technology to provide a reliable location for the pedestrian. Relying on the accurate positioning service, route navigation in airports, shopping malls, and other indoor public areas can be easily achieved [11-12].

At present, there are three main kinds of IoT terminals based indoor and outdoor positioning methods, and their advantages and disadvantages are shown below:

1) Relative localization based on smartphone built-in sensors, usually using strap-down inertial navigation system (SINS) or pedestrian dead reckoning (PDR) algorithm to track the movement of pedestrians, by collecting the data from multiple sensors such as the accelerometer, magnetometer and gyroscope. The advantage of SINS and PDR is that it does not rely on the environment and has the ability to achieve autonomous positioning so that is widely used in positioning environments without external signals. However, due to the cumulative error caused by the inertial sensors and navigation algorithm, the positioning error increases with time and cannot be easily eliminated by itself. However, it is always difficult to acquire the absolute heading and initial location indoors, thus, this kind of technology is always combined with the indoor map or the other positioning methods [13-14];

2) Absolute localization based on radio frequency (RF) signals or computer vision (CV) [15-16]. Multiple characteristics extracted from RF signals can be used for indoor localization purposes such as received signal strength indication (RSSI) [17], time of arrival (TOA) [18], round-trip time (RTT) [19], time difference of arrival (TDOA) [20]. Besides, fingerprinting-based methods can also be used in complex indoor scenarios [21]. The advantage of RF signals based indoor localization is that the positioning error does not increase with time, therefore it can be used as a long-term and stable positioning source. The complex indoor environments also affect the accuracy of RF signals. For example, the occlusion and the shelters indoors can lead to non-line-of–sight (NLOS) influences and multipath propagation, which would seriously affect the performance of RF signals based indoor positioning. Beside, CV based method always needs a large amount of calculation, which would improve the calculation complexity of location updating;

3) Multi-source fusion based localization which combines the advantages of both relative and absolute location sources and provides more stable and accurate location information. There are always some limitations in positioning principle and distribution of single location source, thus, in order to achieve universal location, different location sources need to be combined to adapt to complex and changeable indoor environments [22]. To meet the requirements of indoor localization in complex and large-scale smart city based scenes, the multiple sources based fusion method becomes the most effective localization algorithm, which can be applied in different indoor environments under existing location sources [23]. In outdoor open environments, the GNSS based positioning approach has already been integrated in the most IoT terminals. In large-scaled urban spaces, the GNSS signal is easily affected by the block of dense buildings, therefore is usually integrated with inertial sensors to combine the advantage of each. In GNSS-denied indoor environments, RF signals are regarded as an effective approach for acquiring absolute reference and can further combined with IoT terminal integrated sensors to provide more robust indoor localization performance [24-25]. The sensors and RF radios integrated in IoT terminals which can be applied for navigation purpose are shown in Figure 1-1:

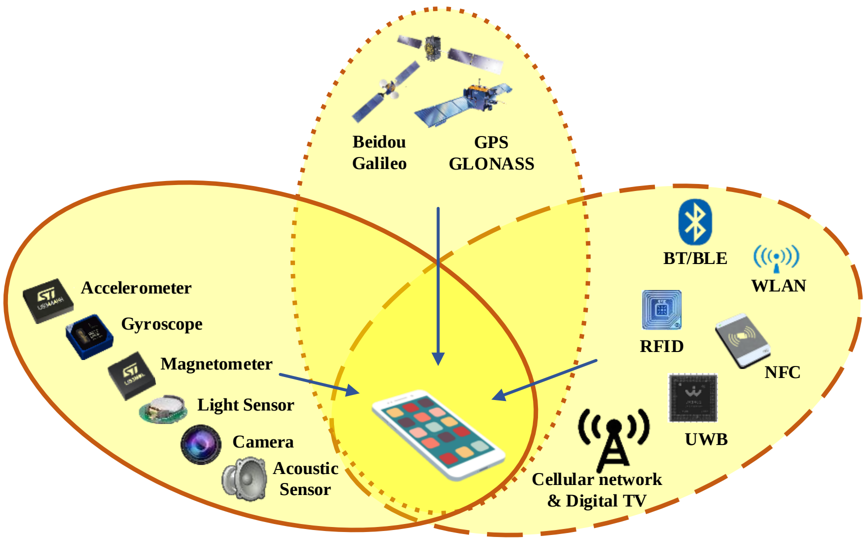

Figure 1-1 Positioning sensors and RF radios in IoT Terminals [4]

The description and comparison between different location sources supported by IoT terminals are described in Table 1-1:

Table 1-1 Comparison of Existing Positioning Technologies Using Smartphone Sensor

Location Sources	Accuracy	Robustness	Complexity	Scalability	Cost
Wi-Fi	Fingerprinting: 2~5m; RTT ranging: 1~3m;	Affected by environmental factors and human bodies;	Time-consuming for database generation;	Easy	No additional cost;
Bluetooth/BLE	Fingerprinting: 2~5m; AOA Array: < 1 m	Limited by the changeable environments;	Time-consuming to construct the database;	Easy	High cost of antenna array;
NFC	Centi-meter level, short effective distance;	Good	Low	Easy	A large number of NFC tags are required;
Cellular Network	Ten meters to tens of meters;	Affected by environments;	Medium	Good	High

UWB	Centi-meter level	Good	Medium	Medium	High
RFID	1~5 m	Affected by environments;	Medium	Medium	Medium
Infrared Ray	Meter-level	LOS required;	Medium	Low	Medium, additional transceivers are required;
Visible Light	1~5 m	Medium	Medium	Good	Low
Ultrasound	Centi-meter level;	Good	Low	Low	Medium, additional transceivers are required;
Acoustic Source	Meter-level	Affected by NLOS factor;	Medium	Good	Medium
INS	Cumulative error exists;	Good	Medium	Good	Low
Magnetic Field	2~5 m	Affected by environments;	High	Good	Low
Computer Vision	Camera rendezvous: Centi-meter level; Others: Meter-level	Medium, affected by the ambient light and quality of the image	Very High	Good	Medium

Wi-Fi positioning system (WPS) has attracted much more attentions compared with other indoor location sources because of its low cost and wide coverage characteristics. Generally, the IoT terminals based WPS always contains two implementation methods: ranging and fingerprinting. The RSSI feature is usually acquired to realize real-time ranging between IoT terminals and Wi-Fi APs and the location information is acquired by the Least squares (LS) algorithm [26]. Besides, the fingerprinting technique is developed to provide location information by collecting signals of opportunity (SOP) in selected indoor environments without knowing the positions of local facilities [27]. In a typical indoor scene, the precision of Wi-Fi RSSI based fingerprinting approach is easily affected by the deployment and sparseness of surrounding facilities and the localization precision would decrease in open environments [28-29]. To improve the robustness of WPS, IEEE 802.11ac standard added the Wi-Fi ranging function in 2016, named the Wi-Fi Fine Time Measurement (FTM) protocol, which can provide accurate time-of-flight information between different initiators such as smartphones and receivers such as Wi-Fi APs [30].

However, in complex and changeable smart city based indoor scenes, the realized precision of Wi-Fi FTM is limited by the multipath propagation and NLOS which would cause the additional deviation in Wi-Fi ranging results [31]. Due to the hardware difference of IoT terminals and Wi-Fi APs, not all IoT devices or Wi-Fi APs support the FTM protocol, and the ranging bias always exists in the procedure of FTM timestamp exchange between different terminals [32]. In addition, the PDR or inertial navigation system (INS) based location update methods are proved to provide shortly precise results by integrating the collected built-in sensors data, while the accuracy of MEMS sensors based approach decreases with time due to the cumulative error and magnetic interference therefore are always integrated with absolute location sources [33-34].

As discussed above, the integrated indoor localization using the combination of different location sources is regarded as an effective approach for realizing much better indoor localization performance. In recent years, indoor wireless localization towards the next generation Wi-Fi access point has attracted considerable attention due to the presentation of the state-of-art Wi-Fi FTM protocol. Aiming at the next generation WPS which supports both RSSI and FTM collection, how to achieve a robust combination of all the supported wireless characteristics using IoT terminals and improve the autonomy, accuracy and universality of traditional WPS becomes a hot issue towards large-scaled and precision-controllable three-dimensional (3D) indoor localization.

It can be found from the state-of-art literatures that the Wi-Fi FTM based high-precision location source is not available in all the Wi-Fi APs, and the RSSI characteristic is regarded as the universal location sources but is subjected to the environmental interference and labor-consuming collection phase. Towards the generation WPS, how to combine the Wi-Fi FTM, crowdsourced Wi-Fi RSSI fingerprinting and MEMS sensors based location sources to provide a large-scaled and accurate indoor localization performance is a facing problem, and how to comprehensively solve the challenges including magnetic interference and cumulative error, hardware deviation, quality evaluation, and efficient Wi-Fi fingerprinting database generation is also an existing challenge. To improve the performance of Wi-Fi and MEMS sensors integrated 3D indoor positioning based on the IoT hardware platform, the following challenges and problems need to be handled:

1) Magnetic Interference, Cumulative Error, Motion and Handheld Modes of MEMS Sensors: In the dead-reckoning (DR) related structure, the location is updated through the calculated step-length/walking speed and heading estimation result, which is affected by the increasing measurement error of MEMS sensors and changeable magnetic field in local environments. In addition, due to the variety of pedestrian's motion modes and handheld modes, the original positioning trajectory may exist a large deviation, which needs to be recognized and calibrated.

2) Hardware Deviation of Different IoT Terminals: Due to the hardware differences between IoT terminals and Wi-Fi APs, the raw measured RSSI or the RTT information always contains additional bias which causes the overall drift of the ranging result. Besides, the estimated value of additional bias depends on both initiator terminals and responder terminals, therefore an adaptive bias estimation framework is required to increase the robustness and precision of multi-terminal contained indoor localization system.

3) Efficient Generation of Crowdsourced Navigation Database: Under the background of geo-spatial big data analysis, massive IoT terminal data information provided by the large amount of users provides a novel approach for autonomous navigation database constructing and crowdsourced positioning. Towards the next generation wireless positioning system, how to improve the accuracy of crowdsourced trajectories provided by the daily-life data, and how to autonomously and effectively select, evaluate and merging the useful data from a large amount of collected navigation information is a facing problem.

4) Effective Integration and Quality Evaluation of Multiple Location Sources. Indoor scenes usually contain structure based influences such as multipath propagation and NLOS. Similar to the TOA based positioning method, Wi-Fi FTM is much more robust indoors compared with RSSI but is also subjected to the indoor interference which should be recognized. Thus, signal quality evaluation is regarded as an essential part in the final multi-source fusion phase and also a unified integration framework is needed for a more autonomous and concrete 3D indoor localization using Wi-Fi and MEMS sensors based location sources.

1.2 Review of Existing Literatures

1.2.1 MEMS Sensors Based Positioning and Optimization

Currently, built-in sensors based pedestrian navigation algorithm usually contains two types: pedestrian gait detection based positioning method such as PDR and INS mechanizations based positioning approaches. In PDR based positioning method, the pedestrian's two-dimensional (2D) position is propagated based on four main phases: step recognition [35], step-length calculation [36], walking direction calculation and calibration [37], and location update [38]. These procedures are subjected to the changeable human motions and complex indoor environments such as the handheld mode of smartphone and artificial magnetic interference [39-40]. The other alternative positioning solution is using strap-down inertial navigation system (SINS), which acquires moving objects' 3D position, velocity, and attitude information among the combination of different kinds of inertial sensors [41]. Compared with PDR, the navigation data estimated by SINS is low latency and more comprehensive. However, the consumer grade SINS is usually composed of MEMS Inertial Measurement Unit (IMU), which is subjected to the fast divergence and cumulative errors therefore cannot be directly used for navigation purpose [42].

To decrease the fast divergence and cumulative error of MEMS sensors based localization, different algorithms are proposed. In case of foot-mounted pedestrian navigation system, the zero-velocity update technology (ZUPT) and zero angular rate update (ZARU) are regarded as an effective way to decrease the cumulative and divergence errors of SINS [43]. Tong *et al*. [44] proposed a double-step unscented Kalman filter (DKF) to reduce the heading error and used the hidden Markov model to increase the precision of ZUPT approach, by which the maximum positioning error is estimated lower than 2%. Li *et al*. [45] developed a self-calibration framework aiming at gyroscope based heading estimation, in which various constraints, including pseudo observations, measurements of MEMS sensors, ZUPT/ZARU, are applied to increase the precision and stability of SINS.

The accuracy of PDR based solution is affected by the walking speed calculation, heading estimation, and handheld modes of the smartphone. Comprehensive experiments are developed and processed by previous works to enhance the performance of PDR mechanization.

Gu *et al*. [46] developed a deep-learning based walking speed calculation structure that the prior knowledge of the pedestrian's height, motion status and handheld modes are not regarded as the essential information, and the disadvantage is that the training dataset is required in the procedure of estimation of the optimal estimation result.

Zhang *et al*. [47] presented the SmartMTra system by learning and extracting features in the period of pedestrian's real-life activities, which are further applied for motion detection and handheld modes classification in order to realize a robust dead reckoning performance.

Poulose *et al*. [48] comprehensively compared the heading estimation performance of five different multi-sensors fusion approaches including the Kalman filter (KF), Extended Kalman filter (EKF), Unscented Kalman filter (UKF), particle filter (PF) and complementary filters (CF). The experimental results prove that the UKF has the highest heading estimation accuracy and the PF shows the poor performance in heading estimation.

Limited by the low-precision of MEMS sensors, the initial INS mechanization is usually applied in foot-mounted positioning system due to the effective detection of ZUPT/ZARU constraints.

Liu *et al*. [49] used EKF to fuse the INS mechanization, QR code, and ZUPT/ZARU detection results to realize accurate forward localization performance. In addition, the Rauch-Tung-Striebel (RTS) smoother is adopted to increase the precision of forward navigation result and meter-level accuracy could be acquired after smoothing phase.

Aiming at smartphone based pedestrian positioning system, ZUPT/ZARU constraints are not enough for eliminating the divergence error of INS mechanization due to the changeable motion statuses and handheld modes. Besides, the performance of PDR mechanization is subjected to performance of long-term heading and walking speed estimation.

Li *et al*. [50] combined INS and PDR mechanizations using smartphone integrated MEMS sensors. The sensors features including external acceleration, magnetic deviation, ZUPT, ZARU, step-length based walking speed are adopted to constrain the INS originated error. The forward-backward smoothing is applied to further optimize the positioning performance. Kuang *et al*. [51] further improved the performance of INS/PDR integration system by adding pseudo observations and comprehensively compared the performance of INS/PDR structure with the enhanced PDR (E-PDR) proposed in state-of-art literatures. Final experimental results proved that the INS/PDR integration structure effectively improve the performance of single PDR mechanization.

Shi *et al.* [52] used the modulus and variance of gyroscope output to realize the real-time step detection, which effectively recognize the swing mode and static mode based on the foot-mount platform. Besides, the zero-velocity-update (ZUPT) detection result and bias error of accelerometer are combined to calibrate the attitude angle. The experimental results shown end-to-end localization error are decreased within 1.2%.

Jin-Shyan Lee and Shih-Min Huang [53] proposed a multi-pose based PDR algorithm including six poses and four modes of the smartphone, and a novel approach of the pedestrian's heading estimation without using magnetometer under different handheld modes is applied. The experimental results proved that the high precision localization performance can be achieved under changing handheld modes.

Yan *et al*. [54] applied the Support Vector Machine (SVM) to classify different handheld modes of the smartphones and the Support Vector Regression (SVR) was applied to calculate the walking speed of the pedestrian from the collected history acceleration and angular velocity, which showed the comparable positioning accuracy to the typical visual positioning system. In addition, they improved the smartphone-based localization using a novel neural framework and acquired 3D trajectories under different motion modes based on the training dataset larger than 40 hours provided by 100 different testers [55].

To further decrease the cumulative error of MEMS sensors based indoor localization, the backward smoothing or the global optimization algorithms are usually applied to increase the precision of forward navigation result, which can provide much higher accuracy of reconstructed trajectory and can further used for navigation database construction.

In recent years, many researchers have devoted to the methods of trajectory optimization based on the crowdsourcing data acquired from a large number of smartphones. There are some existing methods, such as obtaining high-precision positioning database from high-cost inertial sensors [56], map information [57], or various reference points [58-59]. Zhang *et al*. [60] proposed a quality assessment criteria towards the crowdsourced navigation database generation using IoT-based daily-life built-in sensors data, by taking motion modes, sensors biases, and the length of time period into consideration. The comprehensive experiments proved the efficiency and precision of designed framework. Wang *et al*. [61] proposed UnLoc system, realizing the navigation database generation based on the detection of context-related indoor landmarks such as elevators and stairs, which is further applied for trajectory re-calibration and database construction.

The classical smartphone based indoor mapping and navigation database generation structures including Walkie-Markie [62], PiLoc [63], and MPiLoc [64]. In Walkie-Markie, the indoor pathway is generated based on the detection of Wi-Fi AP based landmarks and trajectory matching. The limitation is that the collected RSSI value is subjected to the changeable indoor environments and the absolute location of generated pathway cannot be acquired. The PiLoc classified the similar crowdsourced trajectories by their shapes and the similarity of collected Wi-Fi RSSI information and merged the similar trajectories using point-to-point fusion. The MPiLoc further extended the floor plan from 2D to 3D and using the sparse acquired GNSS reported location as the absolute points. The disadvantage is that both PiLoc and MPiLoc rely on the accurate estimation of heading information, while the precise absolute heading may not be available all the time.

Li *et al*. [65] presented the IndoorWaze system, using the crowdsourced Wi-Fi fingerprinting data and POI information collected by shopping mall employees to generate robust and marked floor plan. The final experiments shown that the designed IndoorWaze framework can accurately mark the pathways and location of the store for indoor navigation purpose.

It can be found from the current built-in sensors based localization and optimization systems proposed by the state-of-art literatures that the INS/PDR integrated framework can achieve better performance due to the richer motion information compared with the INS or PDR mechanization. The existing INS/PDR models are all focused on the 2D indoor localization and not suitable for the complex 3D scene. In addition, the indoor magnetic interference and changeable handheld modes of smartphones are also the facing challenges for realizing a more precise MEMS sensors based forward 3D indoor localization performance.

The existing global optimization algorithms can significantly increase the precision of forward localization while the accuracy of global optimization algorithm depends on the robustness of integration model and the number of landmark points, and the traditional backward smoothing approach always requires high computational complexity due to the large number of matrix inverse operations. Thus, a comprehensive and precise 3D integration structure is required in this stage in order to realize comparable forward localization and a more efficient global optimization algorithm is also needed and the optimization accuracy needs to be comparable with the traditional backward smoothing based optimization approach.

1.2.2 Wi-Fi FTM Based Positioning

In 2016, IEEE 802.11ac protocol expanded the IEEE 802.11mc, which is normally called the Wi-Fi ranging function, and the aim is to provide meter-level distance measurement performance among IoT terminals and Wi-Fi APs, according to the Wi-Fi alliance [66]. Recently, various Wi-Fi chipsets have provided hardware-level support of FTM protocol and the smartphone with the Android system level higher than Android P has been provided with the Wi-Fi FTM ranging support by Google. Beside the IEEE802.11mc standard documents, there are few details about implementation techniques and performance of RTT ranging system on how to use the specified Wi-Fi chipsets [67]. Thus, how to realize accurate indoor positioning using state-of-art Wi-Fi FTM protocol becomes an important and hot issue.

Traditional Wi-Fi based indoor localization methods usually use RSSI to calculate the distance between intelligent terminal and Wi-Fi AP or using fingerprint method. Compared with RSSI, Wi-Fi FTM which measures the RTT of the Wi-Fi signal between initiator and responder/AP promises the following advantages: Firstly, Wi-Fi RTT can be more stable compared with RSSI and is less affected by multipath propagation in case of LOS [68]; Secondly, it is easier to establish a relationship model between measured time and the ground truth distance after data processing [69]; Thirdly, Wi-Fi FTM based localization does not require the preliminary efforts for obtaining environmental information compared with the fingerprinting based methods [70].

However, in the real-word positioning phase among a typical indoor environment, the direct transmission path between the transceiver is blocked and only the NLOS transmission exists, the distance errors measured by Wi-Fi FTM cannot be easily eliminated due to its ranging mechanism [30]. Due to the different realizing approaches of hardware manufactory, the raw Wi-Fi FTM based ranging results exist initial biases among changeable IoT terminals and Wi-Fi APs [71]. Accuracy of Wi-Fi FTM is also affected by bandwidth of the Wi-Fi signals. For instance, the ranging results are much more accurate using 80 MHz bandwidth than with 40 MHz bandwidth. It is understandable that with larger bandwidth, the ranging errors can be reduced by improving the resolution of the multipath detection [72]. Another important factor is the clock deviation error caused by initial deviation and random error which are inconsistent with different initiators and responders and should be estimated and eliminated.

Wi-Fi FTM protocol is based on the TOA and TOD methods [73-74] which can also be used to measure the time of flight (TOF). Authors in [75] introduces how the TOF works in detail and a series of experiments are designed for localization estimation in a typical indoor environment. In order to reduce the negative impacts on unsynchronized time signal and multipath, they used EKF fusing TOF measurements with IMU to enhance the performance of TOF system [76]. In [77], a "Siamese" artificial neural network (ANN) based on machine learning (ML) approach is proposed, which gives an effective solution to the influence of low bandwidth and go on to improve the ranging precision of Wi-Fi FTM. Niesen U *et al*. [78] proposed an improved dedicated short-range communication method by Wi-Fi FTM to perform outdoor inter-vehicle ranging. A timestamp compression method has been discussed by discarding the most significant bits of each FTM frame.

To evaluate the performance of Wi-Fi FTM based indoor localization system, a lot of efforts have been made by a mount of researchers. Ibrahim M and his partners analyzed the key factors and parameters which affect the Wi-Fi ranging performance based on the open platform and revisited standard error correction techniques for Wi-Fi FTM-based localization system [79]. Yu Y *et al*. [19] proposed a real-time Wi-Fi ranging model which reduce the impacts of clock deviation, non-line-of-sight (NLOS), and multipath, then used unscented Kalman Filter (UKF) to fuse data acquired from multiple sensors and Wi-Fi FTM and got the final positioning error within 2 m. Xu S H *et al*. [23] proposed an enhanced particle filter (PF) to fuse the multi-sensor data and Wi-Fi FTM data, using adaptive tilt compensation to improve the performance of heading estimation. The final localization accuracy is within 1 m in 86.7% of the dynamic cases when the number of particles is 2000.

Because of the complexity and variability of different indoor scenes, the RF signal based location sources cannot cover all the indoor scenes and are subjected to the multipath propagation and NLOS effect. IEEE 802.11mc protocol was proposed towards accurate indoor navigation, which supports real-time distance measurement among Wi-Fi APs and mobile terminals. In previous research, the Wi-Fi FTM is proved to achieve much higher ranging accuracy compared with RSSI based methods in typical indoor scenes, and can also be integrated with other location sources to provide precise location information indoors. Biehl *et al*. [80] combined Wi-Fi FTM and BLE RSSI to realize room-level localization and fully researched the improved performance by combining the PF and the incorporating map geometry. Henry and Montavont [81] applied fingerprinting-based positioning approach to Wi-Fi FTM and examined the corresponding parameters defined for FTM, then used the ML approach to recognize individual machines performing FTM exchanges and significantly improved the ranging performance on individual chipsets. Kevin *et al*. [82] applied MUSIC algorithm to increase the precision of Wi-Fi FTM in NLOS contained environments and verified the room-level positioning accuracy without modifying the original protocol.

In general, Wi-Fi FTM protocol is proposed towards the next generation WPS, which can effectively reduce the environmental effects compared with the RSSI based ranging and fingerprinting approaches. To get the meter-level localization performance, the Wi-Fi FTM is usually integrated with MEMS sensors based location source by previous works. Compared with RSSI, Wi-Fi FTM provides a more robust way for Wi-Fi ranging and can be used as a new location source with high accuracy. However, when giving a complex indoor environment which contains NLOS and multipath propagation, the distance error measured by Wi-Fi FTM cannot be easily eliminated due to the lack of line-of-sight (LOS) path. In addition, PDR-based positioning methods are affected by accuracy of step-length estimation and heading drift therefore cannot be used for a long time period.

Yu *et al*. [19] improved the Wi-Fi FTM based ranging performance in NLOS contained scenes by a comprehensive optimization model and AUKF is further applied to combine the pre-processed Wi-Fi FTM and multi-mode enhanced PDR. The estimated positioning error in several typical 2D indoor scenes is within 2 m. In addition, they extended their work from 2D to 3D indoor environments (3D-WFBS) and enhanced the performance of PDR using an AEKF based heading and walking speed fusion model, and the unscented particle filter (UPF) is adopted to integrate the information acquired from 3D-PDR, Wi-Fi landmark detection, and ranging fusion. The meter-level positioning precision can be realized in different indoor scenes by the proposed 3D-WFBS [83]. Shao *et al.* [84] improved the accuracy of Wi-Fi FTM using temporal-spatial constraints to eliminate the influence of indoor multipath propagation and the RF interference contained environments, and the iterative Wi-Fi ranging and virtual location coordinates are weighted together to get the optimal positioning result.

1.2.3 Wi-Fi RSSI Fingerprinting Based Positioning

Wi-Fi based indoor localization solutions have been widely used compared with other location sources because of its low cost and wide coverage characteristics. Generally, a traditional Wi-Fi based positioning system always uses the RSSI characteristics to measure distance between smartphones and the Wi-Fi APs and then calculates the pedestrian's location by triangulation algorithm. Besides, fingerprinting technique can also be used for universal indoor localization without acquiring the actual location of Wi-Fi APs.

The typical process of Wi-Fi RSSI fingerprinting approach always contains two main parts: on-line phase and off-line phase. For the on-line phase, various matching and classification algorithms have been researched by the previous works [21]. For the off-line phase, also refers to Wi-Fi fingerprinting database construction, which usually contains three main types: 1) Static point-to-point method, usually generates database by averaging the RSSI signal at each reference point (RP), which proves higher reliability but is labor-consuming [26]; 2) Mobile walk-survey method, by collecting Wi-Fi RSSI data among a high-precision walking trajectory between selected landmarks, which is much more efficiency than the static method [85]; 3) Crowdsourcing-based method, usually generates navigation database through spatial big data provided by the amount of IoT terminals, which provides an autonomous way for Wi-Fi fingerprinting database generation and updating [86]. Zhang *et al*. [60] used the optimized crowdsourcing-based inertial sensors localization data in order to obtain a reliable Wi-Fi fingerprinting database and evaluated the reliability and quality of each collected trajectory. The EKF algorithm is applied in both forward-DR and backward-smoothing in the procedure of navigation database construction. Gu *et al*. [87] used the graph-based framework to calibrate user's trajectories for establishing the crowdsourced Wi-Fi radio map. In addition, the multiple sensors data, Wi-Fi information, and GNSS-based coordinates are comprehensively considered to acquire the minimized defined error metric and the optimal trajectory evaluation result. Li *et al*. [88] proposed a robust radio map generation algorithm which effectively reduced the effects of inaccurate PDR trajectories and the requirement of floor information, and the estimated average positioning error is within 2.9 m.

At this stage, the crowdsourcing-based navigation database generation exists several challenges: the poor performance of daily-life data due to the cumulative error of MEMS sensors and indoor magnetic interference [89], the quality evaluation and efficient integration of crowdsourced trajectories and datasets [90], and the deployment and the recognition of RPs [56]. In addition, the single PDR based positioning method can only provide accurate location information in a short time period due to the cumulative error caused by heading calculation and step-length estimation, therefore is usually combined with absolute location sources to improve the localization performance [91].

Multiple Wi-Fi characteristics and corresponding positioning methods can be applied in the WPS, RSSI is regarded as the most universal feature for indoor positioning, which contains triangulation and fingerprinting based positioning methods. However, the other features for instance channel impulse response (CIR) [92], time of arrival (TOA) [93], angle of arrival (AOA) [94], and channel state information (CSI) [95], are usually can not be collected directly by handheld IoT terminals.

Zou *et al.* [96] improved the performance of Wi-Fi fingerprinting by using autonomously constructed navigation database and adaptation model, and proposed a novel Gaussian process regression model, which effectively increased the accuracy of RSSI estimation and final localization.

Li *et al.* [97] developed a passive positioning framework using a group of sniffers to track the Wi-Fi traffic and acquired the locations of Wi-Fi transmitters through TOA information. In addition, this system addressed the problems of clock synchronization and hardware delay and achieved the precision of 0.23 m, 0.62 m, and 1.65 m under outdoor LOS, indoor LOS, and indoor NLOS conditions, respectively.

Wu *et al.* [98] comprehensively investigated the aspects which affect the accuracy of Wi-Fi fingerprinting, for example the RSSI continuity and pedestrian body blockages, and integrated these parameters by a unified model which covers both on-line and off-line phases. The real-world experimental results achieved the mean error within 2.5m.

1.2.4 Integrated Technologies for Wi-Fi and MEMS Sensors

Wi-Fi positioning system (WPS) is regarded as an effective way for realizing universal indoor localization compared with the other location sources. The MEMS sensors based DR approach proves high-accuracy in a short time period but the positioning error cumulates with time, and the WPS proves better long-term performance but is easily affected by the changeable indoor environments. To eliminate environmental influences, the WPS is always combined with MEMS sensors based approach to make both advantages complementary. This section focuses on the Wi-Fi and MEMS sensors based positioning methods, and then introduces some existing solutions of multi-source fusion based positioning and analyzes the corresponding challenges and difficulties.

At this stage, integrated navigation technology becomes more and more popular due to the improved robustness and precision compared with single location source in complex indoor environments [99–101]. Several fusion methods such as the Kalman filter (KF) [102], Extended Kalman filter (EKF) [103], and Particle filter (PF) [104] are applied as the typical integration methods towards multi-source fusion based indoor localization.

Zhuang *et al*. [105] developed a tightly-coupled indoor positioning approach uses the integration of Wi-Fi RSSI based ranging and smartphone integrated sensors. To decrease the influence of environmental factor, the bias of received Wi-Fi RSSI is modeled as the random walk process. The final experiments in a 120m $*$ 40m office area contains 47 APs achieved the mean accuracy within 3.47 m. Wang *et al*. [106] proposed a hybrid Wi-Fi/PDR integrated system based on a novel factor-graph based fusion model. The deep neural network (DNN) is applied to extract more comprehensive features from raw signals. Experiments in corridor scenes reaches meter-level accuracy and better performance compared with traditional approaches.

Zhuang *et al*. [85] compared the performance of two different Wi-Fi based autonomous localization using fingerprinting and trilateration technologies respectively. A smartphone developed application named Trusted Positioning Navigator (T-PN) is applied to provide built-in sensors based navigation information and the estimated localization error is acquired within 5.75m.

Jeongsik Choi and Yang-Seok Choi [40] presented a self-calibrated indoor positioning approach which contains the integration of Wi-Fi FTM and PDR. Instead of calibrating the FTM bias in advance, each parameter in the proposed framework is modeled and estimated in real-time to adapt to the changeable indoor scenes. The experimental results proved 1.04 m localization accuracy in case of 40 MHz bandwidth.

Li *et al*. [41] developed a Wi-Fi fingerprinting based quality evaluation criteria by collecting fingerprinting groups, RSSI difference, and hyperbolic features in the procedure of the off-line procedure, and among the on-line procedure, the multiple supporting sets were generated which can predict the positioning error of estimated location while obtaining positioning results.

Li *et al*. [12] designed a robust DR/Wi-Fi fingerprinting/ magnetic matching (MM) based indoor localization system which can be applied on the low-cost sensors integrated IoT terminals and Wi-Fi covered environments. Three different levels of quality-control methods were applied for the navigation integration in the procedure of real-world application, which decreased the positioning error by the range of 13.3% to 55.2% under different scenes and handheld modes.

1.3 Research Scope and Questions

The overall objective of our research plan is as follows: In case of large-scaled and diversified indoor scenes and ultra-sparse deployment of wireless stations or landmark points, the Wi-Fi fingerprinting database can be automatically constructed and updated by combining sparse local signals/landmark points and crowdsourced daily-life data, and a unified multi-source fusion framework is designed to organically integrate different location sources including Wi-Fi FTM, RSSI fingerprinting, and MEMS sensors. The proposed algorithm can finally realize precise and universal localization in large-scaled and multiple scenes contained indoor spaces, which is not restricted by external equipment and does not need to be collected among time-consuming procedure, and can achieve meter-level positioning accuracy in Wi-Fi FTM supported indoor scenes. Our current research plan mainly consists of the following four parts:

1) Firstly, we intend to study the autonomous 3D indoor positioning algorithm for MEMS sensors integrated in IoT terminals. This algorithm is designed using the INS mechanization as the state model and comprehensively utilizes multi-level observed values including gravity vector, quasi-static magnetic field (QSMF), altitude increment and step-length, and multi-level constraints including ZUPT/ZARU, pseudo velocity, pseudo position, and non-holonomic constraint (NHC). It can be used without any external equipment and in the case of user intervention, and independent 3D indoor positioning can be realized in complex and changeable indoor environments with severe magnetic interference.
2) Secondly, we intend to study the crowdsourced Wi-Fi fingerprinting database generation algorithm based on daily-life data collected from MEMS sensors and sparsely deployed Wi-Fi FTM stations, BLE nodes, and Quick Response (QR) codes based landmark points as reference points. In addition, to further improve the performance of forward navigation, we propose and test two trajectory optimization

algorithms, including the backward smoothing algorithm based on AUKF and RTS filtering and the global optimization algorithm based on gradient descent (GD) method, which can effectively eliminate the cumulative error caused by a single MEMS positioning algorithm, and obtain navigation results that are significantly better than forward filtering, and at the same time reduce the complexity of calculation.

3) Thirdly, we intend to analyze the factors that affect the quality and accuracy of the crowd-sourced trajectories, by modeling these uncertain factors, we can quantitatively evaluate the credibility and positioning error of each trajectory and ensure the weight of each trajectory in the fusion phase and further merge the eligible trajectories in the construction of the final crowdsourced navigation database. Through this method, the high-precision navigation database construction and update are realized without changing the hardware conditions of the IoT terminals and additional installation equipment and scene prior information.
4) Fourthly, we will study the multi-source fusion algorithm and corresponding signal quality evaluation strategy. Through the main location information is provided by the self-generated Wi-Fi fingerprinting database, we further combine it with the local high-accuracy location sources including Wi-Fi FTM and integrated MEMS sensors, and finally realize the universal and precision-controllable 3D indoor localization, which is not restricted by external equipment and does not need to be collected by time-consuming approach in large-scale smart city scenes, and meter-level positioning accuracy can be realized under the Wi-Fi FTM covered indoor scenes.

The first part is named as MEMS sensors based positioning solution, while the second part as autonomous generation of Wi-Fi fingerprinting database, and the third and the fourth parts are described as analysis of crowdsourced pedestrians' trajectories and multi-source fusion based positioning solution. The research questions of each part are presented as follows:

1.3.1 MEMS Sensors Based Positioning Solution

The MEMS sensors based positioning solutions usually contain two kinds: The INS and PDR mechanizations. INS mechanization is updated using inertial sensors data to track the carrier's 3D attitude and position information. Nowadays, with the development of MEMS sensors, the smartphone integrated sensors are already able to meet the requirements of low-cost navigation purposes. PDR is proposed aiming at pedestrians based localization, which contains two main parts: 1) step detection and step-length estimation; 2) heading fusion and calibration. Due to the low accuracy of MEMS sensors, the raw positioning results always can not satisfy the demands of high-accuracy indoor navigation, in order to realize a concrete and accurate MEMS sensors based 3D indoor localization algorithm, we need to handle the following challenges:

1) Cumulative Error of Multiple Sensors: During the DR procedure, the current position is calculated by the estimated heading and speed information based on the previous heading and position, including INS and PDR. The errors of speed estimation and heading deviation lead to the decrease of positioning accuracy.
2) Interference of Artificial Magnetic Field: The Earth's magnetic field maintains an almost constant value at its surface. While in the complex and changeable indoor buildings, the local magnetic field is easily affected by the electronic devices or others indoors which lead to the deviation of magnetic heading.
3) Differences in Pedestrian Characteristics: Pedestrian characteristics include for example heights, motion patterns and their step frequency. These would take into challenges in attitude calculation and step-length estimation. For example, the accuracy of step-length estimation can fluctuate ±40% with different height. Besides, the way how people use smartphones can also influence the method of heading fusion, such as handheld, calling near the ear, swaying in the hand, and putting in the pant pocket. In order to improve the accuracy of localization, these different modes of smartphones should be recognized and classified.

1.3.2 Autonomous Generation of Wi-Fi Fingerprinting Database

The method of Wi-Fi fingerprinting database construction always contains three main types: 1) Static point-to-point method, usually generates database by averaging the RSSI signal at each reference point (RP), which proves higher reliability but is labor-consuming; 2) Mobile walk-survey method, by collecting Wi-Fi RSSI data among a high-precision walking trajectory between selected landmarks, which is much more efficiency than the static method; 3) Crowdsourcing-based method, usually generates navigation database through spatial big data provided by the amount of IoT terminals, which provides an autonomous way for Wi-Fi fingerprinting database generation and update.

At this stage, the crowdsourcing-based Wi-Fi fingerprinting database generation exists several challenges:

1) The poor performance of daily-life data due to the cumulative error of MEMS sensors and indoor magnetic interference. The accuracy of the crowdsourced trajectory collected by IoT terminals will greatly affect the accuracy of the final crowdsourced navigation library. How to improve the positioning accuracy of each crowdsourced trajectory has become a key point.
2) The quality evaluation and efficient integration of crowdsourced trajectories. In the process of building a crowdsourced navigation library, how to deal with redundant crowdsourced data is also one of the challenges that needs to be overcome. In the case of the same path, how to quantitatively evaluate the final error index of each trajectory provides further accuracy support for the subsequent fusion of the navigation database
3) The deployment and the recognition of reference points. Optimizing crowdsourced data through reference points can effectively improve positioning accuracy. However, due to the complexity and variability of real scenes, how to lay out and effectively detect the coordinates of reference points is also a difficult problem for building crowdsourced navigation database.

1.3.3 Analysis of Crowdsourced Pedestrians' Trajectories

Among all kinds of human activity data, trajectory data is of great significance for capturing individual space-time movement and collective crowd dynamics. It has been widely applied among different scientific fields, such as intelligent transportation system, urban planning, mobility analysis and travel data mining. For a long time, motion uncertainty in trajectory has been considered as an inevitable factor in the process of data collection, and will significantly affect the effectiveness of knowledge extraction. At present, the modeling of motion uncertainty in trajectory data has attracted more and more attention, especially the work related to trajectory mining, representation and spatial query. There are two main difficulties in modeling the motion uncertainty of crowdsourcing trajectory data:

1) Interpolation algorithms can easily not represent the actual motion trajectory, because they assume that the motion between two sampling points is close to a specific curve (such as a linearly interpolated line). This cannot be guaranteed due to the complex movement patterns and environmental background in the real-world trajectory.

2) For low sampling trajectories, the effectiveness of the interpolation algorithm decreases significantly, because the low sampling frequency makes the actual motion unknown for a relatively long time, which makes the interpolation result unreliable. Therefore, how to model the positioning error in the case of low sampling trajectory is a big problem.

1.3.4 Multi-source Fusion Based Positioning Solution

Figure 1-1 comprehensively describes that there are more than 12 types of sensors supported and integrated in IoT terminals, including GNSS receiver modules, short-range RF transmitters, Wi-Fi, UWB, and Bluetooth/BLE modules, or other integrated sensors, such as the tri-accelerometers, tri-magnetometers, tri-gyroscopes, barometers, light-intensity sensors, microphones, speakers, and cameras. Among all these modules or sensors, only the GNSS receiver is originally applied for localization purpose. To explore potential navigation capabilities using IoT terminals integrated modules and sensors, various positioning systems and algorithms are proposed in order to acquire the pedestrian's motion information (3D attitude, 3D speed, 3D position) during localization procedure. The mentioned location sources have their own advantages, which can be combined for integrated localization in order to be more adaptive to the complex and changeable indoor scenes. However, to realize an optimal indoor localization performance of multi-source fusion, the following problems have to be tackled:

1) Synchronization of Signal Measurements. Among the various IoT terminals integrated sensors, different sampling features and sampling rates exist one of the problems in fusion phase. For instance, the sampling rate of the Wi-Fi RSSI collection ranges between 1/3 and 1/30 Hz, while the collection rate of inertial sensors can reach 100 Hz or more. Even with the same sampling rate, the sampling time instant may be different too. Therefore, to make the full use of the characteristics of various positioning sources, time synchronization is necessary.
2) Different Precision Level of Sensor Measurements. There are over 12 kinds of wireless receiver modules and sensors supported and integrated in IoT terminals, in which the different measurement methods are applied for corresponding location sources. In addition, the measurement errors vary from different sensors and receivers, make it difficult to improve the real-world positioning performance regarding the changeable integration models of different location sources. For

instance, due to the poor performance of IoT terminals integrated MEMS sensors, the INS mechanization cannot be directly applied, while the PDR mechanization is more suitable for low-cost sensors based navigation.

3) Hardware Deviation of Different IoT Terminals. Different hardware manufacturers usually develop different chipsets or components for the receiver modules or integrated MEMS sensors. Thus, the measurements from different IoT terminals may be biased due to the hardware differences even when applied on the same location source. For instance, due to the hardware differences between IoT Terminals and Wi-Fi APs, the raw measured RSSI signal or the RTT information always contains additional bias which causes the overall drift of the ranging result, which would lead to the changing accuracy of Wi-Fi fingerprinting and Wi-Fi ranging based positioning methods between different terminals.

1.4 Thesis Outline

This thesis covers the design and implementation issues of an autonomous and accurate 3D indoor localization on the IoT terminals based platforms using the combination of Wi-Fi FTM, crowdsourced Wi-Fi RSSI fingerprinting, and MEMS sensors, aiming at providing autonomous and precision-controllable 3D indoor positioning services in smart city based large-scale indoor spaces. The thesis consists of six chapters, and the outline of chapters two through six is as follows:

Chapter Two covers the fundamental knowledge for Wi-Fi FTM based positioning system, Wi-Fi RSSI fingerprinting based positioning system, and MEMS sensors integrated navigation system, including that of separate technology, and the final information-fusion technique which uses Kalman filter, particle filter, and nonlinear least squares related approaches.

Chapter Three develops a robust self-calibrated 3D indoor localization and error optimization system using IoT terminal integrated sensors and sparsely deployed anchors, in which the multi-level constraints and observables are applied for the enhancement of INS mechanization, and Wi-Fi FTM stations, BLE nodes, QR codes are sparsely deployed in large-scaled indoor spaces to provide absolute reference for MEMS based approach. In addition, to further improve the accuracy of MEMS sensors and sparse landmark points based forward localization, this chapter proposes and evaluates two different trajectory optimization algorithms and compares the improved localization performance. In which the backward-AUKF smoothing algorithm can provide more accurate trajectory optimization performance but is time-consuming, and the GD based approach can realize slightly lower optimization precision compared with the backward-AUKF but can effectively reduce the calculation complexity.

Chapter Four proposes two state-of-art WPS frameworks: Wi-Fi FTM based self-calibration and positioning system and crowdsourced Wi-Fi fingerprinting based positioning system. The two different WPS systems are presented respectively towards different application requirements. In which the Wi-Fi FTM based calibration and positioning system is presented towards high-accuracy localization requirement in specific indoor areas, and the crowdsourced Wi-Fi RSSI fingerprinting based positioning system is presented aiming at realizing a more universal and autonomous positioning requirement in smart city based large-scaled indoor spaces.

Chapter Five presents a comprehensive Wi-Fi/MEMS sensors integrated framework, which is consist of a robust MEMS sensors based localization solution described in Chapter Three and three different types of MEMS sensors and Wi-Fi integration models towards different application scenes. In addition, this chapter proposes the signal quality evaluation (QE) algorithm aiming at autonomously estimating the availability and uncertainty of measured Wi-Fi FTM and RSSI fingerprinting results using the misclosure check (MC) and double-stage k-nearest neighbor (DS-KNN) methods, aiming at improving the signal robustness in Wi-Fi/MEMS integration phase.

Chapter Six summarizes the achieved work of this thesis, concludes the results of this research, and gives the recommendations for future research to improve the proposed algorithm structure. Figure 1-2 shows the outline of this thesis and topic classification corresponding to the issues listed in Section 1.4.

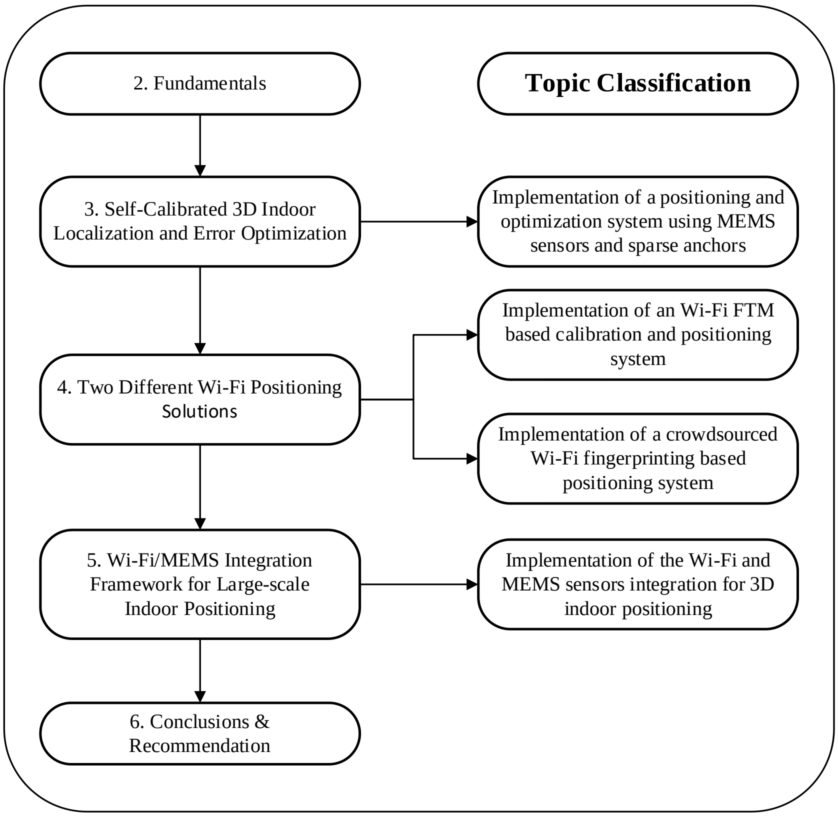

Figure 1-2 Thesis Outline and Detailed Issues

Chapter 2: Fundamentals For Positioning

This chapter will cover the fundamental information for the MEMS sensors and Wi-Fi integrated navigation structure proposed by this thesis. Section 2.1 introduces the necessary coordinate frame; Section 2.2 describes the two commonly applied MEMS solutions for indoor navigation; Section 2.3 – 2.4 detail two different Wi-Fi positioning systems, including Wi-Fi FTM based solution and Wi-Fi fingerprinting based solution. Finally, Section 2.5 describes the three main kinds of existing filtering technologies applied in the navigation system, including the Kalman filter (KF) originated approaches, the particle filter (PF) originated approaches, and the nonlinear least squares (NLS) originated approaches.

2.1 Reference Coordinate Systems

This section focuses on the introduction of most commonly applied reference coordinate systems in the navigation filed, including the inertial coordinate system, the Earth-Centered Earth-Fixed (ECEF) coordinate system, the navigation coordinate system, the vehicle frame, and the body coordinate system.

The inertial coordinate system (i.e., i-frame) is constructed as a reference coordinate system that directly follows Newton's 1st and 2nd laws of motion and has no rotation or acceleration. Because the ideal i-frame cannot be acquired in real-world application, a typical definition of i-frame has its original point located at the center of the Earth and axes with non-rotating/accelerating axes with respect to distant galaxies. The i-frame has its z-axis parallels to the spin axis of the Earth (polar axis), its x-axis points toward the mean vernal equinox, and its y-axis that completes a right-handed orthogonal frame.

The ECEF coordinate system (i.e., e-frame) is constructed as a reference coordinate system which can be applied for GNSS and INS based navigation applications. For instance, the World Geodetic System (WGS) - 84 frame has its original point located at the center of the Earth and axes that are fixed with respect to the earth. The ECEF coordinate system has its x-axis in the equatorial plane points toward the Greenwich meridian, its z-axis along the Earth's polar axis and its y-axis completes a right-handed orthogonal frame.

The navigation coordinate system (i.e., n-frame) is constructed as a local geodetic frame, and is also regarded as the local-level frame (i.e., l-frame). The north-east-down

(NED) frame is adopted as the n-frame in the proposed algorithm in this thesis. This frame has its original points located at the measured center of the carriers, its x-axis points toward geodetic north, its z-axis orthogonal to the reference ellipsoid pointing down, and its y-axis obeys the right-handed orthogonal frame.

The vehicle coordinate system (i.e. v-frame) is constructed as the vehicle fixed coordinate system, which has its original point located with the measurement center of the carriers, its x-axis points toward the forward direction of the vehicle, its y-axis points toward the horizontal right of the vehicle and its z-axis points downwards of the vehicle. The v-frame is widely applied in the field of vehicular technology and applications, aiming at providing enhance performance of navigation algorithm.

The body coordinate system (b-frame) is related to the central of carrier. Its original point is located at the center of the measurement center of the carriers, and its axes are aligned with the roll, pitch and heading axes of the inertial hardware assembly. The b-frame is widely applied in the personal navigation algorithms since most of mobile terminals have integrated the rich sensors which can be applied for navigation purposes.

Figure 2-1 details the e-, n-, v-, and b-frames, in which X, Y, and Z represent the corresponding reference axis and the superscripts denote for the introduced frames in this section. λ and φ indicate the latitude and longitude information of the mobile terminal.

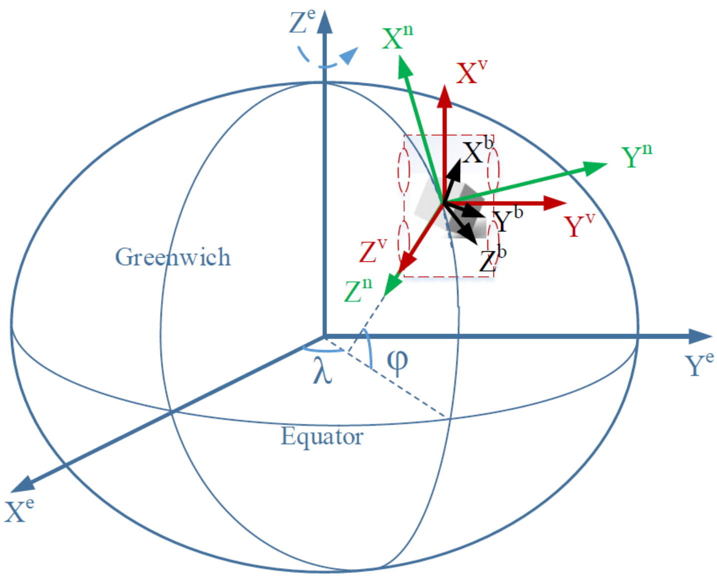

Figure 2-1 Coordinate Systems Used in Navigation [24]

2.2 MEMS Solutions for Indoor Positioning

2.2.1 INS Mechanization for Indoor Positioning

INS mechanization is proposed towards inertial sensors based localization and is widely applied for fields of pedestrian and vehicle navigation, which can provide real-time 3D motion information of the carrier with high sampling rate. The information of acceleration and angular rate acquired from MEMS sensors such as accelerometer and gyroscope are integrated by the INS mechanization for estimation of 3D position, velocity, and attitude of the moving object with high update rate, which is shown as follows [42]:

$$\begin{bmatrix} \dot{\boldsymbol{p}}^n \\ \dot{\boldsymbol{v}}^n \\ \dot{\boldsymbol{C}}_b^n \end{bmatrix} = \begin{bmatrix} \boldsymbol{\varpi}^{-1}\boldsymbol{v}^n \\ \boldsymbol{C}_b^n \boldsymbol{f}^b - (2\boldsymbol{\omega}_{ie}^n + \boldsymbol{\omega}_{en}^n) \times \boldsymbol{v}^n + \boldsymbol{g}^n \\ \boldsymbol{C}_b^n(\boldsymbol{\omega}_{ib}^b \times) - (\boldsymbol{\omega}_{in}^b \times)\boldsymbol{C}_b^n \end{bmatrix} \tag{2-1}$$

where

$$\boldsymbol{\varpi} = diag([R_m + h \quad (R_n + h)\cos\varphi \quad -1]) \tag{2-2}$$

where $\boldsymbol{p}^n = [\varphi \quad \lambda \quad h]^{\mathrm{T}}$ indicates the pedestrian's real-time 3D location (latitude, longitude, and height); $\boldsymbol{v}^n = [v_N \quad v_E \quad v_D]^{\mathrm{T}}$ represents the 3D velocity and $\boldsymbol{C}_b^n$ indicates the rotation matrix between body coordinate system and navigation coordinate system; $\boldsymbol{g}^n$ indicates the local gravity value; $\boldsymbol{\omega}_{ie}^n$ represents the rotation angular rate between the e-frame and i-frame; $\boldsymbol{\omega}_{en}^n$ indicates the rotation angular rate between navigation coordinate system and the ECEF coordinate system; $\boldsymbol{\varpi}^{-1}$ indicates a 3 × 3 matrix related to the latitude p_N and the ellipsoidal height p_D of the moving object. R_m and R_n indicate the radius of curvature of meridian and curvature in the prime vertical, respectively.

For the low-cost sensors based inertial navigation, a more simplified INS mechanization can be applied, which ignores rotation of the earth. The attitude update equation is described as follows:

$$\boldsymbol{Q}_{b(m)}^n = \boldsymbol{Q}_{b(m\text{-}1)}^n \circ \boldsymbol{Q}_{b(m)}^{b(m-1)} \tag{2-3}$$

where $\boldsymbol{Q}_{b(m)}^n$ indicates the quaternion of attitude transformation at epoch m; $\boldsymbol{Q}_{b(m)}^{b(m-1)}$ represents the change of attitude quaternion between epoch m and epoch m-1, which can be described as:

$$\boldsymbol{Q}_{b(m)}^{b(m-1)} = \begin{bmatrix} \cos\dfrac{\Delta\theta_m}{2} \\ \dfrac{\Delta\boldsymbol{\theta}_m}{\Delta\theta_m}\sin\dfrac{\Delta\theta_m}{2} \end{bmatrix} \tag{2-4}$$

where $\Delta\boldsymbol{\theta}_m$ represents the angular increment in the time period (m-1,m), and $\Delta\theta_m = |\Delta\boldsymbol{\theta}_m|$.

In low-cost inertial navigation systems, the influence of the rotation of the earth is generally ignored, therefore the speed update equation can be simplified as:

$$\boldsymbol{v}_m^n = \boldsymbol{v}_{m-1}^n + \Delta\boldsymbol{v}_{sf(m)}^n + \boldsymbol{g}^n T_s \tag{2-5}$$

In which:

$$\Delta\boldsymbol{v}_{sf(m)}^n = \boldsymbol{C}_{b(m-1)}^n (\Delta\boldsymbol{v}_m + \frac{1}{2}\Delta\boldsymbol{\theta}_m \times \Delta\boldsymbol{v}_m) \tag{2-6}$$

where $\boldsymbol{v}_m^n$ indicates the INS based velocity at epoch m, $\boldsymbol{C}_{b(m-1)}^n$ represents the attitude matrix, $\Delta\boldsymbol{v}_m$ represents the specific force increment in the period (t-1, t).

Finally, the position update equation is described as:

$$\boldsymbol{P}_m^n = \boldsymbol{P}_{m-1}^n + \frac{\boldsymbol{v}_{m-1}^n + \boldsymbol{v}_m^n}{2} T_s \tag{2-7}$$

where $\boldsymbol{P}_m^n = \begin{bmatrix} x_m & y_m & z_m \end{bmatrix}^{\mathrm{T}}$, T_s indicates the sampling rate.

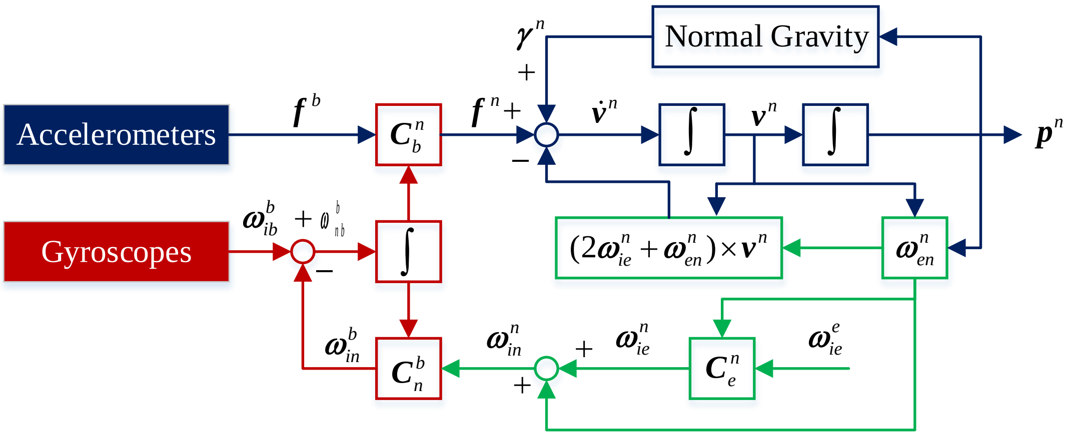

Figure 2-2 Diagram of the INS Mechanization [110]

2.2.2 PDR Mechanization for Indoor Positioning

Limited by the poor performance of low-cost sensors, the original INS mechanization exists deviation error increases with time, which leads to the decreasing positioning performance especially the walking speed estimation. PDR mechanization is proposed aiming at pedestrian tracking, by detecting the step-length, altitude increment and heading information in walking periods in order to update the 3D location of the pedestrian. The main structure of PDR mechanization is shown below:

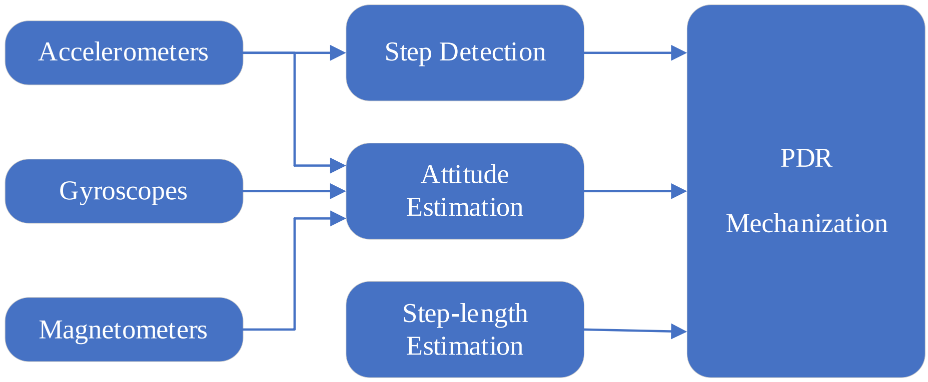

Figure 2-3 Diagram of PDR mechanization

During the procedure of pedestrian's walking periods, the collected acceleration data shows regular changes, therefore the biomechanical models are often used to detect pedestrian gait features and calculate the step-length [111]. The norm of extracted accelerometer data is calculated below:

$$\mathrm{Norm}_{\mathrm{acc}} = \sqrt{a_x{}^2 + a_y{}^2 + a_z{}^2} \tag{2-8}$$

where $\mathrm{Norm}_{\mathrm{acc}}$ represents the norm of real-time accelerometer data, a_x, a_y, and a_z indicate the extracted tri-axial acceleration information.

Due to the complexity and randomness of pedestrian's movement, the raw acceleration data is affected by noises and need to be smoothed. Low-pass filters are usually used to process raw acceleration data in order to obtain more obvious gait characteristics.

Affected by the randomness of the handheld modes of the pedestrian, the filtered acceleration data still contains multiple peaks which may lead to the wrong step count. Thus, the multi-peak recognition method which contains several constrains are presented in (3):

$$\begin{cases} \Delta T_{\mathrm{step}} > \delta_1 \\ \left|\mathrm{Norm}_{\mathrm{acc}} - g\right| < \delta_2 \end{cases} \tag{2-9}$$

where ΔT_{step} represents the time interval calculated by the two adjacent gaits; g indicates the local gravity value; δ_1 represents minimax time threshold of two detected steps; δ_2

indicates the maximum allowable acceleration. The final detected step information is shown below:

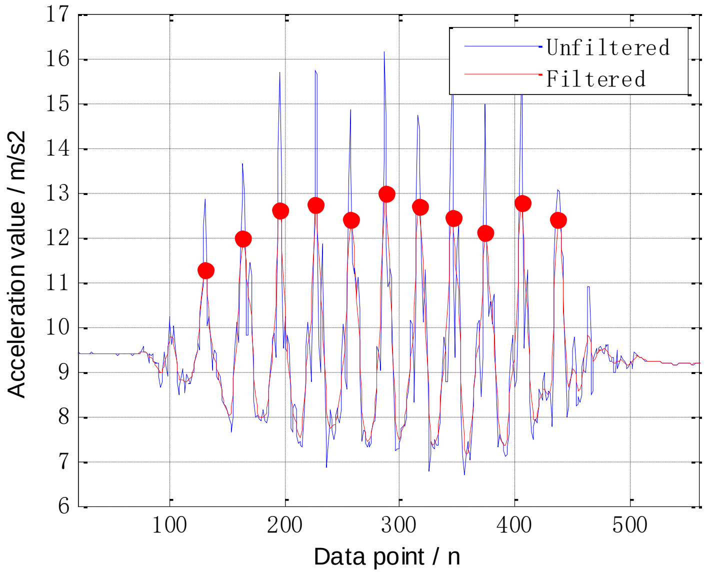

Figure 2-4 The Performance of Step Detection

An empirical model characterizes the relationship between step length and pedestrian's motion characteristics which is proposed by Harvey Weinberg [112] is shown below:

$$L = K\sqrt[4]{A_{\max} - A_{\min}} \tag{2-10}$$

where $A_{\max}$ and $A_{\min}$ indicate the detected peak and valley acceleration values during one gait cycle, K represents the adjustable parameters of the step length which can be calculated in (2-11):

$$K = \frac{d_{\text{estimated}}}{d_{\text{true}}} \tag{2-11}$$

where $d_{\text{estimated}}$ and d_{true} indicate the experimental and ground-truth distance during estimation.

It is found in [113] that the pedestrian's height and step frequency can also affect the accuracy of step-length estimation, in this paper, a linear model including pedestrian height and step frequency is also used:

$$L_{\text{step}}^2 = [0.7 + a(H - 1.75) + b\frac{(SF - 1.79)H}{1.75}]c \tag{2-12}$$

where L_{step}^2 and SF represent the step length and step frequency, respectively, H is the height of the pedestrian which is manually inserted in this step model, and a, b, and c are model parameters.

Because the pedestrian's height, attitude and walking frequency are different, users must train the model before using in order to obtain the optimal model parameters. However, this method is extremely inconvenient for users to use, so it is necessary to design an adaptive algorithm to automatically adjust the calibration parameter in order to meet the needs of users.

Taking pedestrians' height, step frequency and acceleration variation into consideration, two different kinds of walking speeds are calculated as follow:

$$\boldsymbol{V}^i(k) = \boldsymbol{V}^i(k-1) + SF \cdot \Delta L^i_{\text{step}}(k), i = 1,2 \tag{2-13}$$

where SF represents the step frequency, $\Delta L^i_{\text{step}}(k)$ indicates the change of step-length, $\boldsymbol{V}^i(k)$ represents real-time walking speed, the above two kinds of walking speed are fused by AEKF to get the optimized speed estimation result.

According to the discrete time model of attitude updating by gyroscope quaternion method and the velocity parameter calculated by step-length model in (2-10), the state equation of AEKF can be obtained using rotating quaternion and velocity as the state vector:

$$\boldsymbol{x}_k = \begin{bmatrix} \boldsymbol{Q}_k \\ \boldsymbol{V}_k \end{bmatrix} = \begin{bmatrix} F_{k,k-1}(\boldsymbol{\omega}_k, T_s) & 0 \\ 0 & 1 \end{bmatrix} \boldsymbol{x}_{k-1} + \begin{bmatrix} 0 \\ \Delta \boldsymbol{V}^1 \end{bmatrix} + \boldsymbol{w}_k \tag{2-14}$$

where $\boldsymbol{x}_k$ contains current moment's quaternion $\boldsymbol{Q}_k$ and walking speed $\boldsymbol{V}_k$ calculated by (2-12) in case of $i = 1$, $\Delta \boldsymbol{v}^1_{\text{speed}} = SF \cdot \Delta L^1_{\text{step}}(k)$ represents the velocity variation, $\boldsymbol{F}_{k,k-1}(\boldsymbol{\omega}_k, T_s)$ represents the state transition matrix which is used for quaternion updating, $\boldsymbol{\omega}_k$ indicates the angular velocity of gyroscope, T_s indicates the sampling rate, $\boldsymbol{w}_k = [\boldsymbol{w}^q_k \quad w^v_k]^{\mathrm{T}}$ represents the state noise with a state covariance matrix $\boldsymbol{U}_k$.

The sensor data acquired from the accelerometer and magnetometer can also be used to calculate pedestrian's real-time attitude information, the measured values of the normalized tri-axial acceleration, the normalized tri-axial magnetic value and walking speed calculated by (2-12) in case of $i = 2$ are taken as the observed vector, the observation equation is shown in (2-15):

$$\boldsymbol{z_k} = h(\boldsymbol{x_k}) + \boldsymbol{v}_k = \begin{bmatrix} \boldsymbol{T}^b_n(\boldsymbol{Q}_k) & 0 & 0 \\ 0 & \boldsymbol{T}^b_n(\boldsymbol{Q}_k) & 0 \\ 0 & 0 & 1 \end{bmatrix} \begin{bmatrix} \boldsymbol{g} \\ \boldsymbol{m} \\ \boldsymbol{V}_k \end{bmatrix} + \begin{bmatrix} \boldsymbol{v}^a_k \\ \boldsymbol{v}^m_k \\ v^s_k \end{bmatrix} \tag{2-15}$$

In which:

$$\boldsymbol{T}_{\boldsymbol{n}}^{\boldsymbol{b}}=\begin{bmatrix}1-2(q_2^2+q_3^2) & 2(q_1q_2+q_0q_3) & 2(q_1q_3-q_0q_2)\\ 2(q_1q_2-q_0q_3) & 1-2(q_1^2+q_3^2) & 2(q_2q_3+q_0q_1)\\ 2(q_1q_3+q_0q_2) & 2(q_2q_3-q_0q_1) & 1-(q_1^2+q_2^2)\end{bmatrix} \tag{2-16}$$

$$\boldsymbol{g}=\begin{bmatrix}0 & 0 & 1\end{bmatrix} \tag{2-17}$$

$$\boldsymbol{m}=\begin{bmatrix}0 & b_y & b_z\end{bmatrix} \tag{2-18}$$

The observed noise matrix can be expressed as:

$$\boldsymbol{R}=\begin{bmatrix}\sigma_a^2\boldsymbol{I} & 0 & 0\\ 0 & \sigma_m^2\boldsymbol{I} & 0\\ 0 & 0 & \sigma_v^2\end{bmatrix} \tag{2-19}$$

Because the relationship between the state vector and the measurement vector of the observation equation is non-linear, it is necessary to linearize the $h(\boldsymbol{x_k})$ in (2-15), and the measured matrix is linearized by (14). The observation Jacobian matrix obtained is shown in (2-20):

$$\boldsymbol{H}=\frac{\partial h(\boldsymbol{x_k})}{\partial \boldsymbol{x_k}}\bigg|_{x_k=x_k^-} \tag{2-20}$$

$$\boldsymbol{H}=\begin{bmatrix}-2q_2 & 2q_3 & -2q_0 & 2q_1 & 0\\ 2q_1 & 2q_0 & 2q_3 & 2q_2 & 0\\ 4q_0 & 0 & 0 & 4q_3 & 0\\ 2b_yq_3-2b_zq_2 & 2b_yq_2+2b_zq_3 & 2b_yq_1-2b_zq_0 & 2b_yq_0+2b_zq_1 & 0\\ 4b_yq_0+2b_zq_1 & 2b_zq_0 & 4b_yq_2+2b_zq_3 & 2b_zq_2 & 0\\ -2b_yq_1+4b_zq_0 & -2b_yq_0 & 2b_yq_3 & 2b_yq_2+4b_zq_3 & 0\\ 0 & 0 & 0 & 0 & 1\end{bmatrix} \tag{2-21}$$

The measurement noise of accelerometer and magnetometer basically remain unchanged in the static and non-magnetic cases, but when the mobile terminal produces large linear acceleration or magnetic interference exists in the surrounding environment, the actual measurement values of accelerometer and magnetometer contains uncertainty error. To solve the problem, this paper constructs the adaptive observation variance σ_a^2, σ_m^2 and σ_v^2 to adjust the weights of measured values, which can be used in dynamic acceleration and magnetic interference contained environments.

$$\sigma_a^2=k_{a1}(|\|\boldsymbol{a}_k\|-\|\mathbf{g}\||)+k_{a2}var(\|\boldsymbol{a}_{k\text{-}N}\|:\|\boldsymbol{a}_k\|) \tag{2-22}$$

$$\sigma_m^2=k_{m_1}var(\|\theta_{k\text{-}N}\|:\|\theta_k\|)+k_{m_2}var(\|\boldsymbol{m}_{k\text{-}N}\|:\|\boldsymbol{m}_k\|) \tag{2-23}$$

$$\sigma_v^2=k_v var(\|\boldsymbol{V}^1-\boldsymbol{V}^2\|_{k\text{-}N:k}) \tag{2-24}$$

In (2-22), the deviation between acceleration modulus and standard gravity value and the variance of acceleration modulus are used as eigenvalues to adjust the weight of acceleration data in AEKF. In (2-23), the variance of heading calculated by magnetometer and modulus of magnetometer data are used to detect the quasi-static magnetic field (QSMF) in surrounding environments [114], the magnetometer data in QSMF periods can be used after calibration, and the absolute heading reference provided by magnetometer data will be used to correct cumulative error caused by gyroscope. In (2-24), the deviation between two kinds of speed is used to adjust the weight of observed value.

Another usually applied heading estimation is complementary filter, in this work, an enhanced complementary filter (ECF) is described to integrate the real-time data collected from multiple sensors. The original complementary filter (CF) combines the high-frequency characteristics of gyroscope and low-frequency characteristics of accelerometer and magnetometer and finally provides the optimal real-time attitude estimation result, which was first proposed in [115].

In the proposed ECF, the gyroscope plays the most important role in attitude updating, the accelerometer data is used to correct the gyroscope's roll and pitch drift, and the heading drift is corrected by the magnetometer data. When the pedestrian is walking, the accuracy of accelerometer is subject to the interference originated from the external acceleration, which presents the collected data from the magnetometer after removing the local gravity value. Therefore, the weight information of the acceleration needs to be adjusted in real time according to the magnitude of the external acceleration.

In a complex and changing indoor scene, the magnetometer data is also affected by the surrounding artificial magnetic field which leads to a relatively magnetic declination. Therefore, the surrounding magnetic field needs to be detected and analyzed to determine the weight of the magnetometer information. In this work, QSMF periods are recognized in the procedure of pedestrian’s walking when the strength of the local magnetic field (LMF) remains unchanged or fluctuates within a small range in indoor environments.

The ECF proposed in this paper extracts the features of external acceleration and magnetic field during QSMF periods based on the acceleration and magnetometer data and constructs an adaptive way to adjust the weight of each. The main parts of the proposed ECF are described as follows:

1) Complementary of Pitch and Roll Using Accelerometer Data. In the body coordinate, the measured value obtained by the accelerometer can be described as equation (2-25):

$$Acc_b = \begin{bmatrix} a_x & a_y & a_z \end{bmatrix}^{\mathrm{T}} \tag{2-25}$$

where Acc_b is consist of a_x, a_y, and a_z, which indicates the collected accelerometer data in the body coordinate, and the normalized acceleration is calculated in equation (2-26):

$$Acc_{norm} = \begin{bmatrix} \dfrac{a_x}{\mathrm{Norm_{acc}}} & \dfrac{a_y}{\mathrm{Norm_{acc}}} & \dfrac{a_z}{\mathrm{Norm_{acc}}} \end{bmatrix}^{\mathrm{T}} \tag{2-26}$$

where Acc_{norm} represents the normalized acceleration vector, $\mathrm{Norm_{acc}} = \sqrt{a_x^2 + a_y^2 + a_z^2}$ represents the acceleration modulus. The reference normalized gravity value in the navigation coordinate is described in equation (2-27):

$$Acc_n = \begin{bmatrix} 0 & 0 & 1 \end{bmatrix}^{\mathrm{T}} \tag{2-27}$$

Then transform the reference gravity vector from navigation coordinate to body coordinate using current attitude matrix:

$$v = \begin{bmatrix} v_x \\ v_y \\ v_z \end{bmatrix} = \boldsymbol{T_n^b} Acc_n = \begin{bmatrix} 2\,(q_1 q_3 - q_0 q_2) \\ 2\,(q_2 q_3 + q_0 q_1) \\ 1-(q_1^2 + q_2^2) \end{bmatrix} \tag{2-28}$$

where q_0, q_1, q_2, and q_3 represent the attitude quaternion, and the relationship between the attitude matrix and the attitude quaternion is described as:

$$\boldsymbol{T_n^b} = \begin{bmatrix} 1-2(q_2^2+q_3^2) & 2\,(q_1 q_2 + q_0 q_3) & 2\,(q_1 q_3 - q_0 q_2) \\ 2\,(q_1 q_2 - q_0 q_3) & 1-2(q_1^2+q_3^2) & 2\,(q_2 q_3 + q_0 q_1) \\ 2\,(q_1 q_3 + q_0 q_2) & 2\,(q_2 q_3 - q_0 q_1) & 1-(q_1^2+q_2^2) \end{bmatrix} \tag{2-29}$$

Then construct the acceleration error vector through vector cross product between equation (2-26) and equation (2-28):

$$e_{acc} = Acc_{norm} \times v \tag{2-30}$$

where e_{acc} indicates pitch and roll errors in the attitude quaternion obtained from the gyro integration.

2) Complementary of Heading Using Magnetic Data. In the body coordinate, the normalized value obtained by the magnetometer can be described as equation (2-31):

$$Mag_{norm} = \begin{bmatrix} \dfrac{m_x}{\mathrm{Norm_{mag}}} & \dfrac{m_y}{\mathrm{Norm_{mag}}} & \dfrac{m_z}{\mathrm{Norm_{mag}}} \end{bmatrix}^{\mathrm{T}} \tag{2-31}$$

where $\mathrm{Norm_{mag}} = \sqrt{{m_x}^2 + {m_y}^2 + {m_z}^2}$, m_x, m_y, and m_z indicate the collected magnetometer data.

Normally, the magnetic field indoors contains interferences due to the complex interior architecture, and the indoor magnetic field shows large fluctuations, which cannot be integrated directly. In a changeable indoor environment, QSMF detection algorithm can be applied to recognize the relatively stable magnetic field when the pedestrian is walking indoors. In this paper, the QSMF detection algorithm proposed in [114] is used to detect the useful local magnetic data and then transform the local magnetic field from body coordinate to navigation coordinate by equation (2-32):

$$h = \begin{bmatrix} h_x \\ h_y \\ h_z \end{bmatrix} = \boldsymbol{T_b^n} Mag_{norm} \tag{2-32}$$

where *hx*, *hy*, and *hz* indicate the transformed magnetic value in the navigation coordinate system.

Then calibrate the local magnetic field and get the optimal magnetic vector in the navigation coordinate by equation (2-33):

$$Mag^n_{\text{calibrated}} = \begin{bmatrix} b_x \\ 0 \\ b_z \end{bmatrix} = \begin{bmatrix} \sqrt{h_x^2 + h_y^2} \\ 0 \\ h_z \end{bmatrix} \tag{2-33}$$

Transform the calibrated magnetic value from the navigation coordinate to the body coordinate by equation (2-34):

$$Mag^b_{\text{calibrated}} = \begin{bmatrix} w_x \\ w_y \\ w_z \end{bmatrix} = \boldsymbol{T_n^b} Mag^n_{\text{calibrated}} \tag{2-34}$$

Similarly, we can get the magnetic error vector through vector cross product between equation (2-31) and equation (2-34):

$$e_{mag} = Mag_{Norm} \times Mag^b_{\text{calibrated}} \tag{2-35}$$

3) Adaptive Compensation of Gyro angular velocity Using External Acceleration and QSMF Data. The low frequency characteristics of accelerometer and magnetometer can be used to eliminate the constant offset and cumulative error during gyroscope-based attitude estimation.

The constructed error vector of the acceleration is used to calibrate the pitch and roll angle error, the correction parameter obtained from the error can be expressed as:

$$\delta_{acc} = K_{a_1} \cdot e_{acc} + K_{a_2} \cdot \int e_{acc} dt \tag{2-36}$$

where K_{a_1} and K_{a_2} are used to compensate the instantaneous and cumulative errors of gyro angular velocity in the procedure of pitch and roll angle calculation.

The constructed error vector of magnetic field is used to calibrate the heading error, and the correction parameter obtained from the error vector can be expressed as:

$$\delta_{mag} = K_{m_1} \cdot e_{mag} + K_{m_2} \cdot \int e_{mag} dt \tag{2-37}$$

where K_{m_1} and K_{m_2} are used to compensate the instantaneous and cumulative errors of the gyroscope angular velocity in the procedure of heading angle calculation.

The two parameters δ_{acc} and δ_{mag} can be used to calibrate the drift of the gyroscope-based attitude respectively, and adjust the weight according to the calculated external acceleration and QSMF detection. The final compensation model of the gyro angular rate is described as follows:

$$w = \begin{bmatrix} w_x^b \\ w_y^b \\ w_z^b \end{bmatrix} = w_{gyro} + \delta_{acc} + \delta_{mag} \tag{2-38}$$

where w_x^b , w_y^b and w_z^b indicate the compensated data of collected gyroscope angular rate, and the attitude information using the compensated gyro angular rate is updated based on the Runge-Kutta quaternion update equation [60] and the quaternion is normalized after updating:

$$\begin{bmatrix} \dot{q}_0 \\ \dot{q}_1 \\ \dot{q}_2 \\ \dot{q}_3 \end{bmatrix} = \frac{1}{2} \cdot \begin{bmatrix} 0 & -w_x^b & -w_y^b & -w_z^b \\ w_x^b & 0 & w_z^b & -w_y^b \\ w_y^b & -w_z^b & 0 & w_x^b \\ w_z^b & w_y^b & -w_x^b & 0 \end{bmatrix} \cdot \begin{bmatrix} q_0 \\ q_1 \\ q_2 \\ q_3 \end{bmatrix} \tag{2-39}$$

$$q = \frac{\dot{q}_0 + \dot{q}_1 i + \dot{q}_2 j + \dot{q}_3 k}{\sqrt{\dot{q}_0^2 + \dot{q}_1^2 + \dot{q}_2^2 + \dot{q}_3^2}} \tag{2-40}$$

where $\dot{q}_0$, $\dot{q}_1$, $\dot{q}_2$ and $\dot{q}_3$ represent the updated quaternion. The fused attitude maintains much higher accuracy and stability, which is more suitable in complex indoor environments.

In the PDR mechanization, after the estimation of step-length, the required heading information is provided by the fusion of both INS and PDR mechanizations to restrain the accumulative error. The real-time 2D location of the pedestrian is updated based on the last positioning result, which is shown as follows:

$$\begin{cases} P_x(k) = P_x(k\text{-}1) + L(k)\cdot\sin(\theta(k)) \\ P_y(k) = P_y(k\text{-}1) + L(k)\cdot\cos(\theta(k)) \end{cases} \tag{2-41}$$

where $[P_x(k), P_y(k)]$ and $[P_x(k\text{-}1), P_y(k\text{-}1)]$ indicate the pedestrian's location at the moment $k-1$ and k; $L(k)$ and $\theta(k)$ represent the calculated step-length and direction at epoch k.

In order to get the altitude information indoors, the barometer is used to estimate the altitude difference in 3D indoor buildings. The relationship between height and barometer-measured air pressure is described as [116]:

$$h_b = 44330\cdot(1.0-(\frac{100p}{p_0})^{\frac{1.0}{5.255}}) \tag{2-42}$$

where h_b represents the real-time height estimated by the barometer, p and p_0 represent the measured air pressure and the sea level reference pressure, respectively.

2.3 Wi-Fi FTM Solution for Indoor Positioning

Wi-Fi FTM protocol enables distance measurement between initiators and responders such as mobile phones and APs. The whole procedure is described as follows. Firstly, the initiator send a FTM request to responder, then the responder receive the request and return an ACK signal to the initiator which indicates that the responder has received the FTM request, after that several FTM signals are sent from responder to initiator to calculate the mean RTT. This process can be performed between several initiators and responders at the same time. Figure 2 shows the whole protocol. In this procedure, the parameter names 'FTMs per Burst' can be changed to improve the FTM accuracy by multiple measurements. The single RTT among one FTM period is calculated in equation (2-43):

$$\text{RTT}=(t_{4\_\text{n}}-t_{1\_\text{n}})-(t_{3\_\text{n}}-t_{2\_\text{n}}) \tag{2-43}$$

where n indicates one of the FTM structure exchange during the whole FTM procedure, t_{1_n} is the timestamp when the FTM structure first sent by the responder, t_{2_n} is the timestamp when the FTM structure received by the initiator, t_{3_n} is the timestamp when the initiator returns the FTM structure to the responder and t_{4_n} is the timestamp when the FTM structure finally received by the responder. Generally, the protocol excludes the processing time on the initiator by subtracting it (t_{3_n} - t_{2_n}) from the total round trip time (t_{4_n} - t_{1_n}), which represents the time from the instant when the FTM structure is sent (t_{1_n}) by the responder to the instant when the FTM structure is finally received by the responder (t_{4n}). This calculation is repeated for each FTM structure exchange and the final RTT is the average over the number of FTMs per burst. In this paper, we just set the parameter FTMs per burst as 30 to decrease and average the measurement error so as to keep high accuracy [79].

The distance between initiator and responder can be calculated by equation (2-44):

$$\text{distance} = C \cdot \left[(t_{4\_n} - t_{1\_n}) - (t_{3\_n} - t_{2\_n}) \right] / 2 \tag{2-44}$$

where C indicates the speed of radio wave.

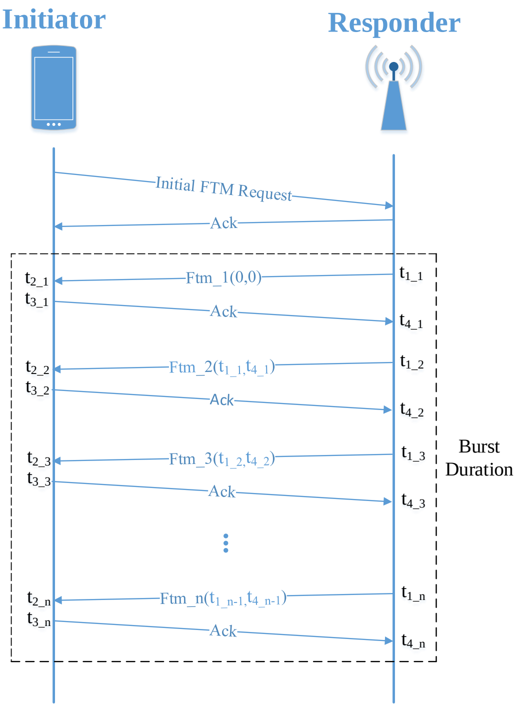

Figure 2-5 Duration of FTM Procedure, FTMs per Burst = n

In Figure 2-5 the parameter which called the 'FTMs per Burst' is defined to increase the ranging precision by averaging series of measurement results. The final output RTT information among one ranging procedure is estimated by equation (2-45):

$$\text{RTT} = \frac{1}{n} \cdot \sum_{k=1}^{n} \left(\left[t_4(k) - t_1(k) \right] - \left[t_3(k) - t_2(k) \right] \right) \tag{2-45}$$

where $t_1(k)$ indicates the recorded timestamp of ranging parameters firstly emitted by the initiator, $t_2(k)$ represents the timestamp of the acquired ranging parameters by the responder, $t_3(k)$ indicates the timestamp when the responder returns back the ACK signal to the initiator, $t_4(k)$ indicates the timestamp of final received ACK signal by the initiator side, and the n represents the definition of "FTMs per burst" during each ranging procedure.

When the required RTT value is calculated, the distance between the initiator and the responder can be converted as follow:

$$D_{\mathrm{RTT}} = \frac{C}{2n} \cdot \sum_{k=1}^{n} \left(\left[t_4(k) - t_1(k) \right] - \left[t_3(k) - t_2(k) \right] \right) \tag{2-46}$$

where $\boldsymbol{C}$ indicates the wireless propagation speed and D_{RTT} indicates the estimated distance during one ranging procedure.

The typical least squares (LS) method [26] is usually applied for positioning purposes, which is consist of following equations:

$$\boldsymbol{x}_p = (\boldsymbol{A}^T \boldsymbol{A})^{-1} \boldsymbol{A}^T \boldsymbol{b} \tag{2-47}$$

$$\boldsymbol{x}_p = \left[x\, y \right]^T, \boldsymbol{A} = 2 \cdot \begin{bmatrix} x_1 - x_2 & y_1 - y_2 \\ x_1 - x_3 & y_1 - y_3 \\ \vdots & \vdots \\ x_1 - x_j & y_1 - y_j \end{bmatrix}, \boldsymbol{b} = \begin{bmatrix} D_{\mathrm{RTT}}(2) - D_{\mathrm{RTT}}(1) - ({x_2}^2 - {x_1}^2) - ({y_2}^2 - {y_1}^2) \\ D_{\mathrm{RTT}}(3) - D_{\mathrm{RTT}}(1) - ({x_3}^2 - {x_1}^2) - ({y_3}^2 - {y_1}^2) \\ \vdots \\ D_{\mathrm{RTT}}(j) - D_{\mathrm{RTT}}(1) - ({x_j}^2 - {x_1}^2) - ({y_j}^2 - {y_1}^2) \end{bmatrix}$$

(2-48)

where $\boldsymbol{x}_p$ indicates the calculated 2D location, j indicates the deployed responders, x_j and y_j represent the location of each deployed local responder, and $D_{\mathrm{RTT}}(j)$ indicates the received RTT value between the initiator and each deployed responder. In a typical LS algorithm, the number of responders will affect the final positioning accuracy. The number of responders needs to be at least three. Appropriately increasing the number of responders will theoretically improve the accuracy of positioning. [117].

In order to analyze the performance of Wi-Fi FTM, a Wi-Fi ranging system including hardware and software support was built up, which can realize real-time data acquisition with a specified frequency. The whole ranging system is composed as follows:

FTM Responder/AP. Implementation of RTT data acquisition requires hardware and software support. We choose the Intel Dual Band Wireless-AC 8260 card as the first type of AP/responder and use the ubuntu 16.04 LTS system and Linux kernel version 4.4.0-21 as the software platform. The original driver pack does not contain the FTM response function so we need to modify the driver and add the FTM response function. By downloading the hostapd-2.3 and open the Wi-Fi hotspot one RTT responder can be made. Then we choose the mobile phone VIVO NEX and VIVO X21 based on Andriod 8.1 which support the IEEE.802.11 FTM as the second and third type of AP, just open the hotspot mode of the phone, RTT information can be got by initiator.

FTM Initiator. We use the same hardware and software platform as the first kind of AP Responder to make a RTT Initiator. By modifying the RTT ranging command and adding FTM function into the driver we can get the RTT information from multi APs by sending the ranging requests from the initiator containing MAC address, bandwidth and frequency. Only APs which support FTM can return the RTT information. With knowing position of three or more APs and RTT information between initiator and APs we can get real-time position of the mobile initiator. In addition, Android P has provided the platform and API which can be used for RTT ranging, so we also use the mobile phone Google Pixel 1 which has installed the latest Android P or higher system as another initiator. In this system, several initiators are supported to use at the same time and acquire RTT data from multi-APs. Different sampling rate of RTT can be set by modifying the parameters of ranging function. The total Wi-Fi FTM based ranging system which contains mobile terminals and the open platform is described in Figure 2-6:

Figure 2-6 Wi-Fi FTM Based Ranging System

At this stage, not all the IoT terminals support the Wi-Fi FTM ranging protocol, the Table 2-1 lists the part of Android based smartphones which support the Wi-Fi FTM protocol, and Table 2-2 lists the part of Wi-Fi APs or wireless cards which support the Wi-Fi FTM protocol:

Table 2-1 Android Devices That Support Wi-Fi FTM Protocol

Manufacturers and Models	Android Version
Xiaomi Redmi Note 5 Pro	Android 9.0 or higher
LG V30	Android 9.0 or higher
Samsung Note 10+	Android 9.0 or higher
Samsung A9 Pro	Android 9.0 or higher
Google Pixel 4	Android 9.0 or higher

Google Pixel 3	Android 9.0 or higher
Google Pixel 2	Android 9.0 or higher
Google Pixel 1	Android 9.0 or higher

Table 2-2 Wi-Fi APs or Wireless Cards That Support Wi-Fi FTM Protocol

Manufacturers and Models	Availability
Compulab WILD AP	Yes
Google Wi-Fi	Yes
Google Nest Wi-Fi	Yes
Aruba 500 Series	Yes
Inter AC 8260	Yes
Inter AC 8265	Yes
Inter AC 9260	Yes
ASUS RT-ACRH13	Not advertise
ASUS RT-ACRH17	Not advertise
Netgear Orbi (RBR20)	Not advertise

2.4 Wi-Fi Fingerprinting Solution for Indoor Positioning

This thesis focuses on two wireless positioning techniques: the Wi-Fi FTM based ranging and Wi-Fi RSSI based fingerprinting. At this stage, the Wi-Fi RSSI based fingerprinting approach can provide more universal localization performance because a large amount of smart city scenes are covered with local wireless facilities.

The Wi-Fi fingerprinting based approaches always contains two main phases: the off-line phase which can also be called as the Wi-Fi fingerprinting database construction. The other is called as the on-line positioning phase, using the classification algorithms to match the optimal position from the collected navigation database. The main procedure of Wi-Fi fingerprinting is described in Figure 2-7:

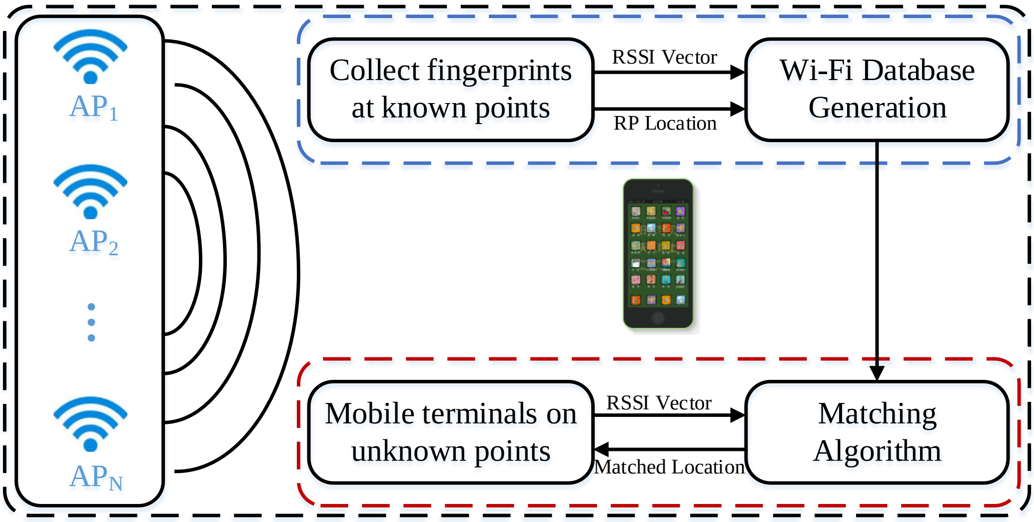

Figure 2-7 Wi-Fi RSSI Fingerprinting Procedure

The method of Wi-Fi fingerprinting database construction always contains three main types:

1) Static point-to-point method, usually generates database by averaging the RSSI signal at each reference point (RP), which proves higher reliability but is labor-consuming;

2) Mobile walk-survey method, by collecting Wi-Fi RSSI data among a high-precision walking trajectory between selected landmarks, which is much more efficiency than the static method;

3) Crowdsourcing-based method, usually generates navigation database through spatial big data provided by the amount of IoT terminals, which provides an autonomous way for Wi-Fi fingerprinting database generation and update.

The raw collected Wi-Fi fingerprinting data needs to be pre-processed before generating the final Wi-Fi fingerprinting database. Normally, multi-level constraints need to be applied to adaptively select the useful local Wi-Fi information:

1) The filtering of Wi-Fi RSSI: The Wi-Fi APs with more obvious strength characteristics are added into database:

$$\begin{cases} RSS_k \geq Th_{01}, \text{remained} \\ RSS_k < Th_{01}, \text{dropped} \end{cases} \tag{2-49}$$

where $Th01$ indicates the applied threshold for APs selection, the received RSSI values below $Th01$ will be dropped. In this work, the value of threshold $Th01$ is set as -90 dBm according to the propagation characteristics of RSSI signals.

2) The number of selected Wi-Fi APs: in the procedure of crowdsourced fingerprinting generation, after filtering the Wi-Fi APs by RSSI information in (2-49), the quantity of Wi-Fi APs is needed in WKNN algorithm in order to get the optimal position matching information:

$$\begin{cases} Num_k \geq Th_{02}, \text{remained} \\ Num_k < Th_{02}, \text{dropped} \end{cases} \tag{2-50}$$

where *Th*02 indicates the needed number of APs in the WKNN algorithm, in this work, the value of threshold is acquired by the amount of experiments in different environments, the overall estimated matching accuracy of WKNN algorithm in case of different number of selected Wi-Fi APs is shown in Figure 2-8:

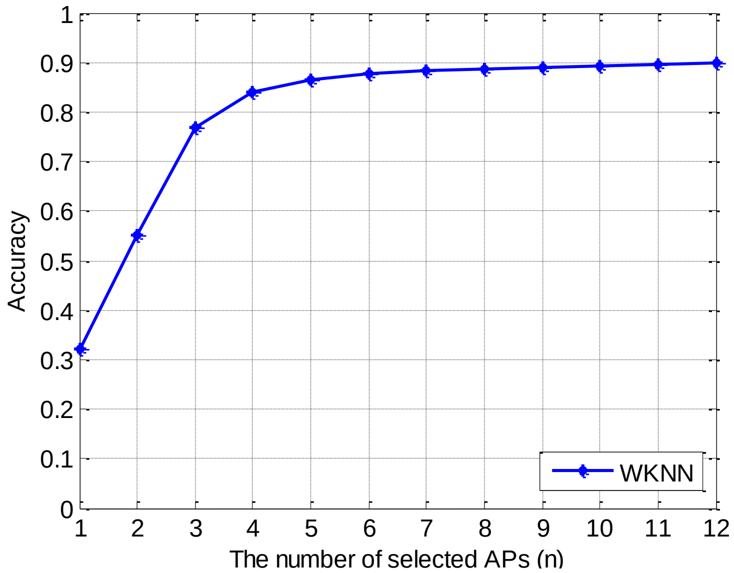

Figure 2-8 The Relationship Between WKNN Accuracy and Number of APs

It can be found from Figure 2-8 that when the number of APs is larger than 6, the accuracy of the WKNN based matching result remains basically unchanged. Thus, the threshold Th_{02} is set as 6 in order to provide the useful matching results in Wi-Fi fingerprinting database.

3) Signal smoothing: The RSSI information between adjacent timestamps can be averaged in the case of low-speed movement:

$$RSS_k = \frac{1}{n}\sum_{k=1}^{n} RSS_k, v_p \leq Th_{03} \tag{2-51}$$

where RSS_k indicates the averaged Wi-Fi AP based RSSI in case of low walking speed. The threshold Th_{03} is used to determine whether the pedestrian is moving slowly. In this work, the value of threshold Th_{03} is set as 0.65 m/s according to the pedestrian's walking characteristics.

The final constructed crowdsourced radio map is described as:

$$\mathbf{RadioMap} = \begin{pmatrix} \boldsymbol{P}_1^w & \mathbf{Array}_1^{RSSI} \\ \boldsymbol{P}_2^w & \mathbf{Array}_2^{RSSI} \\ \cdots & \cdots \\ \boldsymbol{P}_j^w & \mathbf{Array}_j^{RSSI} \end{pmatrix} \tag{2-52}$$

where j indicates the capacity of the final crowdsourced Wi-Fi fingerprinting database. $\boldsymbol{P}_j^w = (x_j, y_j, z_j)$ represents the location of each reference point in database, and $\mathbf{Array}_j^{RSSI}$ is the corresponding RSSI based vector.

In the positioning phase or on-line phase, the IoT terminal measures and collects the local wireless information and models the pre-processed Wi-Fi RSSI as the input value of the classification algorithm. Because the location of the pedestrian in the real-world environments is unknown, the estimated location of the pedestrian can be acquired using the matching approach by comparing the input value of the RSSI vector with the RSSI vectors acquired from the database. The calculated Euclidean distance between each comparison procedure is described as:

$$D_i = |\beta - \gamma_i| \tag{2-53}$$

where D_i indicates the calculated Euclidean distance among real-time constructed RSSI vector β and the ith candidate RSSI vector information γ_i.

After adaptively selecting the parameter K, the eligible reference locations in database are weighted for the final position calculation, the weight of each reference location is provided by the similar degree γ:

$$\mathrm{POS}'(x_r, y_r) = \frac{\sum_{i=1}^{K} \omega_i^{\gamma} \mathrm{POS}(x_i, y_i)}{\sum_{i=1}^{K} \omega_i^{\gamma}} \tag{2-54}$$

In which $\mathrm{POS}'(x_r, y_r)$ is the positioning result of WKNN, $\mathrm{POS}(x_i, y_i)$ indicates the selected reference location in database, ω_i^{γ} represents the weight value of the i^{st} reference position acquired from the generated navigation database.

2.5 Filtering Algorithms for Positioning

This section will discuss the existing classical filtering technologies towards multi-source fusion based indoor navigation, including the basic Kalman filter (KF) and its enhanced structures such as the extended Kalman filter (EKF) and the unscented Kalman filter (UKF), and the basic particle filter (PF) and its extended version such as the unscented particle filter (UPF). In addition, the nonlinear least squares (NLS) based approach is also discussed in this section.

2.5.1 Kalman Filter

The typical KF is firstly proposed in 1960, which overcomes the shortcomings of Wiener filtering and is widely applied in many application fields. It can estimate the current state value based on the system state value at the previous moment and the current observation value using the modeled system state update equation. The original KF framework is also called the basic KF, which is normally designed for solving the state or parameter estimation problems of random linear discrete systems.

The system state equation in the Kalman filtering is normally described as:

$$\boldsymbol{X}(k) = \boldsymbol{AX}(k-1) + \boldsymbol{W}(k) \quad \text{(2-55)}$$

where $\boldsymbol{A}$ is the state transition matrix, and $\boldsymbol{W}(k)$ is a driving noise with i dimension which contains random clock deviation.

The observation equation is defined as:

$$\boldsymbol{Z}(k) = \boldsymbol{HX}(k) + \boldsymbol{V}(k) \quad \text{(2-56)}$$

where $\boldsymbol{Z}(k)$ is an observation of RTT ranging result, $\boldsymbol{H}$ is i dimensional diagonal observation matrix, $\boldsymbol{V}(k)$ is observation noise.

The basic procedure of KF is summarized as follows:

State prediction:

$$\boldsymbol{X}_p(k) = \boldsymbol{AX}_e(k\text{-}1) \quad \text{(2-57)}$$

State updating:

$$\boldsymbol{X}_e(k) = \boldsymbol{X}_p(k) + \boldsymbol{K}(k)\cdot(\boldsymbol{Z}(k) - \boldsymbol{HX}_p(k)) \quad \text{(2-58)}$$

MSE phase:

$$\boldsymbol{p}_p(k) = \boldsymbol{Ap}_e(k-1)\boldsymbol{A}' + \boldsymbol{Q} \quad \text{(2-59)}$$

$$\boldsymbol{P}_e(k) = \boldsymbol{P}_p(k) - \boldsymbol{K}(k)\boldsymbol{P}_p(k) \quad \text{(2-60)}$$

Kalman Gain:

$$\boldsymbol{K}(k) = \boldsymbol{P}_p(k)\boldsymbol{H}'/(\boldsymbol{HP}_p(k)\boldsymbol{H}' + \boldsymbol{R}) \quad \text{(2-61)}$$

where $\boldsymbol{P}_p(k)$ is the prediction mean square error (MSE) of the estimate when the current observation is not considered, $\boldsymbol{X}_p(k)$ indicates the predicted state value, $\boldsymbol{P}_e(k)$ is the covariance matrix, $\boldsymbol{K}(k)$ indicates the Kalman gain. The general process of the discrete time KF is shown in Figure 2-9:

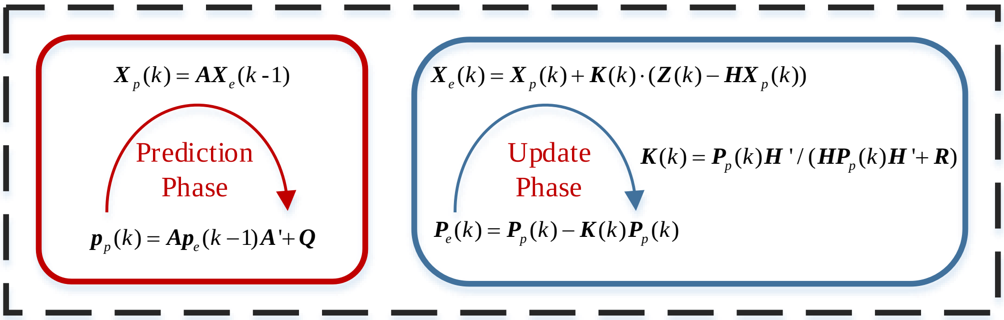

Figure 2-9 Typical Process of Discrete Time KF

The Kalman filter we mentioned above is used in linear systems and is performed under the assumption of Gaussian and linear motion (prediction) and observation models. The transmission result of Gaussian distribution in a nonlinear system will no longer be Gaussian distribution, and nonlinear problems can be solved through local linearity.

EKF is an enhance version of nonlinear approximate filtering algorithm, which is proposed aiming at the situation where the state or the observation model is not linear. EKF linearizes the state or the observation model using first-order Taylor series. In addition, the typical KF and EKF follow the same procedure of filtering, both present the posterior probability density in Gaussian distribution, and both are acquired by updating the Bayesian recursion equation. The biggest difference is that when calculating the variance, the state transition matrix of EKF (the state information k-1|k-1 at the previous moment) and the observation matrix (one-step prediction k|k-1) are both the Jacobian of the state information matrix. The standard procedure of EKF is described as follows:

State vector prediction:

$$\boldsymbol{x}_k^- = \boldsymbol{F}_{k,k-1}\boldsymbol{x}_{k-1} \tag{2-62}$$

Covariance matrix prediction:

$$\boldsymbol{P}_k^- = \boldsymbol{F}_{k,k-1}\boldsymbol{P}_{k-1}\boldsymbol{F}_{k,k-1}{}^{\mathrm{T}} + \boldsymbol{U}_k \tag{2-63}$$

Observation Matrix linearization:

$$\boldsymbol{H}=\frac{\partial h(\boldsymbol{x}_k)}{\partial \boldsymbol{x}_k}\bigg|_{x_k=x_k^-} \tag{2-64}$$

Kalman gain calculation:

$$\boldsymbol{K}_k(k)=\boldsymbol{P}_k^-\boldsymbol{H}_k^{\mathrm{T}}\left[\boldsymbol{H}_k\boldsymbol{P}_k^-\boldsymbol{H}_k^{\mathrm{T}}+\boldsymbol{R}_k\right]^{-1} \tag{2-65}$$

State vector update:

$$\boldsymbol{x}_k=\boldsymbol{x}_k^-+\boldsymbol{K}_k\left[\boldsymbol{z}_k-\boldsymbol{H}_k\boldsymbol{x}_k^-\right] \tag{2-66}$$

Covariance matrix update.

$$\boldsymbol{P}_k=\boldsymbol{P}_k^- -\boldsymbol{K}_k\boldsymbol{H}_k\boldsymbol{P}_k^- \tag{2-67}$$

The typical KF can only applied in case of linear model, and the EKF transforms non-linear state of observation model into the linear Gaussian model, by which the analytical form in the Bayesian recursion formula could be applied in the same way, which is convenient for calculation. But for non-linear problems, EKF not only has a higher complexity of calculation, but also has the influence of linear error, so UKF is further introduced. The main difficulty in solving the Bayesian recursive formula for nonlinear models lies in how to analytically solve the probability of one-step prediction state distribution, the likelihood function distribution density (obtained from the observation equation) and the posterior conditional probability distribution. EKF uses Taylor decomposition to linearize the state and observation models, using Gaussian hypothesis to solve the problem of difficulty in probability calculation. But the introduction of linear error reduces the accuracy of the model. For nonlinear models, it is more difficult to solve the Bayesian recursion formula directly analytically. It is difficult to obtain the mean and variance of each probability distribution analytically. The approximation method of each order moment of the variable can better solve this problem. Through a certain regular sampling and weighting, the mean and variance can be approximated. Moreover, because the insensitive transformation has a high approximation accuracy for statistical moments, the performance of UKF can reach the accuracy of second-order EKF.

The typical UKF is usually consist of eight main steps:

1) Calculating sigma point set using the state value $\hat{\boldsymbol{X}}(t\,|\,t)$ and the corresponding weight at the last timestamp:

$$\begin{cases} \boldsymbol{X}^{(\eta)}(t|t) = [\overset{\eta=0}{\hat{\boldsymbol{X}}(t|t)}, \overset{\eta=1\sim\beta}{\hat{\boldsymbol{X}}(t|t) + \sqrt{(\beta+\lambda)\boldsymbol{\phi}(t|t)}}, \overset{\eta=\beta+1\sim 2\beta}{\hat{\boldsymbol{X}}(t|t) - \sqrt{(\beta+\lambda)\boldsymbol{\phi}(t|t)}}] \\ w^{(0)} = \dfrac{\lambda}{\beta+\lambda}, \eta = 0 \\ w^{(\eta)} = \dfrac{\lambda}{2(\beta+\lambda)}, \eta = 1 \sim 2\beta \end{cases} \tag{2-68}$$

where β indicates the dimension of the state value, η indicates the corresponding number of sigma point set, and λ is the proportional parameter which is used to scale of the weight. $\boldsymbol{\phi}(t|t)$ is the state covariance matrix at the current timestamp *t*.

2) Further prediction of $2\beta+1$ sigma point sets, $\eta = 0,1,2,\cdots,\beta+1$:

$$\boldsymbol{X}^{(\eta)}(t+1|t) = \boldsymbol{\psi}\boldsymbol{X}^{(\eta)}(t|t) + \boldsymbol{B}S(t+1) + v \tag{2-69}$$

3) Calculating the predicted value and covariance matrix using the weighted sigma point set:

$$\hat{\boldsymbol{X}}(t+1|t) = \sum_{\eta=0}^{2\beta} w^{(\eta)}\boldsymbol{X}^{(\eta)}(t+1|t) \tag{2-70}$$

$$\boldsymbol{\phi}(t+1|t) = \sum_{\eta=0}^{2\beta} w(\eta)[\hat{\boldsymbol{X}}(t+1|t) - \boldsymbol{X}^{(\eta)}(t+1|t)][\hat{\boldsymbol{X}}(t+1|t) - \boldsymbol{X}^{(\eta)}(t+1|t)]^T + \boldsymbol{Q} \tag{2-71}$$

4) Acquiring the sigma point set again using UT transform based on the result of state prediction:

$$\boldsymbol{X}^{(\eta)}(t+1|t) = [\hat{\boldsymbol{X}}(t+1|t), \hat{\boldsymbol{X}}(t+1|t) + \sqrt{(\beta+\lambda)\boldsymbol{\phi}(t+1|t)}, \hat{\boldsymbol{X}}(t+1|t) - \sqrt{(\beta+\lambda)\boldsymbol{\phi}(t+1|t)}] \tag{2-72}$$

5) Calculating the predicted observation using the state prediction result of each sigma point, $\eta = 0,1,2,\cdots,2\beta+1$.

$$\boldsymbol{Z}^{(\eta)}(t+1|t) = h(\boldsymbol{X}^{(\eta)}(t+1|t)) = \begin{bmatrix} \sqrt{(x^{(\eta)}(t+1|t) - x_0)^2 + (y^{(\eta)}(t+1|t) - y_0)^2} \\ \sqrt{(x^{(\eta)}(t+1|t) - x_2)^2 + (y^{(\eta)}(t+1|t) - y_2)^2} \\ \vdots \\ \sqrt{(x^{(\eta)}(t+1|t) - x_j)^2 + (y^{(\eta)}(t+1|t) - y_j)^2} \end{bmatrix} \tag{2-73}$$

where $x^{(\eta)}(t+1|t)$ and $y^{(\eta)}(t+1|t)$ are calculated in $\boldsymbol{X}^{(\eta)}(t+1|t)$.

6) Weighting sigma point sets, getting predicted observation value, and corresponding covariance matrix.

$$\hat{\boldsymbol{Z}}(t+1|t)=\sum_{\eta=0}^{2\beta} w^{(\eta)}\boldsymbol{Z}^{(\eta)}(t+1|t) \tag{2-74}$$

$$\boldsymbol{\phi}_{z_t z_t}=\sum_{\eta=0}^{2\beta} w(\eta)[\boldsymbol{Z}^{(\eta)}(t+1|t)-\hat{\boldsymbol{Z}}(t+1|t)][\boldsymbol{Z}^{(\eta)}(t+1|t)-\hat{\boldsymbol{Z}}(t+1|t)]^T+\boldsymbol{R}$$

(2-75) $$\boldsymbol{\phi}_{x_t z_t}=\sum_{\eta=0}^{2\beta} w(\eta)[\boldsymbol{X}^{(\eta)}(t+1|t)-\hat{\boldsymbol{Z}}(t+1|t)][\boldsymbol{X}^{(\eta)}(t+1|t)-\hat{\boldsymbol{Z}}(t+1|t)]^T+\boldsymbol{R}$$

(2-76)

where $\boldsymbol{\phi}_{z_t z_t}$ indicates the covariance matrix provided by $\hat{\boldsymbol{Z}}(t+1|t)$ and $\boldsymbol{Z}^{(\eta)}(t+1|t)$, and $\boldsymbol{\phi}_{x_t z_t}$ indicates the covariance matrix provided by $\hat{\boldsymbol{Z}}(t+1|t)$ and $\boldsymbol{X}^{(\eta)}(t+1|t)$.

7) Updating the Kalman gain.

$$\boldsymbol{K}(t+1)=\boldsymbol{\phi}_{x_t z_t}\boldsymbol{\phi}_{z_t z_t}^{-1} \tag{2-77}$$

8) System status and covariance updating.

$$\hat{\boldsymbol{X}}(t+1|t+1)=\hat{\boldsymbol{X}}(t+1|t)+\boldsymbol{K}(t+1)[\boldsymbol{Z}(t+1)-\hat{\boldsymbol{Z}}(t+1|t)] \tag{2-78}$$

$$\boldsymbol{\phi}(t+1|t+1)=\boldsymbol{\phi}(t+1|t)-\boldsymbol{K}(t+1)\boldsymbol{\phi}_{z_t z_t}\boldsymbol{K}^T(t+1) \tag{2-79}$$

Compared with EKF, UKF has higher accuracy. Its accuracy is equivalent to second-order Taylor expansion, but the speed will be slightly slower. Another great advantage of UKF is that it does not require to estimate the Jacobian matrix, and sometimes the Jacobian matrix is not available. In addition, UKF and PF also have similarities, except that the particles selected in the unscented transformation are clear, while the particles in the particle filter are random. The advantage of random is that it can be used for arbitrary distribution, but it also has its limitations. Therefore, for the distribution that is approximately Gaussian, it is more effective to use UKF.

Kalman filtering is based on the linear Gaussian model. For nonlinear systems, if we want to maintain the basic form of Kalman filtering, we must linearize the model. UKF realizes the update of mean and covariance matrix through Gauss-Hermite sampling points. Since the Gauss-Hermite sampling points are generally very small compared with the sampling points in the particle filter, is there a need for particle filtering? In fact, Gauss-Hermite integration requires that the distribution to be sampled must be Gaussian. This implicitly limits its usage conditions: the posterior distribution must be well approximated by the Gaussian distribution. When the parameters cannot be identified, the posterior distribution is usually multimodal, and it is generally not advisable to approximate the Gaussian distribution. At this time, particle filtering comes in handy. In other words, we can also say that UKF can only handle mild nonlinear problems. Of course, it is already much stronger than EKF, because its estimation accuracy does not depend on the rate of change of the state.

Finally, we make a summary. Both EKF and UKF adopt the idea of linearization, but the former is a priori linearization, and the latter is a posterior linearization. The accuracy of prior linearization is limited by the rate of system state evolution, and the performance is not good when the state changes rapidly. UKF uses posterior linearization, and the accuracy has nothing to do with the rate of state change. No matter what kind of linearization is, it can't handle the problem of high non-linearity, because it can't describe the multimodal distribution well.

2.5.2 Particle Filter

The basic particle filter (PF) is developed using the Monte Carlo theory, which implements recursive Bayesian filtering through non-parametric Monte Carlo simulation methods. It is suitable for any nonlinear system that can be described by a state-space model, and its accuracy can approach the optimal estimation. The PF is simple and easy to implement, and it provides an effective solution for analyzing nonlinear dynamic systems, which has attracted widespread attention in the fields of target tracking, signal processing, and automatic control.

Different from the basic PF applied in various literatures, this section describes the unscented particle filter (UPF), which uses the UKF to calculate the distribution reference in procedure of particle state updating and get a more reliable particle distribution. Thus, the UPF can get the mean and covariance of N particles in real time by UKF and control the distribution range of particles to improve estimation accuracy of object’s motion information. The whole procedure of proposed UPF is shown as follows:

1) Initialization, k=0, For i=1:N, extract the initial state from the prior distribution:

$$\begin{aligned} & X_0^{(i)} = E[X_0^{(i)}] \\ & P_0^{(i)} = E[(X_0^{(i)} - \overline{X}_0^{(i)})(X_0^{(i)} - \overline{X}_0^{(i)})^{\mathrm{T}}] \\ & \overline{X}_0^{(i)a} = E[\overline{X}_0^{(i)a}] = [(\overline{X}_0^{(i)})^{\mathrm{T}}\ 0 \quad 0]^{\mathrm{T}} \\ & P_0^{(i)a} = E[(X_0^{(i)a} - \overline{X}_0^{(i)a})(X_0^{(i)a} - \overline{X}_0^{(i)a})^{\mathrm{T}}] \end{aligned} \tag{2-80}$$

2) Importance sampling. For i=1:N, calculate the mean and variance of state

quantities using the UKF algorithm:

① Calculate Sigma point set:

$$X_{k-1}^{(i)a} = [\overline{X}_{k-1}^{(i)a} \quad \overline{X}_{k-1}^{(i)a} \pm \sqrt{(n_a+\lambda)P_{k-1}^{(i)a}}\,] \tag{2-81}$$

② Further prediction of Sigma point sets:

$$\begin{aligned}
&\overline{X}_{k|k-1}^{(i)a} = f(X_{k-1}^{(i)x}, X_{k-1}^{(i)v}) \\
&\overline{X}_{k-1}^{(i)} = \sum_{j=0}^{2n_a} W_j^{(m)} X_{j,k|k-1}^{(i)x} \\
&P_{k|k-1}^{(i)} = \sum_{j=0}^{2n_a} W_j^{(c)} [X_{j,k|k-1}^{(i)x} - \overline{X}_{k|k-1}^{(i)}][X_{j,k|k-1}^{(i)x} - \overline{X}_{k|k-1}^{(i)}]^{\mathrm{T}} \\
&Z_{k|k-1}^{(i)} = h(X_{k|k-1}^{(i)x}, X_{k-1}^{(i)n}) \\
&\overline{Z}_{k|k-1}^{(i)} = \sum_{j=0}^{2n_a} W_j^{(c)} Z_{j,k|k-1}^{(i)}
\end{aligned} \tag{2-82}$$

③ Integrate with the latest observations and update:

$$\begin{aligned}
&P_{\tilde{z}_k,\tilde{z}_k} = \sum_{j=0}^{2n_a} W_j^{(c)} [Z_{j,k|k-1}^{(i)} - Z_{k|k-1}^{(i)}][Z_{j,k|k-1}^{(i)} - Z_{k|k-1}^{(i)}]^{\mathrm{T}} \\
&P_{X_k,Z_k} = \sum_{j=0}^{2n_a} W_j^{(c)} [X_{j,k|k-1}^{(i)} - \overline{X}_{k|k-1}^{(i)}][X_{j,k|k-1}^{(i)} - \overline{X}_{k|k-1}^{(i)}]^{\mathrm{T}} \\
&K_k = P_{\tilde{z}_k,\tilde{z}_k} P_{X_k,Z_k} \\
&\overline{X}_k^{(i)} = \overline{X}_{k|k-1}^{(i)} + K_k (Z_k - \overline{Z}_{k|k-1}^{(i)}) \\
&\hat{P}_k^{(i)} = P_{k|k-1}^{(i)} - K_k P_{\tilde{z}_k,\tilde{z}_k} K_k^{\mathrm{T}}
\end{aligned} \tag{2-83}$$

④ Calculate samples and update particles:

$$\begin{aligned}
&\hat{X}_k^{(i)} \sim q(X_k^{(i)} \mid X_{0:k-1}^{(i)}, Z_{1:k}) = N(\overline{X}_k^{(i)}, \hat{P}_k^{(i)}) \\
&\hat{X}_{0:k}^{(i)} \sim (X_{0:k-1}^{(i)}, \hat{X}_k^{(i)}) \\
&\hat{P}_{0:k}^{(i)} \sim (P_{0:k-1}^{(i)}, \hat{P}_k^{(i)})
\end{aligned} \tag{2-84}$$

For i=1:N, recalculate weights for each particle:

$$w_k^{(i)} = \frac{p(Z_k \mid \hat{X}_k^{(i)})\, p(\hat{X}_k^{(i)} \mid X_k^{(i)})}{q(\hat{X}_k^{(i)} \mid X_{0:k}^{(i)}, Z_{1:k})} \tag{2-85}$$

For i=1:N, normalize weight:

$$\tilde{w}_k(X_{0:k}^{(i)}) = \frac{w_k(X_{0:k}^{(i)})}{\sum_{i=1}^{N} w_k(X_{0:k}^{(i)})} \tag{2-86}$$

3) Re-sampling: Using the re-sampling algorithm to copy and eliminate the particle set $X_{0:k}^{(i)}$ according to the normalized weight:

$$w_k^i = \tilde{w}_k^i = \frac{1}{N} \tag{2-87}$$

4) Output final filtering result:

$$X_k^{(i)} = \frac{1}{N}\sum_{i=1}^{N} w_{0:k}^i X_{0:k} \tag{2-88}$$

Although the particle filtering (PF) is not constrained by the linearity and Gaussian assumptions of the model, it still has the following shortcomings: 1) Using a large number of random samples to search the state space easily leads to excessive calculation of the algorithm; 2) As time increases, it will appear the phenomenon of particle degradation, the weight degradation would lead to the useless particles and increasing calculation complexity of overall algorithm, reduces the efficiency of the algorithm, which may cause the filter divergence.

2.5.3 Nonlinear Least Squares

The method of least squares (LSQ) is the standard approach to obtain unique values for parameters from related redundant measurements through a known observation model.

In this case, the observation equation is constructed as:

$$\boldsymbol{z} = h(\boldsymbol{x}) + \boldsymbol{v} \tag{2-89}$$

where $h(\boldsymbol{x})$ represents the relationship between the state vector $\boldsymbol{x}$ and the observation vector $\boldsymbol{z}$, $\boldsymbol{v}$ indicates the measured noise.

The loss function in LSQ algorithm is described as:

$$\xi(\boldsymbol{x}) = (\boldsymbol{z} - h(\boldsymbol{x}))^{\mathrm{T}} \boldsymbol{\rho}^{-1} (\boldsymbol{z} - h(\boldsymbol{x})) \tag{2-90}$$

where $\boldsymbol{\rho}$ represents the covariance matrix of the measured value. We need minimize the loss function $\xi(\boldsymbol{x})$ and acquire the optimal estimation result of state vector.

In this work, the non-linear observation model needs to be linearized, and the Taylor series can be applied to linearize the nonlinear measurement vector by expanding the terms around the current estimated state $\boldsymbol{x}$ and only the first order is remained:

$$
\begin{aligned}
\boldsymbol{z} &= h(\boldsymbol{x}) + \boldsymbol{v} \\
&= h(\boldsymbol{x}) + \left.\frac{dh(\boldsymbol{x})}{d\boldsymbol{x}}\right|_{\boldsymbol{x}=\boldsymbol{x}} (\boldsymbol{x} - \boldsymbol{x}) + \frac{1}{2!}\left.\frac{d^2 h(\boldsymbol{x})}{d\boldsymbol{x}^2}\right|_{\boldsymbol{x}=\boldsymbol{x}} (\boldsymbol{x} - \boldsymbol{x})^2 + \cdots + \boldsymbol{v} \\
&\approx h(\boldsymbol{x}) + \left.\frac{dh(\boldsymbol{x})}{d\boldsymbol{x}}\right|_{\boldsymbol{x}=\boldsymbol{x}} (\boldsymbol{x} - \boldsymbol{x}) + \boldsymbol{v} \\
\boldsymbol{z} &= h(\boldsymbol{x}) + \boldsymbol{H}\delta\boldsymbol{x} + \boldsymbol{v}
\end{aligned}
\tag{2-91}
$$

where $\delta\boldsymbol{x} = \boldsymbol{x} - \boldsymbol{x}$ represents the state estimation error, $\boldsymbol{H}$ is the design matrix. The measurement misclosure vector during each iteration is described as:

$$\delta\boldsymbol{z} = \boldsymbol{z} - h(\boldsymbol{x}) = \boldsymbol{H}\delta\boldsymbol{x} + \boldsymbol{v} \tag{2-92}$$

Similar to the linear case derivation process, the result of the nonlinear least squares estimation is calculated by:

$$\delta\boldsymbol{x} = (\boldsymbol{H}^{\mathrm{T}}\boldsymbol{\rho}^{-1}\boldsymbol{H})^{-1}\boldsymbol{H}^{\mathrm{T}}\boldsymbol{\rho}^{-1}\delta\boldsymbol{z} \tag{2-93}$$

The above procedure needs to be repeated and the optimal result can be acquired when the state estimation error reaches the least value. In general, the NLS update is presented as an iterative process until the optimal result is acquired:

$$\boldsymbol{x}_j = \boldsymbol{x}_{j-1} + \delta\boldsymbol{x}_{j-1} \tag{2-94}$$

where j indicates the needed rounds of iteration. The optimized state vector can be acquired when $\xi(\boldsymbol{x})$ less than the set threshold.

Chapter 3: Self-Calibrated 3D Indoor Localization and Error Optimization Based on MEMS Sensors and Sparse Anchors

In smart city based large-scaled indoor spaces, the accuracy of smartphone based 3D indoor localization is always subjected to the poor performance of IoT terminal integrated sensors and limited coverage of absolute location sources. This chapter mainly focus on providing a simple but effective 3D indoor localization and error optimization system that uses the combination of smartphone integrated MEMS sensors and sparse deployed landmark points. The INS mechanization, multi-level constraints and observed values are integrated by the AUKF and the positioning parameters extracted from the state model are calibrated autonomously in order to eliminate effects of cumulative error, indoor magnetic interference, and diversity of handheld modes. In addition, the Wi-Fi FTM station, BLE node, and QR code based landmarks are adopted in this chapter to provide accurate absolute location references for the MEMS sensors based method using robust DTW based landmark detection algorithm. To further improve the accuracy of MEMS sensors and sparse landmark points based forward localization, this chapter proposes and evaluates two different trajectory optimization algorithms and compares the improved localization performance. In which the backward-AUKF smoothing algorithm can provide more accurate trajectory optimization performance but is time-consuming, and the GD based approach can realize slightly lower optimization precision compared with the backward-AUKF but can effectively reduce the calculation complexity. The comprehensive experiments designed in this chapter indicate that the proposed MEMS sensors based self-calibrated 3D indoor localization and optimization system is proved to achieve accurate and stable 3D indoor positioning and trajectory optimization performance under complex indoor environments using sparse wireless stations.

The contributions of this chapter are summarized as follows:

1) This chapter proposes multi-level observed values including gravity vector, QSMF, altitude increment and step-length, and multi-level constraints including ZUPT/ZARU, pseudo velocity, pseudo position, and NHC, which are applied as the hybrid observations in order to eliminate the effects of divergence and accumulative errors, magnetic interference and different handheld modes added on the MEMS sensors based positioning approach.

2) This chapter presents three different landmark detection approaches using Wi-Fi FTM, BLE, and QR code based location sources. The first approach uses the ranging fusion model and the DTW matching to realize the hybrid RSSI and RTT based Wi-Fi landmark recognition. The second approach uses a novel BLE RSSI propagation model, DTW matching, and real-time constructed RSSI map to realize the robust BLE node recognition. The last approach uses QR code to provide absolute location information through camera scanning, which is much more low-cost and easily deployed. After the landmark detection procedure, the real-time recognized landmarks and corresponding fusion models are adopted to provide accurate and absolute reference to built-in sensors based localization approach.

3) This chapter adopts the AUKF to integrate all the navigation data together and adjust the corresponding weight of each observed value dynamically. In the AUKF based fusion structure, the INS mechanization based error vector is adopted as the state model, multi-level constraints and observed values, Wi-Fi FTM anchor and BLE node based ranging and landmark recognition, QR code based landmark are applied as observation models, respectively. Finally, the modified and calibrated INS mechanization is applied to provide accurate and high-speed 3D attitude and localization information. The combination of different positioning approaches significantly improve the final accuracy and robustness of MEMS sensors and sparse landmark points integrated 3D indoor localization.

4) To further enhance the performance of forward 3D positioning trajectory and meet the needs of crowdsourcing-based navigation data collection and processing, this chapter also presents the backward-AUKF optimization algorithm using RTS smoothing to decrease the cumulative error of forward-AUKF. To further reduce the computational complexity of backward-AUKF, this chapter also proposes the GD based global optimization algorithm, which can significantly decrease the complexity of matrix operations compared with backward-AUKF approach and also avoid large loss of accuracy.

The remainder of this chapter is organized as follows. Section 3.1 introduces the background information of proposed system and state the existing problems of MEMS sensors based localization and optimization structure. Section 3.2 presents the multi-level constraints and observed values applied for INS mechanization based error elimination and calibration. Section 3.3 proposes a novel PINS system aiming at provided autonomous and accurate 3D indoor localization and optimization performance in large-scaled indoor spaces, which contains a robust MEMS sensors and sparse landmarks integration approach. Section 3.4 designs comprehensive experiments and gives the test results and the performance analysis. Section 3.5 gives the summary of this chapter.

3.1 Introduction

It can be found from the review of state-of-art literatures in Section 2.1 that the INS and PDR mechanizations are regarded as the two main pedestrian aimed positioning approach using smartphone integrated MEMS sensors, and the global optimization framework can be applied to increase the precision of forward dead reckoning (DR) approach.

There are some facing challenges of existing DR approaches toward real-world applications in smart city based large-scaled indoor spaces. The accuracy of PDR based solution is affected by the walking speed calculation, heading estimation, and handheld modes of smartphones. In addition, the INS mechanization normally cannot be used directly due to the fast divergence error of speed and attitude estimation. Besides, the DR approaches can only provide relative location output due to the lack of absolute initial 3D location and attitude information and the error of location and attitude update is cumulated with time. Thus, the sparse deployed landmark points and optimization algorithms are required for error elimination.

In Section 1.2.1, the current smartphone built-in sensors based localization and optimization systems proposed by the state-of-art literatures proves that the INS/PDR integrated framework can achieve better performance compared with single INS or PDR mechanization due to the richer motion information. The existing INS/PDR models are all focused on the 2D indoor localization and not suitable for the complex 3D scene. In addition, the indoor magnetic interference and changeable handheld modes of smartphones are also the facing challenges for realizing a more precise 3D indoor localization performance. The existing global optimization algorithms can effectively improve the performance of forward indoor localization while the accuracy of global optimization algorithm depends on the robustness of integration model and usually requires high calculation complexity. Thus, a much more comprehensive and precise 3D integration structure is required in this stage in order to realize comparable forward localization and optimization.

Except for the challenge of poor performance of smartphone integrated MEMS sensors, another facing challenge is the limited coverage of absolute location sources. How to maintain the indoor localization accuracy in case of sparse signal covered environments is an essential problem which will be addressed in this chapter. Also in this chapter, we will research and compare different deployment and detection approaches of corresponding indoor landmark points, including Wi-Fi FTM station, BLE node, and QR code with sparse layout, to satisfy the accuracy-level of real-world localization applications.

By considering the facing problems described above, this chapter focuses on developing a light-weight MEMS sensors based 3D indoor positioning framework and further realize integrated localization and optimization with sparse deployed landmark points. In the proposed localization and optimization structure, the INS mechanization based error vector is adopt as the state model, multi-level constraints and observed values, landmark detection results are presented as the observation model to eliminate the effects of cumulative error, the magnetic interference, and changeable handheld modes. In addition, the forward integrated navigation data is further processed by the smoothing and optimization algorithms respectively to increase and compare the robustness and complexity of the final trajectory and provide an alternative solution aiming at different hardware platforms.

3.2 Multi-level Constraints and Observables for Self-calibration

3.2.1 MEMS Sensors Based Multi-level Observables

In the measured model of the proposed MEMS sensors based 3D navigation framework, the QSMF period, gravity value, walking speed and 3D position increment are adopted as the observed values, and can adaptively adjust the corresponding weight to improve the robustness. The combination of INS mechanization and multi-level observed values is served as the basic model in proposed MEMS sensors based 3D navigation framework, which is aiming at providing autonomous 3D indoor positioning performance with long-term accuracy. Compared with the existing INS/PDR integration approach, the proposed basic model improves the QSMF and gravity observation with adaptive weight values, and enhances the positioning ability from 2D to 3D by adding observations of measured barometer related altitude increment and detected Wi-Fi landmarks provided altitude information.

The magnetometer measurement among QSMF period is adopted to calibrate the gyroscope based heading drift and non-QSMF data is not used in this case. In this part, a novel QSMF detection algorithm is proposed to improve the recognition performance. The local magnetic field is regarded as the quasi-static state if the norm of magnetometer data remains constant during the pedestrian's walking period. The detected QSMF periods can be used to provide a relatively accurate local magnetic field reference for gyroscope based heading estimation and can also decrease the effect of artificial interference indoors. The feature of magnetic data can be extracted as [51]:

$$\sum_{k=0}^{n}\left(\left\|\tilde{\boldsymbol{M}}^{b}\right\|_{k+1}-\left\|\tilde{\boldsymbol{M}}^{b}\right\|_{k}\right)\approx 0,\quad \tilde{\boldsymbol{M}}^{b}=\sqrt{{m_x}^{2}+{m_y}^{2}+{m_z}^{2}} \tag{3-1}$$

where $\tilde{\boldsymbol{M}}^{b}$ represents the modulus of collected magnetic data in the body coordinate system; m_x, m_y and m_z indicate the measured tri-magnetometer data; k represents the first epoch of a detected QSMF period and n indicates the length of detected QSMF period. Since the magnetic field strength remains constant when the pedestrian remains static, thus, the QSMF detection algorithm is always performed during pedestrian's walking period.

In this paper, multi-level constraints are used to recognize the QSMF period, the whole detection procedure is shown below:

1) **Pedestrian's Motion Pattern Recognition.** The modulus value of gyroscope data and increment value of accelerometer data are extracted to identify the pedestrian's motion pattern, QSMF is only detected when the pedestrian walks straight or remains static. The modulus value of gyroscope data and increment value of accelerometer are shown in (3-2):

$$\begin{cases} N_{\text{gyro}}=\sqrt{{g_x}^{2}+{g_y}^{2}+{g_z}^{2}} \\ \Delta A_{\text{acc}}=\sqrt{{a_x}^{2}+{a_y}^{2}+{a_z}^{2}}-g \end{cases} \tag{3-2}$$

where g_x, g_y and g_z represent the measured tri-gyroscope data; a_x, a_y and a_z represent the measured tri-accelerometer data; N_{gyro} and ΔA_{acc} remain in a certain range when the pedestrian is walking straight forward or remains static over a short period of time.

2) **Extraction of Pedestrian's Gait Feature.** A complete gait cycle during the pedestrian's walking period includes increment value of accelerometer data ΔA_{acc} changing from zero to peak value, then to valley value and finally return to zero, just like this: $\Delta A_{\text{acc}}:0\to A_{\text{peak}}\to 0\to A_{\text{valley}}\to 0$. The mean-square error (MSE) and

interquartile range (IQR) of magnetic heading in the sliding time window with a length of n are calculated as follows:

$$\begin{cases} \theta_{\mathrm{MSE}}(k) = \dfrac{1}{n} \cdot \sum\limits_{i=0}^{n} (\theta_{mag}^{i}(k) - \theta_{mag}(k))^2 \\ \theta_{\mathrm{IQR}}(k) = \theta_{\mathrm{Q_3}}(k) - \theta_{\mathrm{Q_1}}(k) \end{cases} \tag{3-3}$$

where $\theta_{\mathrm{MSE}}(k)$ and $\theta_{\mathrm{IQR}}(k)$ indicate the MSE and IQR values of the acquired magnetic heading, $\theta_{mag}(k)$ represents the average magnetic heading in the sliding time window. $\theta_{mag}^{i}(k)$ represents the real-time measured magnetic heading.

3) QSMF Detection During Periods of Gait Cycles. After recognizing pedestrian's motion pattern and acquiring the heading information in each gait cycle, multi-level constraints are presented to detect the QSMF state under the above conditions:

$$\begin{cases} 0 < \Delta A_{\mathrm{acc}} < \Delta h_1 \\ 0 < N_{\mathrm{gyro}} < \Delta h_2 \\ \theta_{\mathrm{MSE}} < \Delta h_3, \theta_{\mathrm{IQR}} < \Delta h_4 \\ \dfrac{1}{n} \cdot \sum\limits_{k=0}^{n} \left(\left\| \tilde{\boldsymbol{M}}^{b} \right\|_{k+1} - \left\| \tilde{\boldsymbol{M}}^{b} \right\|_{k} \right) < \Delta h_5 \end{cases} \tag{3-4}$$

where $\Delta h_1 \sim \Delta h_5$ represent the thresholds which are uses to identify the QSMF state in local magnetic field. The extracted magnetic data is fused by the AUKF, which will be described in the following section.

After the QSMF period detected, the local magnetic field is calibrated and regarded as the reference vector at the first epoch of detected QSMF period:

$$\boldsymbol{m}_{\mathrm{refer}}^{n} = \boldsymbol{C}_{b,1}^{n} \cdot \boldsymbol{m}_{k,1}^{b} \tag{3-5}$$

where $\boldsymbol{m}_{k,1}^{b}$ represents the first magnetic vector of detected QSMF period in the body coordinate, $\boldsymbol{C}_{b,1}^{n}$ is the current attitude matrix. $\boldsymbol{m}_{\mathrm{refer}}^{n}$ is calculated and regarded as the reference magnetic field. The final observation model for magnetic field is shown below:

$$\begin{aligned} \delta \boldsymbol{z}_{m}^{n} &= \boldsymbol{C}_{b,k}^{n} \cdot \boldsymbol{m}_{k}^{b} - \boldsymbol{m}_{\mathrm{refer}}^{n} \\ &= (\mathbf{I} - \boldsymbol{\psi}\times)\boldsymbol{C}_{b,k}^{n}(\boldsymbol{m}_{k}^{b} + \boldsymbol{n}_{m}) - \boldsymbol{m}_{\mathrm{refer}}^{n} \\ &= \left[\left(\boldsymbol{C}_{b,k}^{n} \boldsymbol{m}_{k}^{b} \right) \times \right] \boldsymbol{\psi} + \boldsymbol{C}_{b,k}^{n} \boldsymbol{n}_{m} \end{aligned} \tag{3-6}$$

where $\boldsymbol{m}_k^b$ represents the output magnetic data during QSMF period, $\boldsymbol{C}_{b,k}^n$ represents the current attitude matrix, and the noise of acceleration $\boldsymbol{n}_m$ can be adjusted based on the estimation of magnetic deviation $\boldsymbol{n}_m = norm(\boldsymbol{m}_k^b - \boldsymbol{m}_{\text{refer}}^n)$.

In this work, accelerometer data is regarded as the observed value in AUKF to compensate the roll and pitch angle drift. The acceleration based measurement equation is described as follows [51]:

$$\begin{aligned} \delta \boldsymbol{f}^n &= \boldsymbol{f}^n - \boldsymbol{C}_b^n \boldsymbol{f}^b \\ &\approx \boldsymbol{f}^n - (\mathbf{I} - [\boldsymbol{\psi}\times])\boldsymbol{C}_b^n \boldsymbol{f}^b + \boldsymbol{C}_b^n \boldsymbol{n}_a \\ &= [\boldsymbol{\psi}\times]\boldsymbol{f}^n + \boldsymbol{C}_b^n \boldsymbol{n}_a \\ &= [\boldsymbol{f}^n\times]\boldsymbol{\psi} + \boldsymbol{C}_b^n \boldsymbol{n}_a \end{aligned} \tag{3-7}$$

where $\boldsymbol{f}^n$ indicates the local gravity vector, $\boldsymbol{f}^b$ indicates the measured acceleration, and the noise of acceleration $\boldsymbol{n}_a$ can be modified based on the estimation of extra acceleration:

$$\boldsymbol{n}_a = \begin{cases} \sigma_a, A \le Th_{01} \\ (A^2 / P)\sigma_a, Th_{01} < A \le Th_{02} \\ \infty, A > Th_{02} \end{cases} \tag{3-8}$$

where $A = \left| norm(\boldsymbol{f}^b) - g \right|$ indicates the extra acceleration, σ_a represents the acceleration bias stability, P indicates the error covariance in AUKF.

In case of human walking characteristics detected, the pedestrian' step-length information can be estimated by the following linear model, which describes the relationship between step length and pedestrian's height and step frequency [113]:

$$L_s = [0.7 + \lambda_1(\kappa - 1.75) + \lambda_2 \frac{(\xi - 1.79)\kappa}{1.75}]\lambda_3 \tag{3-9}$$

where L_s and ξ indicates the step length and step frequency; κ indicates the pedestrian's height; λ_1, λ_2, and λ_3 are the model parameters. The walking speed is calculated according to the estimated step-length and frequency:

$$V_{\text{walking}} = L_s \cdot \xi \tag{3-10}$$

where V_{walking} indicates the instantaneous walking speed calculated by the detected step. The estimated walking speed is used as the observed value for INS based localization.

The 2D position increment is calculated using the position coordinates provided by the last epoch:

$$\begin{bmatrix} r_x(t) \\ r_y(t) \end{bmatrix} = \begin{bmatrix} r_x(t\text{-}1) \\ r_y(t\text{-}1) \end{bmatrix} + L_s(t) \begin{bmatrix} \cos(\theta(t)) \\ \sin(\theta(t)) \end{bmatrix} \tag{3-11}$$

where $(r_x(t),\ r_y(t))$ represents the real-time updated 2D position, $L_s(t)$ indicates the calculated step-length, and $\theta(t)$ indicates the real-time estimated AUKF heading.

In this work, the barometer is applied to provide the altitude increment in indoor environments, the relationship between altitude and air pressure is calculated as [116]:

$$\beta_b = 44330 \cdot (1.0 - (\frac{100\gamma}{\gamma_0})^{\frac{1.0}{5.255}}) \tag{3-12}$$

where β_b represents the estimated altitude, γ and γ_0 indicate the measured local air pressure and the reference pressure at the sea level.

The observation model aiming at step-length based velocity in the navigation coordinate is modelled as:

$$\delta \boldsymbol{z}_v^n = \boldsymbol{v}_{Step}^n - \boldsymbol{v}_{INS}^n \tag{3-13}$$

where $\boldsymbol{v}_{Step}^n$ indicates the walking speed calculated in (3-10); $\boldsymbol{v}_{INS}^n$ is the INS mechanization based speed updating result. The observation equation for location difference under navigation coordinate frame is calculated as:

$$\delta \boldsymbol{z}_p^n = \boldsymbol{p}_{Step}^n - \boldsymbol{p}_{INS}^n \tag{3-14}$$

where $\boldsymbol{p}_{Step}^n$ indicates the 3D location provided by calculated step-length and AUKF heading, $\boldsymbol{p}_{INS}^n$ indicates the INS mechanization updated 3D location information.

In case of 3D indoor localization, because the barometer originated altitude is subjected to the changeable local air pressure thus cannot provide the accurate absolute altitude information, thus, in this paper, the altitude difference value estimated by barometer is used as the measured value to compensate the step-length based 2D update:

$$\delta \boldsymbol{z}_h^n = h_B^n - h_{INS}^n \tag{3-15}$$

where h_B^n represents the updated altitude information by using the difference of barometer based altitude update result in adjacent timestamps presented in (3-12), and the initial altitude is provided by the detected landmarks, h_{INS}^n indicates the z-axis position increment by INS mechanization.

The initial bias of the low-cost barometer is influenced by the cumulative error and environmental factors such as temperature and humidity. In proposed PINS structure, a novel height-related zero-velocity update technology (H-ZUPT) is proposed to eliminate the speed estimation error in the z-axis. Instead of detecting the quasi-static (QS) period by the acceleration or gyroscope angular rate data, the pressure change information and RF signals based observation are adopt to detect the height-related QS period:

$$\frac{1}{N}\sum_{k=1}^{N}\left(\frac{\left\|p_k^b - p_{average}^b\right\|^2}{\zeta_p^2} + \frac{\left\|u_k^b - u_{k-1}^b\right\|^2}{\zeta_u^2}\right) < \xi \tag{3-16}$$

where $p_{average}^b$ indicates the mean value of real-time measured pressure data in slide window of length N, ζ_p^2 is the measured noise. u_k^b indicates the RF reported floor, and ζ_u^2 is RF based measured noise. When the height-related QS period is detected, the state update model of altitude can be modeled as [116]:

$$\begin{bmatrix} \dot{h} \\ \dot{b}_h \end{bmatrix} = \begin{bmatrix} w_h \\ -\frac{1}{\tau_{b_h}} b_h + \upsilon_{b_h} \end{bmatrix} \tag{3-17}$$

where w_h indicates the state noise for the altitude update, τ_{b_h} and υ_{b_h} represent the correlation time and the driving noise of the random walk process.

During the detected height-related QS periods, the measured model for the H-ZUPT based altitude update is described as:

$$\tilde{h}_b - \hat{h}_0 = \delta h + b_h + n_{h_b} \tag{3-18}$$

where $\tilde{h}_b$ indicates the barometer measured altitude, $\hat{h}_0$ is extracted from the first epoch of each detected height-related QS period. In these periods, the ideal observed value is always regarded as zero, and the change of altitude at the detected height-related QS period is caused by the bias of barometer, which can be calibrated by the proposed model.

3.2.2 MEMS Sensors Based Multi-level Constraints

To further improved the precision of the basic model in described MEMS sensors based 3D navigation framework in Section 3.2.2, the enhanced model contains multi-level constraints is proposed to further decrease the motion modes and handheld modes originated positioning error, which contains the ZUPT, ZARU, pseudo-position and pseudo-velocity, and enhanced NHC (E-NHC) based constraints. Except for the traditional approach using ZUPT/ZARU for error estimation, this work applied the pseudo-position and pseudo-velocity to decrease the effects of harsh motion modes and proposes the E-NHC for forward axis finding from the changeable handheld modes.

This paper uses acceleration and gyroscope output to detect the QS periods [51]:

$$\frac{1}{N}\sum_{k=1}^{N}(\frac{\left\| \boldsymbol{f}_k^b - \boldsymbol{g}^n \right\|^2}{\zeta_f^2} + \frac{\left\| \boldsymbol{\omega}_g^k \right\|^2}{\zeta_w^2}) < \Omega \tag{3-19}$$

where N represents the length of sliding window, $\boldsymbol{f}_k^b$ and $\boldsymbol{\omega}_g^k$ indicate the measured acceleration and angular velocity data at epoch k, ζ_f^2 and ζ_w^2 represent the measured noises of accelerometer and gyroscope, and Ω is the set threshold. Once the QS periods are recognized, the velocity is set as zero for ZUPT, which is described as follows:

$$\delta \boldsymbol{z}_v^n = \boldsymbol{v}_{INS}^n - \boldsymbol{v}_{zero}^n = \delta v^n + n_v \tag{3-20}$$

where $\boldsymbol{v}_{INS}^n$ is the INS based speed, $\boldsymbol{v}_{zero}^n = [0 \quad 0 \quad 0]^{\mathrm{T}}$ in case of QS periods detected.

When QS periods are detected, ZARU measurements are also applied to constrain the heading drift [110]. The observed model aiming at ZARU is shown as follows:

$$\delta \boldsymbol{z}_\theta = \theta_{INS}^n - \theta_{refer}^n = \delta\theta + n_\theta \tag{3-21}$$

where θ_{INS}^n represents the INS mechanization based heading, θ_{refer}^n represents the reference heading collected from the first timestamp recorded during detected QS time procedure, and n_θ indicates the measured noise.

The pseudo-position and pseudo-velocity can normally be applied because of the limited scope of low-cost sensors based 3D location and linear velocity within a specified period. The observation model of pseudo-position is [51]:

$$\hat{\boldsymbol{z}}_p^n - \tilde{\boldsymbol{z}}_p^n = \delta \boldsymbol{z}_p^n + n_p \tag{3-22}$$

The observation model of pseudo-velocity is:

$$\hat{\boldsymbol{z}}_v^n - \tilde{\boldsymbol{z}}_v^n = \delta \boldsymbol{z}_v^n + n_v \tag{3-23}$$

where $\tilde{\boldsymbol{z}}_p^n = \textbf{constant}$, $\hat{\boldsymbol{z}}_p^n$ and $\hat{\boldsymbol{z}}_v^n$ are the INS based location and velocity vectors; $\delta \boldsymbol{z}_p^n$ and $\delta \boldsymbol{z}_v^n$ are the location and velocity errors, n_p and n_v are the measured noises.

NHC is usually used to increase the navigation solvency of INS solution in vehicular and robotic navigation fields [118]. In this paper, E-NHC is proposed to recognize the forward direction of the pedestrian under different handheld modes. The handheld modes of the smartphone are divided into two kinds: the basic mode (reading mode) and the other modes. The different handheld modes are firstly recognized and classified by machine learning (ML) approach using sensors based characteristics [40]. The four different handheld modes of smartphone are shown in Figure 3-1.

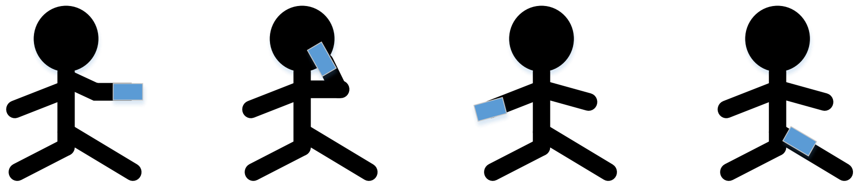

Figure 3-1 Four Different Handheld Modes

The forward under carrier coordinate system is given as:

$$\boldsymbol{v}^b = \begin{bmatrix} v^b_{forward} & 0 & 0 \end{bmatrix}^{\mathrm{T}} \tag{3-24}$$

where $v^b_{forward}$ is calculated by step-length based method.

In order to get the pedestrian's forward speed, the estimated walking speed $\boldsymbol{v}^b$ should be transformed based on the results of handheld mode recognition. The forward speed in navigation coordinate system is calculated as:

$$\boldsymbol{v}^n = \boldsymbol{C}^n_e \boldsymbol{C}^e_{e_1} \boldsymbol{C}^{e_1}_b \boldsymbol{v}^b \tag{3-25}$$

where $\boldsymbol{v}^n$ is converted NHC based speed, $\boldsymbol{C}^{e_1}_b$ represents the calculated attitude matrix from carrier coordinate system to ENU coordinate system; $\boldsymbol{C}^e_{e_1}$ indicates the handheld modes related translation matrix which converts the heading related axis into reading mode based heading related axis based on the results of handheld mode recognition. $\boldsymbol{C}^n_e$ indicates the translation matrix from ENU coordinate system to NED coordinate system.

3.3 Pedestrian Aimed INS Solution for MEMS Sensors and Sparse Anchors Based 3D Indoor Localization and Error Optimization

In this section, a novel MEMS sensors and sparse anchors based 3D indoor navigation and optimization framework, called PINS, is presented. The proposed PINS framework contains an AUKF based forward localization model using the integration of sparse detected landmarks and MEMS sensors. In addition, two different 3D trajectory optimization algorithms are also included aiming at different application platforms: backward-AUKF and GD, which can further enhance the precision of forward 3D indoor positioning.

In order to get a precise and concrete estimation of 3D indoor localization in case of limited signal coverage, different location sources and sensors based characteristics should be effectively combined. In proposed PINS framework, the INS mechanization based error vector is adopt as the state model, multi-level constraints and observed values are presented as the observation model to eliminate the effects of the cumulative error, the magnetic interference, and changeable handheld modes. In addition, three different landmark detection approaches are adopted to further improve the performance of MEMS sensors based 3D indoor localization under complex and sparse wireless stations contained 3D indoor environments. The forward integrated navigation result is finally optimized by the proposed trajectory optimization approaches for a more robust and efficient 3D indoor localization and optimization. The whole procedure of proposed PINS framework is shown in Figure 3-2:

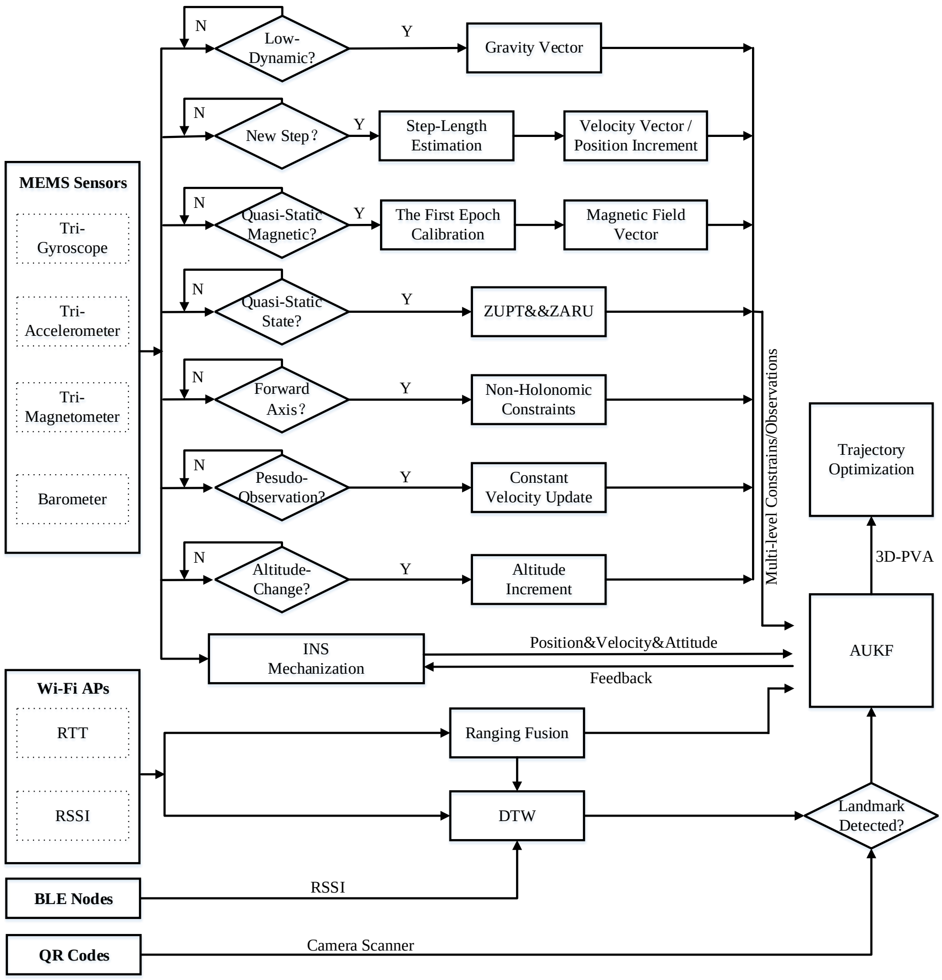

Figure 3-2 Process of PINS Framework

3.3.1 INS Mechanization and Error Model

INS mechanization is proposed towards inertial sensors based localization. The information of acceleration and angular rate acquired from MEMS sensors are integrated by the INS mechanization for estimation of 3D position, velocity, and attitude of the moving object with high update rate, which is shown below [24]:

$$\begin{bmatrix} \dot{\boldsymbol{p}}^n \\ \dot{\boldsymbol{v}}^n \\ \dot{\boldsymbol{C}}_b^n \end{bmatrix} = \begin{bmatrix} \boldsymbol{\varpi}^{-1}\boldsymbol{v}^n \\ \boldsymbol{C}_b^n \boldsymbol{f}^b - (2\boldsymbol{\omega}_{ie}^n + \boldsymbol{\omega}_{en}^n)\boldsymbol{v}^n + \boldsymbol{g}^n \\ \boldsymbol{C}_b^n(\boldsymbol{\omega}_{ib}^b - \boldsymbol{\omega}_{in}^b) \end{bmatrix} \tag{3-26}$$

where $\boldsymbol{p}^n = [p_N \quad p_E \quad p_D]^{\mathrm{T}}$ indicates the pedestrian's real-time 3D location; $\boldsymbol{v}^n = [v_N \quad v_E \quad v_D]^{\mathrm{T}}$ represents the 3D velocity and $\boldsymbol{C}_b^n$ indicates the rotation matrix between body coordinate system and navigation coordinate system; $\boldsymbol{g}^n$ indicates the local gravity value; $\boldsymbol{\omega}_{ie}^n$ represents the rotation angular rate between the ECEF coordinate system and inertial coordinate system; $\boldsymbol{\omega}_{en}^n$ indicates the rotation angular rate between navigation coordinate system and the ECEF coordinate system; $\boldsymbol{\varpi}^{-1}$ indicates a 3×3 matrix related to the latitude p_N and the ellipsoidal height p_D of the moving object.

The Earth related angular rate error vectors $\boldsymbol{\omega}_{ie}^n$ and $\boldsymbol{\omega}_{en}^n$ can be ignored because of the low-precision of MEMS sensors, Thus, the simplified error model of INS can be described as follows [119]:

$$\begin{cases} \delta\dot{\boldsymbol{p}}^n = -\boldsymbol{\omega}_{en}^n \times \delta\boldsymbol{p}^n + \delta\boldsymbol{v}^n \\ \delta\dot{\boldsymbol{v}}^n = -(2\boldsymbol{\omega}_{ie}^n + \boldsymbol{\omega}_{en}^n)\delta\boldsymbol{v}^n + \boldsymbol{f}^n \times \boldsymbol{\psi} + \boldsymbol{C}_b^n(\boldsymbol{\varepsilon}_a + \boldsymbol{w}_{ba}) \\ \dot{\boldsymbol{\psi}} = -(\boldsymbol{\omega}_{ie}^n + \boldsymbol{\omega}_{en}^n) \times \boldsymbol{\psi} - \boldsymbol{C}_b^n(\boldsymbol{\varepsilon}_g + \boldsymbol{w}_{bg}) \\ \dot{\boldsymbol{\varepsilon}}_g = \boldsymbol{\varepsilon}_g / \tau_{bg} + \boldsymbol{w}_{bg} \\ \dot{\boldsymbol{\varepsilon}}_a = -\boldsymbol{\varepsilon}_a / \tau_{ba} + \boldsymbol{w}_{ba} \end{cases} \tag{3-27}$$

where $\delta\boldsymbol{p}^n$, $\delta\boldsymbol{v}^n$ and $\boldsymbol{\psi}$ represent the measured errors of 3D position, velocity and attitude information; $\boldsymbol{\varepsilon}_g$ and $\boldsymbol{\varepsilon}_a$ indicate gyroscope and accelerometer biases, respectively; $\boldsymbol{f}^n$ indicates the converted acceleration data in *n*-frame, τ_{bg} and τ_{ba} represents the sensors noise related parameter; $\boldsymbol{w}_{bg}$ and $\boldsymbol{w}_{ba}$ are the measured noises of $\boldsymbol{\varepsilon}_g$ and $\boldsymbol{\varepsilon}_a$.

In the AUKF, the state vector can be described based on the above INS error model [24]:

$$\delta\boldsymbol{x} = \left[(\delta\boldsymbol{p}^n)_{1\times3} \quad (\delta\boldsymbol{v}^n)_{1\times3} \quad \boldsymbol{\psi}_{1\times3} \quad (\boldsymbol{\varepsilon}_g)_{1\times3} \quad (\boldsymbol{\varepsilon}_a)_{1\times3} \right]^{\mathrm{T}} \tag{3-28}$$

The discrete-time AUKF system model and observation model are described as follows:

$$\begin{cases} \delta\boldsymbol{x}_t = \boldsymbol{F}_{t-1,t}\delta\boldsymbol{x}_{t-1} + \nu_t \\ \delta\boldsymbol{z}_t = \boldsymbol{G}_t\delta\boldsymbol{x}_t + \varsigma_t \end{cases} \tag{3-29}$$

where $\delta\boldsymbol{x}_t$ and $\delta\boldsymbol{z}_t$ represents the state vector and observed vector at the moment *t*; $\boldsymbol{G}_t$ indicates the observation matrix at the moment *t*. ν_t and ς_t indicate the state noise and observation noise at the moment t; $\boldsymbol{F}_{t-1,t}$ represents the 15×15 state transition matrix which is shown below:

$$\boldsymbol{F}_{t-1,t}=\begin{bmatrix} \mathbf{I}_{3\times3} & \mathbf{I}_{3\times3}\times\Delta t & 0_{3\times3} & 0_{3\times3} & 0_{3\times3} \\ 0_{3\times3} & \mathbf{I}_{3\times3} & (\boldsymbol{f}_k^n\times)\cdot\Delta t & 0_{3\times3} & 0_{3\times3} \\ 0_{3\times3} & 0_{3\times3} & \mathbf{I}_{3\times3} & -\boldsymbol{C}_{b,k}^n\cdot\Delta t & 0_{3\times3} \\ 0_{3\times3} & 0_{3\times3} & 0_{3\times3} & \mathbf{I}_{3\times3} & 0_{3\times3} \\ 0_{3\times3} & 0_{3\times3} & 0_{3\times3} & 0_{3\times3} & \mathbf{I}_{3\times3} \end{bmatrix} \tag{3-30}$$

where Δt indicates the sampling date of the inertial data; $\boldsymbol{f}_k^n$ indicates the measured acceleration in the n-frame.

3.3.2 Landmark Selection and Detection Approach

In this section, three different kinds of location sources including Wi-Fi FTM anchors, BLE notes, and QR codes are chosen as the landmark providers, which can provide absolute 3D location information for MEMS sensors based positioning approach. The corresponding landmark detection algorithms towards different location sources are described in this section, and the corresponding uncertainty model and fusion model are also presented in this case.

3.3.2.1 Wi-Fi FTM Station Based Landmark Detection

Wi-Fi FTM can provide accurate ranging performance in case of LOS, but is affected by random and NLOS errors because of its measurement mechanism [30], the observed distance of Wi-Fi FTM is usually described as follows:

$$L_{\text{observed}}=L_{\text{FTM}}+d_N+d_{\text{random}} \tag{3-31}$$

where L_{observed} represents observed value which contains the NLOS error d_N and random error d_{random}, L_{FTM} indicates the ground truth value of Wi-Fi FTM. In addition, the ranging performance of Wi-Fi FTM in short distance is relatively poor because the variance of the ranging error indoors sometimes can reach 1 m or more [22].

The RSSI signal acquired from Wi-Fi AP suffers from multipath propagation in typical indoor environments, besides, RSSI ranging accuracy would decline significantly when distance between smartphone and Wi-Fi AP increases [120]. Thus, the RSSI value acquired from the short distance can be used to judge the proximity. In this paper, Wi-Fi RSSI based ranging model is described in (3-32):

$$P_r(d) = P_0(d_0) - 10\alpha\lg(\frac{d}{d_0}) + \varphi \tag{3-32}$$

where $P_r(d)$ indicates the RSSI at distance d from the source, d_0 is the reference distance, $P_0(d_0)$ is the RSSI at distance d_0, α is the path loss exponent, and φ is the Gaussian random variable with a mean of zero.

In this work, the sparse Wi-Fi FTM supported APs are adopted as the absolute location source which is further fused with built-in sensors based positioning result by AUKF. The final Wi-Fi ranging is the combination of distances calculated by the (3-31) and (3-32) which can improve the short-distance performance of Wi-Fi FTM and also maintain the long-distance accuracy. The real-time RSSI and RTT information collected from sparse Wi-Fi stations are combined to provide more accurate ranging information using the fusion model proposed in [83]:

$$\Delta D_{\text{Fused}} = \delta_1 \cdot L_{\text{observed}} + \delta_2 \cdot P_r(d) \tag{3-33}$$

where $\delta_1 + \delta_2 = 1$, ΔD_{Fused} indicates the fused distance between smartphone and Wi-Fi AP. $\delta_2 = -\gamma / \text{RSSI}$, threshold γ is set to adjust the weight of RSSI based ranging model, which indicates the uncertainty of measured RSSI value, and is set as the standard deviation of real-time measured Wi-Fi RSSI values.

This part uses the Dynamic Time Warping (DTW) algorithm [35] to detect sparse Wi-Fi APs on the pedestrian's walking route, which can decrease effects of different walking speed and multipath propagation. In this work, the ideal distribution of collected distances is generated by the autonomous distance calculation between the pedestrian's ideal locations updated by constant walking speed and Wi-Fi FTM anchor. The real-time collected distribution is provided by the calculated distance information provided by the fusion model in equation (3-33). The DTW result between ideal distribution and real-time collected distribution is shown in equation (3-34):

$$\begin{aligned} &DTW(d_{\text{refer}}, d_k) \\ &= Dist(b_n, c_m) + \min[D(b_{n-1}, c_m), D(b_n, c_{m-1}), D(b_{n-1}, c_{m-1})] \end{aligned} \tag{3-34}$$

where $DTW(d_{\text{refer}}, d_k)$ represents the calculated DTW value among reference distribution and real-time distribution of measured Wi-Fi ranging result, $Dist(b_n, c_m)$ represents the Euclidean distance calculated by each two values of selected distributions. When a pedestrian walks towards a local Wi-Fi AP, the received RSSI value increases with time, and when the pedestrian walks away from the local Wi-Fi AP, the received RSSI value decreases with time. The ideal distribution is generated according to the described walking route and served as the reference distribution in (3-32), and when the real-time collected RSSI distribution follows the same walking route, the calculated DTW would decrease in case of walking towards the Wi-Fi AP and reach the ideally minimal value when the pedestrian is closest to a local Wi-Fi AP. Thus, a new Wi-Fi landmark can be successfully detected when the DTW value reaches the set thresholds Δh .The description of Wi-Fi FTM station based landmark detection is shown in Figure 3-3.

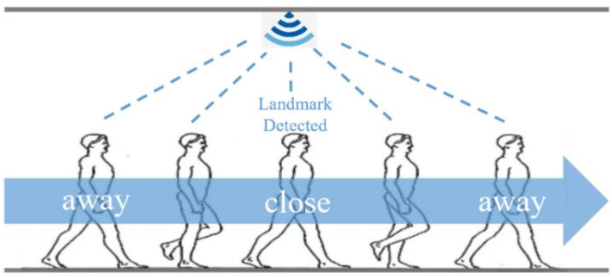

Figure 3-3 Procedure of Proximity Detection

In this paper, the measured Wi-Fi ranging result and the 3D coordinates acquired from recognized Wi-Fi landmarks as the absolute observed values in AUKF:

$$\delta \boldsymbol{z}_d = \begin{bmatrix} \delta \boldsymbol{z}_{1,range} \\ \vdots \\ \delta \boldsymbol{z}_{m,range} \end{bmatrix} = \begin{bmatrix} d_{MEMS,1} - d_{wifi,1} \\ \vdots \\ d_{MEMS,m} - d_{wifi,m} \end{bmatrix} \tag{3-35}$$

where $\delta \boldsymbol{z}_{m,range}$ represents the difference between Wi-Fi ranging results and Euclidean distance between MEMS sensors based location and Wi-Fi APs. In addition, when the pedestrian passes by a local Wi-Fi station, the 3D coordinates provided by the landmarks detection can also be applied as the observed value:

$$\delta \boldsymbol{z}_p^n = \boldsymbol{p}_{wifi}^n - \boldsymbol{p}_{INS}^n = \delta \boldsymbol{p} + n_{wifi} \tag{3-36}$$

where $\boldsymbol{p}_{wifi}^n$ indicates the 3D coordinate provided by the Wi-Fi landmark. Due to the landmark detection delay caused by the set slide window, the location information provided by the detected Wi-Fi landmark contains measurement uncertainty, which is described as follow:

$$n_{wifi} \sim \sum_{\tau=0}^{\partial} \boldsymbol{v}_{AUKF}^n (\tau) d\tau \tag{3-37}$$

where $\boldsymbol{v}_{AUKF}^n(\tau)$ represents the measured walking speed provided by the MEMS sensors based approach, τ is the timestamp, ∂ is the half-length of DTW window.

3.3.2.2 BLE Notes Based Landmark Detection

The stability of RSSI data acquired from local BLE nodes is subjected to the multipath propagation and NLOS effects when the pedestrian walking in the complex indoor environments. The accuracy of RSSI based propagation model may decrease with the growing distance between smartphone and local BLE nodes [102]. In this work, BLE RSSI based propagation model is presented as follows [99]:

$$\xi_r(\mu) = \xi_0(\mu_0) - 10\beta \lg(\frac{\mu}{\mu_0}) + \Omega + \varphi \tag{3-38}$$

where $\xi_r(\mu)$ represents the idealized RSSI value at distance μ, μ_0 is the reference distance, $\xi_0(\mu_0)$ indicates the reference RSSI value at distance μ_0, β represents the path loss exponent, which conforms the Gaussian distribution with the mean of zero. φ is the measured noise which follows Gaussian distribution. Ω represents the human occlusion factor related parameter. When the pedestrian moves towards the BLE node, Ω is set as zero. When the pedestrian moves away from the BLE node, Ω is increased to compensate the RSSI loss due to the occlusion.

Normally, the accuracy of presented RSSI propagation model is subjected to the multipath propagation and NLOS in complex indoor environments. In this work, a novel BLE landmark detection algorithm is proposed to avoid the interference of indoor environments.

When the pedestrian walks along a deployed BLE node, the received RSSI signal will generate signal peaks which can be used for landmark detection, as shown in Figure 3-4. The raw RSSI data contains noises which may cause the signal fluctuation. However, the RSSI signal can also fluctuate even after smoothing because of multipath propagation and NLOS. In this paper, dynamic-time-warping (DTW) algorithm is applied to detect the local BLE landmark, using RSSI data in a period of time. DTW is usually applied to align and measure the similarity between two temporal sequences of data, which is widely applied in fields for example speech recognition and magnetic field based positioning [121].

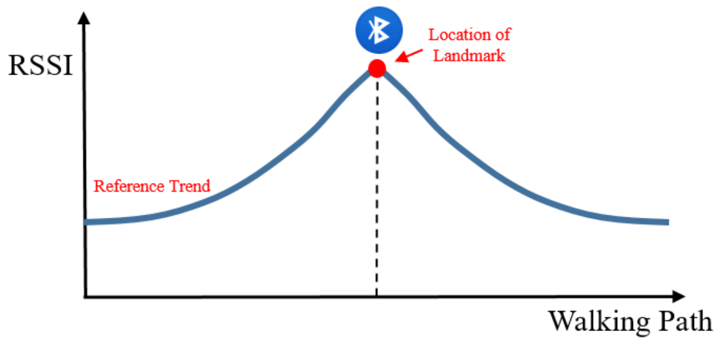

Figure 3-4 The Schematic of RSSI Landmark Detection

The reference BLE RSSI distribution $\delta_{\text{refer}} = \{q_1, q_2, ..., q_n\}$ is shown in Figure 3-4, which can be automatically generated by equation (3-36) within a fixed distance range. The real-time RSSI information acquired from local BLE nodes contained in the database will be collected and described as the RSSI map after smoothed by Gaussian mixture model (GMM) [122], the processed RSSI map is presented in Table 3-1:

Table 3-1 RSSI Map of Local BLE Nodes

Time / Mac_n	T_1	T_2	…	T_m
Mac_1	$RSSI_1^1$	$RSSI_1^2$	…	$RSSI_1^m$
Mac_2	$RSSI_2^1$	$RSSI_2^2$	…	$RSSI_2^m$
…	…	…	…	…
Mac_n	$RSSI_n^1$	$RSSI_n^2$	…	$RSSI_n^m$

After constructing the local RSSI map, the RSSI distribution from each local BLE node will be extracted from the RSSI map, described as $\delta_k = \{c_1, c_2, ..., c_m\}$, and then using DTW algorithm to calculate the similarity between the reference distribution and real-time extracted distribution based on the equation (3-39):

$$\begin{aligned} &DTW(\delta_{\text{refer}}, \delta_k) \\ &= Dist(q_n, c_m) + \min[D(q_{n-1}, c_m), D(q_n, c_{m\text{-}1}), D(q_{n\text{-}1}, c_{m\text{-}1})] < \Delta h \\ &s.t.\ d(t) < \Psi \end{aligned} \tag{3-39}$$

where $DTW(\delta_{\text{refer}}, \delta_k)$ presents the cumulative distance between two RSSI distributions, $Dist(q_n, c_m)$ indicates the Euclidean distance between each two points of distributions. A new BLE landmark is successfully detected when the DTW value and real-time distance between detected BLE node and smartphone $d(t)$ reach the set thresholds Δh and Ψ.

When a new BLE landmark is detected, the 3D location information of detected BLE node is applied as the observed value to further eliminate the cumulative error of INS mechanization, in this case, the equation (3-38) can also be described as:

$$\delta \boldsymbol{z}_p^n = \boldsymbol{p}_{BLE}^n - \boldsymbol{p}_{INS}^n = \delta \boldsymbol{p} + n_{BLE} \tag{3-40}$$

where $\boldsymbol{p}_{BLE}^n$ represents the 3D location of the detected BLE landmark, the measured uncertainty in this case is described as:

$$n_{BLE} \sim \sum_{\tau=0}^{\partial} \boldsymbol{v}_{INS}^n(\tau) d\tau \tag{3-41}$$

where $\boldsymbol{v}_{INS}^n(\tau)$ indicates the measured INS based velocity during the period of time window used in GMM smoother, τ is the timestamp, ∂ is the length of time window.

3.3.2.3 QR Code Based Landmark Detection

In this section, the QR code is introduced to acquire the reference 3D location for the low-cost sensors based method. The QR codes and the corresponding location information can be generated from the on-line website [27], which are deployed in indoor scenes and can be scanned by the smartphone integrated camera, which is shown in Figure 3-5:

Figure 3-5 Acquirement of QR Code Based Reference Points

When the pedestrians walked into a new building deployed with QR codes, they can use the smartphones to scan the QR code to get their 3D locations, which contains longitude, latitude, and floor information. The 3D location information of detected QR code is also applied as the observed value to further eliminate the cumulative error of INS mechanization, in this case, the equation (3-40) can also be described as:

$$\delta \boldsymbol{z}_p^n = \boldsymbol{p}_{QR}^n - \boldsymbol{p}_{INS}^n = \delta \boldsymbol{p} + n_{QR} \tag{3-42}$$

where $\boldsymbol{p}_{QR}^{n}$ represents the 3D location of the detected QR code, the measured uncertainty in this case is described as:

$$n_{QR} \sim \sum_{\tau=0}^{\partial} \boldsymbol{v}_{INS}^{n}(\tau) d\tau \tag{3-43}$$

where $\boldsymbol{v}_{INS}^{n}(\tau)$ indicates the measured INS based velocity during the period of camera scanning, τ is the timestamp, ∂ is the length of camera scanning time.

3.3.3 Backward-AUKF Smoothing Approach Based on Forward-AUKF Data

In this work, AUKF is applied to fuse multi-source based navigation information, which contains the adaptive weight adjustment of each location source. In order to make full use of all the observations and obtain the optimal estimation of 3D localization trajectory, the forward-AUKF based navigation data needs to be smoothed to further eliminate the navigation error occurred in the forward trajectory.

The RTS algorithm [60] is a smoother with a fixed window. Compared with the traditional reverse smoothing algorithm, RTS does not require a full set of reverse calculations. It only needs to calculate the reverse covariance based on the results of the forward filtering and the covariance matrix. The matrix is combined with forward filtering. RTS is widely used for navigation and mobile surveying tasks in vehicle, airborne and pipeline carriers. The whole AUKF based RTS algorithm proposed in this paper is shown below:

1) Localization Initialization:

$$\begin{cases} \boldsymbol{x}_0 = E[\boldsymbol{x}_0] \\ \boldsymbol{P}_0 = E[(\boldsymbol{x}_0 - \boldsymbol{x}_0)(\boldsymbol{x}_0 - \boldsymbol{x}_0)^{\mathrm{T}}] \end{cases} \tag{3-44}$$

2) Sigma Points Calculation:

$$\boldsymbol{X}_{k-1} = (\boldsymbol{x}_{k-1}, \boldsymbol{x}_{k-1} + \gamma\sqrt{\boldsymbol{P}_{k-1}}, \boldsymbol{x}_{k-1} - \gamma\sqrt{\boldsymbol{P}_{k-1}}) \tag{3-45}$$

3) State Model Update:

$$\boldsymbol{X}_{k|k-1}^{i} = \boldsymbol{\phi}\boldsymbol{X}_{k-1}^{i} \tag{3-46}$$

$$\boldsymbol{x}_k^{-} = \sum_{i=0}^{2n+1} \omega_i \boldsymbol{X}_{k|k-1}^{i} \tag{3-47}$$

$$\boldsymbol{P}_k^{-} = \sum_{i=0}^{2n+1} \omega_i (\boldsymbol{X}_{k|k-1}^{i} - \boldsymbol{x}_k^{-})(\boldsymbol{X}_{k|k-1}^{i} - \boldsymbol{x}_k^{-}) + \boldsymbol{G}\boldsymbol{Q}_k\boldsymbol{G}^{\mathrm{T}} \tag{3-48}$$

$$\boldsymbol{Z}_{k|k-1}^{i} = h(\boldsymbol{X}_{k|k-1}^{i}) \tag{3-49}$$

$$\boldsymbol{z}_k^{-} = \sum_{i=0}^{2n+1} \omega_i \boldsymbol{Z}_{k|k-1}^{i} \tag{3-50}$$

4) Measurement Update:

$$\boldsymbol{P}_{\tilde{z}_k \tilde{z}_k} = \sum_{i=0}^{2n+1} \omega_i (\boldsymbol{Z}_{k|k-1}^{i} - \hat{\boldsymbol{z}}_k^{-})(\boldsymbol{Z}_{k|k-1}^{i} - \hat{\boldsymbol{z}}_k^{-}) + \boldsymbol{R}_k \tag{3-51}$$

$$\boldsymbol{P}_{x_k z_k} = \sum_{i=0}^{2n+1} \omega_i (\boldsymbol{X}_{k|k-1}^{i} - \bar{\boldsymbol{x}}_k)(\boldsymbol{Z}_{k|k-1}^{i} - \hat{\boldsymbol{z}}_k^{-})^{\mathrm{T}} \tag{3-52}$$

$$\boldsymbol{K}_k = \boldsymbol{P}_{x_k z_k} \boldsymbol{P}_{\tilde{z}_k \tilde{z}_k}^{-1} \tag{3-53}$$

$$\boldsymbol{x}_k = \boldsymbol{x}_k^{-} + \boldsymbol{K}_k (\boldsymbol{z}_k - \hat{\boldsymbol{z}}_k^{-}) \tag{3-54}$$

$$\boldsymbol{P}_k = \boldsymbol{P}_k^{-} - \boldsymbol{K}_k \boldsymbol{P}_{\tilde{z}_k \tilde{z}_k} \boldsymbol{K}_k^{\mathrm{T}} \tag{3-55}$$

5) Backward Smoothing:

$$\boldsymbol{x}_{k-1|k} = \boldsymbol{x}_{k-1} + \boldsymbol{P}_{k-1} \boldsymbol{\phi}_k^{\mathrm{T}} (\boldsymbol{P}_{k-1}^{-})^{-1} (\boldsymbol{x}_k - \boldsymbol{x}_k^{-}) \tag{3-56}$$

$$\boldsymbol{P}_{k-1|k} = \boldsymbol{P}_{k-1} - (\boldsymbol{P}_{k-1} \boldsymbol{\phi}_k^{\mathrm{T}} (\boldsymbol{P}_k^{-})^{-1})(\boldsymbol{P}_k - \boldsymbol{P}_k^{-}) \cdot (\boldsymbol{P}_{k-1} \boldsymbol{\phi}_k^{\mathrm{T}} (\boldsymbol{P}_k^{-})^{-1})^{\mathrm{T}} \tag{3-57}$$

where $\boldsymbol{x}_k$ and $\boldsymbol{z}_k$ represent the state value and measured value which are represented in Section IV. The equation (3-44) to (3-55) define the forward-DR based on AUKF, and the equation (3-56) and (3-57) define the backward-smoothing procedure using results of forward-DR.

3.3.4 Global Optimization Based on Gradient Descent

The proposed backward-AUKF smoothing algorithm requires a large number of matrix operations, therefore it may not be conducive to building a lightweight navigation trajectory using mobile terminals based platforms. Thus, the gradient descent (GD) based global optimization approach is proposed to enhance the performance of forward-AUKF and decrease the algorithm complexity of backward-AUKF.

In the proposed GD, the location increment and the heading results at zero-crossing time during each step period are extracted as the raw navigation data, and all the navigation data during two detected landmarks is modeled as a nonlinear least squares problem. Thus, the observation model can be set as:

$$\boldsymbol{z} = \xi(\boldsymbol{x}) + \varpi \tag{3-58}$$

where $\boldsymbol{x}$ indicates the state vector of proposed optimization model, $\boldsymbol{z}$ is the observed value, ϖ represents the measured noise. The function $\xi(\boldsymbol{x})$ is defined as:

$$\xi(\boldsymbol{x}) = \boldsymbol{P}_0 + \sum_{i=1}^{n} L_i \begin{bmatrix} \cos(\theta_i) \\ \sin(\theta_i) \end{bmatrix} \tag{3-59}$$

where $\boldsymbol{P}_0$ indicates the location of the last reference point; L_i and θ_i represent the extracted location increment and heading information during each step period.

The loss function in proposed GD optimization approach is defined as follows:

$$L(\boldsymbol{x}) = (\boldsymbol{z} - \xi(\boldsymbol{x}))^{\mathrm{T}} \boldsymbol{R}^{-1} (\boldsymbol{z} - \xi(\boldsymbol{x})) \tag{3-60}$$

where $\boldsymbol{R}$ is the covariance matrix of the observation error.

Because the observation model is nonlinear, the linearization phase is required and Taylor series is applied to expand the current state estimate and take the first order term:

$$\begin{aligned} \boldsymbol{z} &= \xi(\boldsymbol{x}) + \varpi \\ &= \xi(\boldsymbol{x}) + \left.\frac{d\xi(\boldsymbol{x})}{d\boldsymbol{x}}\right|_{\boldsymbol{x}=\boldsymbol{x}} (\boldsymbol{x} - \boldsymbol{x}) + \frac{1}{2!} \left.\frac{d^2\xi(\boldsymbol{x})}{d\boldsymbol{x}^2}\right|_{\boldsymbol{x}=\boldsymbol{x}} (\boldsymbol{x} - \boldsymbol{x})^2 + \cdots + \varpi \\ &\approx \xi(\boldsymbol{x}) + \left.\frac{d\xi(\boldsymbol{x})}{d\boldsymbol{x}}\right|_{\boldsymbol{x}=\boldsymbol{x}} (\boldsymbol{x} - \boldsymbol{x}) + \varpi \\ &= \xi(\boldsymbol{x}) + \boldsymbol{G}\delta\boldsymbol{x} + \varpi \end{aligned} \tag{3-61}$$

where $\delta\boldsymbol{x}$ indicates the state estimation error, $\boldsymbol{G}$ indicates the Jacobian matrix. The difference between each iteration phase is presented as follow:

$$\boldsymbol{z} - \xi(\boldsymbol{x}) = \boldsymbol{G}\delta\boldsymbol{x} + \varpi \tag{3-62}$$

The updated difference of the state vector after each iteration phase is calculated by:

$$\delta\boldsymbol{x} = (\boldsymbol{G}^{\mathrm{T}} \boldsymbol{R}^{-1} \boldsymbol{G})^{-1} \boldsymbol{G}^{\mathrm{T}} \boldsymbol{R}^{-1} \delta\boldsymbol{z} \tag{3-63}$$

Non-linear least squares need to iterate the above process until the state estimation error is lower than the threshold. In general, the nonlinear least squares update can be written as:

$$\boldsymbol{x}_j = \boldsymbol{x}_{j\text{-}1} + \delta\boldsymbol{x}_{j\text{-}1} \tag{3-64}$$

where j represents the number of iteration. Since the observation error is not affected by the state estimation, the observation error covariance matrix $\boldsymbol{R}$ remains unchanged. The optimal solution reaches in the case when $L(\boldsymbol{x})$ less than the set threshold. Compared with backward-AUKF, the GD improves the calculation efficiency by reducing the complexity of matrix operations.

3.4 Tests and Results

In this section, comprehensive experiments are organized to evaluate the performance of proposed PINS framework. The Google Pixel 3 and Google Pixel 4 are used for pedestrian tracking which contains rich MEMS sensors and supports the Wi-Fi FTM protocol, BLE protocol, and QR code scanning. The sampling rates of MEMS sensors and Wi-Fi RSSI/FTM/BLE RSSI are set as 50 Hz and 5 Hz, respectively. Two indoor environments are adopted as experimental sites, which are deployed with sparse landmark points including Wi-Fi FTM station, BLE node, and QR code. The performance of proposed PINS framework is evaluated according to the following arrangement: Section 3.4.1 evaluates the performance of MEMS sensor based self-calibrated solution; Section 3.4.2 estimates the performance of proposed landmark detection algorithm; Section 3.4.3 evaluates the overall performance of PINS based 3D indoor localization and optimization framework.

3.4.1 Performance Evaluation of Multi-level Observables and Constraints

In this section, comprehensive experiments are organized to evaluate the performance of proposed MEMS sensors based self-calibrated framework. The Google Pixel 3 and Google Pixel 4 are used for pedestrian tracking which contains rich MEMS sensors and supports the Wi-Fi FTM protocol, BLE protocol, and QR code scanning. The sampling rates of built-in sensors and Wi-Fi RSSI/FTM/BLE RSSI are set as 50 Hz and 5 Hz, respectively. Two adjacent floors in a teaching building are selected as the 3D experimental site, which contains complex corridors and electro-magnetic interference, and the corresponding sparse landmarks are deployed at the positions A, D, L, J, as shown in Figure 3-6 and Figure 3-7.

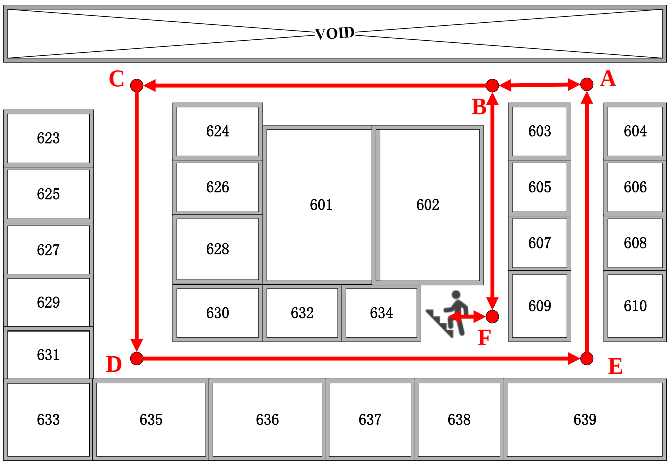

Figure 3-6 Sixth Floor and Route

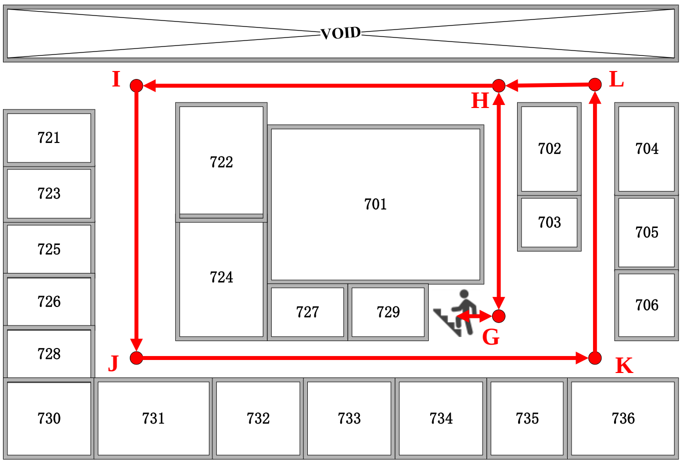

Figure 3-7 Seventh Floor and Route

To improve the performance of INS mechanization based positioning, multi-level observed values and constraints are proposed in this work, in which gravity vector, QSMF, ZARU are adopted to decrease the cumulative error of attitude estimation and the effect of magnetic interference. Step-length based velocity and position increment, ZUPT, E-NHC, pseudo observations are used to further decrease the divergence error of speed estimation under different handheld modes and motion modes. In addition, the AUKF is applied as the fusion method in order to get more robust integration performance under non-linear cases.

A long-term experiment is designed in this case to estimate the accuracy of attitude estimation, the pedestrian walked from the test point A, passed points B, C, D, and E, and then returned to the point A, the whole procedure repeated 10 times in a time period of 10min. The performance comparison between gyroscope-based heading, magnetic heading and proposed AUKF based heading is compared in Figure 3-8:

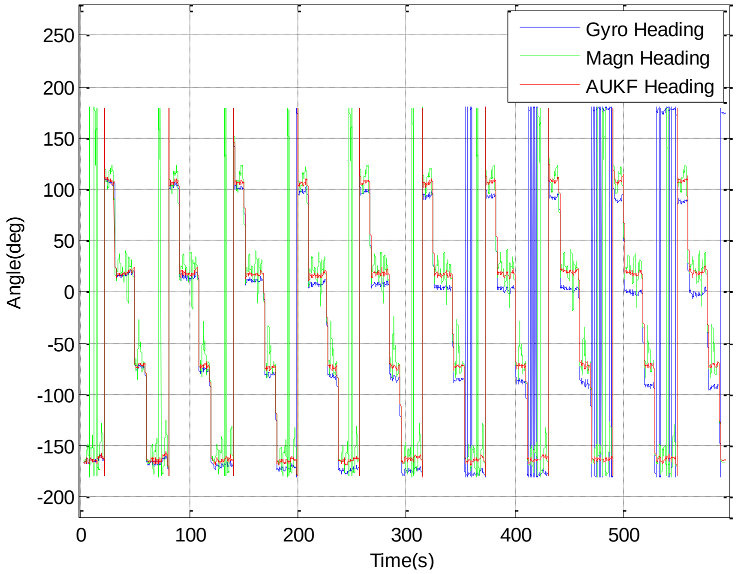

Figure 3-8 Long-term Performance Comparison of Heading Estimation

Figure 3-8 presents that the accuracy of gyroscope based heading is limited by the cumulative error, which grows about 15° after 10 minutes walking, and the magnetic heading exists large fluctuations due to the artificial interference indoors. The proposed AUKF based heading estimation combines multi-level observations and maintain the accuracy after long-term use, the final heading error is the least among three different heading estimation approaches, the detailed error comparison result is further described in the Table 3-2.

In order to provide a general evaluation of AUKF based attitude estimation, three more attitude fusion algorithms in literatures are compared with the proposed AUKF: AEKF in [83], DUKF in [44], and DKF in [124]. The tester's walking route is the same as in Figure 3-5. The final attitude error comparison result is shown in Table 3-2.

Table 3-2 Attitude Estimation Comparison Results

Index		AUKF	AEKF	DUKF	DKF
RMSE	Roll(°)	0.18	0.19	0.23	0.25
	Pitch(°)	0.15	0.22	0.12	0.21
	Yaw(°)	0.32	1.17	0.82	3.05
Max	Roll(°)	0.37	0.41	0.45	0.51
	Pitch(°)	0.31	0.47	0.26	0.45
	Yaw(°)	1.38	6.05	4.28	10.66
Median	Roll(°)	0.14	0.16	0.21	0.15
	Pitch(°)	0.16	0.18	0.11	0.16
	Yaw(°)	0.19	0.73	0.75	2.19
Mean	Roll(°)	0.14	0.16	0.22	0.15
	Pitch(°)	0.16	0.17	0.11	0.17
	Yaw(°)	0.22	0.82	0.73	2.21
Final	Roll(°)	0.16	0.21	0.25	0.31
	Pitch(°)	0.18	0.25	0.13	0.29
	Yaw(°)	1.34	5.87	4.12	10.66

Table 3-2 shows the overall comparison results between four different state-of-art attitude estimation algorithms. According to the. Table 3-2, the DUKF gets the best pitch estimation accuracy, and the RMSE is within 0.12°. The proposed AUKF gets the best roll estimation accuracy, and the RMSE is within 0.18°. For the yaw estimation, the proposed AUKF proves the best accuracy among four algorithms, the final yaw drift error is within 1.34°, and the DKF has the highest error larger than 10.66°, which may be the lack of bias estimation. The AEKF proves better performance than DKF but has larger cumulative error than DUKF, and the DUKF uses error vector to estimates the bias of gyroscope but the performance is not good as multi-level observations based AUKF.

The accuracy of walking speed estimation is compared between step-length based positioning method in equation (3-13) and proposed AUKF. To be fair, the two algorithms using the same heading provided by AUKF. The location and accuracy comparisons between step-length proposed in [113] and MEMS sensors based framework proposed in this section are described in Figure 3-9 and Figure 3-10:

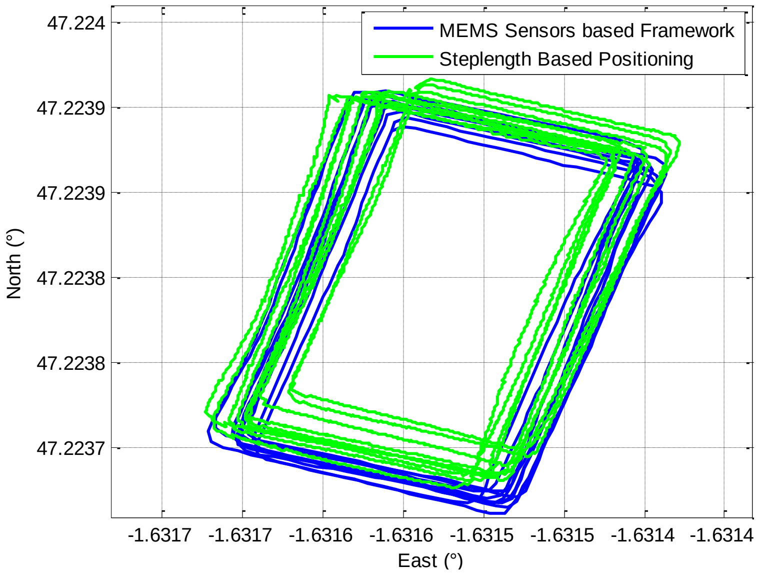

Figure 3-9 2D Localization Results

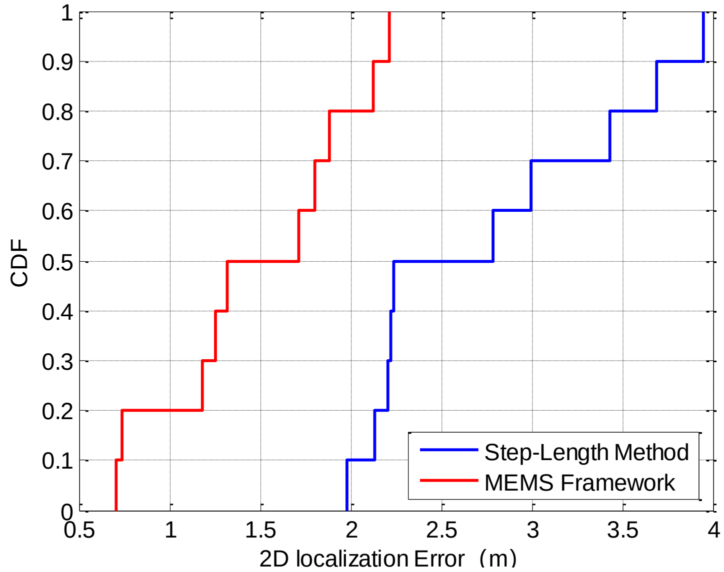

Figure 3-10 Cumulative Errors Comparison

In Figure 3-9, the World Geodetic System (WGS84) coordinate system is adopted to present the absolute location of the pedestrian, the X and Y coordinate represent the east and north of the latitude and longitude based 2D location information. Figure 3-10 presents that the proposed MEMS sensors based localization framework proves much better localization performance compared with the step-length based method, the Cumulative Distribution Function (CDF) error is within 2.13 m in 90% after a long-term use.

The handheld modes of the smartphone also prove significantly influences to MEMS sensors based positioning method. In this work, the positioning accuracy of E-NHC algorithm under four typical handheld modes is calculated using the walking route from the point A to the point E in Figure 3-6. The performance of 2D positioning in case of different handheld modes is described in Figure 3-11 and Figure 3-12:

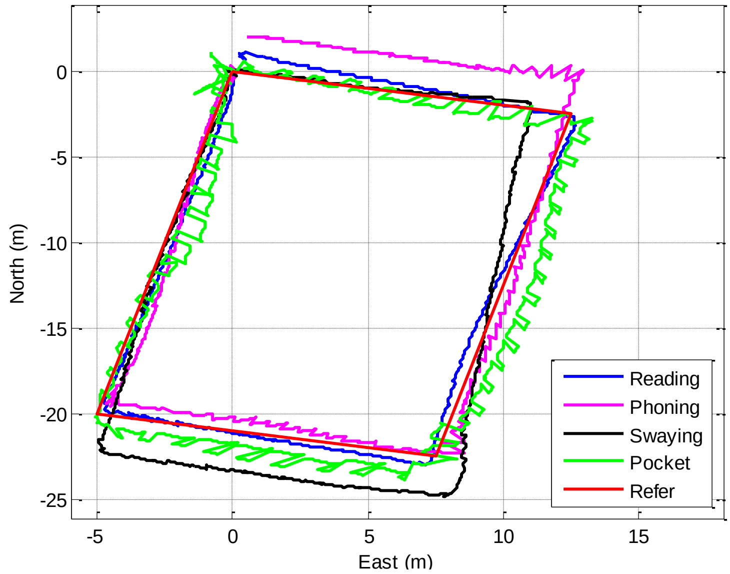

Figure 3-11 2D Localization Routes

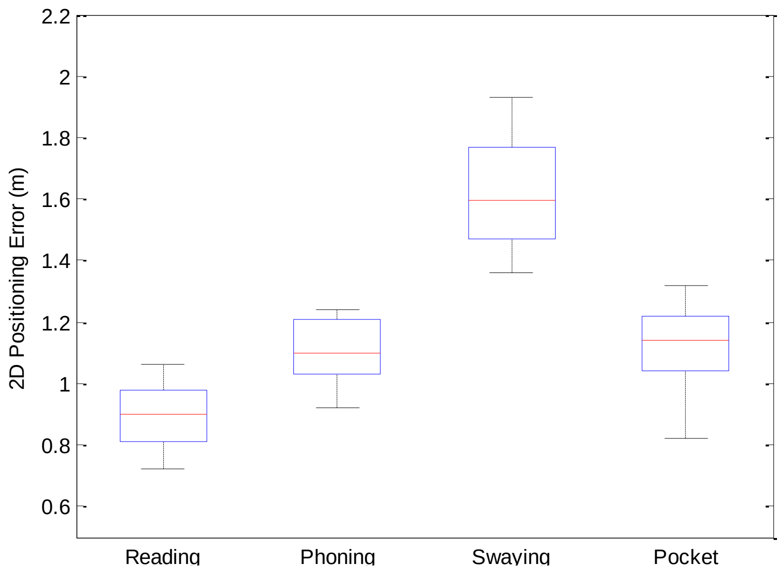

Figure 3-12 Positioning Error Comparison

It can be found from Figure 3-12 that the reading mode proves the best performance, the position error is within 0.98 m in case of 75%. The swaying mode gets the worst performance mainly due to the effects of external acceleration during pedestrians' walking periods, and the positioning error is within 1.77 m in case of 75%.

3.4.2 Performance Evaluation of Landmark Detection

In this section, the performance of Wi-Fi FTM anchor and BLE note based landmark detection is evaluated respectively, in this part, sparse Wi-Fi FTM and BLE anchors are deployed to provide accurate and absolute ranging and 3D location information for built-in sensors based method contained in PINS. The DTW algorithm is proposed for dynamic Wi-Fi based landmark detection, and the comparison between reference distribution and real-time collected distribution is shown in Figure 3-9(a). In real-time DTW estimation of Wi-Fi FTM station based landmark detection, the length of DTW slide window is choose as 10 which contains Wi-Fi ranging data in a 2s period. The performance of calculated DTW is described in Figure 3-13 and Figure 3-14.

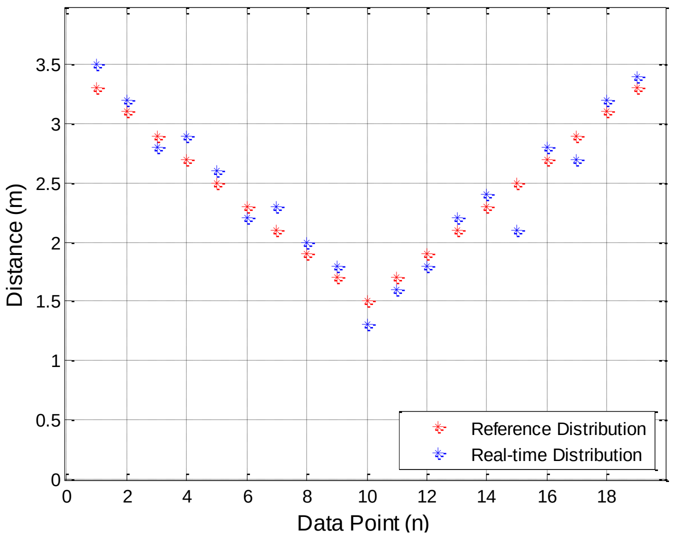

Figure 3-13 Comparison Between Real-time and Reference Distribution

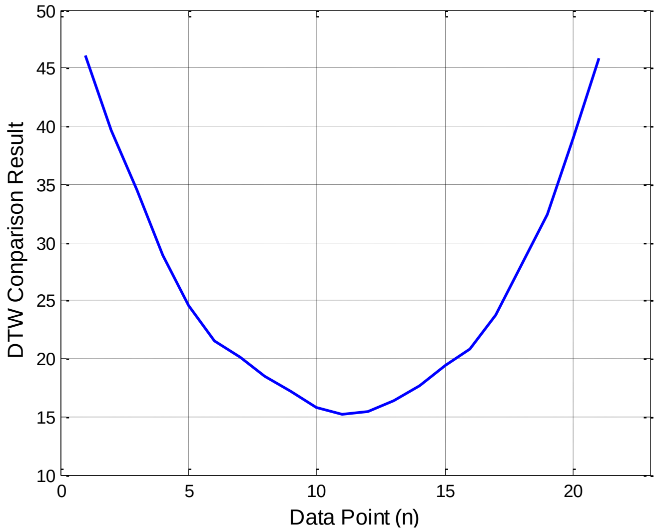

Figure 3-14 DTW Detection Result

Figure 3-14 described the real-time calculated DTW result between collected distribution and reference distribution in a length of 2s slide window. It can be found from Figure 3-13 and Figure 3-14 that the calculated DTW value decreases when the pedestrian walks towards the Wi-Fi AP and reaches the minimum when the pedestrian is closest to Wi-Fi AP, and a new Wi-Fi based landmark can be recognized when the calculated minimum DTW value reaches the set threshold. In this work, the threshold is set as 16 according to the length of the DTW slide window and sampling rate of Wi-Fi FTM.

In this work, the accuracy of DTW based landmark detection is compared with the hybrid landmark detection algorithm proposed in [83], the detection error comparison result is shown in Figure 3-15:

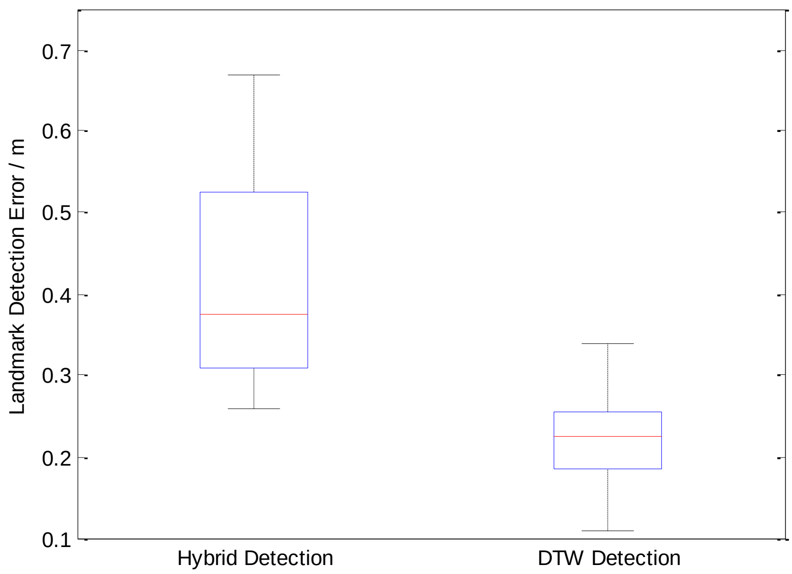

Figure 3-15 Error Comparison of Landmark Detection

It can be found from Figure 3-15 that the proposed DTW based landmark detection algorithm prove much high accuracy, the detection error is within 0.26 m in case of 75%.

For the BLE node based landmark detection, the processed RSSI value are directly applied for recognition purpose. The received RSSI will produce signal peak when the pedestrian walks by a local BLE node. In this paper, DTW algorithm is used to detect the BLE based landmark, a real-time RSSI distribution extracted from RSSI map is used to calculate the similarity with the reference distribution. The reference distribution can be acquired by fitting the measured RSSI value at each position in the range of effective distance of the BLE node by equation (3-38), which is shown in Figure 3-16:

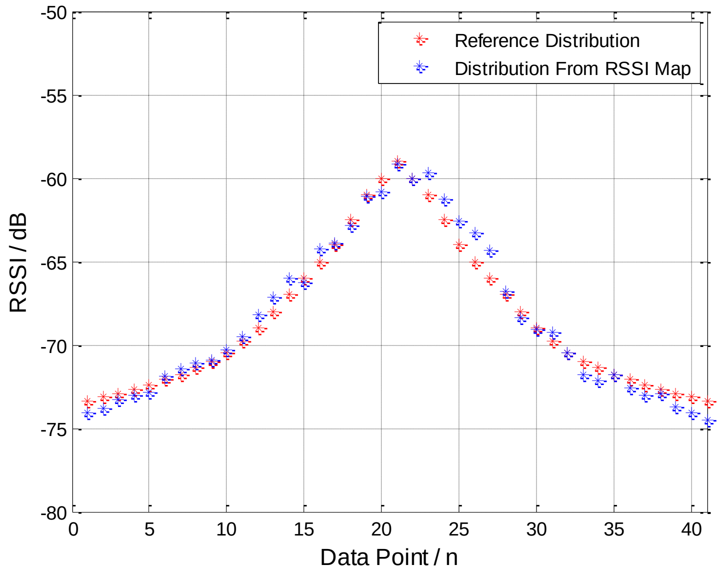

Figure 3-16 Reference Distribution of BLE Based Landmark

Figure 3-16 indicates the difference between reference RSSI distribution and real-time collected RSSI distribution. In the proposed BLE landmark detection algorithm, a time window of length 15 is used to collect real-time RSSI data from RSSI map for DTW comparison with the reference distribution extracted in Figure 3-16, which can store received RSSI in a walking period of 3s. The DTW comparison result between real-time RSSI data from RSSI map and reference distribution is shown in Figure 3-17:

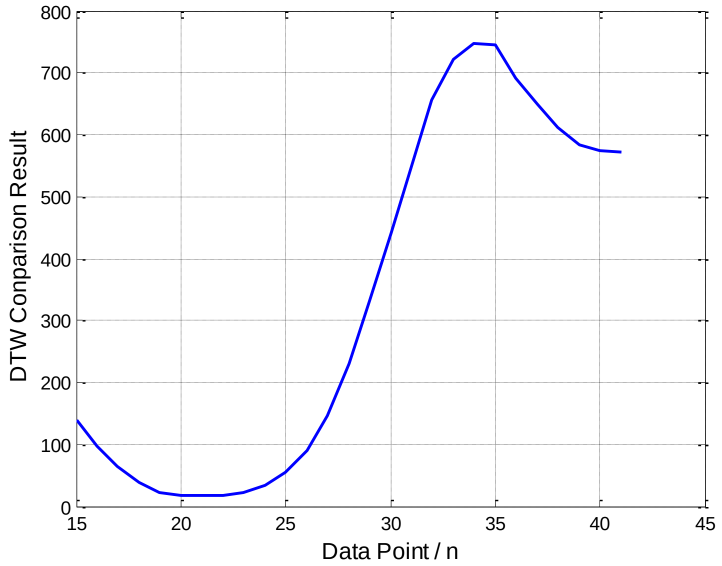

Figure 3-17 DTW Comparison Result of BLE Landmarks

In Figure 3-17, the calculation result of DTW proved the minimum value when the pedestrian reached the position of the BLE node at the data point 22, and then the DTW value began to increase. The final accuracy of BLE based landmark detection is shown in Figure 3-18:

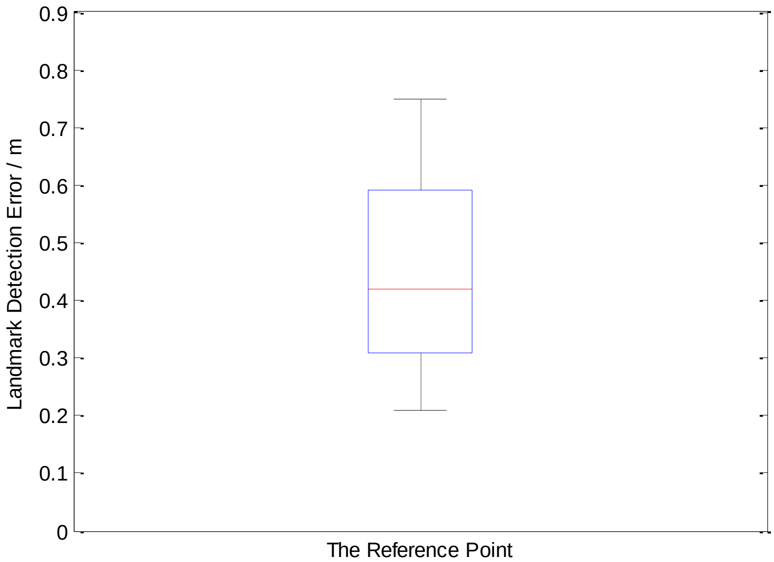

Figure 3-18 Accuracy of BLE based Landmark Detection

Figure 3-18 demonstrates the precision of proposed BLE landmark detection algorithm, the average detection error is within 0.42 m, and the maximum detection error is not greater than 0.75 m. The 3D location information provided by the detected BLE landmarks is further integrated with multiple sensors based method in proposed AUKF to realize a robust and concrete multi-source based 3D indoor localization.

Thus, the performance comparison of three introduced landmarks is described in Table 3-3:

Table 3-3 Performance Comparison of Three Different Landmarks

Landmarks	Accuracy	Time	Cost
Wi-Fi Station	< 0.35 m	Quick	High
BLE Node	< 0.75 m	Quick	Medium
QR Code	0.5 m ~ 1 m	Slow	Low

3.4.3 Performance Evaluation of Pedestrian Aimed INS Solution

In this part, the accuracy of PINS based 3D indoor localization and navigation trajectory optimization is evaluated among the typical 3D indoor scene shown in Figure 3-6 and Figure 3-7. The walking route of the pedestrian is from point A, continuously passed the points B, C, D, E, A, B, F, G, H, I, J, K, L, H, G, F, B, and returned to point A. The forward-AUKF proposed in 3D-LOWS framework combines the INS mechanization and multi-level constraints and observed values to improve the built-in sensors based 3D localization performance, and Wi-Fi based ranging and landmark detection is applied to further improve the robustness of multi-source fusion based indoor positioning. In addition, the pedestrian's attitude and position information is finally optimized respectively by the proposed backward-AUKF and GD algorithms at the time of Wi-Fi landmarks detected to construct the optimal 3D navigation trajectory. The comparison of the localization and optimization performance between forward-AUKF, backward-AUKF and GD algorithm in case of reading mode is compared in Figure 3-19 and Figure 3-20:

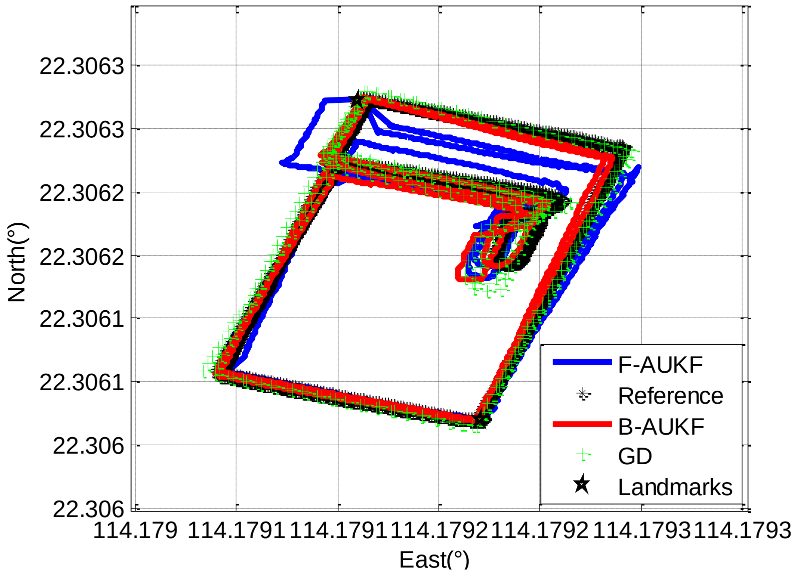

Figure 3-19 Performance of 2D PINS Framework in First Scene

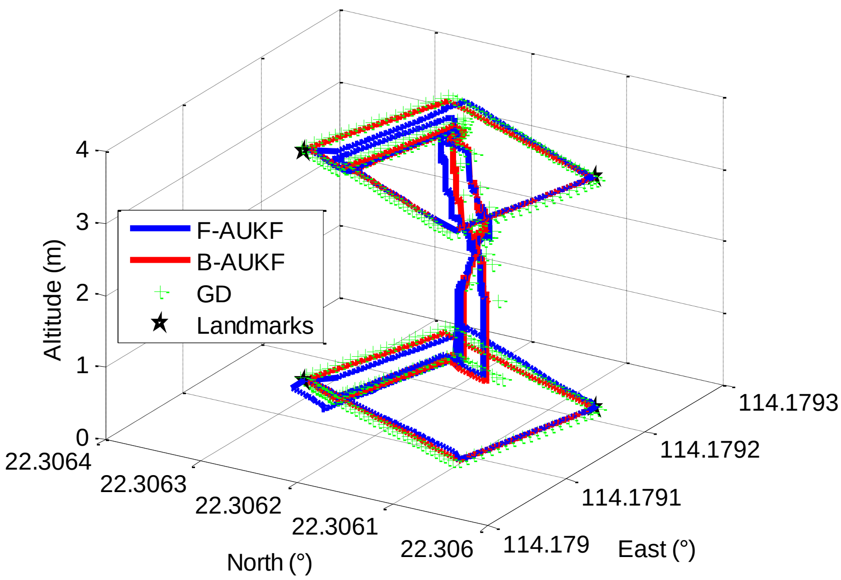

Figure 3-20 Performance of 3D PINS Framework in First Scene

The precision comparison between forward-AUKF, backward-AUKF, and GD under different handheld modes is described in Figure 3-21 and Figure 3-22:

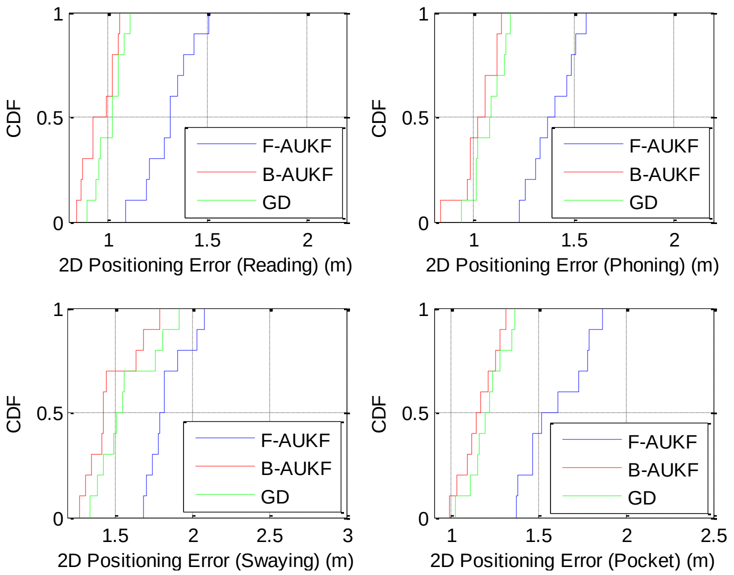

Figure 3-21 2D Error Comparison of Different Handheld Modes

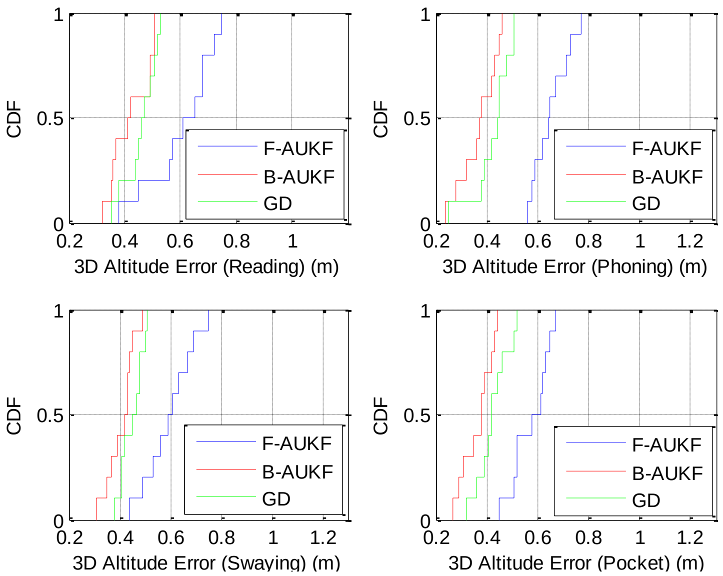

Figure 3-22 Altitude Error Comparison of Different Handheld Modes

Figure 3-21 shows that the proposed forward-AUKF proves precise 3D indoor localization performance under four handheld modes, the 2D positioning errors are within 1.38m, 1.49m, 1.91m, and 1.73m in case of 80%. The proposed backward-AUKF proves higher accuracy compared with GD algorithm in all the handheld modes, and both two algorithms have much better performance than the forward-AUKF, the ratios of accuracy improvement in reading mode are 26.09% and 23.91%, in phoning mode are 25.5% and 22.82%, in swaying mode are 14.14% and 7.85%, in pocket mode are 27.75% and 26.01%.

For the altitude calculation presented in Figure 3-22, the proposed backward-AUKF and GD algorithm also effectively improve the performance of forward-AUKF. The measured altitude error of forward-AUKF in four different handheld modes are 0.68m, 0.71m, 0.67m, 0.63m in case of 80%, respectively. The ratios of accuracy improvement of backward-AUKF and GD in reading mode are 27.94% and 25%, in phoning mode are 39.44% and 32.39%, in swaying mode are 34.33% and 28.36%, in pocket mode are 33.33% and 26.98%. In some cases, the accuracy of proposed GD algorithm proves comparable results than backward-AUKF, therefore, these two database construction algorithms can be selected organically according to the performance of different platforms and the application scenes.

To compare the improved precision of developed PINS structure and state-of-art literatures, one more typical office scene contains two adjacent floors is selected as the other experimental site, which is shown in Figure 3-23 and Figure 3-24:

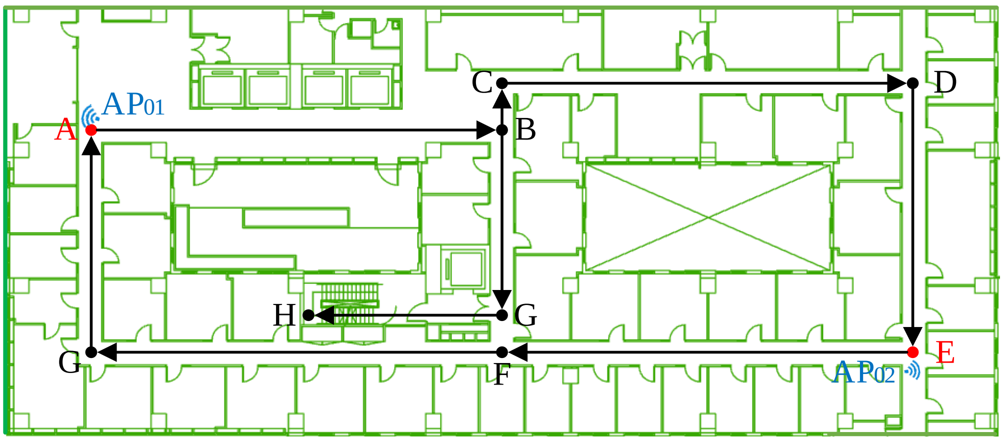

Figure 3-23 Ninth Floor and Walking Route

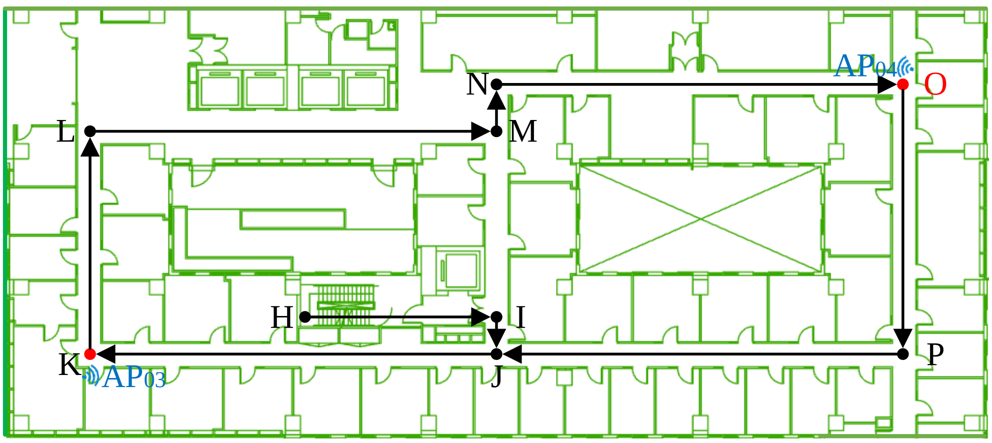

Figure 3-24 Eighth Floor and Walking Route

In Figure 3-23 and Figure 3-24, two Wi-Fi FTM supported anchors are deployed in each adjacent floor, respectively. The testers began from the point A, passed points B, C, D, E, F, G, A, B, G, H, went down stairs to the eighth floor, passed points I, J, K, L, M, N, O, P, J, K, and finally reached the point L. The estimated trajectories provided by the proposed PINS structure are shown as follows:

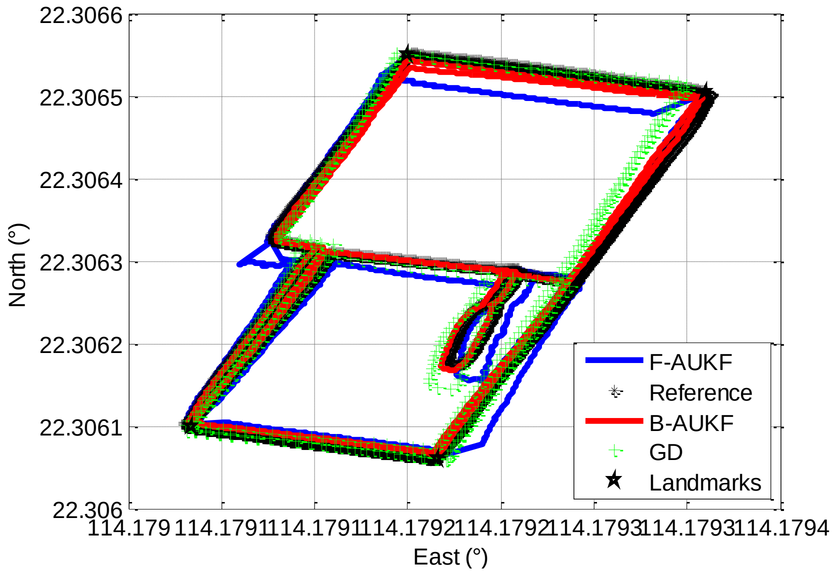

Figure 3-25 2D Trajectory Evaluation of PINS Structure in Second Scene

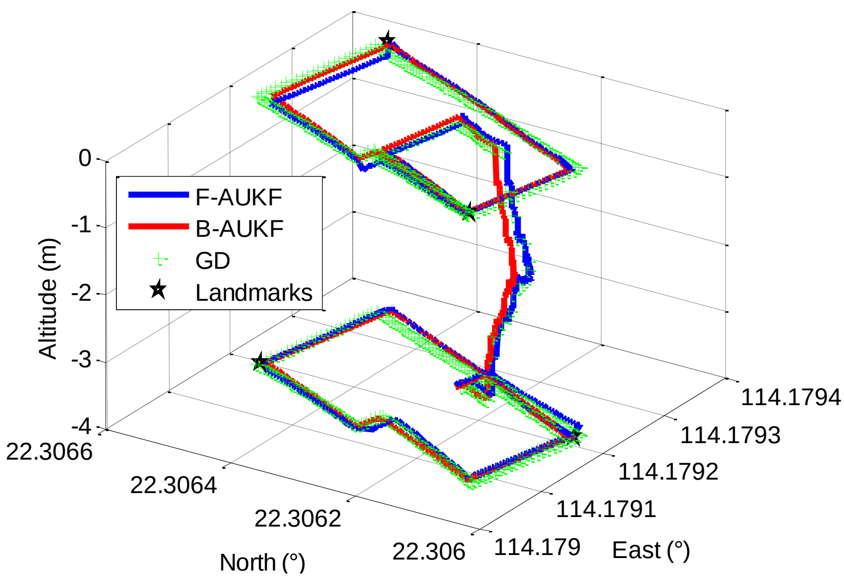

Figure 3-26 3D Trajectory Evaluation of PINS Structure in Second Scene

Figure 3-25 and Figure 3-26 compare results of trajectory estimation of proposed PINS structure which contains the forward-AUKF, backward-AUKF, and GD based estimation and optimization results. To further evaluate the positioning precision of proposed PINS structure and state-of-art approaches, two different integration models of Wi-Fi FTM and MEMS sensors are applied for comparison: enhanced particle filter (EPF) presented in [23] and 3D-WFBS proposed in [83]. To be fair, the same deployment of Wi-Fi FTM anchors and the same test route are applied, the positioning error comparison results is shown in Figure 3-27:

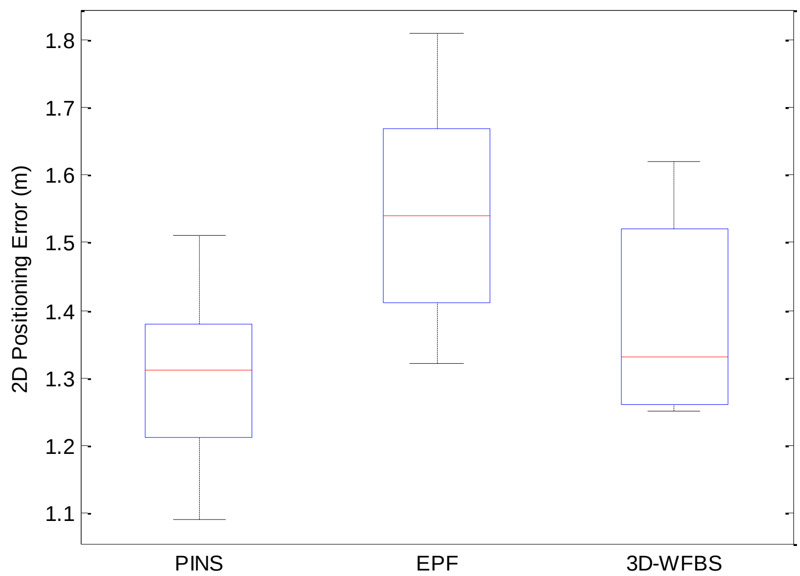

Figure 3-27 Comparison of Different Integration Approaches

The Figure 3-27 presents that the proposed PINS structure proves much better performance compared with the state-of-art Wi-Fi FTM and MEMS sensors integration approaches in case of sparse Wi-Fi FTM anchors contained indoor environments, the estimated positioning errors of three different algorithms are 1.38m, 1.67m, and 1.52m, respectively. Thus, the proposed forward-AUKF integration model effectively increases the positioning accuracy of MEMS sensors during the time period when the wireless signal is unavailable, and the proposed trajectory optimization approaches can further improve the positioning performance for high-accuracy requirements.

3.5 Summary

This chapter proposes the PINS framework, aiming at providing robust 3D indoor localization and optimization performance in case of large-scaled and sparse landmark points contained indoor spaces. The contribution of this chapter contains three main parts:

(1) This chapter proposes multi-level constraints and multi-level observed values, which are applied as the MEMS sensors based observation model in AUKF in order to eliminate effects of cumulative and divergence errors, magnetic interference, and different handheld modes added on the INS mechanization based 3D attitude and location update. The described MEMS sensors based integrated localization approach is regarded as the most important part in the proposed PINS framework, which can

maintain the accuracy of 3D indoor localization in complex indoor environments and changeable motion modes in a long time period through self-calibration procedure provided by the multi-level constraints and observed values; The comprehensive experiments in two complex 3D indoor environments indicate that the proposed PINS structure reaches the 2D positioning accuracy of 1.38 m, 1.44m, 1.91m, 1.73 m in 80%, and altitude calculation accuracy of 0.68 m, 0.71 m, 0.67 m, 0.63 m in 80%, under four different kinds of handheld modes: reading, phoning, swaying, and pocket.

(2) This chapter proposes and compares three different location sources based landmark point detection and fusion methods, including the Wi-Fi FTM stations, BLE nodes, and QR codes. For the Wi-Fi FTM station based location source, the hybrid Wi-Fi ranging and DTW landmark detection based approach is applied to provide high-precision absolute reference to built-in sensors based positioning method. For the BLE node based location source, the real-time constructed RSSI map and DTW matching is combined for more accurate landmark detection, and the QR code can be directly scanned through the smartphone integrated camera. In addition, the uncertainty of detected landmark points is calculated respectively, and the 3D location information of detected landmark point is further integrated with MEMS sensors based approach to provide absolute reference and decrease the cumulative error. The maximum landmark detection errors of different location sources are estimated as 0.35 m (Wi-Fi FTM station), 0.75 m (BLE node), and between 0.5 m ~ 1 m (QR Code).

(3) To fully complete the functions of PINS structure, two different types of navigation trajectory optimization algorithms including backward-AUKF and GD are proposed and evaluated in this chapter, aiming at different platforms and application scenes, which achieve meter-level accuracy of reconstructed 3D navigation trajectory. The optimized 3D navigation trajectory information provided by the PINS structure is further adopted in the next chapter and served as an important way to collect and process the crowdsourced navigation trajectories. The experimental results prove that the ratios of precision improvement of backward-AUKF and GD in reading mode are 27.94% and 25%, in phoning mode are 39.44% and 32.39%, in swaying mode are 34.33% and 28.36%, in pocket mode are 33.33% and 26.98% in typical 3D indoor environments.

In conclusion, in this chapter, after the presentation of theoretical framework of PINS algorithm, we design comprehensive experiments to evaluate the accuracy of developed PINS structure in different 3D indoor scenes under different walking routes, handheld modes, and time periods, and compare the PINS structure with multiple state-of-art multi-source fusion algorithms. The experimental results prove that the proposed PINS structure in this chapter effectively improves the accuracy and robustness of MEMS sensors and sparsely deployed landmark points based 3D indoor positioning and the can further provide stable and precise localization and trajectory optimization result in complex, large-scaled, and limited wireless stations covered 3D indoor environments.

Chapter 4: Hybrid Wi-Fi Positioning Solutions

Wi-Fi positioning system (WPS) has attracted much more attentions compared with other location sources because of its low-cost and wide coverage characteristics. Generally, the IoT terminals based WPS always contains two implementation methods: ranging and fingerprinting. The collected RSSI feature is usually acquired to realize real-time ranging between IoT terminals and Wi-Fi APs and the location information is acquired by the Least squares (LS) algorithm [26]. Besides, the fingerprinting technique is developed to provide location information by collecting signals of opportunity (SOP) in selected indoor environments without knowing the positions of local facilities [21]. In a typical indoor scene, the precision of Wi-Fi fingerprinting is seriously influenced by the deployment and sparseness of surrounding facilities and the localization precision would decrease in open environments [28-29]. To improve the robustness of WPS, IEEE 802.11ac added the Wi-Fi FTM protocol, which can provide accurate time-of-flight information between IoT terminals and Wi-Fi APs [30]. Ibrahim M *et at*. [79] realized and confirmed the meter-level ranging precision of Wi-Fi FTM on the Intel wireless card supported open platform under line-of-sight (LOS) and high bandwidth. The experimental results demonstrate that the Wi-Fi FTM based location source provides a much precise and stable approach for indoor localization compared with RSSI based positioning method.

In this chapter, two state-of-art WPS systems: Wi-Fi FTM based calibration and positioning system and crowdsourced Wi-Fi fingerprinting based positioning system are presented respectively towards different application requirements. In which the Wi-Fi FTM based calibration and positioning system is presented towards high-accuracy localization requirement in specific indoor areas, and the crowdsourced Wi-Fi fingerprinting based positioning system is presented aiming at realizing a more universal and autonomous positioning requirement in smart city based large-scaled indoor spaces.

The contributions of this chapter are summarized as follows:

1) This chapter proposes three different Wi-Fi FTM calibration strategies which take different application scenes into consideration. In which the Polynomial-based (PB) calibration strategy towards the known types of smartphones and Wi-Fi APs. Gradient descent (GD) based FTM bias estimation with the combination of quasi-static (QS) recognition, and the estimated bias value is used to calibrate the

measured RTT in real-time without the known types of smartphones and Wi-Fi APs. Tightly-coupled (TC) integration model with the consideration of all error sources, in which all the navigation parameters are calibrated and optimized at the same time to get the final positioning results.

2) This chapter proposes a comprehensive structure for crowdsourced trajectories modelling, pre-calibration, optimization, and classification. In which the collected crowdsourced trajectory is modeled as a non-linear function contains the extracted landmarks, heading and step-length information, and the raw trajectory is matched with the reference vector for pre-calibration in order to decrease the effects of initial heading error and installation error caused by the handheld mode of the pedestrian. In addition, an iterative extended Kalman filter (iEKF) is proposed for robust trajectory optimization to further improve the accuracy of pre-calibrated trajectory, and the optimized trajectories are finally classified into similar groups using the multi-level constraints, correlation coefficient and DTW indexes.
3) This chapter proposes a novel multi-layer perceptron (MLP) based deep-learning network which can autonomously evaluate the positioning error of optimized trajectories during each step period based on the extracted motion features. To construct an accurate and efficient crowdsourced Wi-Fi fingerprinting database, the evaluated trajectories in same similar group are further segmented and merged according to the detected turning points information, and the final crowdsourced Wi-Fi fingerprinting database is reconstructed using the turning/landmark points generated collection points to reduce the dimension and complexity.

The remainder of this chapter is organized as follows. Section 4.1 introduces the background information of two proposed Wi-Fi positioning system and state the existing problems in case of realizing a more robust and autonomous WPS. Section 4.2 presents a Wi-Fi FTM Based calibration and positioning system, which contains three different kinds of Wi-Fi ranging bias calibration strategies. Section 4.3 proposes a crowdsourced Wi-Fi fingerprinting based positioning system, including a comprehensive crowdsourced trajectories processing structure and the MLP based crowdsourced trajectories evaluation and merging architecture. Section 4.4 designs comprehensive experiments and gives the test results and the performance analysis. Section 4.5 gives the summary of this chapter.

4.1 Introduction

The indoor positioning ability has become an essential requirement towards smart city and IoT based applications as people spend more time indoors. Due to the variability of indoor scenes, it is still challenging to provide universal and precise pedestrian navigation services under GNSS-denied indoor environments. The Wi-Fi based navigation system has attracted attentions of researchers due to its low-cost and wide distribution characteristics.

Aiming at the IoT terminals based indoor localization, most of above extracted characteristics are not supported due to the hardware or time synchronization based limitations. The Wi-Fi RSSI is the most commonly used wireless indoor positioning source, which usually contains two approaches: triangulation and fingerprinting. It can be found from state-of-art literatures that the Wi-Fi RSSI based ranging and fingerprinting methods are difficult to fulfil the requirements of meter-level indoor localization due to changeable local environments and artificial interference. To improve the ability of the WPS, IEEE 802.11mc protocol was presented in 2016, which can provide meter-lever round-trip-time (RTT) based distance measurement results among different mobile terminals and Wi-Fi access points (APs) [30]. However, due to the hardware differences between smartphones and Wi-Fi APs, the raw measured RTT value always contains additional bias which causes the overall drift of the ranging result. Ibrahim M *et al*. [79] confirmed the existence of FTM based ranging bias between different wireless devices, and calibrated the initial deviation error by the measured ground-truth distance on an open platform. In addition, [125] provided the theoretical analysis of various factors which influence the Wi-Fi ranging bias and proved that both smartphones and Wi-Fi APs can influence the value of FTM based ranging bias, also included the Gaussian distributed random error added by the measurement mechanism and environmental factors.

The crowdsourcing-based localization approach is developed using the analysis of geo-spatial big data, which provides an effective way for the realization of autonomous Wi-Fi positioning in smart city based large-scaled indoor scenarios. In order to generate a robust crowdsourced Wi-Fi fingerprinting database, the following challenges need to be tackled: 1) The low accuracy of collected daily-life MEMS sensors data which is seriously affected by the cumulative error and local artificial interference [90]. The performance of crowdsourced trajectories is also subjected to the number of detected landmark points and the complexity of the floor plan; 2) The requirements of autonomous evaluation and accurate combination of crowdsourced trajectories [56]. Due to the huge amount of collected trajectories provided by various mobile terminals, a robust trajectory evaluation model is needed to predict the uncertainty of collected trajectories, which is an essential step before trajectory merging phase and navigation database generation phase; 3) The efficient deployment and the accuracy detection of RPs [91]. Because the smartphone integrated sensors can only provide relatively location information, thus, sparsely deployed landmarks are required in order to provide absolute reference to the MEMS sensors originated trajectory.

By considering the facing problems described above, this chapter focuses on developing two robust Wi-Fi positioning systems aiming at providing precision-controllable indoor localization performance towards different requirements of location based services. The target of Wi-Fi FTM Based calibration and positioning system is to provide meter-level indoor localization performance in Wi-Fi FTM protocol supported environments. The advantages of proposed Wi-Fi FTM Based calibration and positioning system including the strong anti-interference ability compared with RSSI based ranging approach and realization of the potential of integration of communication and accurate indoor navigation. The target of crowdsourced Wi-Fi fingerprinting system is to provide autonomous localization service in large-scaled indoor environments. The advantages of proposed crowdsourced Wi-Fi fingerprinting system including the autonomous collection, generation, updating of Wi-Fi fingerprinting database using crowdsourced data provided by a huge amount of IoT terminals, and the universal characteristics that almost all the mobile terminals support the Wi-Fi scanning function. Therefore, the two Wi-Fi positioning systems proposed in this chapter have their own advantages respectively, and a more robust integrated navigation system combining Wi-Fi FTM / Wi-Fi RSSI / MEMS sensors will be introduced in Chapter Five.

4.2 Wi-Fi FTM Based Calibration and Positioning Solution

Wi-Fi FTM based indoor localization has become the state-of-art approach for pedestrian tracking. Due to the hardware differences between smartphones and Wi-Fi access points, the raw measured round-trip-time exists additional deviation which needs to be calibrated. In order to solve this problem, this section proposes and compares three different self-calibration strategies towards Wi-Fi FTM and MEMS sensors based localization. Polynomial-based, Gradient Descent and tightly-coupled integration models are applied respectively towards different application scenarios. Final experimental results prove that the proposed self-calibration strategies significantly eliminate the ranging bias, and meter-level indoor localization accuracy can be achieved after calibration. The basic framework proposed calibration and integrated localization is shown in Figure 4-1.

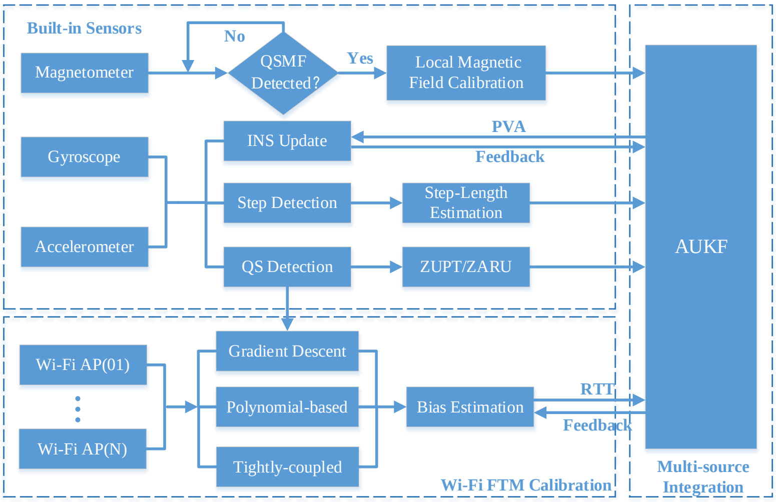

Figure 4-1 Calibration and Localization Framework

Figure 4-1 shows the main procedure of the proposed calibration and localization framework. In the built-in sensors module, the INS mechanization based heading and location update is combined with the step-length estimation and quasi-static magnetic field (QSMF) detection results. In the Wi-Fi FTM calibration module, three different strategies are proposed for real-time RTT bias estimation aiming at different application conditions. In the multi-source integration module, the calibrated RTT measurements and built-in sensors based positioning results are fused by the adaptive unscented Kalman filter (AUKF) in order to provide meter-level indoor localization performance. This section focuses on the PB and GD based Wi-Fi FTM calibration methods.

4.2.1 Polynomial Based Calibration Method

As discussed in literature [19], the measured bias of Wi-Fi FTM depends on the types of IoT terminals and Wi-Fi APs. In addition, the measured RTT based distance is affected by both initial bias and environmental factors such as multipath propagation, NLOS, and random error. Thus, the raw ranging result can be modeled as follow:

$$L_{\mathrm{raw}} = L_{\mathrm{RTT}} + d_{bias} + d_E + d_{\mathrm{random}} \tag{4-1}$$

where L_{raw} indicates the smartphone reported distance; L_{RTT} represents; d_{bias} is the bias of Wi-Fi FTM which will be addressed in our paper; d_{E} is the environment related error; d_{random} represents the measured random error which is subjected to the Gaussian distribution.

In case of the known kinds of smartphones and Wi-Fi APs, the parameter d_{bias} remains as a constant value, which can be calculated by the proposed PB calibration approach. The PB model is described as:

$$D_{\text{true}} = \sum_{i=0}^{\beta} \mu_i L_{raw}^{i} \tag{4-2}$$

where D_{true} represents the calibrated distance, μ_i indicates the calibration parameter, and L_{raw}^{i} is the raw Wi-Fi FTM result. In this paper, the random measurement error is eliminated by the KF algorithm proposed in [125]. When the $\beta = 1$, the equation (4-2) can be transferred into a linear calibration model:

$$D_{\text{true}} = \mu_1 L_{raw} + \mu_0 \tag{4-3}$$

In which the calibration parameter μ_1 and μ_0 can be acquired by the linear-fit method using the measured distance distribution and ground-truth distance distribution. In this case, we use the Google Pixel 1 to 4 and Google Wi-Fi to get the final linear-fit result and the corresponding calibration parameters respectively, and the linear-fit result is shown in Figure 4-2.

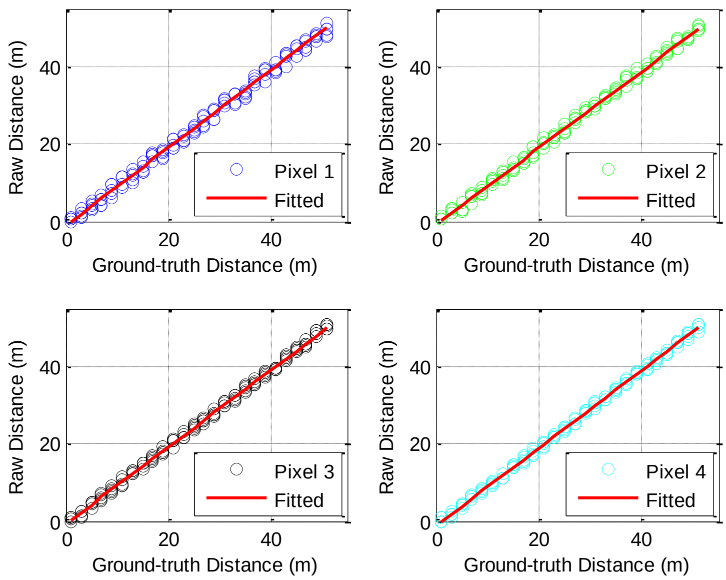

Figure 4-2 Polynomial Based Calibration Result

In this case, the calibration parameters μ_0 and μ_1 using Google Pixel 1 to 4 are finally calculated and shown in Table 4-1:

Table 4-1 Calibration Parameters Estimation

Parameter	Pixel 1	Pixel 2	Pixel 3	Pixel 4
μ_0	1.006	1.004	1.002	1.001
μ_1	-1.24m	-0.95m	-0.88m	-1.06m

4.2.2 Gradient Descent Based Calibration Method

In real application scenarios, due to the unknown types of smartphones and Wi-Fi APs, the proposed PB calibration approach is often unavailable. Aiming at dynamically estimating the Wi-Fi FTM bias, the GD based calibration algorithm is proposed. The QS periods are recognized during the pedestrian's walking procedure using the real-time collected inertial sensors data [51]:

$$\frac{1}{N}\sum_{k=1}^{N}\left(\frac{\left\|\boldsymbol{f}_k^b-\boldsymbol{g}^n\right\|^2}{\zeta_f^2}+\frac{\left\|\boldsymbol{\omega}_g^k\right\|^2}{\zeta_w^2}\right)<\Omega \tag{4-4}$$

where N represents the length of sliding window, $\boldsymbol{f}_k^b$ and $\boldsymbol{\omega}_g^k$ indicate the measured acceleration and angular velocity data at epoch k, ζ_f^2 and ζ_f^2 represent the measured noises of accelerometer and gyroscope, and Ω is the set threshold.

Once the QS periods are recognized, the least square (LS) algorithm is applied to acquire the location of the pedestrian based on the real-time RTT measurements [19]:

$$\boldsymbol{P}_{\mathrm{RTT}}=(\boldsymbol{A}^{\mathrm{T}}\boldsymbol{A})^{-1}\boldsymbol{A}^{\mathrm{T}}\boldsymbol{B} \tag{4-5}$$

where $\boldsymbol{P}_{\mathrm{RTT}}$ is the optimal position of the pedestrian, and the matrix $\boldsymbol{A}$ and $\boldsymbol{B}$ are defined as:

$$\boldsymbol{A}=2\cdot\begin{bmatrix}(\boldsymbol{P}_{\mathrm{AP}(2)}-\boldsymbol{P}_{\mathrm{AP}(1)})^{\mathrm{T}}\\ \vdots\\ (\boldsymbol{P}_{\mathrm{AP(N)}}-\boldsymbol{P}_{\mathrm{AP}(1)})^{\mathrm{T}}\end{bmatrix} \tag{4-6}$$

$$\boldsymbol{B}=\begin{bmatrix}\left\|\boldsymbol{P}_{\mathrm{AP}(2)}\right\|^2-\left\|\boldsymbol{P}_{\mathrm{AP}(1)}\right\|^2-(L_{raw(2)}-d_{bias})^2+(L_{raw(1)}-d_{bias})^2\\ \vdots\\ \left\|\boldsymbol{P}_{\mathrm{AP}(N)}\right\|^2-\left\|\boldsymbol{P}_{\mathrm{AP}(1)}\right\|^2-(L_{raw(N)}-d_{bias})^2+(L_{raw(1)}-d_{bias})^2\end{bmatrix} \tag{4-7}$$

where $\boldsymbol{P}_{\mathrm{AP(N)}}$ indicates the position of local Wi-Fi AP, $L_{\mathrm{raw}(N)}$ represents the measured RTT value, d_{bias} is the RTT bias exists between the smartphone and Wi-Fi AP.

Under ideal circumstances, the position of the pedestrian remains theoretically unchanged in the detected QS periods. Thus, the differences between estimated positions during each detected QS period approximately equal to zero, the GD based RTT bias optimization model is presented as:

$$h(\boldsymbol{x}) = \sum_{i=1}^{M-1}\sum_{j=i}^{M-1}\left\|\boldsymbol{P}_{\mathrm{RTT}}^{j+1} - \boldsymbol{P}_{\mathrm{RTT}}^{i}\right\|^{2} \tag{4-8}$$

where $\boldsymbol{x}$ represents the RTT bias, M indicates the collected Wi-Fi FTM based positioning results during the detected QS period using LS algorithm, the difference between each estimated location is cumulated to get the optimal bias value. The loss function in GD algorithm is described as:

$$L(\boldsymbol{x}) = (\boldsymbol{z} - h(\boldsymbol{x}))^{\mathrm{T}} R^{-1}(\boldsymbol{z} - h(\boldsymbol{x})) \tag{4-9}$$

Because the optimization model is not linear, Taylor series are applied to linearize the proposed model:

$$\begin{aligned}
\boldsymbol{z} &= h(\boldsymbol{x}) + \boldsymbol{v} \\
&= h(\boldsymbol{x}) + \left.\frac{dh(\boldsymbol{x})}{d\boldsymbol{x}}\right|_{\boldsymbol{x}=\boldsymbol{x}} (\boldsymbol{x} - \boldsymbol{x}) + \frac{1}{2!}\left.\frac{d^2 h(\boldsymbol{x})}{d\boldsymbol{x}^2}\right|_{\boldsymbol{x}=\boldsymbol{x}} (\boldsymbol{x} - \boldsymbol{x})^2 + \cdots + \boldsymbol{v} \\
&\approx h(\boldsymbol{x}) + \left.\frac{dh(\boldsymbol{x})}{d\boldsymbol{x}}\right|_{\boldsymbol{x}=\boldsymbol{x}} (\boldsymbol{x} - \boldsymbol{x}) + \boldsymbol{v} \\
&= h(\boldsymbol{x}) + \boldsymbol{H}\delta\boldsymbol{x} + \boldsymbol{v}
\end{aligned} \tag{4-10}$$

where $\delta\boldsymbol{x}$ represents the state estimation error, $\boldsymbol{H}$ indicates the Jacobian matrix. The difference between each iteration is described as follow:

$$\boldsymbol{z} - h(\boldsymbol{x}) = \boldsymbol{H}\delta\boldsymbol{x} + \boldsymbol{v} \tag{4-11}$$

Similar to the linear case derivation process, the result of the nonlinear least squares estimation is:

$$\delta\boldsymbol{x} = (\boldsymbol{H}^{\mathrm{T}}\boldsymbol{R}^{-1}\boldsymbol{H})^{-1}\boldsymbol{H}^{\mathrm{T}}\boldsymbol{R}^{-1}\delta\boldsymbol{z} \tag{4-12}$$

Non-linear least squares need to iterate the above process and stops when the state estimation error reaches the set threshold. In general, the nonlinear least squares update can be written as:

$$\boldsymbol{x}_{\gamma} = \boldsymbol{x}_{\gamma-1} + \delta\boldsymbol{x}_{\gamma-1} \tag{4-13}$$

where γ represents the number of iterations, and the optimal bias value can be acquired when $L(\boldsymbol{x})$ less than the set threshold.

4.2.3 Tightly-coupled Calibration and Localization Method

In order to estimate the RTT bias in dynamic scenes and realize the integrated localization at the same time, this paper proposes the TC based bias estimation and indoor localization algorithm, which provides a comprehensive solution by taking all the Wi-Fi FTM and MEMS sensors based location sources into consideration.

The state value in the proposed TC integration model contains two parts. The first part is the built-in sensors based error model, which can be described as:

$$\delta \dot{\boldsymbol{X}}_s = \boldsymbol{F}_s \delta \boldsymbol{X}_s + \boldsymbol{G}_s \varepsilon_s \tag{4-14}$$

where $\delta \boldsymbol{X}_s$ is consist of 15 dimensions state error, which is presented in [105], $\varepsilon_s = [\varepsilon_1 \cdots \varepsilon_{15}]$ indicates the error sources that comply the Gaussian distribution. $\boldsymbol{G}_s$ is the noise driven matrix with the rank of 15.

The second part is the Wi-Fi FTM bias based error model. In our work, the bias of Wi-Fi FTM is applied to compensate the differences between different kinds of smartphones and Wi-Fi APs, which is modeled as the random walk process:

$$\dot{b}_{\mathrm{RTT}} = \varepsilon_{b_{\mathrm{RTT}}} \tag{4-15}$$

where $\varepsilon_{b_{\mathrm{RTT}}}$ is the white noise. The RTT bias based error model is described as:

$$\delta \dot{\boldsymbol{X}}_W = \boldsymbol{F}_W \delta \boldsymbol{X}_W + \boldsymbol{G}_W \varepsilon_W \tag{4-16}$$

where $\delta \boldsymbol{X}_W = b_{\mathrm{RTT}}$, $\boldsymbol{F}_W = 0$, $\boldsymbol{G}_W = 1$, and $\varepsilon_W = \varepsilon_{b_{\mathrm{RTT}}}$.

The augmented form of TC calibration and localization state model is presented as:

$$\begin{bmatrix} \delta \dot{\boldsymbol{X}}_s \\ \delta \dot{\boldsymbol{X}}_W \end{bmatrix} = \begin{bmatrix} \boldsymbol{F}_s & 0 \\ 0 & \boldsymbol{F}_W \end{bmatrix} \begin{bmatrix} \delta \boldsymbol{X}_s \\ \delta \boldsymbol{X}_W \end{bmatrix} + \begin{bmatrix} \boldsymbol{G}_s & 0 \\ 0 & \boldsymbol{G}_W \end{bmatrix} \begin{bmatrix} \varepsilon_s \\ \varepsilon_W \end{bmatrix} \tag{4-17}$$

The observation value is this work contains four parts. The first part is the zero-velocity update (ZUPT) and zero angular rate update (ZARU), which is applied in order to eliminate the cumulative error of speed and attitude estimation in case of QS periods detected, the detailed presentation of ZUPT/ZARU can be refer by [51]. The second part is the pedestrian based step recognition and step-length calculation, which are applied to constrain the fast divergence error of INS mechanization and can be refer from [24]. The third part is the QSMF based constraint, which is served as the absolute reference and decrease the cumulative error of gyroscope based heading estimation in complex indoor environments, which can be refer from [45].

This model focuses on the fourth part of the observation. In case of Wi-Fi FTM covered indoor environments, the observed ranging model can be described as:

$$\delta \boldsymbol{Z} = \begin{bmatrix} \delta \boldsymbol{z}_{1,range} \\ \delta \boldsymbol{z}_{2,range} \\ \vdots \\ \delta \boldsymbol{z}_{m,range} \end{bmatrix} = \begin{bmatrix} d_{MEMS,1} - d_{FTM,1} \\ d_{MEMS,2} - d_{FTM,2} \\ \vdots \\ d_{MEMS,m} - d_{FTM,m} \end{bmatrix} \tag{4-18}$$

where $\delta \boldsymbol{z}_{m,range}$ indicates the ranging difference between Wi-Fi FTM and MEMS sensors based ranging estimation; The MEMS sensors based ranging $d_{MEMS,m}$ is described as follow:

$$d_{MEMS,m} = \sqrt{(E^k_{MEMS} - P^E_m)^2 + (N^k_{MEMS} - P^N_m)^2} \tag{4-19}$$

where($E^k{}_{MEMS}$, $N^k{}_{MEMS}$) indicates the MEMS sensors based localization result, ($P_m{}^E$, $P_m{}^N$) represents the location of the m^{st} Wi-Fi AP.

The raw measured RTT value contains bias factor acquired from m^{th} Wi-Fi AP is calculated by:

$$d_{FTM,m} = L_{raw} - b_{RTT} - v_{RTT} \tag{4-20}$$

Finally, the TC calibration and localization model is presented as:

$$\delta \boldsymbol{Z} = \boldsymbol{H} \delta \boldsymbol{X} + \xi \tag{4-21}$$

where $\delta \boldsymbol{Z}$ and $\delta \boldsymbol{X}$ are given in equation (4-20) and (4-21), ξ indicates the measurement noise, $\boldsymbol{H}$ is the design matrix.

4.3 Crowdsourced Wi-Fi Fingerprinting Based Positioning System

In this section, a comprehensive structure for crowdsourced trajectories modelling, pre-calibration, optimization, and classification. In which the collected crowdsourced trajectory is modeled as a non-linear function contains the extracted landmarks, heading and step-length information, and the raw trajectory is matched with the reference vector for pre-calibration. In addition, an iterative extended Kalman filter (iEKF) is proposed for robust trajectory optimization to further improve the accuracy of pre-calibrated trajectory, and the optimized trajectories are finally classified into similar groups. Besides, a novel multi-layer perceptron (MLP) network which can autonomously evaluate the positioning error of optimized trajectories during each step period based on the extracted motion features. To construct an accurate and efficient crowdsourced Wi-Fi fingerprinting database, the evaluated trajectories in same similar group are further segmented and merged according to the detected turning points information, and the final crowdsourced Wi-Fi fingerprinting database is reconstructed using the turning/landmark points generated collection points to reduce the dimension and complexity.

4.3.1 Crowdsourced Trajectories Pre-calibration and Optimization

In the off-line phase of navigation database construction, the raw data of crowdsourced trajectories are consist of the PINS structure originated heading and location increment proposed in Chapter Three, and the each collected crowdsourced trajectory can be modeled as:

$$\boldsymbol{Loc}(t) = \begin{bmatrix} Pos_0^x \\ Pos_0^y \end{bmatrix} + \sum_{t=1}^{n} \begin{bmatrix} L_t \cdot \cos(\theta_t) \\ L_t \cdot \sin(\theta_t) \end{bmatrix} \tag{4-22}$$

where $\boldsymbol{Loc}(t)$ indicates the current location of the pedestrian, Pos_0^x and Pos_0^y represent the first detected reference point which is regarded as the start point. L_t and θ_t are the calculated step-length and heading at each step period.

Due to the positioning mechanism of dead reckoning (DR) based method, the accuracy of raw trajectory decreases with time. Besides, the single DR approach can only provide relative position information, thus, to select a comprehensively reliable trajectory, two reference landmark points are required in each independent trajectory.

When the second landmark point is detected, raw trajectory is matched with the reference vector for pre-calibration in order to decrease the effects of initial heading error and installation error caused by the handheld mode of the pedestrian, which is described in Figure 4-3:

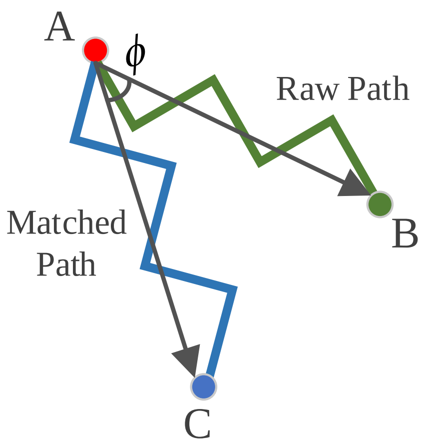

Figure 4-3 Trajectory Pre-calibration Procedure

In Figure 4-3, A and C indicate two detected reference points, which are constructed as a reference vector. The point B is the end point of the raw path, the raw vector can be constructed using the points A and B. Thus, the raw path can be pre-calibrated by rotating and scaling based on the comparison of the raw vector and the reference vector:

$$\begin{aligned}\overrightarrow{AC_i} &= \overrightarrow{AB_i} \cdot \boldsymbol{P}_r \cdot \boldsymbol{C}_s \\ &= \overrightarrow{AB_i}\begin{bmatrix}\cos(\phi) & -\sin(\phi) \\ \sin(\phi) & \cos(\phi)\end{bmatrix}\begin{bmatrix}S_x & 0 \\ 0 & S_y\end{bmatrix}\end{aligned} \tag{4-23}$$

where $\overrightarrow{AB_i}$ indicates the 2D location coordinates extracted from raw trajectory and $\overrightarrow{AC_i}$ is the pre-calibrated 2D location coordinates. ϕ represents the rotation angle, and S_x, S_x indicate the scale parameters of *x* and *y* axis.

To further eliminate the cumulative error of step-length calculation and heading estimation, the pre-calibrated trajectory which contains two reference points is modeled as an optimization problem, an iterative extended Kalman filter (iEKF) is proposed for robust trajectory optimization. To comprehensively express the whole trajectory, the state vector of iEKF is constructed as:

$$\boldsymbol{x}(t) = \begin{bmatrix} L_t^1, L_t^2, ..., L_t^k \\ \theta_t^1, \theta_t^2, ..., \theta_t^k \end{bmatrix} \tag{4-24}$$

1) State model prediction based on the acquired step-length and heading information:

$$\begin{aligned}\boldsymbol{x}_t^- &= f(\boldsymbol{x}_{t-1}) \\ &= \begin{bmatrix} Pos_0^x \\ Pos_0^y \end{bmatrix} + \sum_{k=1}^{n} \begin{bmatrix} L_t^k \cdot \cos(\theta_t^k) \\ L_t^k \cdot \sin(\theta_t^k) \end{bmatrix}\end{aligned} \tag{4-25}$$

2) State function linearization by the first-order Taylor series to get the linearized state matrix:

$$\begin{aligned}\boldsymbol{F}_t &= \frac{\partial f(\boldsymbol{x}_t)}{\partial \boldsymbol{x}_t}\Big|_{x_t = x_t^-} \\ &= \begin{bmatrix} \cos(\theta_t^1) & \cos(\theta_t^2) & \cdots & \cos(\theta_t^k) \\ L_t^k \cdot \sin(\theta_t^k) & L_t^k \cdot \sin(\theta_t^k) & \cdots & L_t^k \cdot \sin(\theta_t^k) \end{bmatrix}\end{aligned} \tag{4-26}$$

2) Covariance matrix prediction:

$$\boldsymbol{P}_t^- = \boldsymbol{F}_{t,t-1} \boldsymbol{P}_{t-1} \boldsymbol{F}_{t,t-1}^T + \boldsymbol{Q}_t \tag{4-27}$$

4) Kalman gain matrix update:

$$\boldsymbol{K}_t = \boldsymbol{P}_t^- \boldsymbol{H}_t^{\mathrm{T}} \left[\boldsymbol{H}_t \boldsymbol{P}_t^- \boldsymbol{H}_t^{\mathrm{T}} + \boldsymbol{R}_t \right]^{-1} \tag{4-28}$$

5) State vector update:

$$\boldsymbol{x}_t = \boldsymbol{x}_t^- + \boldsymbol{K}_t\left[\boldsymbol{z}_t - \boldsymbol{H}_t\boldsymbol{x}_t^-\right] \tag{4-29}$$

6) Covariance matrix update.

$$\boldsymbol{P}_t = \boldsymbol{P}_t^- - \boldsymbol{K}_t\boldsymbol{H}_t\boldsymbol{P}_t^- \tag{4-30}$$

After completing each round of iEKF iteration, the calculated Kalman gain is extracted to evaluate the degree of convergence, the whole procedure of iEKF will stop if the value of Kalman gain reaches the set threshold.

4.3.2 Deep Learning Based Uncertainty Prediction of Crowdsourced Trajectories

When the optimal reconstructed trajectory is acquired, the accuracy evaluation is required for further trajectory merging. In this work, MLP [126] based evaluation framework is proposed to predict the accuracy of optimized trajectory using only motion features extracted from the optimized trajectory. Considering various factors which would affect the accuracy of optimized trajectory, the non-linear mapping relationship can be established between extracted features and positioning error at each step period, which include:

1) Estimated step-length L_t at each step period.

2) Calculated heading information θ_t at each step period.

3) Cumulative number of steps ζ_t at the current moment.

4) Cumulative change in heading, which can be described as:

$$\Delta\psi(t) = \sum_{t=1}^{n}\sqrt{\left|\theta_t^2 - \theta_{t\text{-}1}^2\right|} \tag{4-31}$$

where $\Delta\psi(t)$ indicates the cumulated heading difference, θ_t is the real-time heading information.

5) Percentage of progress on distance:

$$p_d(t) = \frac{\sum_{t=1}^{k} L_t}{\sum_{t=1}^{n} L_t} \tag{4-32}$$

where n indicates the total step number of the selected trajectory, k is the current step number.

6) Percentage of progress on time:

$$p_t(t) = T(t) / T_{total} \tag{4-33}$$

where T_{total} indicates the total time of the selected trajectory $T(t)$ is the spent time at current step.

7) Percentage of progress on step number:

$$p_s(t) = step(t) / step_{total} \tag{4-34}$$

where $step_{total}$ indicates the total step number of the selected trajectory, $step(t)$ is the spent step number at current time.

The above extracted motion features can effectively describe the performance of selected optimized trajectory, and these features are further modelled as the input vector of proposed MLP based network, the detailed structure of proposed MLP is shown in Figure 4-4:

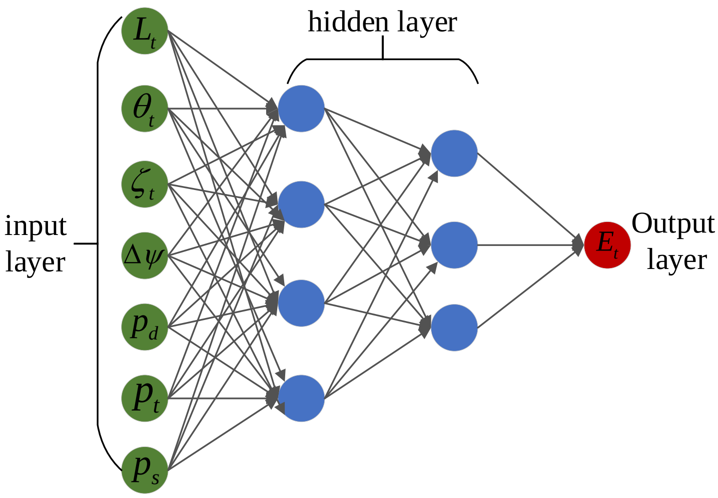

Figure 4-4 Framework of Proposed MLP Network

The loss function of proposed MLP is described as:

$$C(\boldsymbol{\omega}, \boldsymbol{b}) = \frac{1}{2n} \sum_{x} \left\| y(\boldsymbol{x}) - \alpha \right\|^2 \tag{4-35}$$

where the $\boldsymbol{\omega}$ and $\boldsymbol{b}$ indicate the weight values and biases, $\boldsymbol{x}$ represents the input vector, $y(\boldsymbol{x})$ is the trained result of each epoch. The stochastic gradient descent (SGD) algorithm [127] is adopted to in the procedure of MLP training phase in this work:

$$\begin{cases} \omega_k \to \omega_k = \omega_k - \dfrac{\eta}{m}\sum_j \dfrac{\partial C_{\boldsymbol{x}_j}}{\partial \boldsymbol{\omega}_k} \\ b_l \to b_l = b_l - \dfrac{\eta}{m}\sum_j \dfrac{\partial C_{\boldsymbol{x}_j}}{\partial \boldsymbol{b}_l} \end{cases} \tag{4-36}$$

where the η indicates the learning rate of SGD. The optimal weight values and biases can be acquired when the loss function gradually converges to the expected result.

4.3.3 Crowdsourced Trajectories Segmentation and Merging

In this part, the crowdsourced navigation database is generated based on the error evaluation result of crowdsourced trajectories. Due to the difference between pedestrians' motion mode, step error, instability heading biases and other factors, even the positioning results of the same walking route are significant different from each other. To solve this problem, multi-level constraints are applied for trajectories selection, partition, and merging for the final crowdsourced navigation database construction.

1) Crowdsourced trajectories pre-selection: Due to the changeable motion modes, cumulative error of DR, requirement of landmark points, not all the collected trajectories can be used for database construction. In this work, three indexes are applied for selecting the eligible trajectories. Firstly, at least two landmark points are required in each selected trajectory for optimization purpose. Secondly, the navigation time between each two detected landmark points should less than 2 min to maintain the positioning accuracy [88]. Thirdly, the trajectory contains complex handheld modes and intense movements is not suitable for database construction. In this work, we use an enhanced F-score index to evaluate the influenced degree of motion modes and handheld modes during each collected crowdsourced trajectory [128]:

$$G = \frac{\gamma_b}{(\gamma_b + \mu_b)} \tag{4-37}$$

$$M = \frac{r_h}{(r_h + \varsigma_h)} \tag{4-38}$$

$$F = \frac{2\times(1-G)\times(1-M)}{(1-G)+(1-M)} \tag{4-39}$$

where γ_b represents the recorded step count which follows the forward-walking motion; μ_b indicates the recorded step count does not follow the forward-walking motion; r_h is the recorded step count that consistent with the reading handheld mode; ς_h is the recorded step count which is not consistent with the reading handheld mode, and F is the calculated F-score which varies between 0 and 1. The larger the value of F, and the higher the credibility of the trajectory.

2) Detection of the pedestrian's motion modes: two pedestrian's walking modes in this work are extracted, including the walking straight forward and turning, and the modulus of gyroscope output is used:

$$Norm_{gyro}(t) = \sqrt{g_x{}^2 + g_y{}^2 + g_z{}^2} \tag{4-40}$$

where g_x, g_y, and g_z indicate the collected angular velocity of each axis. The turning point is detected based on the peak detection of modulus of gyroscope output, similar to the step detection procedure. The detected straight forward mode and turning point are further combined as the reference for crowdsourced trajectory partition and merging, and navigation database construction.

3) Trajectory partition based on the results of motion modes detection and trajectories classification: In our work, each of selected trajectory is divided into fragments with a straight line and two turning points, which is shown in Figure 4-5:

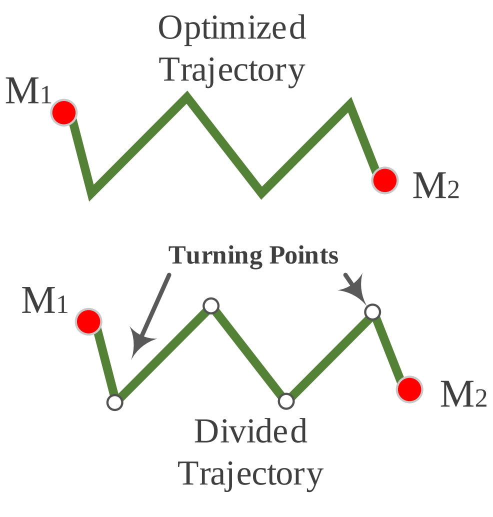

Figure 4-5 Illustration of Trajectory Partition

The turning points of classified trajectories which have the same walking route are extracted, and the uncertainty error of each turning point is provided by the proposed MLP based evaluation model. The eligible turning points extracted from crowdsourced trajectories follow the same walking route are weighted to get reference turning point set. Suppose that each walking route contains k turning points, each of detected turning point is weighted by the N different trajectories:

$$\boldsymbol{r}^k_{turning} = \sum_{i=1}^{N} \frac{E_i^k \cdot \boldsymbol{P}_i^k}{\sum_{i=1}^{N} E_i^k} \tag{4-41}$$

where $\boldsymbol{r}^k_{turning}$ indicates the weighted result of k^{th} turning point, and $\boldsymbol{P}_i^k$ represents the turning point extracted from the i^{th} trajectory, and E_i^k is the corresponding predicted location error.

4) Crowdsourced trajectories classification: this work firstly extracts trajectories with the same walking route and reference points for merging purpose. To recognize the trajectories using the same walking route, the correlation coefficient index and DTW index are applied to find the similar trajectories using the information detected turning points in each trajectory:

$$\begin{aligned} &DTW(\beta_{\tau-1}, \beta_\tau) \\ &= Dist(p_j, s_k) + \min[D(s_{j-1}, p_k), D(s_j, p_{k\text{-}1}), D(s_{j\text{-}1}, p_{k\text{-}1})] \end{aligned} \tag{4-42}$$

where $DTW(\delta_{\text{refer}}, \delta_k)$ presents the cumulative distance between two turning points distributions, $Dist(q_n, c_m)$ indicates the Euclidean distance between each two points of distributions.

$$\begin{aligned} &\rho_{cor}(x,y) = \rho_{cor}(x_{\tau\text{-}1}, x_\tau) + \rho_{cor}(y_{\tau\text{-}1}, y_\tau) \\ &= \frac{\sum_{i=1}^{M}\left(x_{\tau-1}^i - \overline{x_{\tau\text{-}1}}\right)\left(x_\tau^i - \overline{x_\tau}\right)}{\sqrt{\sum_{i=1}^{M}\left(x_{\tau-1}^i - \overline{x_{\tau\text{-}1}}\right)^2}\sqrt{\sum_{i=1}^{2m+1}\left(x_\tau^i - \overline{x_\tau}\right)^2}} \\ &+ \frac{\sum_{i=1}^{M}\left(y_{\tau-1}^i - \overline{y_{\tau\text{-}1}}\right)\left(y_\tau^i - \overline{y_\tau}\right)}{\sqrt{\sum_{i=1}^{M}\left(y_{\tau-1}^i - \overline{y_{\tau\text{-}1}}\right)^2}\sqrt{\sum_{i=1}^{2m+1}\left(y_\tau^i - \overline{y_\tau}\right)^2}} \end{aligned} \tag{4-43}$$

where $\rho_{cor}(x_{\tau\text{-}1}, x_\tau)$ and $\rho_{cor}(y_{\tau\text{-}1}, y_\tau)$ indicate the results of correlation coefficient on x and y axis, respectively. To get all the classification groups, the crowdsourced trajectories are compared and iterated, and the similar trajectories are classified and regarded as one group.

5) Trajectory partitions merging problem: The extracted and weighted turning points provide a robust reference locations for further optimizing the crowdsourced trajectory partitions. In this work, crowdsourced trajectories based on the same walking route are

firstly divided by the detected turning points, and then the trajectory partitions under the same route are modeled as a problem of searching the optimal vector of rotation and scaling in order to get the least distance between each bundle of trajectory partitions and the weighted turning points, which is similar as in [129]:

$$\left\{\boldsymbol{P}_{\text{opt}}, \boldsymbol{C}_{\text{opt}}\right\} = \arg\min_{\boldsymbol{P},\boldsymbol{C}}\ f(\boldsymbol{D}) \tag{4-44}$$

where $\boldsymbol{P}_{\text{opt}}$ and $\boldsymbol{C}_{\text{opt}}$ indicate the rotation matrix and scaling matrix, respectively. $f(\boldsymbol{D})$ represents the cumulated distance between turning points of each trajectory partition:

$$f(\boldsymbol{D}) = \sum_{i=1}^{N} \left| \boldsymbol{U}_k^i \cdot \boldsymbol{P}_{\text{opt}}^i \cdot \boldsymbol{C}_{\text{opt}}^i - \boldsymbol{r}_{turning}^k \right| \tag{4-45}$$

where $\boldsymbol{U}_k^i$ indicates the turning point extracted from the i^{st} trajectory partition, corresponding to the i^{st} reference turning point calculated by the equation (4-45). To get the convergent result of $f(\boldsymbol{D})$, the optimal $\left\{\boldsymbol{P}_{\text{opt}}, \boldsymbol{C}_{\text{opt}}\right\}$ group needs to be found.

We firstly calculate the optimal $\boldsymbol{P}_{\text{opt}}$ by iteration, each trajectory partition is rotated around its formal turning point $\boldsymbol{U}_k^i$:

$$T_k = \sum_{i=1}^{N} T_{i,k} = \sum_{i=1}^{N} \boldsymbol{F}_{i,k} \times (\boldsymbol{U}_k^i - \boldsymbol{r}_{turning}^k) \tag{4-46}$$

where $T_{i,k}$ indicates rotation related resultant moment, $\boldsymbol{F}_{i,k}$ is the force vector provided by the last $f(\boldsymbol{D})$.

The rotate angle of the j^{th} iteration for the k^{th} trajectory partition is calculated as:

$$\theta_k^j = \sum_{\mu=1}^{j} \Delta\theta_k^{\mu} = \sum_{\mu=1}^{N} \frac{\alpha T_k^j}{\sum_{l=1}^{M} \left| \boldsymbol{U}_{l.k}^j - \boldsymbol{r}_{turning}^k \right|^2} \tag{4-47}$$

where $\sum_{l=1}^{M} \left| \boldsymbol{U}_{l.k}^j - \boldsymbol{r}_{turning}^k \right|^2$ indicates the momentum of inertia. α is a constant scale parameter. Similarly, we can get the optimal scaling value by:

$$\boldsymbol{D}_k^j = \sum_{\mu=1}^{j} \Delta\boldsymbol{D}_k^{\mu} = \sum_{\mu=1}^{N} \frac{\alpha \boldsymbol{F}_k^j}{L_k} \tag{4-48}$$

where L_k indicates the total length of kth trajectory partition, $\Delta\boldsymbol{D}_k^{\mu} = (\Delta x_k^{\mu}, \Delta y_k^{\mu})$ represents the value of scaling adjustment of each iteration epoch. After acquiring the optimal $\left\{\boldsymbol{P}_{\text{opt}}, \boldsymbol{C}_{\text{opt}}\right\}$ group, the final adjusted trajectory partitions under same walking route are described as:

$$\boldsymbol{U}_{l.k}^{j} = \begin{bmatrix} \cos(\theta_k^j) & -\sin(\theta_k^j) \\ \sin(\theta_k^j) & \cos(\theta_k^j) \end{bmatrix} (\boldsymbol{U}_{l.k}^{0} - \boldsymbol{r}_{turning}^{k,0}) + \boldsymbol{D}_k^j \tag{4-49}$$

where $\boldsymbol{U}_{l.k}^{j}$ is optimized turning point of each trajectory partition under same route, after repeating the above optimization procedure, crowdsourced trajectory partitions can be adjusted and built up as the complete trajectories.

4.3.4 Crowdsourced Wi-Fi Fingerprinting Database Generation

The above steps provide a robust approach of crowdsourced trajectories pre-selection, classification, partition, and merging. The final constructed crowdsourced radio map is described as:

$$\mathbf{RadioMap} = \begin{pmatrix} \boldsymbol{P}_1^w & \mathbf{Array}_1^{RSSI} \\ \boldsymbol{P}_2^w & \mathbf{Array}_2^{RSSI} \\ \cdots & \cdots \\ \boldsymbol{P}_j^w & \mathbf{Array}_j^{RSSI} \end{pmatrix} \tag{4-50}$$

where j indicates the capacity of the final crowdsourced Wi-Fi fingerprinting database. $\boldsymbol{P}_j^w = (x_j, y_j, z_j)$ represents the location of each reference point in database, and $\mathbf{Array}_j^{RSSI}$ is the corresponding RSSI based vector.

The preliminary constructed crowdsourced radio map described in (4-50) contains a large amount of similar trajectories and is labor-consuming to further conduct the on-line phase by mobile terminal based platform. Thus, to decrease the complexity and dimension of preliminary constructed radio map, the collected RSSI fingerprinting points need to be further merged according to be performance of RSSI vector. The detailed procedure of RSSI merging is shown as follows:

1) Search trajectory partition group between the same two turning points or landmark points: The partition group contains various similar trajectories can be further merged according to the crowdsourced trajectories classification and partition results, which has been presented in the formulas introduced above.

2) Generate virtual reference Wi-Fi fingerprinting collection points using the adjacent turning/landmark points:

$$\begin{cases} \gamma_x^j = \boldsymbol{r}_{turning}^k(x) + \dfrac{\boldsymbol{r}_{turning}^{k+1}(x) - \boldsymbol{r}_{turning}^k(x)}{\text{floor}(\left|\boldsymbol{r}_{turning}^{k+1}(x) - \boldsymbol{r}_{turning}^k(x)\right| / \tau) + 1} \cdot i \\ \gamma_x^j = \boldsymbol{r}_{turning}^k(y) + \dfrac{\boldsymbol{r}_{turning}^{k+1}(y) - \boldsymbol{r}_{turning}^k(y)}{\text{floor}(\left|\boldsymbol{r}_{turning}^{k+1}(x) - \boldsymbol{r}_{turning}^k(x)\right| / \tau) + 1} \cdot i \\ st.\ \ i = 1, 2, ..., \text{floor}(\left|\boldsymbol{r}_{turning}^{k+1}(x) - \boldsymbol{r}_{turning}^k(x)\right| / \tau) \end{cases} \tag{4-51}$$

where $\boldsymbol{\gamma}_x^j$ and $\boldsymbol{\gamma}_y^j$ indicate autonomously generated Wi-Fi fingerprinting collection points, τ is the distance between two adjacent collection points. $\boldsymbol{r}_{turning}^k(x)$ and $\boldsymbol{r}_{turning}^k(x)$ represent the merged turning point in selected partition group. In this work, the generated Wi-Fi fingerprinting collection points are applied as the reference points to reduce the dimension of preliminary constructed radio map.

3) Radio map reconstruction from the preliminary result: After acquiring the generated collection points, the corresponding RSSI vector received from crowdsourced trajectories is weighted to provide a more stable and robust fingerprinting information. In this work, the fluctuation degree of received RSSI vector is applied as the weight of crowdsourced RSSI vectors searched by the same collection points:

$$\omega_j = \frac{\left|u_\beta\right|}{\sum_{\beta=1}^{N}\left|u_\beta\right|} \tag{4-52}$$

where u_β indicates the average RSSI value collected from one of the crowdsourced trajectories. In the fingerprinting merging phase, the RSSI vectors acquired common Wi-Fi APs in different trajectories searched by the same collection point are merged and reconstructed as the final radio map:

$$\mathbf{RadioMap_{new}} = \begin{pmatrix} \gamma_1^w & \mathbf{Array}_1^{RSSI} \\ \gamma_2^w & \mathbf{Array}_2^{RSSI} \\ \cdots & \cdots \\ \gamma_\kappa^w & \mathbf{Array}_\kappa^{RSSI} \end{pmatrix} \tag{4-53}$$

Compared with the preliminary constructed crowdsourced radio map, the final radio map effectively reduces the complexity and dimension of generated database, and also maintains the characteristics of Wi-Fi RSSI fingerprinting and the accuracy of matching phase.

4.4 Tests and Results

In this section, comprehensive experiments are organized to evaluate the performance of proposed Wi-Fi FTM based calibration and positioning system and crowdsourced Wi-Fi fingerprinting based positioning system. The Google Pixel 1, Google Pixel 2, Google Pixel 3 and Google Pixel 4 are used for pedestrian tracking which contains rich MEMS sensors and supports the Wi-Fi FTM protocol and also supports the typical Wi-Fi scanning. The sampling rates of low-cost sensors and Wi-Fi FTM, RSSI scanning are set as 50 Hz, 5 Hz, and 0.3 Hz, respectively. Different indoor environments are adopted as experimental sites, which contains comprehensive indoor scenes such as office scene, shopping mall, and corridor scene. The precision of proposed two Wi-Fi positioning systems are estimated according to the following arrangement: Section 4.4.1 evaluates the precision of Wi-Fi FTM based calibration and positioning system; Section 4.4.2 estimates the performance of crowdsourced trajectory optimization and error prediction; Section 4.4.3 estimates the performance of crowdsourced navigation database generation approach; Section 4.4.4 evaluates the overall performance of crowdsourced Wi-Fi fingerprinting based positioning system in large-scale indoor spaces.

4.4.1 Performance Evaluation of Wi-Fi FTM Based Calibration and Positioning Solution

We analyzed in Chapter Two that the initial clock deviation has been existed before FTM procedure which causes the initial ranging error. In order to analyze the relationship between initial clock deviation and types of Wi-Fi FTM responders and initiators, we choose the corridor with length of 50 m as the experimental scene. The responder and initiator were placed on the brackets respectively at the same height (0.8 m). We marked the ground truth distance in advance and then set 2 m as the measuring interval when the distance is shorter than 10 m, set 5 m as the measuring interval when distance is longer than 10 m, 2 Hz as sampling rate, measured for 10 min at each estimation point, collected RTT data from three different AP responders (Intel 8260, VIVO X21, VIVO NEX) with the same initiator (Intel 8260), the average result at each estimation point is shown in figure 4. Then we use two different kinds of initiators (Intel 8260 and Pixel 1) to collect RTT data from the same AP (Intel 8260), the average result at each estimation point is shown in Figure 4-6.

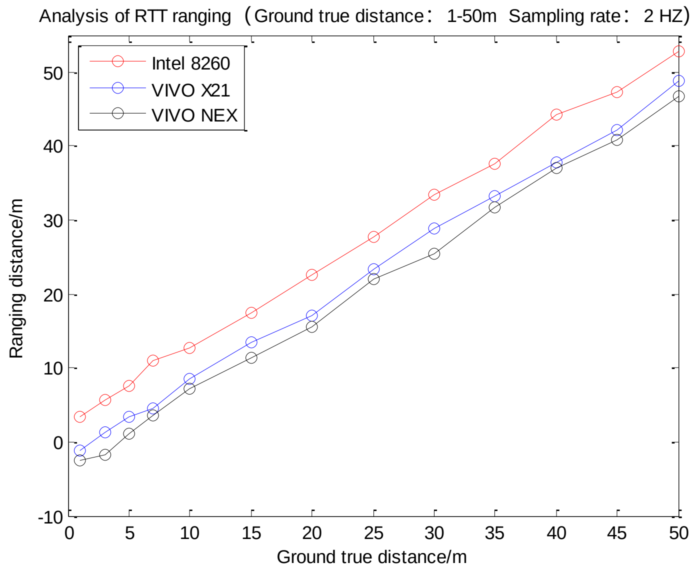

Figure 4-6 The Same Initiator with Three Different APs

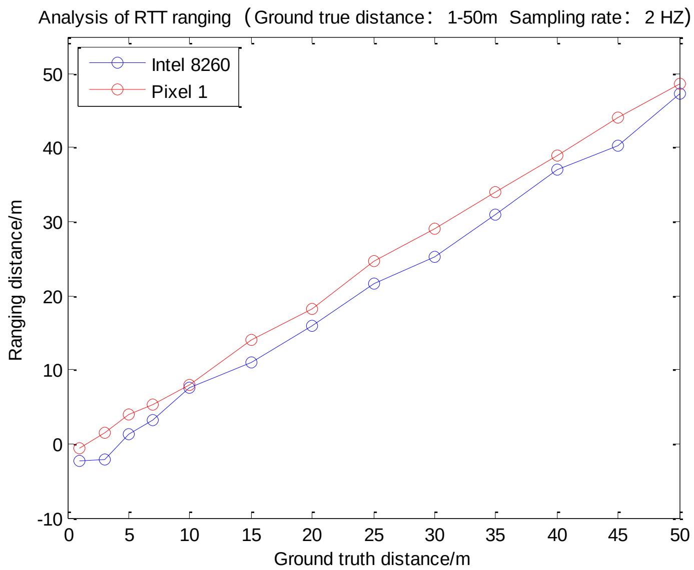

Figure 4-7 Same AP with Two Different Initiators

It can be found by comparing Figure 4-6 and Figure 4-7 that the initial clock deviation is influenced by both initiator and responder, thus, calibration is needed before ranging.

We firstly calibrate the initial clock deviation using the PB calibration algorithm. A playground was chosen as the calibration scene which is shown in Figure 4-8 where we can minimize the multipath effect. We choose the length of 50 m as the effective measurement range, set different calibration interval as mentioned above, set sampling rate as 2 Hz, collected RTT data from AP responder with 2.4 GHz frequency and 20 MHz bandwidth. Each group of data was collected for 10 min. Ranging bias of each group can be calculated by subtracting the true distance with the average ranging distance. After removing the maximum and minimum deviation of bias, we choose average bias of remaining data as the initial clock deviation of RTT, take into the raw data of ranging bias, result is show in Figure 4-8:

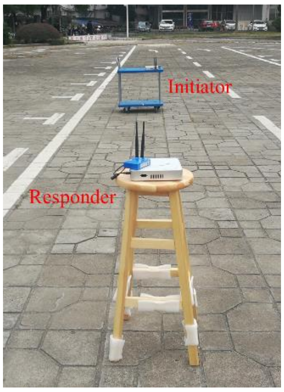

Figure 4-8 Wi-Fi FTM Calibration Field

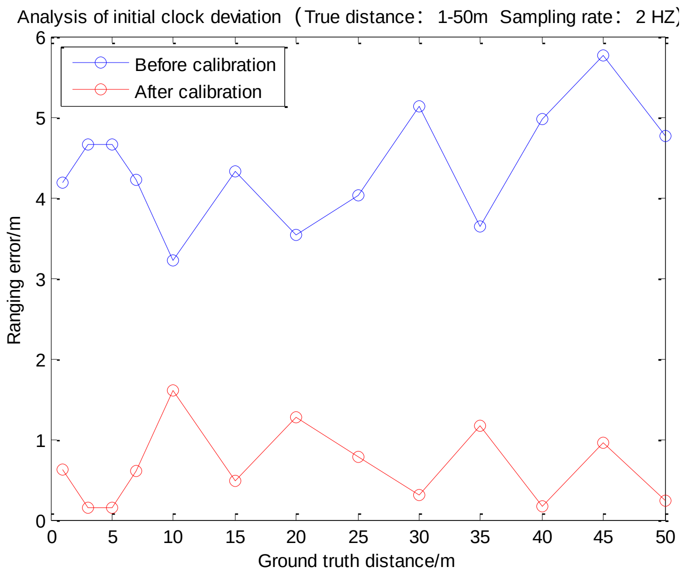

Figure 4-9 Error Comparison before and after calibration

It can be found in Figure 4-9 that initial clock deviation has been effectively corrected after calibration, we also find that with longer ranging distance, accuracy of RTT signal does not decline in the case of LOS due to its measuring mechanization. However, several factors such as bandwidth, frequency and hardware condition can affect the initial clock deviation of Wi-Fi FTM. Therefore, when changing parameters of the AP responder or initiator, the same calibration procedure should be made. We compared several APs with different chipsets, bandwidth and frequency, as shown in Table 4-2:

Table 4-2 Influence of Different Factors on Ranging Bias

AP Category	20 MHz(2.4 G)	40 MHz(2.4 G)	40 MHz(5 G)	80 MHz(5 G)
Wi-Fi card A	-6.21 m	-4.56 m	Not supported	Not supported
Wi-Fi card B	Not supported	Not supported	-1.74 m	-1.07 m
Mobile Phone 1	-1.86 m	Not supported	Not supported	Not supported
Mobile Phone 2	-1.35 m	Not supported	Not supported	Not supported

Then we evaluated the accuracy and stability of the calibrated data collected from Wi-Fi card A and Wi-Fi card B and another Wi-Fi card A was used as the initiator. We used the same calibration interval than in Figure 4-9 and got the calibrated ranging results shown in Figure 4-10:

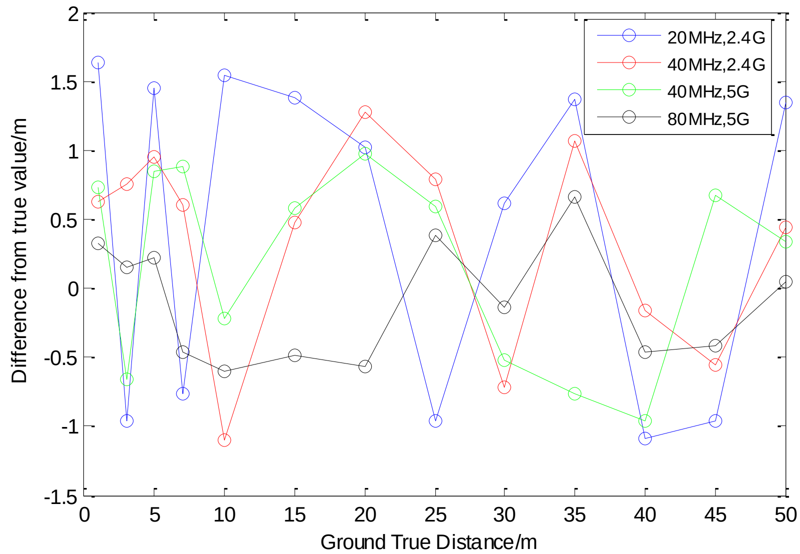

Figure 4-10 Comparison of Ranging Errors

It can be found in Figure 4-10 that the results of Wi-Fi FTM show higher accuracy and stability when using frequency and bandwidth with 5 GHz and 80 MHz. Meter-level ranging precision is realized in case of 5 GHz, 80 MHz.

Then we applied different mobile terminals Google Pixel 1 to 4 as the evaluation platforms. The result of PB calibration algorithm has been presented in Figure 4-9. The proposed GD based calibration algorithm realizes RTT bias estimation in case of QS periods detected. In this work, 50 pairs of Wi-Fi RTT values in a time period of 10s are collected for GD based bias calibration, and the final number of iterations γ and optimized RTT bias θ are presented in Table 4-3:

Table 4-3 Iteration Number and Optimized Bias

Parameter	Pixel 1	Pixel 2	Pixel 3	Pixel 4
γ	21	25	19	23
θ	-1.16 m	-1.09m	-1.03m	-1.15m

It can be found from Table 4-3 that the proposed GD algorithm proves high efficiency of bias calibration, the number of iterations is not larger than 25 by different kinds of smartphones.

In TC calibration algorithm, the Wi-Fi RTT bias is estimated in real-time. To estimate the overall precision, the pedestrian remains static in the first 10s, and starts walking for the next 40s, and remain static for the last 10s. The RTT bias estimation results are described in Figure 4-11:

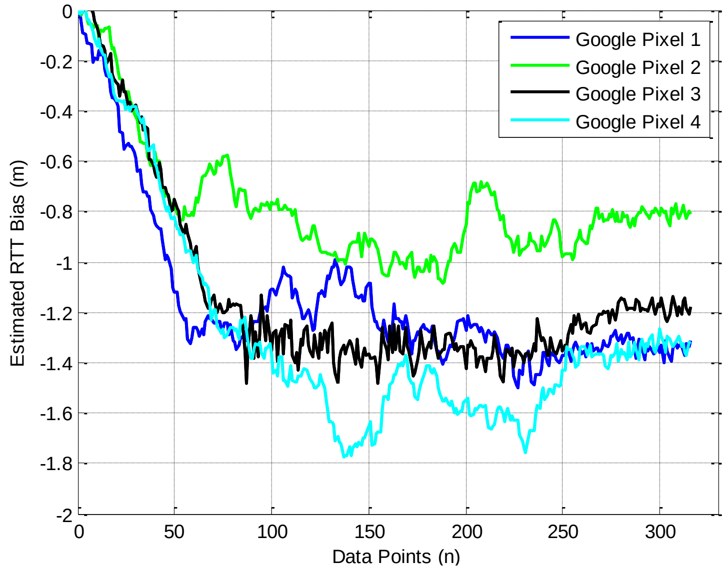

Figure 4-11 Tightly-coupled Calibration Results

It can be found from Figure 4-11 that the RTT bias reaches the optimal estimation result when the pedestrian remains static, and the estimation result fluctuates when the pedestrian begins walking because of the changeable environmental effects in the procedure of the pedestrian's walking period.

To further estimate the indoor positioning precision of proposed calibration strategies and multi-source integration model, a typical office scene is chosen as the experimental site, and four Wi-Fi FTM supported APs are deployed in corners of the office, which are shown in Figure 4-12:

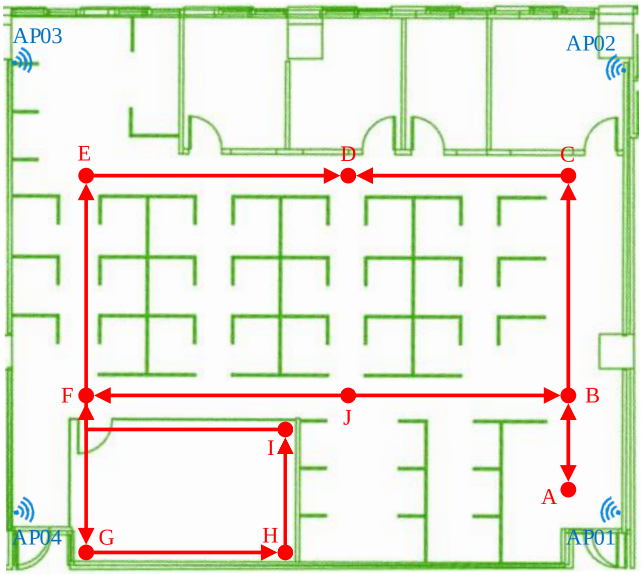

Figure 4-12 Experimental Site and Test Route

To be fair, the three calibration algorithms are evaluated using the same integration model described in equation (14) and (18). In this case, the PB calibration result is applied directly into the collected RTT values, and the GD based calibration result is applied after the initial QS period of 10s, and the TC calibration result is feedback in real-time. The tester started at point A, passed the points B, C, D, E, F, G, H, I, J, B, and returned to the point A. The indoor localization performance using three different calibration strategies is shown in Figure 4-13:

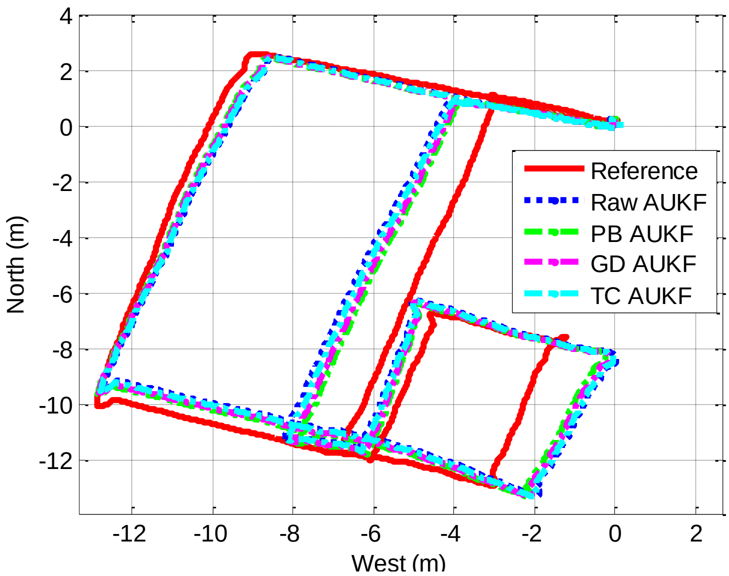

Figure 4-13 Performance of Proposed Calibration Strategies

To evaluate the positioning accuracy of proposed calibration strategies, 12 volunteers walk through the same route shown in Figure 4-12, and different types of Google Pixels are hold respectively. The real-time positioning accuracy is evaluated when the pedestrian passed the test points B, C, D, E, F, G, H, J. The final comparison of localization accuracy between different calibration algorithms is shown in Figure 4-14:

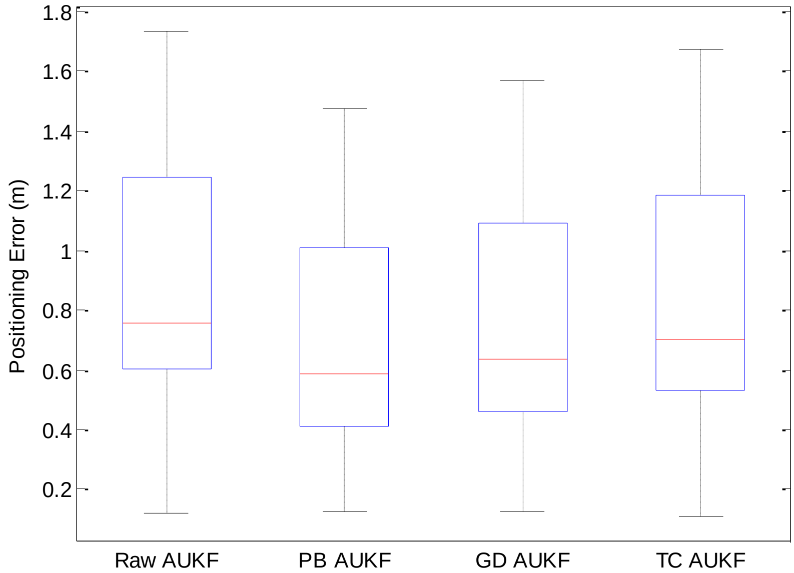

Figure 4-14 Positioning Errors of Proposed Calibration Strategies

It can be found from Figure 4-14 that the built-in sensors based positioning methods exists cumulative error even the integration model has been applied, and the combination of Wi-Fi FTM significantly improves the performance of final indoor localization of raw AUKF, which is within 1.25 m in 75%. In addition, the proposed three RTT bias calibration algorithms further improves the positioning accuracy. The PB AUKF proves the best localization performance, and the positioning error reaches the 1.01 m in 75%. The accuracy of GD AUKF is a little higher than TC AUKF, and the positioning errors of two algorithms are 1.09 m and 1.19 m in 75%, respectively.

4.4.2 Performance Evaluation of Crowdsourced Trajectory Optimization and Uncertainty Prediction

This work enhances the raw crowdsourced trajectories by pre-calibration and iEKF based optimization, which effectively improve the performance of collected trajectories, and then a novel MLP based trajectory error prediction framework is applied to evaluate the positioning error of the trajectory at each step. The tester firstly walked through an indoor trajectory for about 2min, and the comparison between raw trajectory, pre-calibrated trajectory, and optimized trajectory is compared in Figure 4-15:

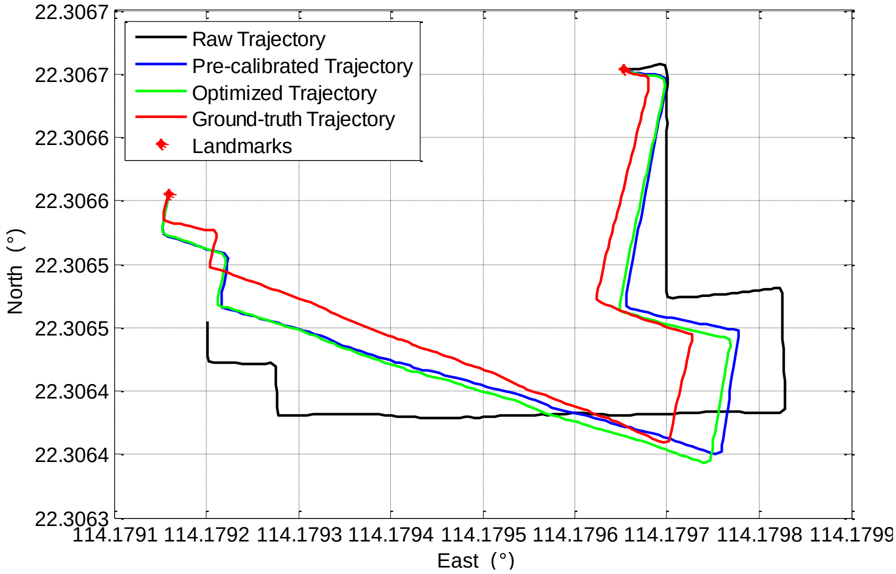

Figure 4-15 Comparison of Pre-calibration and Optimization Trajectories

Figure 4-15 presents that the proposed pre-calibration and optimization framework effectively improves the accuracy of raw trajectory, the positioning errors are calculated by comparing with the ground-truth trajectory:

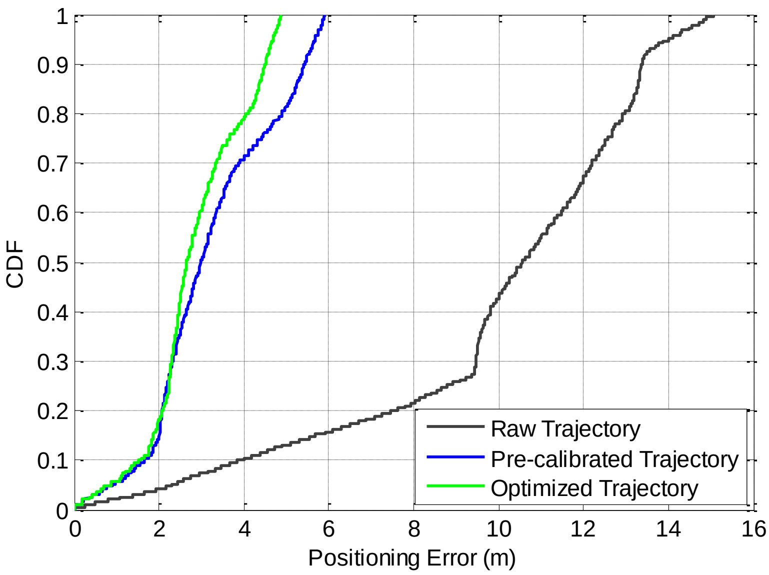

Figure 4-16 CDF Errors Comparison

It can be found from Figure 4-16 that the proposed pre-calibration approach significantly decreases the positioning error of raw trajectory from 12.57 m in 75% to 4.41 m in 75%, and the optimization algorithm further improve the performance of pre-calibration from 4.41 m in 75% to 3.67 m in 75%. Due to the effect of cumulative error, the performance of optimized trajectory needs to be evaluated by the proposed MLP based error prediction model, which can provide a robust error reference for the further trajectory merging phase.

The training dataset of proposed MLP in this case is provided by the number of 30 daily-life trajectories provided by the IPIN-2018 indoor competition, track 3 [130], which are learned by the MLP and the trained model is applied for error prediction of optimized trajectories with two landmark points. The constructed input vector contains extracted features are applied to train the MLP model and the training phase completed when the value of loss function is convergent. The training phase of MLP model is shown in Figure 4-17:

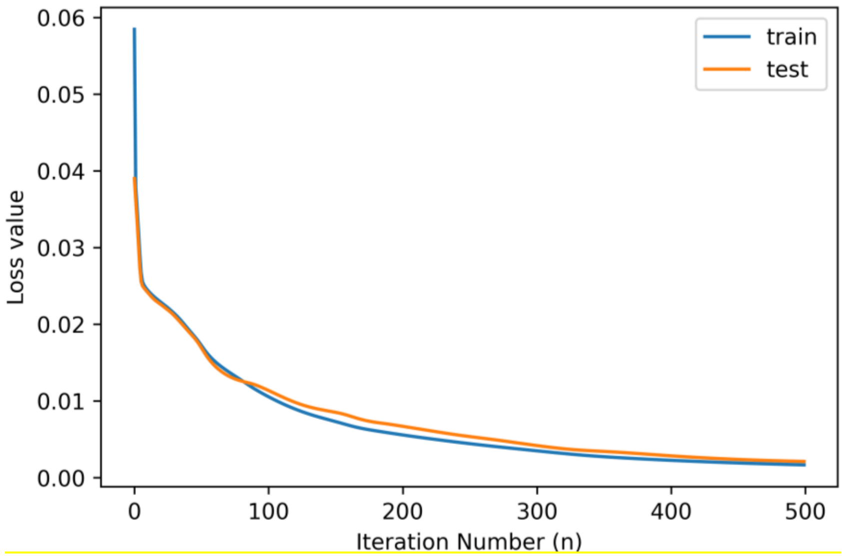

Figure 4-17 Training Phase of MLP Model

Figure 4-17 presents that the MLP model reaches the convergent status after 500 iterations. The performance of error prediction of optimized trajectory in Figure 4-15 is further predicted by the trained MLP model, and the predicted positioning error during each step period and the prediction error of total trajectory is described in Figure 4-18:

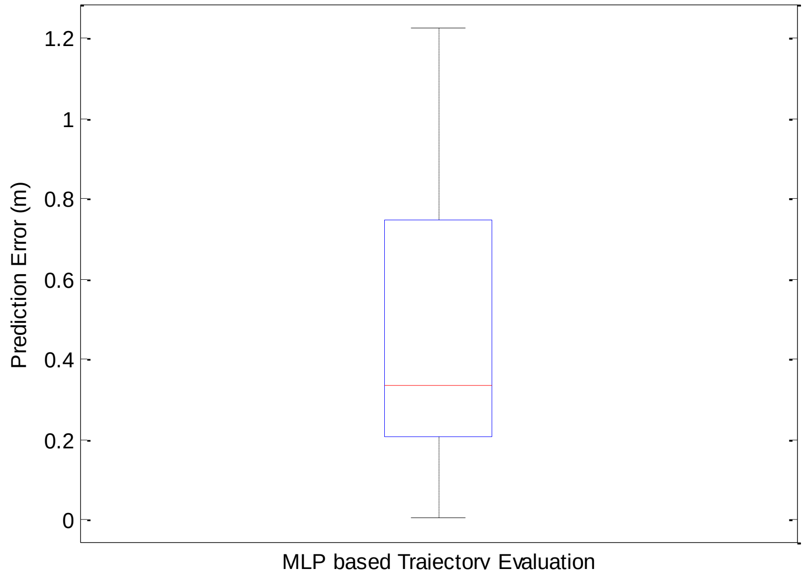

Figure 4-18 Performance of Trajectory Error Prediction

Figure 4-18 shown that the accuracy of proposed MLP based trajectory error prediction reaches 0.75 m in case of 75%. The results of error prediction are further applied for crowdsourced navigation generation.

4.4.3 Performance Evaluation of Crowdsourced Wi-Fi Fingerprinting Database Generation

In order to generate a robust and unified navigation database, the collected crowdsourced trajectories are pre-selected, separated, classified and merged. The selected trajectory in Figure 4-15 is separated by the detected turning points and forward walking periods, which is shown in Figure 4-19:

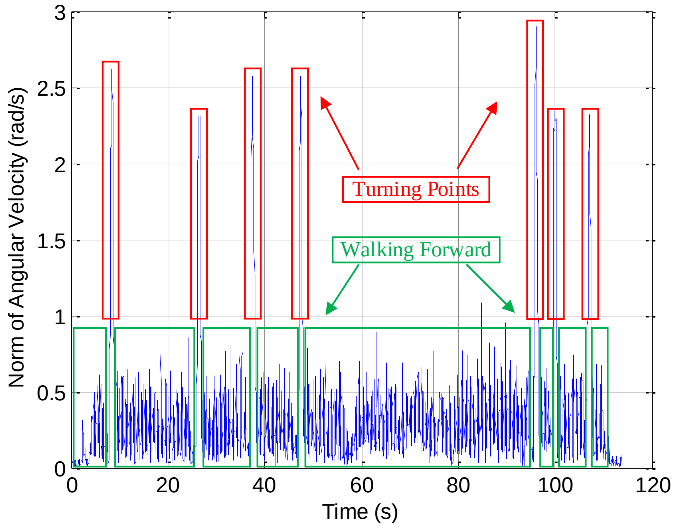

Figure 4-19 Predicted Error of Collected Trajectory

It can be found from Figure 4-19 that the trajectory is accurately separated into the combination of forward walking periods and turning points. After the separation of crowdsourced trajectories, the extracted turning points and landmarks points of each trajectory are modeled as a unified vector, and the values of DTW and correlation coefficient are further used for trajectories classification, the result of one of the classification iterations is show in Figure 4-20:

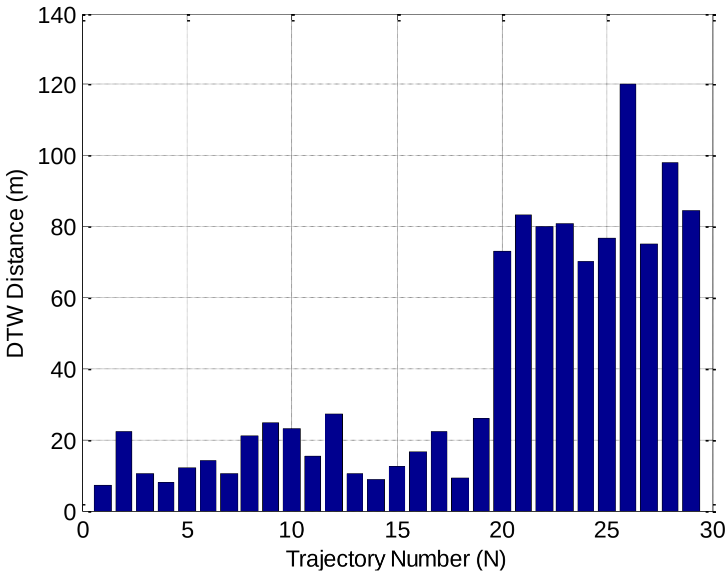

Figure 4-20 DTW Result of Classification Iteration

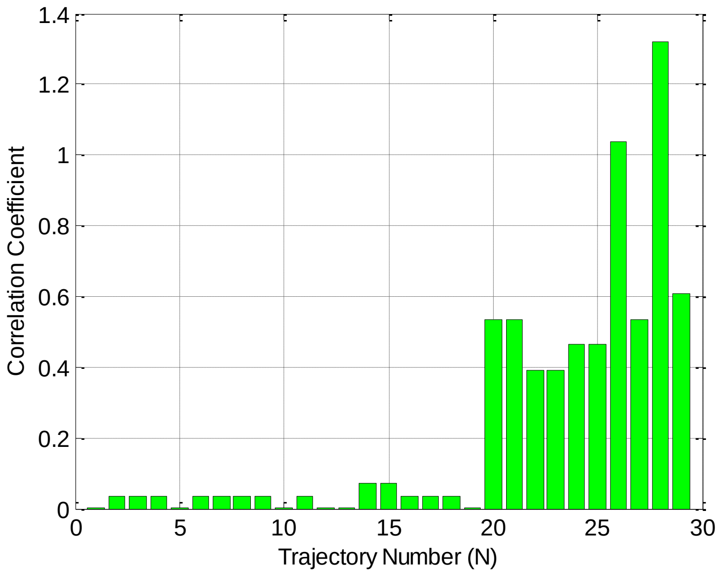

Figure 4-21 Correlation Coefficient Result of Classification Iteration

Figure 4-20 and Figure 4-21 presents that one similar group can be effectively found after the comparison of DTW and correlation coefficient indexes. In Figure 4-20, the trajectories which DTW distance lower than 30 m and the correlation coefficient lower than 0.1 are classified into the same group.

After the classification phase, each group contains similar trajectories are merged to further improve the performance of crowdsourced trajectories. Firstly, turning points belong to the same point are weighted to get the reference location of merged turning point according to the error prediction results of MLP model, and then partitions extracted from each trajectory are merged and adjusted based on the calculated turning points. The performance of trajectory partitions merging is described in Figure 4-22 and Figure 4-23:

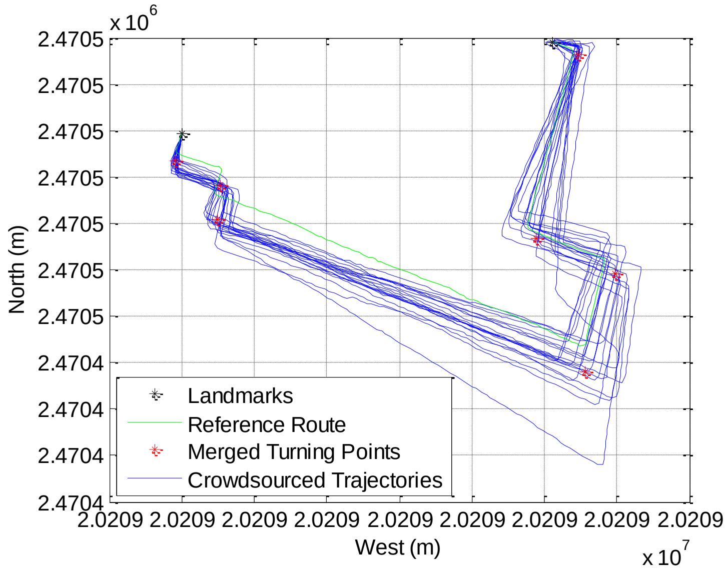

Figure 4-22 Result of Turning Points Merging

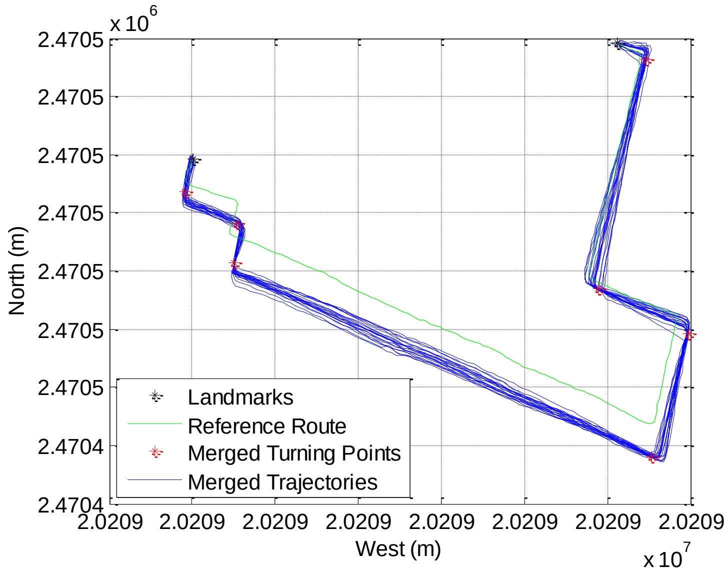

Figure 4-23 Result of Crowdsourced Trajectories Merging

Figure 4-22 and Figure 4-23 present that the merged trajectories further improve the performance of crowdsourced data. The abnormal trajectories have been revised and the trajectory group becomes more compact. In order to generate a more comprehensive and wide-covered wireless navigation database, more crowdsourced trajectories are collected, classified, and merged. The final constructed trajectory based pathway information is shown in Figure 4-24:

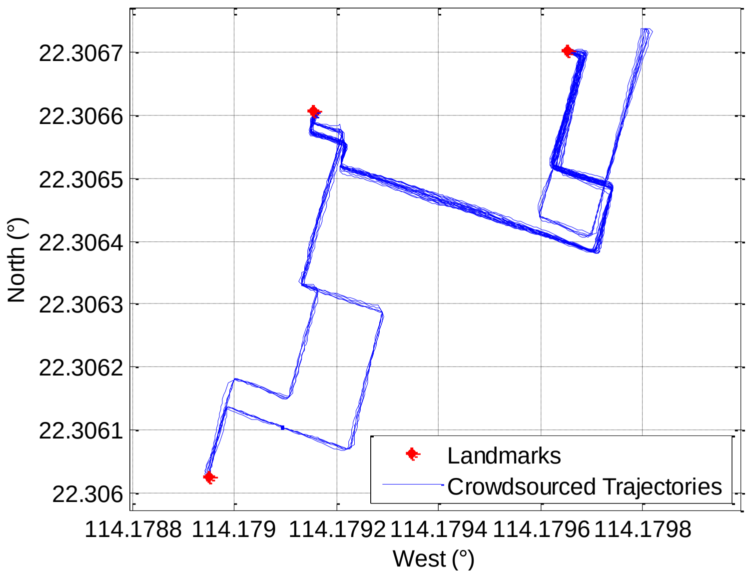

Figure 4-24 Performance of Trajectory Merging Phase

The trajectory error comparison before and after trajectory merging phase is shown in Figure 4-25:

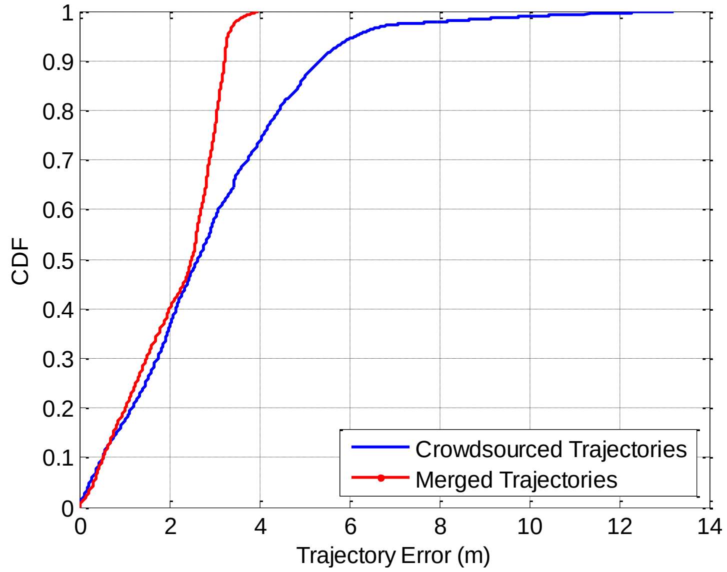

Figure 4-25 Accuracy Comparison of Trajectory Merging

It can be found from Figure 4-25 that the merged crowdsourced trajectories prove much high overall positioning accuracy within 2.99 m in 75%, compared with optimized crowdsourced trajectories within 4.09 m in 75%, and the information of merged trajectories finally applied for crowdsourced navigation database generation. In this work, the positioning performance of constructed Wi-Fi fingerprinting database is compared with state-of-art crowdsourced navigation database generation methods: quality assessment criteria (QAC) proposed in [60], trace matching (TM) algorithm proposed in [131] and our crowdsourced trajectory merging (CTM) approach. To be fair, the same Weighted K-Nearest Neighbors (WKNN) classifier is applied for off-line phase of Wi-Fi fingerprinting in each algorithm [132]. The comparison of all the estimated positioning errors is compared in Figure 4-26:

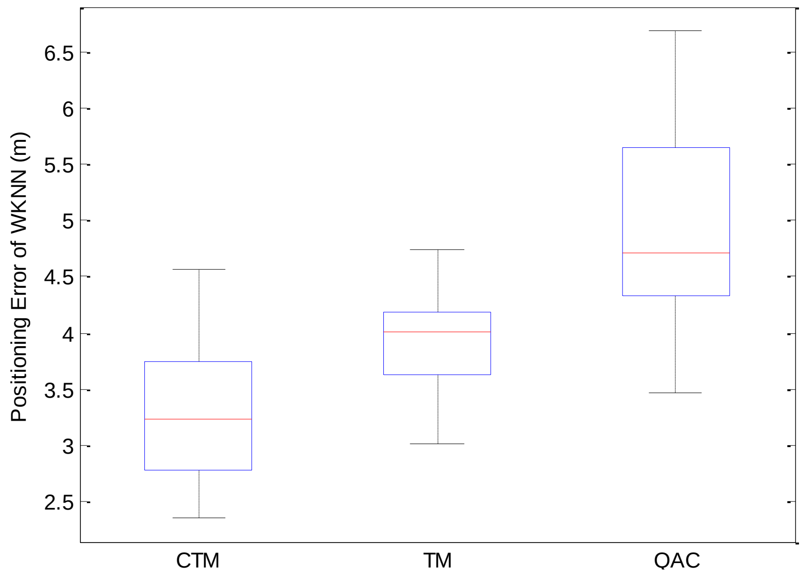

Figure 4-26 Accuracy Comparison of Different Generation Methods

Figure 4-26 demonstrates that the proposed CTM approach proves higher positioning accuracy within 3.75 m in 75%, compared with the TM approach within 4.18 m in 75%, and the accuracy of QAC approach is within 5.64 m in 75%. Thus, the trajectories merging phase effectively improves the robustness of final constructed navigation database and much better localization performance can be achieved.

4.4.4 Performance Evaluation of Crowdsourced Wi-Fi Fingerprinting solution in Large-scale Indoor Spaces

In order to evaluate the accuracy of proposed crowdsourced Wi-Fi fingerprinting based positioning system in large-scale indoor spaces, one typical shopping mall based 3D indoor environment which contains multi-floor structure and large-scaled open areas is chosen as the experimental site, one of the selected floor is shown in Figure 4-27:

Figure 4-27 Large-scale Scene of IPIN-2018 Dataset

In the selected shopping mall scene, the crowdsourced dataset acquired from a shopping mall is provided by IPIN-2018 indoor competition, track 3 [130], in which 37 the crowdsourced trajectories contain the data acquired from smartphone integrated sensors and corresponding scanned local Wi-Fi information are collected respectively. In addition, in order to estimate the absolute localization trajectory, the sparse landmark points are added in the procedure of trajectory data collection. The part of the collected trajectories and corresponding landmark points are presented in Figure 4-28:

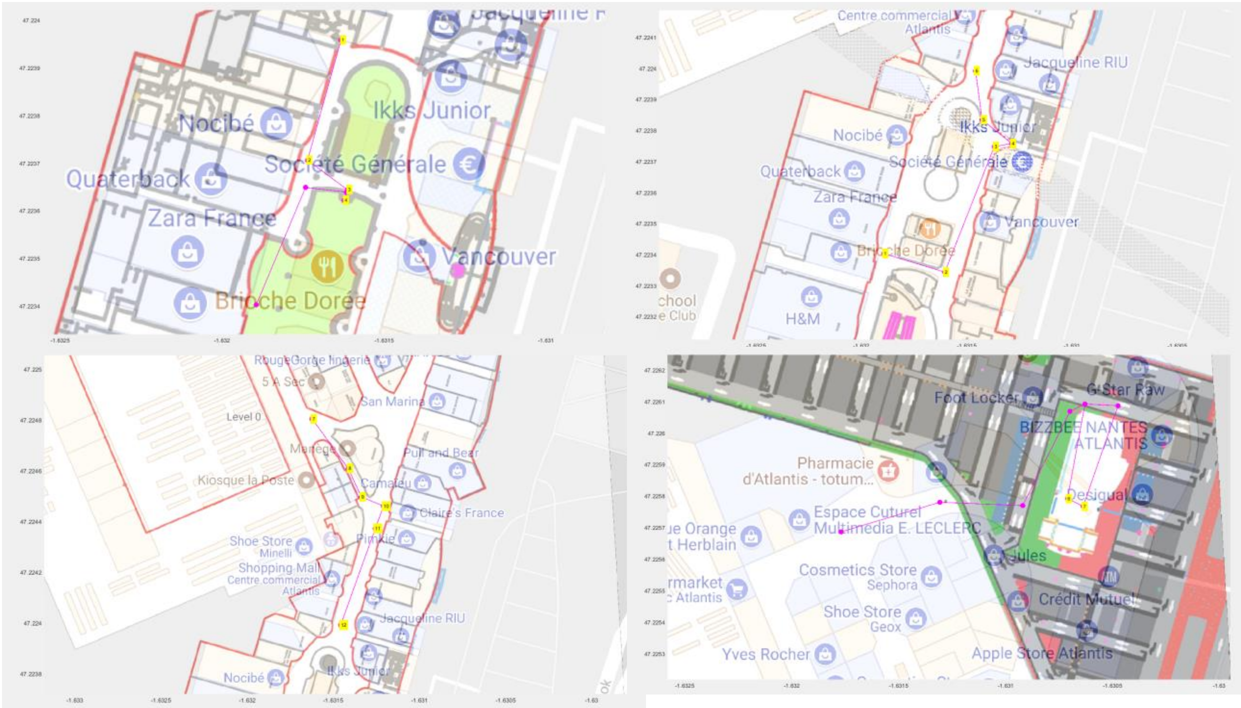

Figure 4-28 Crowdsourced Trajectories Provided by IPIN-2018 Dataset

The raw MEMS sensors data is firstly processed by forward PINS framework proposed in Chapter Three, after that the GD algorithm is applied to optimize the crowdsourced trajectories and quality evaluation is used to evaluate the accuracy and weight of each trajectory. The final crowdsourced Wi-Fi fingerprinting database in this indoor scene is generated based on the weighted results of selected Wi-Fi data provided by crowdsourced trajectories, MLP based trajectory evaluation model and multi-level constrains. In this case, the raw trajectories which contain detected landmarks are firstly processed by the proposed PINS structure, then the optimization phase is conducted to further improve the performance, which is shown as follows:

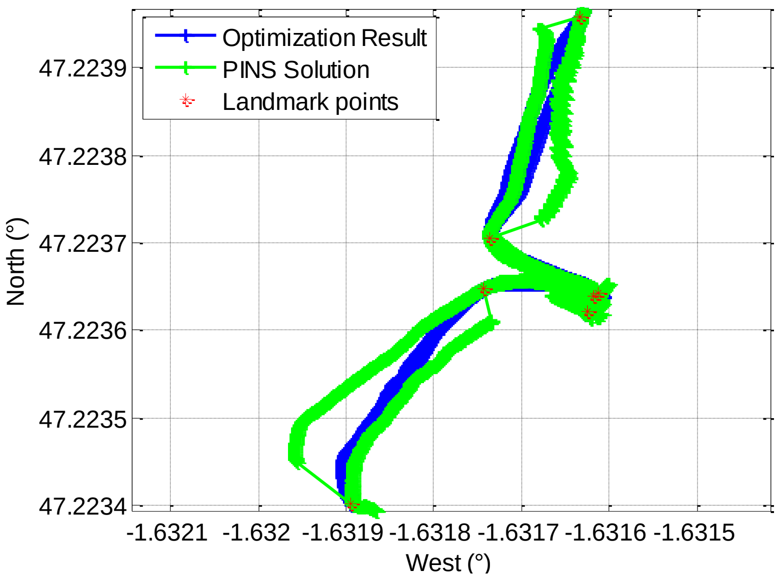

Figure 4-29 Performance of PINS Optimization Phase

The optimized crowdsourced trajectories are further evaluated by the proposed MLP model and uncertainty of each trajectory at each step period is provided for further trajectory partition and merging. In which the training dataset and the test dataset are both provided by the collected crowdsourced trajectories acquired from IPIN-2018 dataset. In this case, a number of overall 50 selected trajectories are finally applied as the training dataset of the MLP, and the number of training iterations is set as 800 in order to get the optimal result, which is shown as follow:

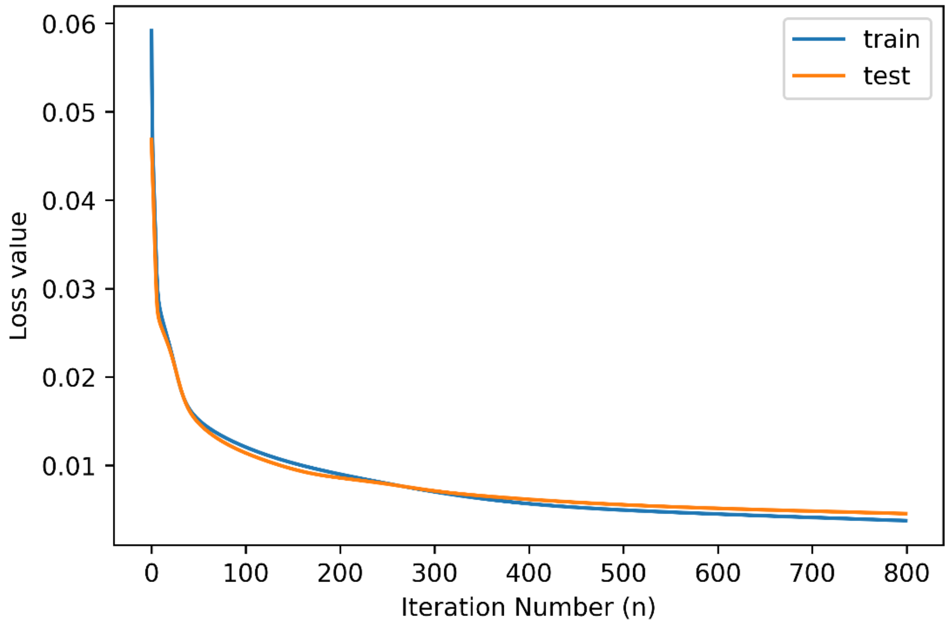

Figure 4-30 Performance of MLP Training Result

The predicted result of positioning error of total dataset are described in Figure 4-31 and Figure 4-32, respectively:

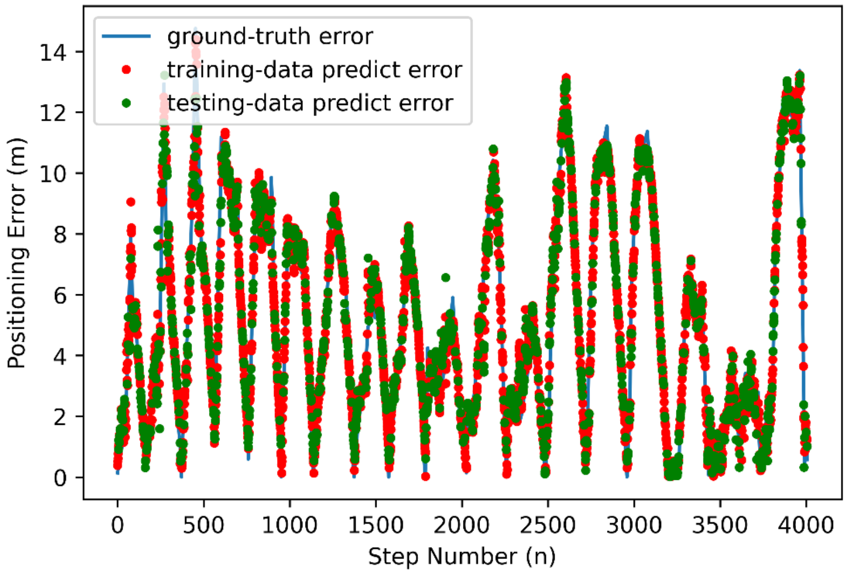

Figure 4-31 Training and Prediction Result of Positioning Error

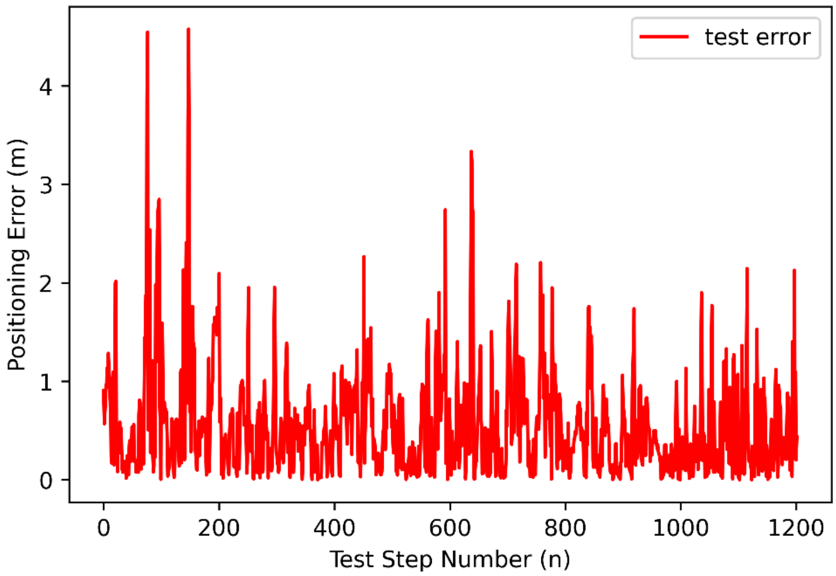

Figure 4-32 Prediction Result of Positioning Error

It can be found from Figure 4-32 that the proposed MLP based trajectory uncertainty prediction model proves impressive performance, which reaches the accuracy of 0.76 m in case of 75%.

Finally, we draw the uncertainty region of predicted trajectory to shown the performance of our proposed MLP based uncertainty prediction approach, the uncertainty regions of all the step are combined together to get the total uncertainty region, which is shown as follow:

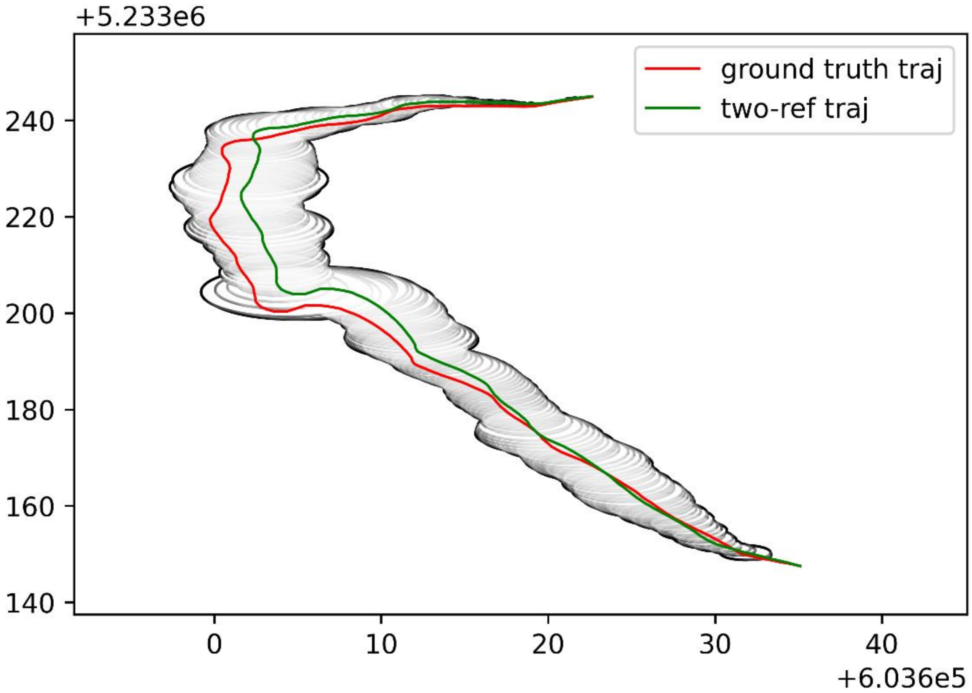

Figure 4-33 Uncertainty Region of Optimized Trajectory

After evaluating the crowdsourced trajectories, the partition and merging phase is further applied to generate an efficient and accurate database. The final constructed 3D crowdsourced Wi-Fi fingerprinting database is shown in Figure 4-34:

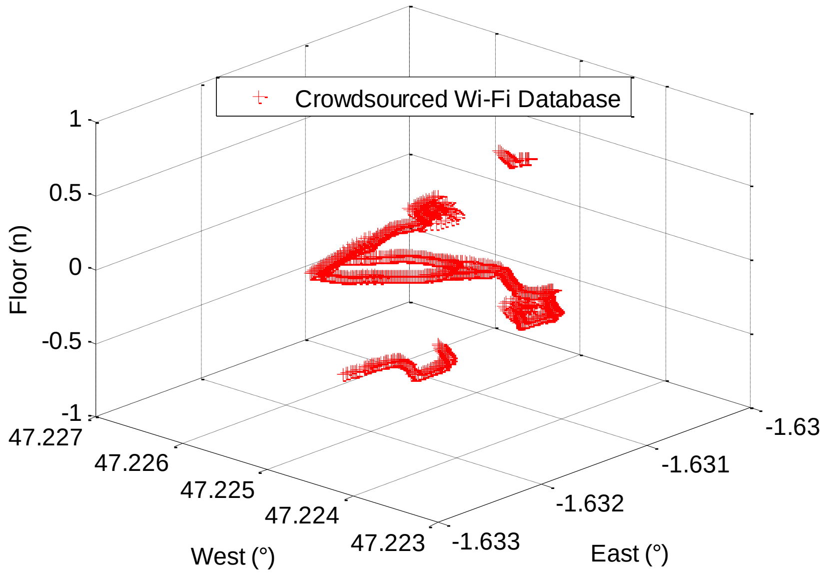

Figure 4-34 Crowdsourced Wi-Fi Fingerprinting Database

In the on-line phase, the Samsung SM-A520F is used as the hardware platform, and the reading mode described in [51] is applied. The real-time Wi-Fi fingerprinting based 3D location of the pedestrian is provided by combination of the signal quality evaluation of Wi-Fi fingerprinting and double-stage k-nearest neighbor (DS-KNN).

The single Wi-Fi fingerprinting result may fluctuate due to the indoor interference, thus, in this work, the PDR and Wi-Fi fingerprinting result are integrated by a typical particle filter (PF) to realize robust and stable crowdsourcing-based 3D localization performance. The final evaluation dataset contains cross-floor motion modes, and the 2D and 3D comparison results between forward PDR mechanization, Wi-Fi fingerprinting and the PF are presented in Figure 4-35 and Figure 4-36, respectively:

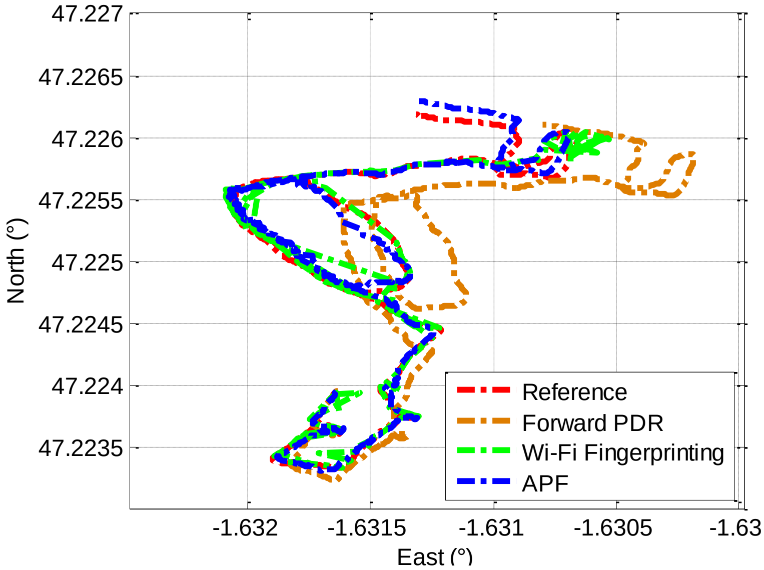

Figure 4-35 2D Comparison of Different Positioning Approaches

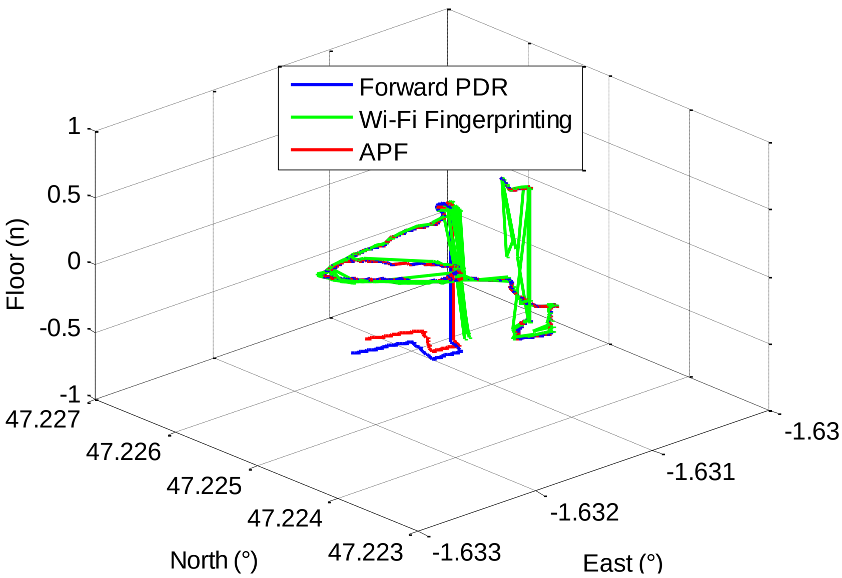

Figure 4-36 3D Comparison of Different Positioning Approaches

It can be found from Figure 4-36 that the forward PDR is subjected to the cumulative error thus cannot maintain accuracy in a long time period, and the location information provided by the Wi-Fi fingerprinting method proves significant fluctuations due to the multipath propagation effect indoors. The proposed PF effectively combines the advantages of different location sources and provides reliable and accurate 3D indoor location information. The final positioning error comparison result is shown in Figure 4-37:

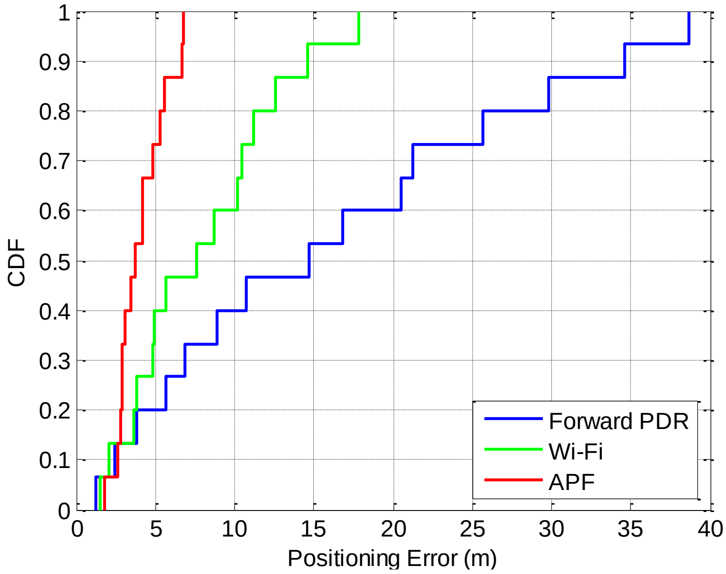

Figure 4-37 Comparison of Different Positioning Methods

Figure 4-37 describes that the proposed PF realizes much higher localization precision compared with single location source. The average positioning error is within 3.7m and the CDF error is within 5.18m in case of 75% in the open scene of the shopping mall.

Finally, we give a comprehensive discussion between the performance of crowdsourced Wi-Fi fingerprinting methods applied in IPIN-2018. In Figure 4-35, the back part of the fusion result proves larger error due to the lack of useful Wi-Fi fingerprinting database in the underground parking scene. The HFTS team in [130] used standard PF to fuse the results of Wi- Fi RSSI fingerprint and PDR, and used the map information to detect the most likely path to improve the accuracy in case of Wi-Fi database missing. The EGEC team in [130] combined the magnetic fingerprinting with PDR, Wi-Fi fingerprinting, and map information, which further improved the multi-source indoor localization performance.

4.5 Summary

This chapter proposes two different Wi-Fi positioning systems, including Wi-Fi FTM based calibration and positioning system and crowdsourced Wi-Fi fingerprinting based positioning system, aiming at providing autonomous and precision-controllable 3D indoor localization performance in large-scale and multiple scenes contained indoor spaces. The contribution of this chapter contains three main parts:

1) This chapter proposes three different Wi-Fi FTM calibration strategies which take different application scenes into consideration. In which the Polynomial-based (PB) calibration strategy towards the known types of smartphones and Wi-Fi APs. Gradient descent (GD) based FTM bias estimation with the combination of quasi-static (QS) recognition, and the estimated bias value is used to calibrate the measured RTT in real-time without the known types of smartphones and Wi-Fi APs. Tightly-coupled (TC) integration model with the consideration of all error sources, in which all the navigation parameters are calibrated and optimized at the same time to get the final positioning results. The real-world estimation in typical office scene shows that the PB approach proves the best positioning performance within 1.01 m in 75%, and the accuracy of GD AUKF is a little higher than TC approach, and the positioning errors of two algorithms are 1.09 m and 1.19 m in 75%, respectively.

2) This chapter proposes a comprehensive structure for crowdsourced trajectories modelling, pre-calibration, optimization, and classification. In which the collected crowdsourced trajectory is modeled as a non-linear function contains the extracted landmarks, heading and step-length information, and the raw trajectory is matched with the reference vector for pre-calibration in order to decrease the effects of initial heading error and installation error caused by the handheld mode of the pedestrian. In addition, an iterative extended Kalman filter (iEKF) is proposed for robust trajectory optimization to further improve the accuracy of pre-calibrated trajectory, and the optimized trajectories are finally classified into similar groups using the multi-level constraints, correlation coefficient and DTW indexes.

3) This chapter proposes a novel multi-layer perceptron (MLP) network which can autonomously evaluate the positioning error of optimized trajectories during each step period based on the extracted motion features. To construct an accurate and efficient crowdsourced Wi-Fi fingerprinting database, the evaluated trajectories in same similar group are further segmented and merged according to the detected turning points

information, and the final crowdsourced Wi-Fi fingerprinting database is reconstructed using the turning/landmark points generated collection points to reduce the dimension and complexity. The performance evaluation of MLP model on the daily-life dataset proves the meter-level accuracy in positioning error prediction, and the proposed crowdsourced trajectory merging approach reaches the better accuracy compared with state-of-art crowdsourced Wi-Fi fingerprinting database generation algorithms, which is within 3.75 m in 75% under office scene and also has the good performance under large-scaled shopping mall scene, the accuracy of PDR/Wi-Fi fingerprinting integration approach reaches 5.18 m in 75%.

In conclusion, in this section, we present two different Wi-Fi positioning systems (WPS) and design comprehensive experiments to evaluate the precision of two developed WPS in different 3D indoor scenes, including the office scene, corridor scene and shopping mall scene. The experimental results prove that the Wi-Fi FTM based calibration and positioning system proposed in this chapter can realize meter-level localization accuracy after self-calibration phase of ranging bias, and the proposed crowdsourced Wi-Fi fingerprinting based positioning system can autonomously generate an efficient and accurate navigation database using large amount of crowdsourced navigation data and realize universal localization towards large-scale indoor spaces and avoid the labor-consuming collection phase. We will combine the advantages of both two Wi-Fi positioning systems together with the MEMS sensors based positioning approach and realize a more autonomous, more accurate, and more stable multi-source fusion based 3D indoor localization framework.

Chapter 5: Wi-Fi/MEMS Integration Framework For Large-Scaled 3D Indoor Positioning

Indoor wireless localization towards the next generation Wi-Fi access point has attracted considerable attention due to the presentation of the state-of-art Wi-Fi Fine Time Measurement (FTM) protocol. In order to increase the precision and universality of wireless positioning based on the Internet of Things (IoT) terminals, this chapter proposes a multi-source fusion based indoor localization framework which contains the integration of Wi-Fi FTM, RSSI fingerprinting and IoT terminal integrated MEMS sensors

In the Chapter Four, two state-of-art WPS systems: Wi-Fi FTM based calibration and positioning system and crowdsourced Wi-Fi fingerprinting based positioning system are presented respectively towards different application requirements. The disadvantages of two Wi-Fi positioning system are that, in a complex and changeable smart city indoor scene, the realized precision of Wi-Fi FTM is constrained by the multipath propagation and NLOS effect which would cause the additional deviation in Wi-Fi ranging results [19]. Due to the hardware difference of IoT terminals and Wi-Fi APs, not all IoT devices or Wi-Fi APs support the FTM protocol, and the ranging bias always exists in the procedure of FTM timestamp exchange between different terminals [125]. In addition, the single MEMS sensors based location update approach is proved to provide shortly precise results in a short time period, while the accuracy of MEMS sensors based approach decreases with time due to the cumulative error and magnetic interference therefore are always integrated with absolute location sources [33-34].

In this chapter, in order to enhance the precision and universality of indoor positioning towards the next generation wireless positioning based on IoT terminals, this paper presents the Wi-Fi/MEMS sensors integrated framework, which is consist of a robust MEMS sensors based localization solution and three kinds of MEMS sensors and Wi-Fi integration models towards different application scenes. In addition, this chapter proposes the signal quality evaluation (QE) algorithm aiming at autonomously estimating the availability and uncertainty of measured Wi-Fi FTM and RSSI fingerprinting results using the misclosure check (MC) and double-stage k-nearest neighbor (DS-KNN) methods, which effectively improves the signal robustness in final multi-source fusion phase. At this stage, the integrated indoor localization using the combination of different location sources is regarded as an effective approach for realizing much better indoor localization performance. Aiming at the next generation WPS which supports both RSSI and FTM collection, how to achieve a robust combination of all the supported wireless characteristics using IoT terminals becomes a hot issue towards large-scaled and controllable indoor localization.

The contributions of this chapter are summarized as follows:

1) This chapter simplifies the original INS mechanization described in the MEMS sensors based 3D indoor localization structure by ignoring the rotation of the earth, which can significantly increase the efficiency and decrease the complexity of proposed PINS structure. Compared with existing MEMS Sensors based approaches, our proposed PINS realizes the integration of INS and multi-level constraints and observed values. In addition, the proposed PINS integration approach can further be expanded into different multi-source fusion models towards specific location sources and positioning scenes.

2) This chapter proposes the signal quality evaluation (QE) algorithm aiming at evaluating the availability and uncertainty of measured Wi-Fi FTM and RSSI fingerprinting results aiming at improving the signal robustness in final fusion phase. In which the misclosure check (MC) method is applied to detect the received round-trip-time (RTT) indoors which contains NLOS measurement and initial bias, and the double-stage k-nearest neighbor (DS-KNN) method is proposed to improve the matching performance of crowdsourced RSSI fingerprinting and evaluate the location uncertainty of Wi-Fi RSSI fingerprinting result.

3) This chapter proposes three different types of multi-source fusion structures, in which the self-calibrated tightly-coupled integration model based on Wi-Fi FTM and MEMS sensors can provided meter-level positioning accuracy without calibration phase of Wi-Fi ranging; the loosely-coupled integration model based on Wi-Fi RSSI fingerprinting and MEMS sensors can realize autonomous localization and navigation database updating; and the hybrid fusion model organically combined all the location sources together aiming at providing precision-controllable positioning in complex and large-scaled indoor spaces. The use of different fusion structures significantly increases the accuracy and universality of 3D indoor localization.

The remainder of this chapter is organized as follows. Section 5.1 introduces the overall Wi-Fi and MEMS sensors integrated framework. Section 5.2 presents self-calibrated tightly-coupled integration model of Wi-Fi FTM and MEMS sensors and corresponding Wi-Fi FTM based signal quality evaluation approach. Section 5.3

proposes a loosely-coupled integration model of crowdsourced Wi-Fi fingerprinting and MEMS sensors and corresponding Wi-Fi RSSI fingerprinting based signal quality evaluation approach. In addition, a hybridly-coupled integration model using the combination of all the Wi-Fi FTM, RSSI fingerprinting and MEMS sensors based location sources is further presented. Section 5.4 designs comprehensive experiments and gives the test results and the performance analysis. Section 5.5 gives the summary of this chapter.

5.1 System Overview

It can be found from the previous work that the Wi-Fi FTM based high-precision location source is not available in all the Wi-Fi APs, and the RSSI characteristic is regarded as the universal location sources. Towards the generation WPS, how to integrate the Wi-Fi FTM/RSSI and MEMS sensors based location sources to provide a large-scaled and accurate indoor localization performance is a facing problem, and how to comprehensively solve the challenges including magnetic interference and cumulative error, hardware deviation, and quality evaluation is also an existing challenge. To enhance the precision of multi-source fusion based indoor localization using the IoT hardware platform, the following mentioned challenges need to be handled:

1) Magnetic interference and cumulative error of MEMS sensors: In the traditional dead-reckoning (DR) algorithm, the position is updated using the calculated walking speed and heading information, which is affected by the increasing measurement error of MEMS sensors and changeable magnetic field in local environments.

2) Hardware deviation of different IoT terminals: Due to the hardware differences between IoT Terminals and Wi-Fi APs, the raw measured RSSI or the round-trip-time (RTT) information always contains additional bias which causes the overall drift of the ranging result.

3) Effective quality evaluation of multiple location sources: Indoor scenes usually contain structure based influences such as multipath propagation and NLOS. Similar to the TOA based positioning method, Wi-Fi FTM is much more robust indoors compared with RSSI but is also subjected to the indoor interference which should be recognized.

To improve the accuracy and universality of the multi-source fusion based wireless positioning, this chapter proposes the multi-source fusion based Wi-Fi FTM/RSSI fingerprinting/MEMS sensors integration framework (MS-WFRS). The proposed MS-

WFRS combines the Wi-Fi FTM, Wi-Fi RSSI fingerprinting and MEMS sensors based location sources to make all the three approaches complementary. Firstly, the raw magnetic data is used to detect QSMF periods and step detection is applied to provide reference walking speed and position increment as the measured value to eliminate the drift error of INS mechanization; In addition, the MC and DS-KNN algorithms are proposed in signal QE procedure to increase the robustness of Wi-Fi FTM and RSSI fingerprinting and provide the adaptive weight of each location source in fusion phase; Finally, the AUKF is applied to fuse the information of PINS, Wi-Fi FTM and RSSI fingerprinting to realize precise and universal IoT terminals based indoor localization performance. The whole framework of proposed Wi-Fi FTM/RSSI fingerprinting/MEMS sensors framework is shown in Figure 5-1.

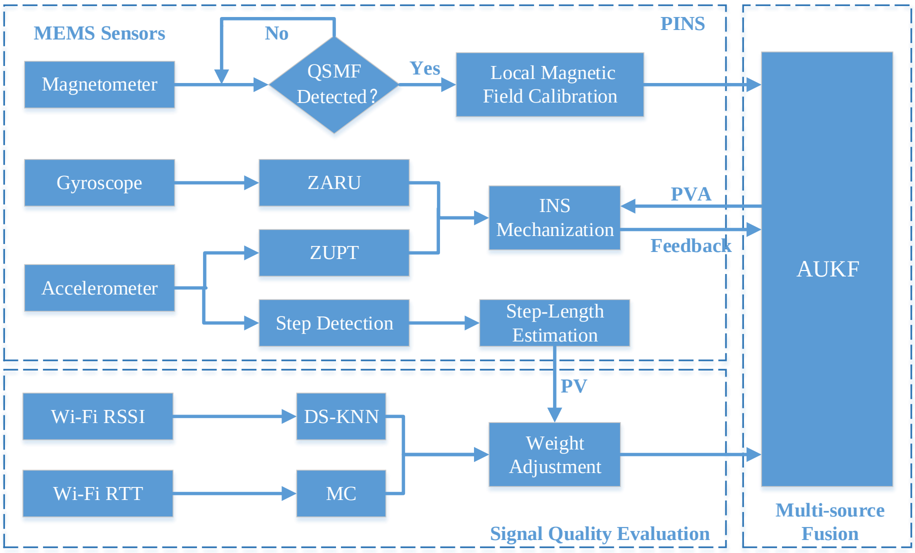

Figure 5-1 Framework of Wi-Fi and MEMS Sensors Integration

5.2 Self-calibrated Tightly-coupled Integration Model of Wi-Fi FTM and MEMS Sensors

When pedestrians move into the Wi-Fi FTM covered environments, the self-calibrated tightly-coupled integration model is applied for meter-level localization. After Wi-Fi FTM based signal QE procedure, the Wi-Fi FTM based location source is adopted as the observation. The raw ranging result existing initial bias due to the deviation between different IoT terminals and Wi-Fi APs, to estimate the ranging bias in dynamic indoor scenes and realize the integrated localization at the same time, this section proposes the TC-S integration model, which provides a comprehensive solution by taking both Wi-Fi FTM and MEMS sensors based location sources into consideration in Wi-Fi FTM supported indoor spaces.

5.2.1 Signal Quality Evaluation of Wi-Fi FTM

Wi-Fi FTM is proved to provide meter-level ranging result in LOS contained environment, while is influenced by the initial bias, random error and NLOS deviation due to its measurement mechanism [30], because the multipath propagation added on the Wi-Fi ranging results can be largely eliminated by increasing the bandwidth and frequency of Wi-Fi signals [79]. Thus, the actually collected Wi-Fi FTM based distance is defined as:

$$L_{\text{observed}} = L_{\text{FTM}} + d_{bias} + d_N + d_{\text{random}} \tag{5-1}$$

where L_{observed} indicates the observed distance which is consist of the initial bias d_{bias}, NLOS error d_N and random error d_{random}, L_{FTM} represents the ground-truth ranging distance. In addition, the random error of ranging result d_{random} always subjected to Gaussian distribution, therefore, the aim of Wi-Fi signal QE is to detect the accuracy of initial bias and NLOS error contained ranging results and adaptively adjust the weight of corresponding location sources.

In this section, the misclosure check (MC) method [133] is applied to detect the received round-trip-time (RTT) indoors which contains NLOS measurement and initial bias. The description of proposed MC detection is described in Figure 5-2. In Figure 5-2, the point B and C indicates Wi-Fi APs with fixed location, and the point A is the location of the pedestrian. In ideal case, the vectors organized by the point A, B, and C meet the following condition:

$$\overrightarrow{BC} = \overrightarrow{AB} - \overrightarrow{AC} \tag{5-2}$$

where $\overrightarrow{BC}$ indicates the vector between two known APs. $\overrightarrow{AB}$ and $\overrightarrow{AC}$ represent the vectors of the distance provided by the Wi-Fi ranging result between the pedestrian and Wi-Fi APs.

In Figure 5-2, the random error of the predicted location A and measured noise is modeled as a confidence region, in this case, the equation (5-2) is represented as:

$$\overrightarrow{AB} - \overrightarrow{AC} - \overrightarrow{BC} = d_{bias} + d_N + d_{\text{random}} + d_p \tag{5-3}$$

where d_p indicates the approximate error and the error of d_{random} and d_p can be described by the variance Q_r and Q_p. The initial deviation d_{bias} is estimated in real-time by the proposed integration model in the following part, thus, the error of d_{bias} can be described by the variance Q_b. Therefore, the size of the confidence region is acquired by values of Q_r, Q_b and Q_p. If the calculated misclosure out of the confidence region range, it is regarded as the effect of NLOS bias. The definition of Wi-Fi FTM based signal QE is described in Figure 5-2:

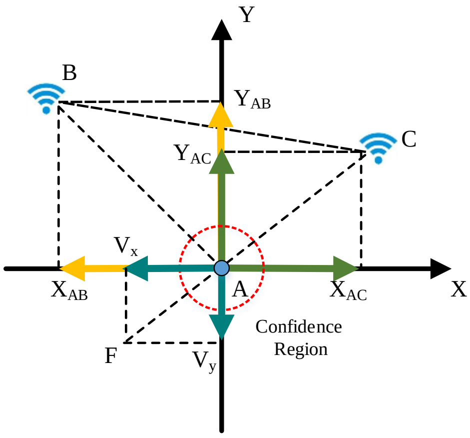

Figure 5-2 Diagram of Wi-Fi FTM Based Signal QE

In the 2D positioning scene, the predicted location of the pedestrian is consist of *X* and *Y* coordinates. The misclosure equation is rewritten as:

$$\begin{cases} X_{BC} = X_{AB} \pm X_{AC} \\ Y_{BC} = Y_{AB} \pm Y_{AC} \end{cases} \tag{5-4}$$

where *X* and *Y* indicate the components of the calculated misclosure vector. The Wi-Fi FTM based distance can be modeled as the vector form by the following equation:

$$\begin{cases} \overline{X}_{AB} = \dfrac{X_{AB}\overline{\xi}_{AB}}{\varpi_{AB}} \\ \overline{Y}_{AB} = \dfrac{Y_{AB}\overline{\xi}_{AB}}{\varpi_{AB}} \end{cases} \tag{5-5}$$

where $\overline{\xi}_{AB}$ indicates the FTM based distance between point A and point B. $\left(\overline{X}_{AB}, \overline{Y}_{AB}\right)$ indicates the organized vector provided by the measure Wi-Fi ranging at the predicted location A. ϖ_{AB} represents the Euclidean distance between point B and the estimated position A, which can be calculated with $\varpi_{AB} = \sqrt{X_{AB}^2 + Y_{AB}^2}$. The Wi-Fi FTM based misclosure vector in this case can be described as:

$$\begin{cases} V_x = \overline{X}_{AB} \pm \overline{X}_{AC} - X_{BC} \\ V_y = \overline{Y}_{AB} \pm \overline{Y}_{AC} - Y_{BC} \end{cases} \tag{5-6}$$

where $\vec{V} = [V_x, V_y]^{\mathrm{T}}$ indicates the misclosure vector, defining that the variance of Wi-Fi FTM ranging result is D_r, then calculate the variance of $\vec{V}$:

$$D(\vec{V}) = \begin{pmatrix} \left(\frac{X_{AB}}{R_{AB}} + \frac{X_{AC}}{R_{AC}}\right)^2 & 0 \\ 0 & \left(\frac{Y_{AB}}{R_{AB}} + \frac{Y_{AC}}{R_{AC}}\right)^2 \end{pmatrix} \begin{pmatrix} D_r & 0 \\ 0 & D_r \end{pmatrix} \tag{5-7}$$

After the construction of misclosure model, the t-test [134] can be described as following:

$$\left\|\vec{V}\right\| > \mu(\sqrt{D_r} + \sqrt{D_p}) \tag{5-8}$$

In each quality evaluation procedure, the $D(\vec{V})$ is finally compared with the sum of D_r and D_p, and the variance of D_p is provided by MEMS sensors based method. The NLOS bias exists when the deviation between $D(\vec{V})$ and sum of D_r and D_p larger than the set threshold. The misclosure vector is constructed from every group of two Wi-Fi APs and one IoT terminal, thus there would be N*(N-1)/2 triangles that need to be organized based on N Wi-Fi APs.

5.2.2 Tightly-coupled and Self-calibrated Integration Model Based on Wi-Fi FTM and MEMS Sensors

When pedestrians move into the Wi-Fi FTM covered environments, the tightly-coupled and self-calibrated integration model is applied for meter-level localization. After signal QE procedure, the Wi-Fi FTM based location source is adopted as the observation. The raw ranging result existing initial bias due to the deviation between different IoT terminals and Wi-Fi APs, to estimate the ranging bias in dynamic indoor scenes and realize the integrated localization at the same time, this paper proposes the TC-S integration model, which provides a comprehensive solution by taking both Wi-Fi FTM and MEMS sensors based location sources into consideration.

The state value in the proposed TC-S integration model contains two parts. The first part is the built-in sensors based error model, which can be described as:

$$\delta \dot{\boldsymbol{X}}_s = \boldsymbol{F}_s \delta \boldsymbol{X}_s + \boldsymbol{G}_s \varepsilon_s \tag{5-9}$$

where $\delta \boldsymbol{X}_s$ is consist of 15 dimensions state error, which is presented in (3-28), $\varepsilon_s = [\varepsilon_1 \cdots \varepsilon_{15}]$ indicates the error sources that comply the Gaussian distribution. $\boldsymbol{G}_s$ is the noise driven matrix with the rank of 15.

For the low-cost sensors based inertial navigation, a more simplified INS mechanization can be applied, which ignores rotation of the earth. The attitude update equation is described as follows:

$$\boldsymbol{Q}_{b(m)}^{n} = \boldsymbol{Q}_{b(m\text{-}1)}^{n} \circ \boldsymbol{Q}_{b(m)}^{b(m-1)} \tag{5-10}$$

where $\boldsymbol{Q}_{b(m)}^{n}$ indicates the quaternion of attitude transformation at epoch m; $\boldsymbol{Q}_{b(m)}^{b(m-1)}$ represents the change of attitude quaternion between epoch m and epoch m-1, which can be described as:

$$\boldsymbol{Q}_{b(m)}^{b(m-1)} = \begin{bmatrix} \cos\dfrac{\Delta\theta_m}{2} \\ \dfrac{\Delta\boldsymbol{\theta}_m}{\Delta\theta_m}\sin\dfrac{\Delta\theta_m}{2} \end{bmatrix} \tag{5-11}$$

where $\Delta\boldsymbol{\theta}_m$ represents the angular increment in the time period (m-1,m), and $\Delta\theta_m = \left|\Delta\boldsymbol{\theta}_m\right|$.

In low-cost inertial navigation systems, the influence of the rotation of the earth is generally ignored, therefore the speed update equation can be simplified as:

$$\boldsymbol{v}_m^n = \boldsymbol{v}_{m-1}^n + \Delta\boldsymbol{v}_{sf(m)}^n + \boldsymbol{g}^n T_s \tag{5-12}$$

In which:

$$\Delta\boldsymbol{v}_{sf(m)}^n = \boldsymbol{C}_{b(m-1)}^n(\Delta\boldsymbol{v}_m + \frac{1}{2}\Delta\boldsymbol{\theta}_m \times \Delta\boldsymbol{v}_m) \tag{5-13}$$

where $\boldsymbol{v}_m^n$ indicates the INS based velocity at epoch m, $\boldsymbol{C}_{b(m-1)}^n$ represents the attitude matrix, $\Delta\boldsymbol{v}_m$ represents the specific force increment in the period (t-1, t).

Finally, the position update equation is described as:

$$\boldsymbol{P}_m^n = \boldsymbol{P}_{m-1}^n + \frac{\boldsymbol{v}_{m-1}^n + \boldsymbol{v}_m^n}{2} T_s \tag{5-14}$$

where $\boldsymbol{P}_m^n = \begin{bmatrix} x_m & y_m & z_m \end{bmatrix}^{\mathrm{T}}$, T_S indicates the sampling rate.

In this section, the bias of Wi-Fi FTM is estimated in real-time to compensate the differences between different kinds of smartphones and Wi-Fi APs, which is modeled as the random walk process:

$$\dot{b}_{\mathrm{RTT}} = -(1/\tau_{b_{\mathrm{RTT}}})b_{\mathrm{RTT}} + \varepsilon_{b_{\mathrm{RTT}}} \tag{5-15}$$

where $\tau_{b_{\mathrm{RTT}}}$ represents the correlation time, $\varepsilon_{b_{\mathrm{RTT}}}$ indicates the white noise. The RTT bias based error model is described as:

$$\delta\dot{\boldsymbol{X}}_W = \boldsymbol{F}_W\delta\boldsymbol{X}_W + \boldsymbol{G}_W\varepsilon_W \tag{5-16}$$

where $\delta\boldsymbol{X}_W = b_{\mathrm{RTT}}$, $\boldsymbol{F}_W = 0$, $\boldsymbol{G}_W = 1$, and $\varepsilon_W = \varepsilon_{b_{\mathrm{RTT}}}$.

The augmented form of TC-S calibration and localization state model is presented as:

$$\begin{bmatrix} \delta\dot{\boldsymbol{X}}_s \\ \delta\dot{\boldsymbol{X}}_W \end{bmatrix} = \begin{bmatrix} \boldsymbol{F}_s & 0 \\ 0 & \boldsymbol{F}_W \end{bmatrix} \begin{bmatrix} \delta\boldsymbol{X}_s \\ \delta\boldsymbol{X}_W \end{bmatrix} + \begin{bmatrix} \boldsymbol{G}_s & 0 \\ 0 & \boldsymbol{G}_W \end{bmatrix} \begin{bmatrix} \varepsilon_s \\ \varepsilon_W \end{bmatrix} \tag{5-17}$$

The observed model is described as:

$$\delta\boldsymbol{z}_d = \begin{bmatrix} \delta\boldsymbol{z}_{1,range} \\ \delta\boldsymbol{z}_{2,range} \\ \vdots \\ \delta\boldsymbol{z}_{m,range} \end{bmatrix} = \begin{bmatrix} d_{MEMS,1} - d_{FTM,1} \\ d_{MEMS,2} - d_{FTM,2} \\ \vdots \\ d_{MEMS,m} - d_{FTM,m} \end{bmatrix} \tag{5-18}$$

where $\delta\boldsymbol{z}_{m,range}$ indicates the ranging difference between Wi-Fi FTM and MEMS sensors based ranging estimation; The Wi-Fi FTM ranging model is defined in (5-1), and the MEMS sensors based ranging $d_{MEMS,m}$ is described as follow:

$$d_{MEMS,m} = \sqrt{(E^k_{MEMS} - P^E_m)^2 + (N^k_{MEMS} - P^N_m)^2} \tag{5-19}$$

where($E^k{}_{MEMS}$, $N^k{}_{MEMS}$) indicates the MEMS sensors based localization result, ($P_m{}^E$, $P_m{}^N$) represents the location of the m^{st} Wi-Fi AP.

The raw measured RTT value contains bias factor acquired from m^{th} Wi-Fi AP is calculated by:

$$d_{FTM,m} = L_{raw} - b_{RTT} - v_{RTT} \tag{5-20}$$

Finally, the TC calibration and localization model is presented as:

$$\delta\boldsymbol{Z} = \boldsymbol{H}\delta\boldsymbol{X} + \xi \tag{5-21}$$

where $\delta\boldsymbol{Z}$ and $\delta\boldsymbol{X}$ are given in equation (5-20) and (5-21), ξ indicates the measurement noise, $\boldsymbol{H}$ is the design matrix.

5.3 Loosely-coupled Integration of Crowdsourced Wi-Fi Fingerprinting and MEMS Sensors

Section 5.2 describes the TC-S integration model using Wi-Fi FTM and MEMS sensors based location sources. For some indoor environments where the Wi-Fi APs do not support the FTM protocol, the Wi-Fi RSSI fingerprinting is regarded as a more universal and wide-covered indoor location source which is supported by almost all the mobile terminals. This section describes the Wi-Fi RSSI fingerprinting and MEMS sensors based loosely-coupled integration model, which is applied for a more universal 3D indoor localization combining with the signal QE procedure.

5.3.1 Signal Quality Evaluation of Wi-Fi RSSI Fingerprinting

The Wi-Fi RSSI fingerprinting method is widely applied due to its extensive coverage and universality characteristics, while the accuracy of RSSI based fingerprinting is limited by complex indoor environments. In this paper, DS-KNN is proposed to enhance the precision of RSSI fingerprinting based positioning, which contains three main steps: the adaptive selection of the optimal parameter K, the weighted location based on the averaged distance, and the error variance prediction of weighted position.

First, the averaged Euclidean distances $Dis_{t,other}$ between real-time collected RSSI array and each reference RSSI array in the Wi-Fi fingerprinting database are compared and sorted to extract the nearest average distance Dis_{t,r_1} as the reference value instead of using the total distance, then the similar constraint parameter is applied to get the optical parameter K, which are defined as [135]:

$$\begin{cases} \gamma = Dis_{t,other} \,/\, Dis_{t,r_1} - 1 \\ \text{case01}: Dis_{t,r_1} < Dis_{t,other}, \gamma > \kappa \\ \text{case02}: Dis_{t,r_1} \approx Dis_{t,other}, \gamma \le \kappa \end{cases} \tag{5-22}$$

where γ represents the similar degree of two RSSI arrays and κ indicates the threshold of similar degree. Based on the similar constrain of calculated Euclidean distances, the parameter K can be adjusted adaptively.

After adaptively selecting the parameter K, the eligible reference locations in database are weighted for the final position calculation, the weight of each reference location is provided by the similar degree γ :

$$\text{POS}'(x_r, y_r) = \frac{\sum_{i=1}^{K} \omega_i^{\gamma} \text{POS}(x_i, y_i)}{\sum_{i=1}^{K} \omega_i^{\gamma}} \tag{5-23}$$

In which $\text{POS}'(x_r, y_r)$ is the positioning result of WKNN, $\text{POS}(x_i, y_i)$ indicates the selected reference location in database, ω_i^{γ} represents the weight value of the i^{st} reference position acquired from the generated navigation database.

In this work, a more intelligent MLP network based signal quality evaluation model is applied for error prediction of the Wi-Fi fingerprinting matching result, and the features that can affect the precision of Wi-Fi fingerprinting based positioning are extracted and modeled as the input features for training purpose, which are described as follows:

1) Collected step-length L_t and heading information between adjacent Wi-Fi fingerprinting matched results:

$$Feature_{MEMS}(k) = \begin{pmatrix} L_1^{W/G} & \theta_1^{W/G} \\ L_2^{W/G} & \theta_2^{W/G} \\ \cdots & \cdots \\ L_M^{W/G} & \theta_M^{W/G} \end{pmatrix} \tag{5-24}$$

where M is the step number detected between two reported Wi-Fi fingerprinting reported locations, $L_M^{W/G}$ and $\theta_M^{W/G}$ indicate the corresponding step-length and heading information collected in this period.

2) Updated locations and corresponding Euclidean distance between different updated locations:

$$\begin{cases} Dis_k^{MEMS} = \sqrt{\left(\sum_{i=1}^{M} L_i \cdot \cos(\theta_i)\right)^2 + \left(\sum_{i=1}^{M} L_i \cdot \sin(\theta_i)\right)^2} \\ Dis_k^{Wi-Fi} = \sqrt{\left(x_G^W(k) - x_G^W(k-1)\right)^2 + \left(y_G^W(k) - y_G^W(k-1)\right)^2} \end{cases} \tag{5-25}$$

where $\{x_G^W(k), y_G^W(k)\}$ indicates the Wi-Fi fingerprinting reported location.

3) Location update interval and calculated speed provided by different location sources:

$$\begin{cases} Speed_k^{MEMS} = Dis_k^{MEMS} / \tau_k^{MEMS} \\ Speed_k^{Wi-Fi} = Dis_k^{Wi-Fi} / \tau_k^{Wi-Fi} \end{cases} \tag{5-26}$$

where $Speed_k^{MEMS}$ and $Speed_k^{Wi-Fi}$ are the walking speeds estimated by MEMS sensors and Wi-Fi fingerprinting approaches, respectively. τ_k^{MEMS} and τ_k^{Wi-Fi} indicate update intervals of different location sources.

4) Virtual headings originated from the MEMS sensors and Wi-Fi fingerprinting approaches:

$$\begin{cases} \vartheta_{virtual}^{MEMS}(k) = \arctan\left(\dfrac{\sum_{i=1}^{M} L_i \cdot \sin(\theta_i)}{\sum_{i=1}^{M} L_i \cdot \cos(\theta_i)}\right) \\ \vartheta_{virtual}^{Wi-Fi}(k) = \arctan\left(\dfrac{x_G^W(k) - x_G^W(k-1)}{y_G^W(k) - y_G^W(k-1)}\right) \end{cases} \tag{5-27}$$

where $\vartheta_{virtual}^{MEMS}(k)$ and $\vartheta_{virtual}^{Wi-Fi}(k)$ indicate the MEMS sensors based virtual heading and Wi-Fi fingerprinting based virtual heading between adjacent sampling points, respectively.

5) Average RSSI difference between scanned Wi-Fi APs and reference Wi-Fi APs.

$$\Delta RSSI(k) = \frac{\sum_{j=1}^{\beta}(RSSI_j^{scanned} - RSSI_j^{reference})}{\beta} \tag{5-28}$$

where $RSSI_j^{scanned}$ and $RSSI_j^{reference}$ represent the scanned and corresponding reference Wi-Fi APs and at current collection point, respectively. β is the number of Wi-Fi APs. Due to the dimension requirement of collected Wi-Fi RSSI vector in order to get an effective and accurate WKNN based matching result, the changing parameter β would also affect the precision of Wi-Fi fingerprinting result. Thus, the minimum value of β is required and it is proved that the increasing dimension of collected Wi-Fi RSSI vector has the limited effect on the accuracy of WKNN based matching phase, which is described in [132].

The final error variance of the crowdsourced Wi-Fi fingerprinting based positioning can be predicted according to the above extracted input features, the MLP based error variance distribution of the Wi-Fi fingerprinting reported location is presented as:

$$\begin{cases} p\left(x_k^{rssi} \mid x_k^i\right) \sim N(0, \sigma_{rssi}^2) \\ p\left(y_k^{rssi} \mid \mathrm{y}_k^i\right) \sim N(0, \sigma_{rssi}^2) \end{cases} \tag{5-29}$$

where σ_{rssi} indicates the measured noise of MEMS sensors based localization result, which is consist of x_k and y_k directions.

5.3.2 Loosely-coupled Integration Model of Wi-Fi RSSI Fingerprinting and MEMS Sensors

For some indoor environments where the Wi-Fi APs do not support the FTM protocol, the Wi-Fi RSSI fingerprinting and MEMS sensors based loosely-coupled navigation model is applied for more universal localization purpose after signal QE. The state model is the same as equation (5-9) and the observed model of Wi-Fi RSSI fingerprint can be described as:

$$\begin{cases} \delta \mathbf{z}_p^n = p_{rssi}^n - p_{MEMS}^n \\ \delta \mathbf{z}_v^n = v_{rssi}^n - v_{MEMS}^n \end{cases} \tag{5-30}$$

where p^n_{rssi} and v^n_{rssi} represent the received Wi-Fi RSSI fingerprinting based position and speed results, p^n_{MEMS} and v^n_{MEMS} represent the MEMS sensors based navigation results.

5.4 Hybridly-coupled Integration Model of Wi-Fi FTM/RSSI Fingerprinting and MEMS Sensors

In Wi-Fi FTM covered indoor environments, Wi-Fi RSSI fingerprinting based location source can also be combined after signal QS to further enhance the final localization performance. In this case, the confidence region of MEMS/Wi-Fi FTM integrated localization result in signal QE algorithm can be limited to the ellipse region.

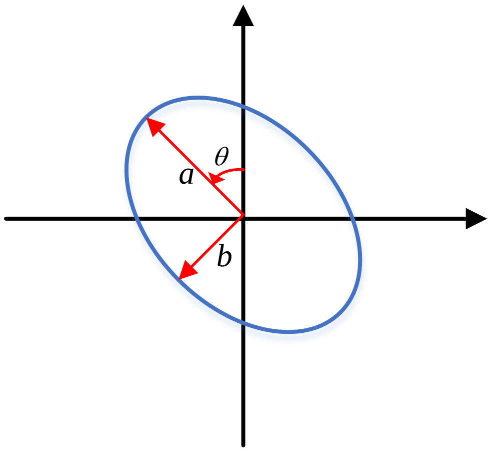

Figure 5-3 Ellipse-based Confidence Region

The center of the ellipse region is chosen as the output result of MEMS/Wi-Fi FTM integration model, and the major and minor semi-axis, and the azimuth can be acquired from the covariance matrix in the procedure of AUKF fusion:

$$\boldsymbol{F} = \begin{bmatrix} \sigma_N^2 & \sigma_{NE} \\ \sigma_{EN} & \sigma_E^2 \end{bmatrix} \tag{5-31}$$

where σ_N^2 and σ_E^2 indicate measured errors of the north and east location; σ_{EN} and σ_{NE} represent the covariance error calculated by north and east positions. Regarding the definition of confidence ellipse in engineering field [136], the major semi-axis of the ellipse is presented as:

$$a = s_e \cdot \sqrt{0.5(\sigma_N^2 + \sigma_E^2) + \sqrt{0.25(\sigma_E^2 - \sigma_N^2)^2 + \sigma_{NE}^2}} \tag{5-32}$$

The minor semi-axis can be described as:

$$b = s_e \cdot \sqrt{0.5(\sigma_N^2 + \sigma_E^2) - \sqrt{0.25(\sigma_E^2 - \sigma_N^2)^2 + \sigma_{NE}^2}} \tag{5-33}$$

The azimuth of the major semi-axis can be calculated by:

$$\theta = 0.5 \tan_4^{-1}(2\sigma_{NE} / (\sigma_E^2 - \sigma_N^2)) \tag{5-34}$$

At the beginning of crowdsourcing-based localization when people move from Wi-Fi FTM supported scenes to unsupported scenes, the initialization of localization has larger error variance due to insufficient iterations; therefore, the value of the parameter s_e is turned up to avoid removing the useful RSSI fingerprinting result. With the increasing amount of filter iterations, the value of s_e becomes smaller. Finally, it is remained unchanged to eliminate the gross error of Wi-Fi RSSI fingerprinting result.

The observed model in this case is described as:

$$\begin{cases} \delta \mathbf{z}_p^n = p_{rssi}^n - p_{MEMS/FTM}^n \\ \delta \mathbf{z}_v^n = v_{rssi}^n - v_{MEMS/FTM}^n \end{cases} \tag{5-35}$$

where p_{rssi}^n and v_{rssi}^n represent the Wi-Fi RSSI fingerprinting based position and speed in navigation coordinate, $p_{MEMS/FTM}^n$ and $v_{MEMS/FTM}^n$ indicate the MEMS/Wi-Fi FTM based fusion result.

Compared with existing multi-source fusion based wireless indoor localization approaches, our proposed multi-model integration framework comprehensively takes all the Wi-Fi FTM, RSSI fingerprinting, and MEMS sensors base location sources into consideration, and designs the corresponding integration models towards different indoor scenes contains different location sources. In addition, the proposed multi-model integration framework contains the robust signal QE module which provides the adaptive error prediction of each kind of location source and can maintain positioning accuracy in case of changing environments and terminals. Thus, the proposed hybrid positioning framework are more suitable for the large-scale indoor spaces and can adapt the complex real-word environments.

5.5 Tests and Evaluations

In this section, comprehensive experiments are organized to evaluate the accuracy and stability of proposed PINS algorithm and Wi-Fi/MEMS sensors integrated framework. Three typical indoor scenes are selected as experimental sites. Four Google Wi-Fi APs are deployed in the office scene to provide the Wi-Fi FTM function, Google Pixel 3 and Google Pixel 4 are used as the IoT terminals which support Android 10 based Wi-Fi ranging and can acquire RTT and RSSI information from surrounding Wi-Fi APs and also contain rich MEMS sensors required by proposed Wi-Fi and MEMS sensors integration framework. The sampling rates of MEMS sensors, Wi-Fi FTM, RSSI are 50 Hz, 5 Hz and 0.3 Hz, respectively. The selected experimental sites, installed Wi-Fi APs, and IoT terminals are shown in Figure 5-4.

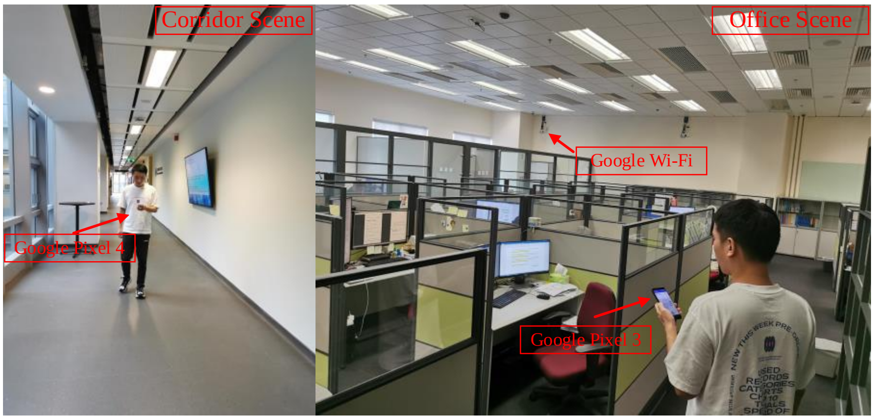

Figure 5-4 Total Experimental Sites and Equipment

5.5.1 Accuracy Evaluation of Hybrid Integration Models in Office Scene

In this section, three different kinds of multi-source integration models are proposed aiming at various wireless signals covered indoor scenes. In our work, a rectangular office which contains the serious multipath propagation and NLOS influences is applied for accuracy evaluation, and the tester's walking route is shown in Figure 5-5.

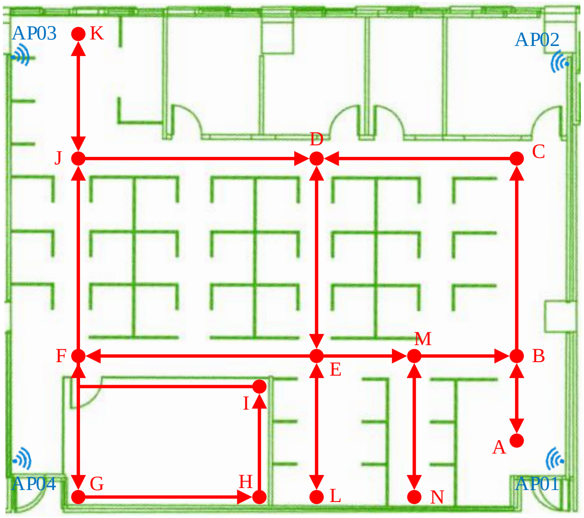

Figure 5-5 Office Scene and Testing Route

The tester began with the point A, passed by the points B, C, D, E, F, G, H, I, J, K, D, E, L, M, N, B, and returned to the point A. The performance comparison between PINS and three different types of integration models are compared in Figure 5-6:

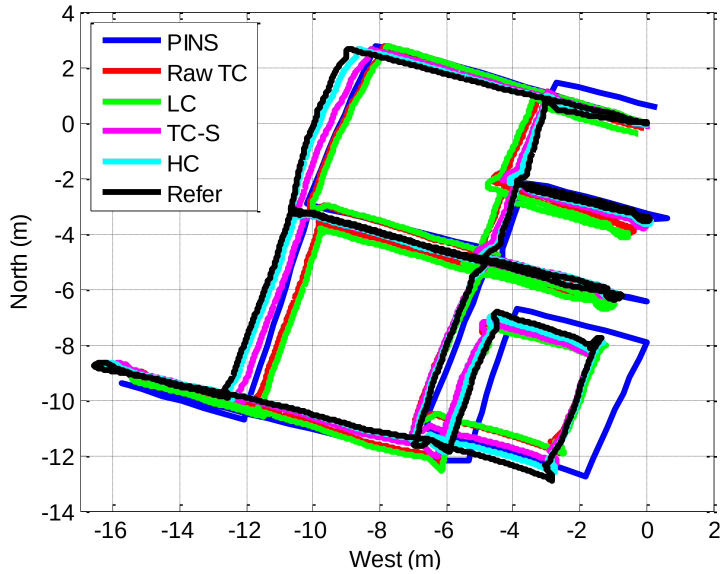

Figure 5-6 Performance of Different Integration Models

In addition, this procedure is repeated 15 times to estimate the long-term accuracy of proposed positioning integration structure, which is compared in Figure 5-7:

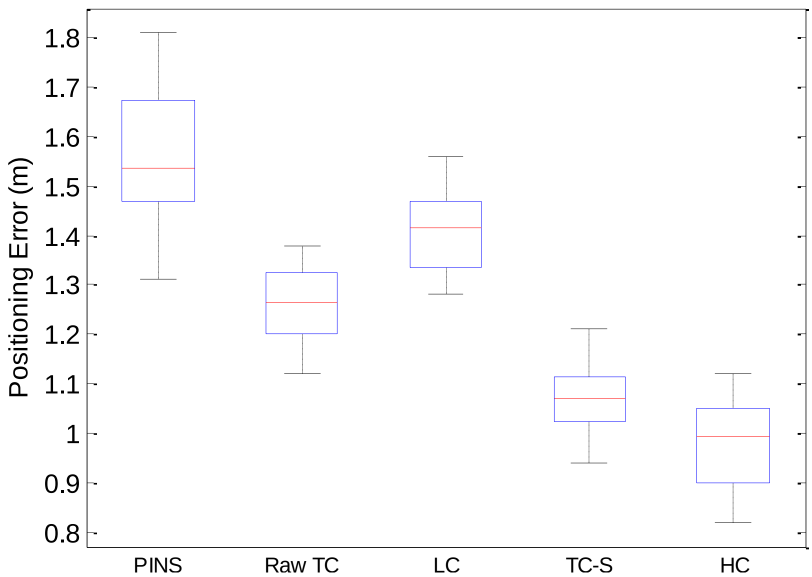

Figure 5-7 Positioning Errors Comparison

Figure 5-7 presents that in the Wi-Fi FTM supported environment, the proposed TC-S integration model effectively reduces the effect of ranging bias of Wi-Fi FTM, the estimated localization error is within 1.12 m in 75% compared with the positioning error of raw TC model within 1.33 m in 75%. The performance of LC model proves lower positioning accuracy than the TC-S model due to the fluctuations of collected RSSI signal. The HC model proves the highest positioning accuracy compared with the other three kinds of integration models, and the final positioning errors of five different localization models in office scene are 1.68 m, 1.33 m, 1.47 m, 1.12 m, and 1.05 m in case of 75%, respectively.

To give a comprehensive comparison of proposed QS approach and state-of-art algorithms, the Wi-Fi FTM outlier detection (OD) method proposed in [23] and the RSSI fingerprinting adaptive K selection (AKS) method proposed in [135] are applied for comparison. The positioning errors comparison of four models before and after using different signal QE approaches based on the same walking route in Figure 5-6 is described in Table 5-1:

Model / Error (m)	RAW TC	LC	TC-S	HC
Non-QE	1.51	1.75	1.29	1.22
QE	1.33	1.47	1.12	1.05
OD+AKS	1.41	1.65	1.21	1.14
Increased Ratio (%)	11.9/6.6	16/5.71	13.2/6.2	13.9/6.56

Table 5-1 Performance of Signal QS Algorithm

Table 5-1 presents the improved performance of proposed signal QE algorithm compared with non-QE. In non-QE, the measurement error variances of the Wi-Fi FTM and RSSI fingerprinting based location sources are fixed at constant values. In this case, the measurement errors of the Wi-Fi FTM and RSSI fingerprinting are set as 1m and 3m according to previous literatures. It can be found from Table 5-1 that the proposed signal QE algorithm effectively increases the accuracy of final integration models. The positioning errors of different integration models are decreased by 11.9%, 16%, 13.2%, and 13.9%, respectively. Compared with state-of-art quality control approaches, the proposed QE also reaches higher improvement of localization performance.

Besides, we give a comprehensive comparison between signal QE contained TC-S integration model with the state-of-art calibration-free positioning system (CPS) proposed in [107]. To be fair, the same location sources (Wi-Fi FTM and MEMS sensors) and the same walking route and test points in described Figure 5-5 are applied, Google Pixel 3 and Google Pixel 4 are adopted as the IoT platforms to provide Wi-Fi FTM functions and built-in sensors support. The CDF localization error of two algorithms is compared in Figure 5-8:

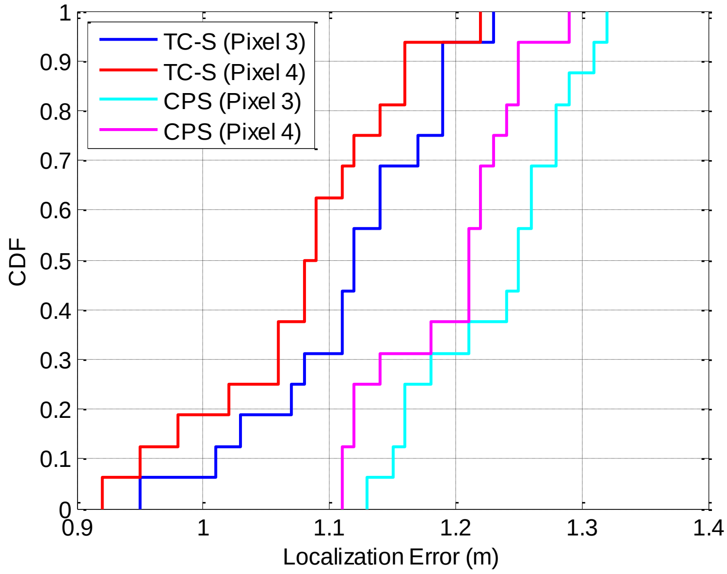

Figure 5-8 CDF Errors Comparison Between TC-S and CPS

Figure 5-8 describes that the proposed TC-S integration model proves better performance that the CPS algorithm under both Google Pixel 3 and Google Pixel 4 platforms. The final estimated mean error of proposed TC-S is 1.14 m in 75%, compared with the CPS's positioning error of 1.26 m in 75%.

5.5.2 Performance Evaluation of Hybrid Integration Models in Large-scaled Scenes

To evaluate the overall accuracy and university of proposed multi-source fusion based wireless integration framework in large-scaled indoor environments, two comprehensive indoor environments are selected, the first one is the teaching building contains two adjacent floors consist of corridor and office scenes, which are shown in Figure 5-9 and Figure 5-10:

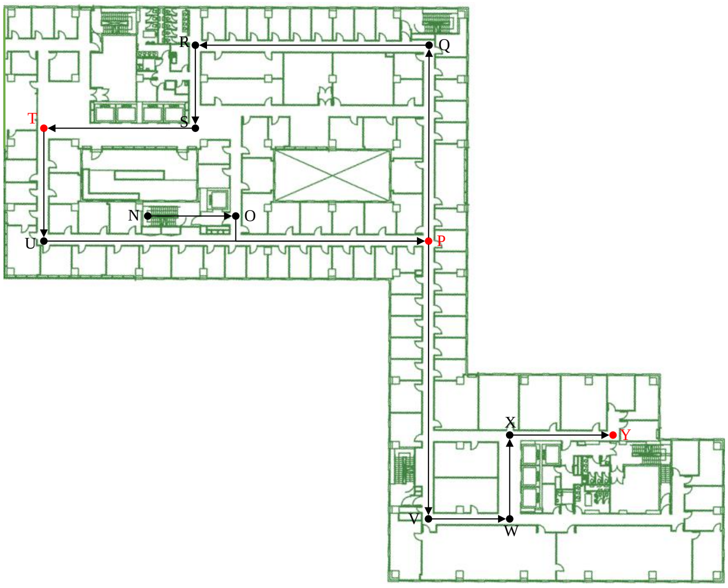

Figure 5-9 Experimental Site and Walking Route in 9th Floor

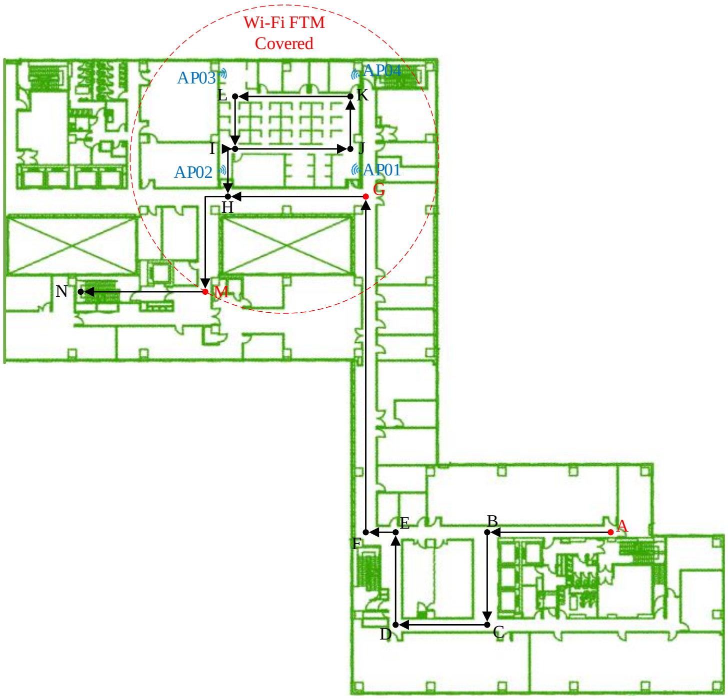

Figure 5-10 Experimental Site and Walking Route in 10th Floor

In Figure 5-10, four FTM supported Google APs are deployed in one of the laboratories, the theoretical coverage of Wi-Fi FTM signals is shown in the red circle, and other areas are FTM unsupported. The Wi-Fi fingerprinting database is constructed using the deep-learning based crowdsourced Wi-Fi fingerprinting database generation framework and over the number of 80 trajectories are selected and combined, which covers all the pedestrians' walking routes and can provide the priori information of specific indoor scenes by marking upon the on-line phase of Wi-Fi fingerprinting database generation. To evaluate the precision of proposed MS-WFRS, the testers walked from the test point A at the 10th floor, continuously passed by the points B, C, D, E, F, G, H, I, J, K, L, I, J, K, L, I, H, M, N, went down to the 9th floor, and passed by the route O, P, Q, R, S, T, U, P, V, W, X, Y. In this experiment, the hybrid integration model is applied in the laboratory area deployed with Wi-Fi FTM supported APs where both Wi-Fi fingerprinting/FTM exist, and loosely-coupled model is applied in the other areas covered with Wi-Fi fingerprinting. The 2D and 3D indoor positioning performance of proposed PINS and integration model is shown as follows:

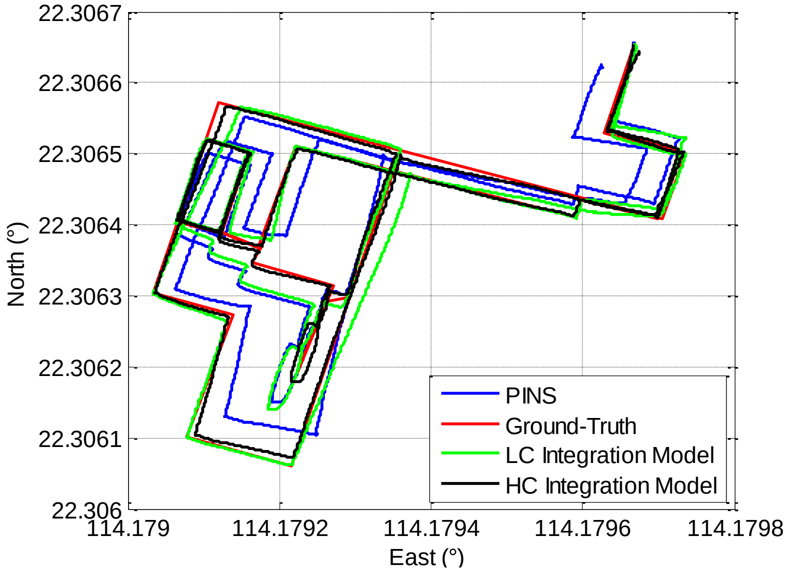

Figure 5-11 2D Positioning of Different Integration Models

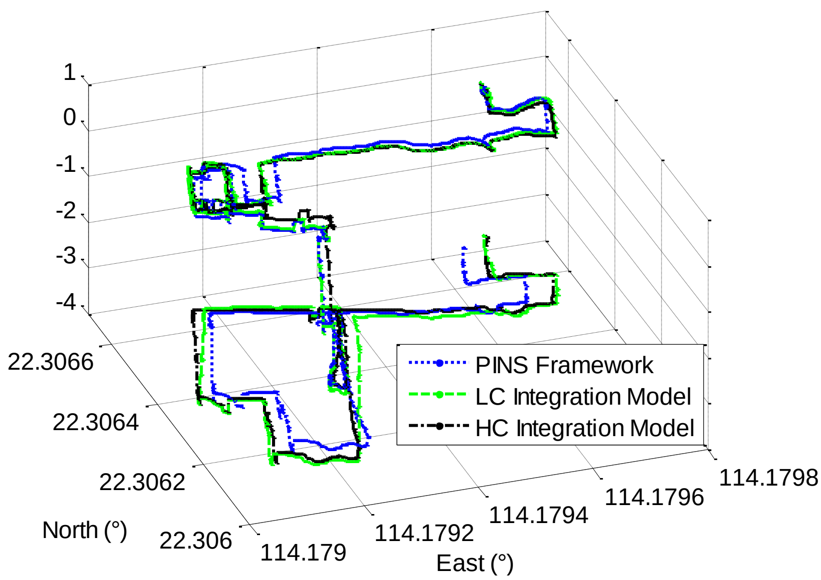

Figure 5-12 3D Positioning of Different Integration Models

Figure 5-12 shows that the MEMS sensors based PINS solution approach exists cumulative error even after heading and walking speed fusion by INS/PDR/magnetic integration, and larger positioning error exists in 3D indoor environments compared with 2D indoor environments due to the multi-floor switching. The proposed LC positioning model provides a wide-coverage solution by combining crowdsourced Wi-Fi fingerprinting and MEMS sensors, and the HC positioning model further takes all the location sources into consideration and enhances the location ability, especially in Wi-Fi FTM covered indoor spaces. The 2D and altitude positioning errors comparison results in 75% between MEMS, RSSI fingerprinting, LC, and HC based solutions in office, corridor and stairwell indoor scenes are described in Table 5-2:

Table 5-2 Error Comparison in Different Indoor Scenes

Model / Scenes	PINS	RSSI	LC	HC
Office Scene	2.42 m	2.89 m	1.67 m	1.08 m
Corridor Scene	3.84 m	3.55 m	1.89 m	1.76 m
Stairwell (Altitude)	1.53 m	1.76 m	0.48 m	0.44 m

Table 5-2 compares the positioning performance of different integration models, PINS, and RSSI fingerprinting in three different indoor scenes. It can be found from Table 5-2 that the PINS and RSSI fingerprinting approaches both prove larger positioning errors, which are originated by cumulative error and environmental interference, respectively. The LC integration model combines the advantages of short-term accuracy of MEMS sensors approach and long-term accuracy of crowdsourced RSSI fingerprinting approach and realizes the final positioning accuracy of 1.67 m and 1.89 m in 75% in two typical indoor scenes, respectively. The HC integration model further enhances the localization performance of LC model and achieves the meter-level accuracy within 1.08 m in 75% in Wi-Fi FTM covered office scene and also improves the positioning accuracy in corridor scene within 1.76 m in 75%. For the altitude estimation, the HC model also proves the best performance compared with the three other approaches, which reaches the 0.44 m in 75%.

Furthermore, the overall localization accuracy of proposed MS-WFRS is compared with the state-of-act literatures in corresponding indoor scenes, respectively, in which the Wi-Fi/DR structure (WDS) proposed in [12] is applied in the corridor scene using the Wi-Fi fingerprinting and MEMS sensors based location sources, to be fair, the same crowdsourced Wi-Fi fingerprinting database is applied The DRWMs algorithm proposed in [19] is applied in the office scene using the Wi-Fi FTM and MEMS sensors based location sources. In addition, the same walking route is applied which is described in Figure 5-11 and Figure 5-12, and the final localization comparison results in different indoor scenes are presented in Figure 5-13 and Figure 5-14:

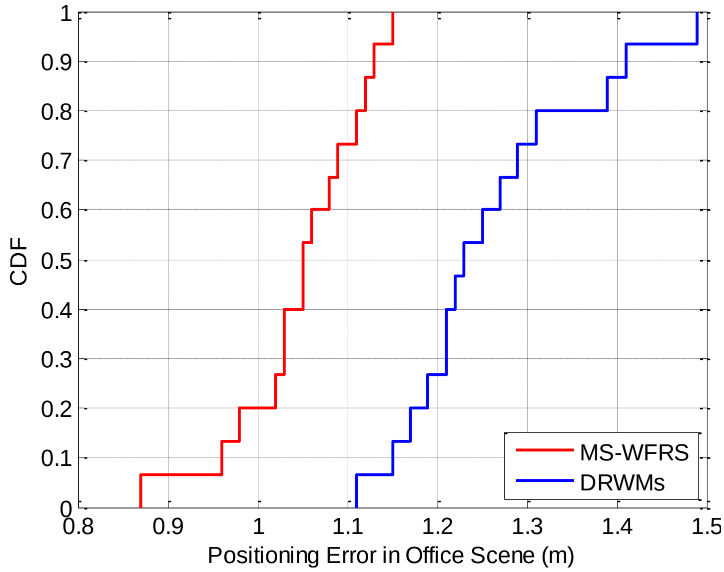

Figure 5-13 Errors Comparison under Office Scene

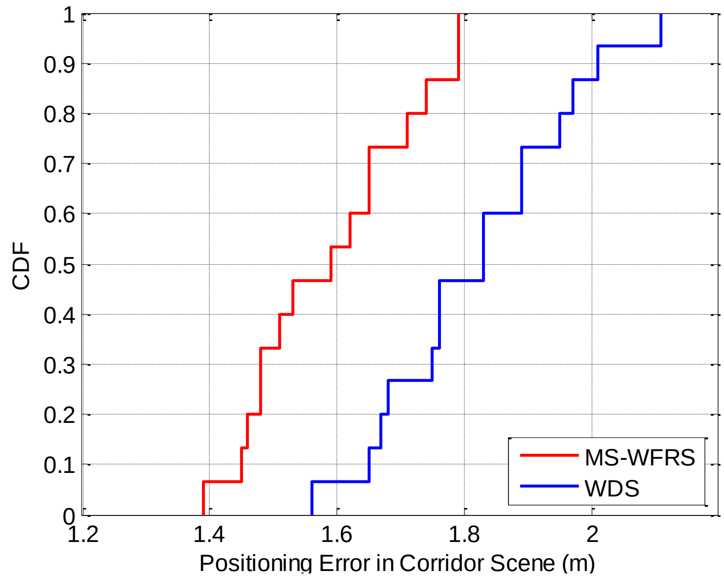

Figure 5-14 Errors Comparison under Corridor Scene

It can be found in Figure 5-14 that the proposed MS-WFRS framework achieves much better localization performance in both office and corridor scenes compared with state-of-art algorithms using the same location sources and fingerprinting database. In corridor scene, the proposed MS-WFRS reaches the higher positioning accuracy within 1.71 m in 75%, compared with the WDS approach with the accuracy of 1.94 m in 75%. In office scene, meter-level accuracy can be provided by the proposed MS-WFRS, which is within 1.11 m in 75%, compared with the positioning accuracy of 1.31 m in

75% provided by DRWMs approach.

Finally, we give a comprehensive comparison using multi-source fusion solution contains Wi-Fi FTM-Vhattachayya and RSS-Euclidean based fingerprinting (WFS-F) described in [137] with MS-WFRS framework proposed in this work. To be fair, the same crowdsourced RSSI based fingerprinting database is applied, and the FTM based fingerprinting database is collected using the method provided in [137]. The accuracy comparison under different positioning scenes is shown in Figure 5-15:

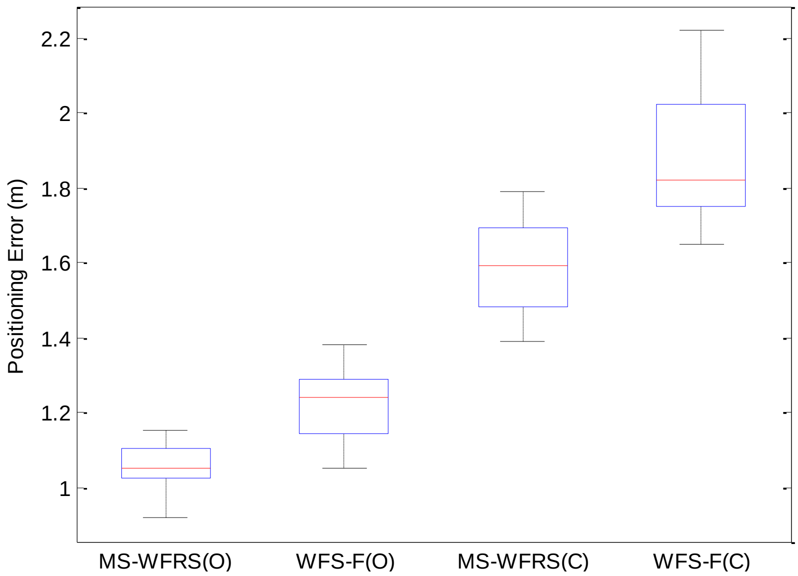

Figure 5-15 Errors Comparison in Different Scenes

Figure 5-15 presents that the proposed MS-WFRS framework proves much more robust localization performance compared with WFS-F approach in both office and corridor scenes. The positioning errors of two algorithms under office scene are within 1.11 m and 1.29 m in 75%, respectively. The positioning errors of two algorithms under corridor scene are within 1.71 m and 2.03 m in 75%, respectively.

The second selected test environment is a multi-floor contained shopping mall building, and the basic positioning solution has been provided in Section 4.4.4 using the APF based integration model based on the crowdsourced Wi-Fi RSSI fingerprinting and typical PDR solution [132], and the final estimated accuracy is acquired within 5.18 m in 75%. In this section, the proposed loosely-coupled (LC) integration model is applied to improve the accuracy of APF based integration model. The overall 3D structure of selected shopping mall is described in Figure 5-16.

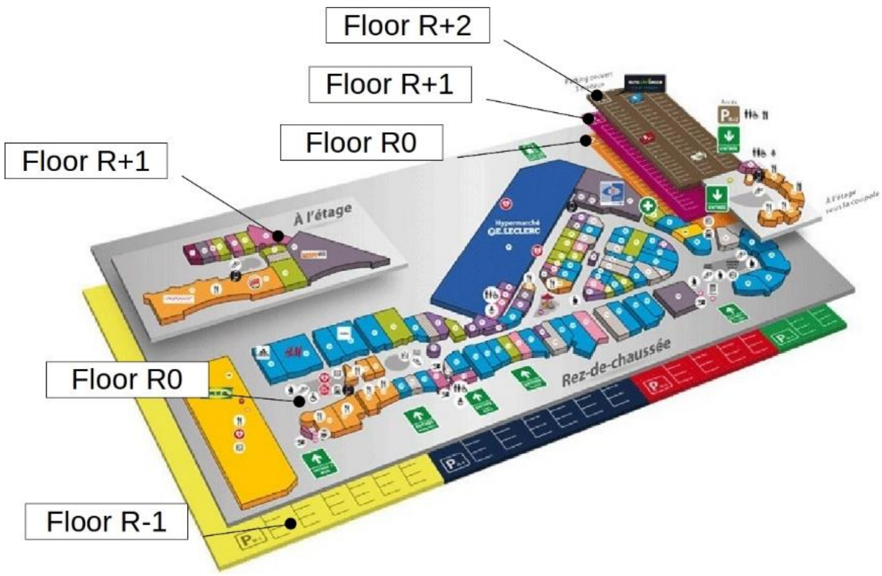

Figure 5-16 3D map of Shopping Mall Environment [130]

To provide the accuracy comparison between proposed APF in [132] and loosely-coupled integration model proposed in this chapter, the same test route is applied and the comparison results between Wi-Fi fingerprinting, APF and LC integration model are shown in Figure 5-17:

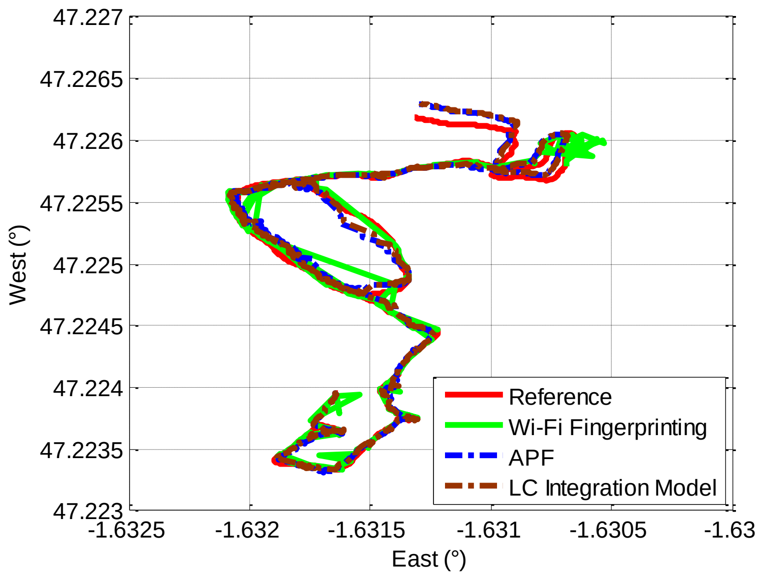

Figure 5-17 Comparison of Positioning Results in Shopping Mall Scene

Figure 5-17 shows that the proposed LC integration model further improve the performance of APF fusion proposed in [132], which is closer to the ground-truth trajectory. Also it can be found in Figure 5-17 that the completeness of final constructed Wi-Fi fingerprinting database proves significant effects on the final precision of integrated localization. The larger deviation of the trajectory from the ground-truth trajectory exists in the back part of the estimated trajectory due to the lack of effective fingerprint database information.

In general, we evaluate the accuracy of proposed Wi-Fi and MEMS sensors integration models in different indoor environments including the teaching building which contains the office scene and corridor scene, and shopping mall building which contains large-scaled open spaces. The estimated positioning errors in case of CDF 75% using different integration models under different indoor scenes are summarized in Table 5-3:

Table 5-3: Positioning Errors Comparison Between Different Model and Indoor Scenes

Scenes / Models	Office	Corridor	Shopping Mall
TC-S	1.12 m	-	-
LC	1.47 m	1.89 m	4.45 m
HC	1.05 m	1.71 m	-

In conclusion, the proposed hybrid integration models effectively combine the advantages of Wi-Fi FTM, crowdsourced Wi-Fi RSSI fingerprinting and MEMS sensors, and realize the impressive 3D indoor localization performance in large-scaled indoor spaces compared with state-of-art approaches. In addition, the proposed hybrid integration models can provide autonomous localization services through crowdsourced Wi-Fi fingerprinting database construction and can also provide meter-level positioning performance in Wi-Fi FTM supported environments. The overall positioning accuracy between 1.5 m to 4.5 m in CDF 75% can be acquired among the comprehensive experiments in different indoor environments.

5.6 Performance Analysis and Results

In order to enhance the accuracy and universality of Wi-Fi and MEMS sensors integrated 3D indoor navigation towards the next generation wireless positioning based on mobile terminals, this chapter presents the multi-source fusion based positioning framework, which is consist of a robust simplified MEMS sensors based localization solution, three different integration models, and corresponding signal quality evaluation approaches. The main contributions and the estimated results of Wi-Fi/MEMS sensors integrated location framework are summarized as follows:

(1) This chapter simplifies the original INS mechanization described in the MEMS sensors based 3D indoor localization structure by ignoring the rotation of the earth, which can significantly improve the efficiency and decrease the complexity of proposed PINS structure. Compared with existing MEMS sensors based approaches, our proposed PINS realizes the integration of INS and multi-level constraints and observed values. In addition, the proposed PINS integration approach can further be expanded into different multi-source fusion models towards specific location sources and positioning scenes.

2) This chapter proposes the signal quality evaluation (QE) algorithm aiming at evaluating the availability and uncertainty of measured Wi-Fi FTM and RSSI fingerprinting results aiming at improving the signal robustness in final fusion phase. In which the misclosure check (MC) method is applied to detect the received round-trip-time (RTT) indoors which contains NLOS measurement and initial bias, and the double-stage k-nearest neighbor (DS-KNN) method is developed to improve the matching performance of Wi-Fi RSSI fingerprinting and evaluate the location uncertainty of Wi-Fi RSSI fingerprinting result. The experimental results describes that the developed QE strategy can effectively eliminate positioning errors of different integration models, including 11.9% of raw TC model, 16% of LC model, 13.2% of TC-S model, and 13.9% of HC model respectively, which also prove better performance compared with other algorithms.

3) This chapter proposes three different types of multi-source fusion structures aiming at different location sources contained indoor scenes, in which the self-calibrated tightly-coupled integration model based on Wi-Fi FTM and MEMS sensors can provided meter-level positioning accuracy without calibration phase of Wi-Fi ranging; the loosely-coupled integration model based on Wi-Fi RSSI fingerprinting and MEMS sensors can realize autonomous localization and navigation database updating; and the hybrid fusion model organically combined all the location sources together aiming at providing precision-controllable positioning in complex and large-scaled indoor spaces. The use of different fusion structures significantly increases the accuracy and universality of 3D indoor localization.

Finally, we design comprehensive experiments to evaluate the performance of proposed Wi-Fi and MEMS sensors integrated structure in different 3D indoor environments using different walking routes time periods. The experimental results show that the integration of Wi-Fi FTM, RSSI fingerprinting, and MEMS sensors effectively improve the 3D positioning performance compared with the single location sources. In which the Wi-Fi FTM and MEMS sensors based tightly-coupled integration model is proved to provide meter-level location information in case of Wi-Fi FTM protocol supported indoor spaces, and the crowdsourced Wi-Fi RSSI fingerprinting and MEMS sensors based loosely-couple integration model can provide more universal and autonomous localization performance without known the deployment information of location stations. In addition, the hybridly-coupled integration model can further improve the performance of multi-source fusion based indoor localization and realize the positioning scene switching aiming at changeable location sources contained environments. The comprehensive experiments show that the proposed LC integration model combines the advantages of short-term accuracy of MEMS sensors approach and long-term accuracy of crowdsourced RSSI fingerprinting approach and realizes the final positioning accuracy of 1.67 m and 1.89 m in 75% in two typical indoor scenes, respectively. The HC integration model further enhances the localization performance of LC model and achieves the meter-level accuracy within 1.08 m in 75% in Wi-Fi FTM covered office scene and also improves the positioning accuracy in corridor scene within 1.76 m in 75%. For the altitude estimation, the HC model also proves the best performance compared with the three other approaches, which reaches the 0.44 m in 75%.

In the future, with the development of IoT terminals, more and more LBS aimed location sources and protocols will be applied, such as AOA, CSI, and angle of departure (AOD). In addition, the improved signal detection technology and signal bandwidth further enhance the performance of time-of-flight (TOF) based localization methods such as Wi-Fi RTT and UWB two-way ranging (TWR). The application of high precision location features would make the IoT terminals based sub-meter indoor wireless localization more possible.

Chapter 6: Conclusion and Future Works

This chapter summarizes the conclusions and contributions of the research and provides recommendations and possible future work.

6.1 Conclusion

This thesis provides a reliable 3D indoor pedestrian positioning solution by using MEMS sensors integrated in IoT terminals, Wi-Fi FTM, crowdsourced Wi-Fi RSSI fingerprinting. By taking better advantage of the merits of DR, Wi-Fi FTM, Wi-Fi RSSI fingerprinting, the proposed algorithm can provide a robust 3D indoor pedestrian positioning solution that has the accuracy of 1.5-4.5 m (CDF in 75%) and can autonomously generate the Wi-Fi fingerprinting database instead of point-to-point collection. Furthermore, this algorithm can provide precision-controllable positioning performance by combining different location sources and meter-level positioning accuracy can be realized in Wi-Fi FTM covered indoor spaces.

Also, by taking better advantage of the merits of DR, Wi-Fi FTM, and crowdsourced Wi-Fi RSSI fingerprinting, the proposed algorithm has the following advantages:

1) The algorithm can significantly improve the attitude estimation and 3D DR results using IoT terminals integrated MEMS sensors without the need for any external calibration equipment or user intervention, which can be applied in case of complex and changeable indoor environments under different handheld modes.
2) The algorithm can provide accurate forward localization and trajectory optimization results based on the daily-life data acquired from MEMS sensors and sparsely deployed Wi-Fi FTM stations, BLE nodes, and QR codes based landmarks, which can further be applied for autonomous crowdsourced navigation database construction.
3) The algorithm can realize automatic error prediction of crowdsourced trajectories, and develop two different WPS systems including self-calibrated Wi-Fi FTM positioning system and crowdsourced Wi-Fi RSSI fingerprinting positioning system, aiming at providing precision-controllable location services in hybrid indoor scenes.
4) The algorithm can organically integrate the two different WPS solutions and PINS solution towards large-scale indoor spaces covered by different location sources. In addition, the corresponding signal QE strategy is combined in the

final multi-source fusion model to increase the robustness of single location source.

To be specific, compared with previous hybrid navigation algorithms or structures, the main innovation points of this research are:

1) Chapter 3 develops a simple but robust 3D indoor localization and optimization system uses the combination of smartphone integrated MEMS sensors and sparse deployed landmark points including the Wi-Fi FTM station, BLE node, and QR code. Multi-level constraints and multi-level observed values, which are applied as the MEMS sensors based observation model in AUKF in order to eliminate effects of cumulative and divergence errors, magnetic interference, and different handheld modes added on the INS mechanization based 3D attitude and location update. In addition, two different types of navigation trajectory optimization algorithms including backward-AUKF and GD are proposed and evaluated in this chapter, aiming at different platforms and application scenes, which achieve meter-level accuracy of reconstructed 3D navigation trajectory. Comprehensive experiments in two complex 3D indoor environments indicate that the proposed PINS structure reaches the 2D positioning accuracy of 1.38 m, 1.44m, 1.91m, 1.73 m in 80%, and altitude calculation accuracy of 0.68 m, 0.71 m, 0.67 m, 0.63 m in 80%, under four different kinds of handheld modes: reading, phoning, swaying, and pocket. The proposed backward-AUKF and GD algorithms can further improve the accuracy of forward navigation, the estimated ratios of accuracy improvement backward-AUKF and GD in reading mode are 27.94% and 25%, in phoning mode are 39.44% and 32.39%, in swaying mode are 34.33% and 28.36%, in pocket mode are 33.33% and 26.98%.
2) Chapter 4 presents two different Wi-Fi positioning systems, including Wi-Fi FTM based calibration and positioning system and crowdsourced Wi-Fi fingerprinting based positioning system, aiming at providing autonomous and precision-controllable 3D indoor localization performance in large-scale and multiple scenes contained indoor spaces. For the Wi-Fi FTM positioning system, three different Wi-Fi FTM calibration strategies are proposed and compared for the estimation of changing bias between different IoT terminals and Wi-Fi APs. The real-world estimation in office scene shows that the PB approach proves the best positioning performance within 1.01 m in 75%, and the accuracy of GD AUKF is a little higher than TC approach, and the positioning errors of two

algorithms are 1.09 m and 1.19 m in 75%, respectively. For the crowdsourced Wi-Fi RSSI fingerprinting system, a comprehensive structure for crowdsourced trajectories modelling, pre-calibration, optimization, and classification is proposed and a novel deep-learning based trajectory error prediction and crowdsourced trajectory merging is presented for the final Wi-Fi fingerprinting database construction, and the estimated matching accuracy Wi-Fi fingerprinting is within 3.75 m in 75% under office scene and also has the good performance under large-scaled shopping mall scene with the PDR/Wi-Fi fingerprinting integration accuracy of 5.18 m in 75%.

3) Chapter 5 proposes a unified Wi-Fi/MEMS sensors integration framework, which is consist of a robust simplified MEMS sensors based localization solution, three different integration models (TC-S integration model, LC integration model, HC integration model), and corresponding signal quality evaluation (QE) strategies. The comprehensive experiments show that the proposed LC integration model combines the advantages of short-term accuracy of MEMS sensors approach and long-term accuracy of crowdsourced RSSI fingerprinting approach and realizes the final positioning accuracy of 1.67 m and 1.89 m in 75% in two typical indoor scenes, respectively. The HC integration model further enhances the localization performance of TC-S model and LC model and achieves the meter-level accuracy within 1.08 m in 75% in Wi-Fi FTM covered office scene and also improves the positioning accuracy in corridor scene within 1.76 m in 75%. For the altitude estimation, the HC model also proves the best performance compared with the three other approaches, which reaches the 0.44 m in 75%. In addition, the proposed LC model further improves the positioning accuracy under large-scaled shopping mall scene, which is increased from 5.18 m in 75% to 4.45 m in 75%.

6.2 Recommendations for Future Works

Based on the achieved results and conclusions about the implementation of an autonomous localization algorithm using the integration of Wi-Fi FTM, crowdsourced RSSI fingerprinting and MEMS sensors towards large-scale indoor spaces, it is recommended to optimize it and extend this research for future developments. The future works include:

- Conducting deeper investigations on the requirements for different application scenarios (e.g., hospitals, malls, underground, etc.), and optimizing the algorithm framework according to the specific application scenario.
- Further reducing the time- and manpower- cost of generating and updating the crowdsourced Wi-Fi fingerprinting database. In addition, mobile mapping technology can be further combined for providing accurate indoor map information and constructing the navigation database simultaneously.
- Taking more complex motion and handheld modes into consideration and expanding the proposed algorithm to improve the adaptability.
- It is also worth exploring the more state-of-art location technologies and location sources which will be supported by emerging IoT terminals, such as the BLE AOA, UWB, LiDAR.
- As the most economical and efficient system is desired, a more simplified version of the multi-source integration algorithm needs to be developed for the IoT terminals.

Last but not least, the real-time algorithm needs to be tested thoroughly using different hardware platforms for a variety of scenarios such as large-scaled buildings with multiple floors and with more complex internal structures.

Reference

[1] Potorti F, Torres-Sospedra J, Quezada-Gaibor D, et al. Off-line Evaluation of Indoor Positioning Systems in Different Scenarios: The Experiences from IPIN 2020 Competition[J]. IEEE Sensors Journal, 2021.

[2] Liu Z, Zhang A, Yao Y, et al. Analysis of the performance and robustness of methods to detect base locations of individuals with geo-tagged social media data[J]. International Journal of Geographical Information Science, 2021, 35(3): 609-627.

[3] Li Y, Zhuang Y, Hu X, et al. Toward location-enabled IoT (LE-IoT): IoT positioning techniques, error sources, and error mitigation[J]. IEEE Internet of Things Journal, 2020, 8(6): 4035-4062.

[4] Ruizhi C, Liang C. Indoor Positioning with Smartphones: The State-of-the-art and the Challenges[J]. Acta Geodaetica et Cartographica Sinica, 2017, 46(10): 1316.

[5] Deng Z, Yu Y, Yuan X, et al. Situation and development tendency of indoor positioning[J]. China Communications, 2013, 10(3): 42-55.

[6] A. R. J. Ruiz, and S. G. Fernando, "Comparing ubisense, bespoon, and decawave uwb location systems: Indoor performance analysis," IEEE Transactions on instrumentation and Measurement, vol.66, no.8, pp.2106-2117, 2017.

[7] N W. He, P. H. Ho, J. Tapolcai, “Beacon Deployment for Unambiguous Positioning,” IEEE Internet of Things Journal, vol.4, no.5, pp.1370-1379, 2017.

[8] B. Jang, and H. Kim., "Indoor positioning technologies without offline fingerprinting map: A survey," *IEEE Communications Surveys & Tutorials*, vol.21, no.1, pp.508-525, 2018.

[9] X. D. Dang, C. Qi, and H. Y. Zhu., "Indoor Multiple Sound Source Localization via Multi-Dimensional Assignment Data Association," IEEE/ACM Transactions on Audio, Speech, and Language Processing, vol.27, no.12, pp.1944-1956, 2019.

[10] B. Stéphane, and K. Martin., "Indoor PDR performance enhancement using minimal map information and particle filters," IEEE/ION Position, Location and Navigation Symposium, IEEE, 2008.

[11] Li Y, Hu X, Zhuang Y, et al. Deep reinforcement learning (DRL): Another perspective for unsupervised wireless localization[J]. IEEE Internet of Things Journal, 2019, 7(7): 6279-6287.

[12] Zhuang Y, Wang Q, Shi M, et al. Low-power centimeter-level localization for indoor mobile robots based on ensemble Kalman smoother using received signal strength[J]. IEEE Internet of Things Journal, 2019, 6(4): 6513-6522.

[13] B. Zhou, Q. Li, Q. Mao, et al., “Activity sequence-based indoor pedestrian localization using smartphones,” IEEE Transactions on Human-Machine Systems, vol.45, no.5, pp.562-574, 2014.

[14] J. Shang, X. Hu, W. Cheng, et al., “Gridiloc: A backtracking grid filter for fusing the grid model with PDR using smartphone sensors,” Sensors, vol.16, no.12, pp.2137-2159, 2016.

[15] D. Jiang, N. Marius, Y. U. Xiao, et al., “ViNav: A Vision-based Indoor Navigation System for Smartphones,” IEEE Transactions on Mobile Computing, vol.18, no.6, pp.1461-1475, 2018.

[16] W. Elloumi, A. Latoui, R. Canals, et al., “Indoor Pedestrian Localization With a Smartphone: A Comparison of Inertial and Vision-Based Methods,” IEEE Sensors Journal, vol.16, no.13, pp.5376-5388, 2016.

[17] K. Chintalapudi, A. P. Iyer, V. N. Padmanabhan., “Indoor localization without the pain,” Sixteenth International Conference on Mobile Computing and NETWORKING, pp.173-184, 2010.

[18] K. Liu, X. Liu, and X. Li, “Guoguo: Enabling fine-grained smartphone localization via acoustic anchors,” IEEE Transactions on Mobile Computing, vol.15, no.5, pp.1144-1156, 2016.

[19] Y. Yu, R. Z. Chen, L. Chen, et al., “A Robust Dead Reckoning Algorithm Based on Wi-Fi FTM and Multiple Sensors,” Remote Sensing, vol.11, no.5, pp.504-526, Mar.2019.

[20] X. Zhong, and J. R. Hopgood, “Particle filtering for tdoa based acoustic source tracking: Nonconcurrent multiple talkers,” Signal Process, vol.96, pp.382-394, 2014.

[21] S. He, S. H. G. Chan., “Wi-fi fingerprint-based indoor positioning: recent advances and comparisons,” IEEE Communications Surveys & Tutorials, vol.18, no.1, pp.466-490, 2015.

[22] Chen R, Li Z, Ye F, et al. Precise Indoor Positioning Based on Acoustic Ranging in Smartphone[J]. IEEE Transactions on Instrumentation and Measurement, 2021, 70: 1-12.

[23] S. H. Xu, R. Z. Chen, et al., “Locating Smartphones Indoors Using Built-In Sensors and Wi-Fi Ranging With an Enhanced Particle Filter,” IEEE Access, vol.7, pp.95140-95153, 2019.

[24] Li Y. Integration of MEMS sensors, WiFi, and magnetic features for indoor pedestrian navigation with consumer portable devices[J]. 2016.

[25] Y. Zhuang, J. Yang, L. Qi, et al., “A Pervasive Integration Platform of Low-Cost MEMS Sensors and Wireless Signals for Indoor Localization,” IEEE Internet of Things Journal, vol.5, no.6, pp.4616-4631, 2017.

[26] H. Liu, et al., "Survey of wireless indoor positioning techniques and systems," *IEEE Transactions on Systems, Man, and Cybernetics, Part C (Applications and Reviews)*, vol.37, no.6, pp.1067-1080, 2007.

[27] Li Y, Yan K, He Z, et al. Cost-effective localization using RSS from single wireless access point[J]. IEEE Transactions on Instrumentation and Measurement, 2019, 69(5): 1860-1870.

[28] X. S. Guo, et al., "Accurate WiFi localization by fusing a group of fingerprints via a global fusion profile," *IEEE Transactions on Vehicular Technology*, vol.67, no.8, pp.7314-7325, 2018.

[29] W. Sun, et al., "Augmentation of fingerprints for indoor WiFi localization based on Gaussian process regression," *IEEE Transactions on Vehicular Technology*, vol.67, no.11, pp.10896-10905, 2018.

[30] IEEE Standard for Information technology–Telecommunications and information exchange between systems Local and metropolitan area networks–Specific requirements - Part 11: Wireless LAN Medium Access Control (MAC) and Physical Layer (PHY) Specifications". "IEEE Std 802.11-2016 (Revision of IEEE Std 802.11-2012)", pages 1–3534, Dec 2016.

[31] Han K, Yu S M, Kim S L, et al. Exploiting User Mobility for Wi-Fi RTT Positioning: A Geometric Approach[J]. IEEE Internet of Things Journal, 2021.

[32] L. Banin, et al., "Scalable Wi-Fi client self-positioning using cooperative FTM-sensors," *IEEE Transactions on Instrumentation and Measurement*, vol.68, no.10, pp.3686-3698, 2018.

[33] J. Z. Lu, et al., "Hybrid navigation method of INS/PDR based on action recognition," *IEEE Sensors Journal*, vol.18, no.20, pp.8541-8548, 2018.

[34] R. Z. Chen, et al., "Sensing strides using EMG signal for pedestrian navigation," *GPS solutions*, vol.15, no.2, pp.161-170, 2011.

[35] Y. Yu, R. Chen, L. Chen, et al., “A Novel 3-D Indoor Localization Algorithm Based on BLE and Multiple Sensors,” IEEE Internet of Things Journal, vol.8, DOI 10.1109/JIOT.2021.3055794, no.11, pp.9359-9372, 2021.

[36] L. E. Díez, A. Bahillo, J. Otegui, and T. Otim, “Step Length Estimation Methods Based on Inertial Sensors: A Review,” IEEE Sensors Journal, vol. 18, DOI 10.1109/JSEN.2018.2857502, no. 17, pp. 6908-6926, Jul. 2018.

[37] Y. Li, Y. Zhuang, et al., “Self-Contained Indoor Pedestrian Navigation Using Smartphone Sensors and Magnetic Features,” IEEE Sensors Journal, vol. 16, DOI 10.1109/JSEN.2016.2591824, no. 19, pp. 7173- 7182, Oct. 2016.

[38] H. Zhao, Z. Wang, et al., “Adaptive gait detection based on foot-mounted inertial sensors and multi-sensor fusion,” Information Fusion, vol. 52, DOI 10.1016/j.inffus.2019.03.002, no. 1, pp. 157-166, Dec. 2019.

[39] N. El-Sheimy, Y. Li., “Indoor navigation: state of the art and future trends,” Satellite Navigation, vol.2, DOI 10.1186/s43020-021-00041-3, no.1, pp.1-23, 2021.

[40] G. Y. Guo, R. Z. Chen, et al., “A Pose Awareness Solution for Estimating Pedestrian Walking Speed,” remote sensing, vol. 11, DOI 10.3390/rs11010055, no. 5, pp. 55-73, Dec. 2018.

[41] Li Y, Chen R, Niu X, et al. Inertial Sensing Meets Machine Learning: Opportunity or Challenge?[J]. IEEE Transactions on Intelligent Transportation Systems, 2021.

[42] E. Foxlin, “Pedestrian tracking with shoe-mounted inertial sensors,” IEEE Computer Graphics and Applications, vol. 25, DOI 10.1109/MCG.2005.140, no. 6, pp. 28-46, Nov. 2005.

[43] S. Rajagopal, “Personal dead reckoning system with shoe mounted inertial sensors,” Master’s Degree Project, Stockholm, Sweden, 2008.

[44] X. Tong, Y. Su, et al., “A Double-Step Unscented Kalman Filter and HMM-Based Zero-Velocity Update for Pedestrian Dead Reckoning Using MEMS Sensors,” IEEE Transactions on Industrial Electronics, vol. 67, DOI 10.1109/TIE.2019.2897550, no. 1, pp. 581-591, Feb. 2019.

[45] Y. Li, J. Georgy, et al., “Autonomous Calibration of MEMS Gyros in Consumer Portable Devices,” IEEE Sensors Journal, vol. 15, DOI 10.1109/JSEN.2015.2410756, no. 7, pp. 4062-4072, Mar. 2015.

[46] F. Gu, K. Khoshelham, C. Yu, et al., “Accurate step length estimation for pedestrian dead reckoning localization using stacked autoencoders,” IEEE Transactions on Instrumentation and Measurement, vol.68, DOI 10.1109/TIM.2018.2871808, no.8, pp.2705-2713, 2018.

[47] P. Zhang, X. Chen, X. Ma, et al., “SmartMTra: Robust indoor trajectory tracing using smartphones,” IEEE Sensors Journal, vol.17, DOI 10.1109/JSEN.2017.2692263, no.12, pp.3613-3624, 2017.

[48] A. Poulose, B. Senouci, D. S. Han, “Performance analysis of sensor fusion techniques for heading estimation using smartphone sensors,” IEEE Sensors Journal, vol.19, DOI 10.1109/JSEN.2019.2940071, no.24, pp.12369-12380, 2019.

[49] T. Liu, J. Kuang, W. Ge, et al., “A Simple Positioning System for Large-Scale Indoor Patrol Inspection Using Foot-Mounted INS, QR Code Control Points, and Smartphone,” IEEE Sensors Journal, vol.21, DOI 10.1109/JSEN.2020.3030934, no.4, pp.4938-4948, 2021.

[50] Y. Li, Z. He, Z. Gao Z, et al., “Toward robust crowdsourcing-based localization: A fingerprinting accuracy indicator enhanced wireless/magnetic/inertial integration approach,” IEEE Internet of Things Journal, vol.6, DOI 10.1109/JIOT.2018.2889303, no.2, pp.3585-3600, 2018.

[51] Kuang J, Niu X , Chen X . Robust Pedestrian Dead Reckoning Based on MEMS-IMU for Smartphones[J]. Sensors, 2018, 18(5):1391.

[52] L. F. Shi, et al., "A robust pedestrian dead reckoning system using low-cost magnetic and inertial sensors," IEEE Transactions on Instrumentation and Measurement, vol.68, no.8, pp.2996-3003, 2018.

[53] J. S. Lee, and S. M. Huang., "An Experimental Heuristic Approach to Multi-Pose Pedestrian Dead Reckoning Without Using Magnetometers for Indoor Localization," IEEE Sensors Journal, vol.19, no.20, pp.9532-9542, 2019.

[54] H. Yan, Q. Shan, Y. Furukawa., “RIDI: Robust IMU double integration,” Proceedings of the European Conference on Computer Vision (ECCV). pp.621-636, 2018.

[55] S. Herath, H. Yan, Y. Furukawa., “RoNIN: Robust Neural Inertial Navigation in the Wild: Benchmark, Evaluations, & New Methods,” 2020 IEEE International Conference on Robotics and Automation (ICRA). IEEE, pp.3146-3152, 2020.

[56] K. Chang, D. Han, “Crowdsourcing-based radio map update automation for Wi-Fi positioning systems,” Proceedings of the 3rd ACM SIGSPATIAL International Workshop on Crowdsourced and Volunteered Geographic Information, DOI 10.1145/2676440.2676441, pp. 24-31, Nov. 2014.

[57] H. Y. Luo, F. Zhao, et al., “Constructing an Indoor Floor Plan Using Crowdsourcing Based on Magnetic Fingerprinting,” sensors, vol. 17, DOI 10.3390/s17112678, no. 11, pp. 2678-2693, Oct. 2017.

[58] D. Taniuchi, T. Maekawa, "Automatic update of indoor location fingerprints with pedestrian dead reckoning," ACM Transactions on Embedded Computing Systems, vol. 14, DOI 10.1145/2667226, no. 2, pp. 1-23, Feb. 2015.

[59] N. Yu, C. X. Xiao, Y. F. Wu, and R. J. Feng, "A Radio-Map Automatic Construction Algorithm Based on Crowdsourcing," sensors, vol. 16, DOI 10.3390/s16040504, no. 4, pp. 504-536, Apr. 2016.

[60] P. Zhang, R. Z. Chen, et al., "A Localization Database Establishment Method Based on Crowdsourcing Inertial Sensor Data and Quality Assessment Criteria," IEEE Internet of Things Journal, vol. 5, DOI 10.1109/JIOT.2018.2817599, no. 6, pp. 4764-4777, Dec. 2018.

[61] Wang H, Sen S, Elgohary A, et al. No need to war-drive: Unsupervised indoor localization[C]//Proceedings of the 10th international conference on Mobile systems, applications, and services. 2012: 197-210.

[62] G. Shen, Z. Chen, P. Zhang, T. Moscibroda, and Y. Zhang, "Walkie–Markie: Indoor pathway mapping made easy," in Proc. NSDI, 2013, pp. 85–98.

[63] C. Luo, H. Hong, and M. C. Chan, "PiLoc: A self-calibrating participatory indoor localization system," in Proc. Int. Symp. Inf. Process. Sensor Netw. (Ipsn), 2014, pp. 143–154.

[64] C. Luo, H. Hong, M. C. Chan, J. Li, X. Zhang, and Z. Ming, "MpiLoc: Self-calibrating multi-floor indoor localization exploiting participatory sensing," IEEE Trans. Mobile Comput., vol. 17, no. 1, pp. 141–154, Jan. 2018.

[65] Li T, Han D, Chen Y, et al. IndoorWaze: A crowdsourcing-based context-aware indoor navigation system[J]. IEEE Transactions on Wireless Communications, 2020, 19(8): 5461-5472.

[66] Wi-Fi CERTIFIED Location. (2017). https://google/BSUCdG. Wi-Fi CERTIFIED Location. Accessed 9 September 2018.

[67] Leor Banin, Uri Schatzberg, and Yuval Amizur. (2016). Wi-Fi ftm and map information fusion for accurate positioning. In 2016 International Conference on Indoor Positioning and Indoor Navigation, Sapporo, Japan.

[68] Zheng Yang, Zimu Zhou, & Yunhao Liu. (2013). From rssi to csi:indoor localization via channel response. ACM Computing Surveys (CSUR), 46(2), 1-32.

[69] Sharp, I., & Yu, K. (2014). Indoor toa error measurement, modeling, and analysis. IEEE Transactions on Instrumentation & Measurement, 63(9), 2129-2144.

[70] Bisio, I., Cerruti, M., Lavagetto, F., Marchese, M., Pastorino, M., & Randazzo, A., et al. (2014). A trainingless wifi fingerprint positioning approach over mobile devices. IEEE Antennas & Wireless Propagation Letters, 13(1), 832-835.

[71] Chan, Y. T., Tsui, W. Y., & So, H. C. (2006) Time-of-arrival based localization under NLOS conditions. IEEE Transactions on Vehicular Technology, 55(1):17-24.

[72] Al-Jazzar, S., Caffery, J., & You, H. R. (2007). Scattering-model-based methods for TOA location in NLOS environments. IEEE Transactions on Vehicular Technology, 56(2), 583-593.

[73] He, Z., Ma, Y., & Tafazolli, R. (2013). Improved High Resolution TOA Estimation for OFDM-WLAN Based Indoor Ranging. IEEE Wireless Communications Letters, 2(2):163-166.

[74] Rea, M., Fakhreddine, A., & Giustiniano, D., (2017). Filtering Noisy 802.11 Time-of-Flight Ranging Measurements From Commoditized WiFi Radios. IEEE/ACM Transactions on Networking, 2017:1-14.

[75] Banin, L.; Schatzberg, U.; Amizur, Y. (2013). Next generation indoor positioning system based on WiFi time of flight. In Proceedings of Proc. 26th Int. Tech. Meeting Satellite Division Inst. Navigat.(ION GNSS+); pp. 975-982.

[76] Schatzberg, U.; Banin, L.; Amizur, Y. (2014). Enhanced WiFi ToF indoor positioning system with MEMS-based INS and pedometric information. In Proceedings of 2014 IEEE/ION Position, Location and Navigation Symposium-PLANS 2014; pp. 185-192.

[77] Dvorecki, N.; Bar-Shalom, O.; Banin, L.; Amizur, Y. (2019). A Machine Learning Approach for Wi-Fi RTT Ranging. Proceedings of the 2019 International Technical Meeting of The Institute of Navigation, January 28-31, Hyatt Regency Reston, Reston, Reston Virginia.

[78] Niesen, U.; Ekambaram, V.N.; Jose, J.; Wu, X.J.I.T.o.V.T. (2017). Intervehicle Range Estimation From Periodic Broadcasts, 66, 10637-10646.

[79] Mohamed Ibrahim, et al., "Verification: Accuracy evaluation of WiFi fine time measurements on an open platform," Proceedings of the 24th Annual International Conference on Mobile Computing and Networking, pp.417-427, Nov 2018.

[80] Jacob T Biehl, Andreas Girgensohn, and Mitesh Patel., "Achieving Accurate Room-Level Indoor Location Estimation with Emerging IoT Networks," Proceedings of the 9th International Conference on the Internet of Things, pp.1-8, Oct 2019.

[81] Jérôme Henry, and Montavont Nicolas. "Fingerprinting using Fine Timing Measurement," Proceedings of the 17th ACM International Symposium on Mobility Management and Wireless Access, pp.49-56, Nov 2019.

[82] K. Jiokeng, G. Jakllari, A. Tchana, et al., “When FTM discovered MUSIC: accurate WiFi-based ranging in the presence of multipath,” IEEE Conference on Computer Communications. IEEE, DOI 10.1109/INFOCOM41043.2020.9155464, pp. 1857-1866, 2020.

[83] Yu Y, Chen R, Chen L, et al. Precise 3-D indoor localization based on Wi-Fi FTM and built-in sensors[J]. IEEE Internet of Things Journal, 2020, 7(12): 11753-11765.

[84] W. Shao, H. Luo, F. Zhao, et al., “Accurate Indoor Positioning Using Temporal–Spatial Constraints Based on Wi-Fi Fine Time Measurements,” IEEE Internet of Things Journal, vol.7, no.11, pp.11006-11019, 2020.

[85] Zhuang, Yuan, et al. "Evaluation of two WiFi positioning systems based on autonomous crowdsourcing of handheld devices for indoor navigation." IEEE Transactions on Mobile Computing 15.8 (2015): 1982-1995.

[86] Yoo, Jaehyun, Karl Henrik Johansson, and Hyoun Jin Kim. "Indoor localization without a prior map by trajectory learning from crowdsourced measurements." IEEE Transactions on Instrumentation and Measurement 66.11 (2017): 2825-2835.

[87] Gu, Yang, et al. "Trajectory estimation and crowdsourced radio map establishment from foot-mounted imus, wi-fi fingerprints, and gps positions." IEEE Sensors Journal 19.3 (2018): 1104-1113.

[88] Li Z, Zhao X, Liang H. Automatic construction of radio maps by crowdsourcing PDR traces for indoor positioning[C]//2018 IEEE International Conference on Communications (ICC). IEEE, 2018: 1-6.

[89] Li, You, et al. "WiFi-aided magnetic matching for indoor navigation with consumer portable devices." Micromachines 6.6 (2015): 747-764.

[90] Zhuang, Yuan, et al. "Wireless access point localization using nonlinear least squares and multi-level quality control." IEEE Wireless Communications Letters 4.6 (2015): 693-696.

[91] Ju, Hojin, So Young Park, and Chan Gook Park. "A smartphone-based pedestrian dead reckoning system with multiple virtual tracking for indoor navigation." IEEE Sensors Journal 18.16 (2018): 6756-6764.

[92] D. Zhang, et al., "On distinguishing the multiple radio paths in rss-based ranging," 2012 Proceedings IEEE INFOCOM. IEEE, 2012.

[93] W. H. Xiong, et al., "High resolution TOA estimation based on compressed sensing," Wireless Personal Communications, vol.84, no.4 pp.2709-2722, 2015.

[94] S. F. Chuang, W. R. Wu, and Y. T. Liu., "High-resolution AoA estimation for hybrid antenna arrays," IEEE Transactions on Antennas and Propagation, vol.63, no.7, pp.2955-2968, 2015.

[95] K. S. Wu, et al., "CSI-based indoor localization," IEEE Transactions on Parallel and Distributed Systems, vol.24, no.7, pp.1300-1309, 2012.

[96] H. Zou, et al., "WinIPS: WiFi-based non-intrusive indoor positioning system with online radio map construction and adaptation," IEEE Transactions on Wireless Communications, vol.16, no.12, pp.8118-8130, 2017.

[97] S. H. Li, et al., "Passive localization of standard WiFi devices." IEEE Systems Journal, vol.13, no.4, pp.3929-3932, 2019.

[98] C. S. Wu, Z. Yang, Z. Zhou, et al., “Mitigating large errors in WiFi-based indoor localization for smartphones,” IEEE Transactions on Vehicular Technology, vol.66, no.7, pp.6246-6257, 2016.

[99] Wu, X.; Shen, R.; Fu, L.; Tian, X.; Liu, P.; Wang, X. iBILL: Using iBeacon and inertial sensors for accurate indoor localization in large open areas. IEEE Access 2017, 5, 14589–14599.

[100] Yoon, P.K.; Zihajehzadeh, S.; Kang, B.S.; Park, E.J. Robust biomechanical model-based 3-D indoor localization and tracking method using UWB and IMU. IEEE Sens. J. 2017, 17, 1084–1096.

[101] Davidson, P.; Piché, R. A survey of selected indoor positioning methods for smartphones. IEEE Commun. Surv. Tutor. 2017, 19, 1347–1370.

[102] Yu, N.; Zhan, X.; Zhao, S.; Wu, Y.; Feng, R. A Precise Dead Reckoning Algorithm Based on Bluetooth and Multiple Sensors. IEEE Internet Things J. 2018, 5, 336–351.

[103] Feng D, Wang C, He C, et al. Kalman-filter-based integration of IMU and UWB for high-accuracy indoor positioning and navigation[J]. IEEE Internet of Things Journal, 2020, 7(4): 3133-3146.

[104] Xie, H.; Gu, T.; Tao, X.; Ye, H.; Lu, J. A reliability-augmented particle filter for magnetic fingerprinting based indoor localization on smartphone. IEEE Trans. Mobile Comput. 2016, 15, 1877–1892.

[105] Y. Zhuang, N. El-Sheimy., “Tightly-coupled integration of WiFi and MEMS sensors on handheld devices for indoor pedestrian navigation,” IEEE Sensors Journal, vol.16, DOI 10.1109/JSEN.2015.2477444, no.1, pp.224-234, 2015.

[106] Y. Wang, Z. Li, J. Gao, et al., “Deep neural network-based Wi-Fi/pedestrian dead reckoning indoor positioning system using adaptive robust factor graph model,” IET Radar, Sonar & Navigation, vol.14, DOI 10.1049/iet-rsn.2019.0260, no.1, pp.36-47, 2019.

[107] J. Choi, and Y. S. Choi., "Calibration-free positioning technique using Wi-Fi ranging and built-in sensors of mobile devices," IEEE Internet of Things Journal, vol.8, no.1, pp.541-554, 2020.

[108] L. Li, X. Guo, N. Ansari, et al., “A hybrid fingerprint quality evaluation model for wifi localization,” IEEE Internet of Things Journal, vol.6, no.6, pp.9829-9840, 2019.

[109] Y. Li, Y. Zhuang, P. Zhang, et al., “An improved inertial/wifi/magnetic fusion structure for indoor navigation,” Information Fusion, vol.34, no.1, pp.101-119, 2017.

[110] SHIN, E.-H. 2005a. Estimation techniques for low-cost inertial navigation. UCGE report, 20219.

[111] S. H. Shin, C. G. Park, “Adaptive step length estimation algorithm using optimal parameters and movement status awareness,” Medical engineering & physics, vol.33, no.9, pp.1064-1071, 2011.

[112] Harvey WeinBerg, “AN-602: Using the ADXL202 in Pedometer and Personal Navigation Applications,” Analog Devices, vol.2, no.2, pp.1-6, 2002.

[113] R. Chen, L. Pei L and Y. Chen, “A smart phone based PDR solution for indoor navigation,” in Proceedings of the 24th international technical meeting of the satellite division of the institute of navigation, 2011, pp.1404-1408.

[114] M. Ma, Q. Song, Y. Li, et al., “A heading error estimation approach based on improved Quasi-static magnetic Field detection,” in 2016 International Conference on Indoor Positioning and Indoor Navigation (IPIN). IEEE, 2016, pp.1-8.

[115] Mahony, Robert, Tarek Hamel, and Jean-Michel Pflimlin. "Nonlinear complementary filters on the special orthogonal group." IEEE Transactions on automatic control 53.5 (2008): 1203-1218.

[116] L. You, et al., “Multi-sensor multi-floor 3D localization with robust floor detection,” IEEE Access, vol.6, pp.76689-76699, 2018.

[117] Li, Z.; Trappe, W.; Zhang, Y.; Nath, B. Robust statistical methods for securing wireless localization in sensor networks. In Proceedings of the Information Processing in Sensor Networks (IPSN 2005), Los Angeles, CA, USA, 25–27 April 2005; pp. 1–9.

[118] H. W. Chae, J. H. Choi, J. B. Song., “Robust and Autonomous Stereo Visual-Inertial Navigation for Non-Holonomic Mobile Robots,” IEEE Transactions on Vehicular Technology, vol.69, DOI 10.1109/TVT.2020.3004163, no.9, pp.9613-9623, 2020.

[119] T. Liu, X. J. Niu, et al., “Doppler shift mitigation in acoustic positioning based on pedestrian dead reckoning for smartphone,” IEEE Transactions on Instrumentation and Measurement, vol. 1, DIO 10.1109/TIM.2020.3010384, no. 1, pp. 1-1, Jul 2020.

[120] W. Xue, W. Qiu, X. Hua, et al., “Improved Wi-Fi RSSI measurement for indoor localization,” IEEE Sensors Journal, vol.17, no.7, pp.2224-2230, Apr. 2017.

[121] D. J. Berndt, J. Clifford, “Using dynamic time warping to find patterns in time series,” KDD workshop, vol.10, no.16, pp.359-370, 1994.

[122] P. Malekzadeh, M. Salimibeni, M. Atashi, et al., “Gaussian Mixture-based Indoor Localization via Bluetooth Low Energy Sensors,” IEEE sensors, 2019.

[123] https://www.the-qrcode-generator.com

[124] S. Sabatelli, M. Galgani, L. Fanucci, et al., “A double-stage Kalman filter for orientation tracking with an integrated processor in 9-D IMU,” IEEE Transactions on Instrumentation and Measurement, vol.62, DOI 10.1109/TIM.2012.2218692, no.3, pp.590-598, 2012.

[125] Yu Y, Chen R, Liu Z, et al. Wi-Fi fine time measurement: Data analysis and processing for indoor localisation[J]. J. Navigat., 2020, 73(5): 1-23.

[126] Sun Z, Zhang Y, Ren Q. A Reliable Localization Algorithm Based on Grid Coding and Multi-Layer Perceptron[J]. IEEE Access, 2020, 8: 60979-60989.

[127] Basu D, Data D, Karakus C, et al. Qsparse-local-SGD: Distributed SGD with quantization, sparsification, and local computations[J]. arXiv preprint arXiv:1906.02367, 2019.

[128] Zhou B, Zheng T, Huang J, et al. A pedestrian network construction system based on crowdsourced walking trajectories[J]. IEEE Internet of Things Journal, 2020, 8(9): 7203-7213.

[129] Li Z, Zhao X, Zhao Z, et al. WiFi-RITA positioning: Enhanced crowdsourcing positioning based on massive noisy user traces[J]. IEEE transactions on wireless communications, 2021, 20(6): 3785-3799.

[130] Renaudin V, Ortiz M, Perul J, et al. Evaluating indoor positioning systems in a shopping mall: The lessons learned from the IPIN 2018 competition[J]. IEEE Access, 2019, 7: 148594-148628.

[131] Li Z, Zhao X, Hu F, et al. SoiCP: A seamless outdoor–indoor crowdsensing positioning system[J]. IEEE internet of things journal, 2019, 6(5): 8626-8644.

[132] Yu Y, Chen R, Chen L, et al. Autonomous 3D Indoor Localization Based on Crowdsourced Wi-Fi Fingerprinting And MEMS Sensors[J]. IEEE Sensors Journal, 2021.

[133] L. Wang, et al., "NLOS Mitigation in Sparse Anchor Environments with the Misclosure Check Algorithm," Remote Sensing vol.11, no.7, pp.773-796, 2019.

[134] K. R. Koch., “Parameter estimation and hypothesis testing in linear models,” Springer Science & Business Media, 2013.

[135] J. S. Hu, et al., "Experimental Analysis on Weight K-Nearest Neighbor Indoor Fingerprint Positioning," IEEE Internet of Things Journal, vol.6, no.1, pp.891-897, 2018.

[136] R. C. Luo, and C. C. Chang., "Multi-sensor fusion and integration: A review on approaches and its applications in mechatronics," IEEE Transactions on Industrial Informatics, vol.8, no.1, pp.49-60, 2011.

[137] S. Huilla, C. Pepi, M. Antoniou, et al., “Indoor Localization with Wi-Fi Fine Timing Measurements Through Range Filtering and Fingerprinting Methods,” IEEE 31st Annual International Symposium on Personal, Indoor and Mobile Radio Communications. IEEE, pp. 1-7, 2020.